

FAHRTBERICHT zur Forschungsreise SO101 - CONDOR

CRUISE REPORT SO101 - CONDOR

Roland von Huene, José Corvalán, John Korstgard
and the scientific party of the CONDOR cruises



95 S 2

GEOMAR
- Bibliothek -
Wischhofstr. 1-3
D-24148 Kiel

Fahrtberichte

GEOMAR

Forschungszentrum für marine Geowissenschaften
der Christian-Albrechts-Universität zu Kiel
Wischhofstraße 1-3
24148 Kiel
GERMANY

[1995]

**TEILNEHMERLISTE
SHIPBOARD SCIENTISTS**

CONDOR 101

Name	Institution	Leg.No.		
von Huene, R.	GEOMAR, GERMANY	1	2	3
Weinrebe, W.	GEOMAR, GERMANY	1	2	3
Klaeschen, D.	GEOMAR, GERMANY		2	
Díaz, J.	GEOMAR, GERMANY	1	2	3
Ranero, C.	GEOMAR, GERMANY	1	2	
Harms, G.	GEOMAR, GERMANY	1	2	3
Spiegler, D.	GEOMAR, GERMANY			3
Biebow, N.	GEOMAR, GERMANY			3
Locker, S.	GEOMAR, GERMANY			3
Krüger, D.	UNI BOCHUM, GERMANY	1	2	3
Morales, E.	Universidad Católica de Valparaíso, CHILE			3
Vergara, H.	SHOA, CHILE	1	2	3
Yáñez, G.	SERNAGEOMIN, CHILE		2	
Corvalán, J.	SERNAGEOMIN, CHILE			3
Valenzuela, E.	Universidad de Chile, CHILE			3
Wall, R.	SERNAGEOMIN, CHILE			3
Korstgard, J.	UNI AARHUS, DENMARK		2	
Trinhammer, P.	UNI AARHUS, DENMARK		2	
Laursen, J.	UNI AARHUS, DENMARK		2	
Scholl, D.	USGS, USA		2	
Kay, S.	Cornell University, USA			3
Domínguez, S.	UNI MONTPELLIER, FRANCE	1	2	3
Segl, M.	UNI BREMEN, GERMANY			3
Beese, D.	UNI BREMEN, GERMANY			3
Lamy, F.	UNI BREMEN, GERMANY			3

Institutionen/Institutions

GEOMAR

Forschungszentrum für
marine Geowissenschaften der
Christian-Albrechts-Universität zu Kiel
Wischofstraße 1-3, 24148 Kiel, GERMANY

Tel.: 0049-431-72-02-272
FAX: 0049-431-72-02-293

SERNAGEOMIN

Servicio Nacional de Geología y Minería
Avda. Santa María 0104
Casilla 1347
Santiago, CHILE

Tel.: 0056-27-37-50-50
FAX: 0056-27-37-20-26

SHOA

Servicio Hidrografico y Oceanografico
de la Armada de Chile
Casilla 324
Valparaiso, CHILE

Tel.: 0056-32-28-26-97
FAX: 0056-32-28-35-37

Universidad de Chile

Depto. de Geología
Facultad de Ciencias Físicas y Matemáticas
Plaza Ercilla
Santiago
CHILE

Tel: 0056-2-67-84-532

Geologisk Institut

Aarhus Universitet
Finlandsgade 6-8
DK-8000 Aarhus N, DENMARK

Tel.: 0045-86-13-43-11
FAX: 0045-86-10-10-03

U.S. Geological Survey

Branch of Pacific Marine Geology, MS 999
345 Middlefield Road
Menlo Park, CA 94025, U.S.A.

Tel.: 001-415-354-3127
FAX: 001-415-354-3191

Universität Bremen

Fachbereich 5 - Geowissenschaften -
Postfach 33 04 40
D-28334 Bremen, GERMANY

Tel.: 0049-421-218-3920
FAX: 0049-421-218-3166

Ruhr-Universität Bochum

Institut für Geophysik
Postfach 10 21 48
D-4630 Bochum 1

Tel.: 0049-234-700-3270
FAX: 0049-234-709-4181

Université de Montpellier II-ISTEEM

Laboratoire de Geophysique
et Tectonique
Place E. Bataillon
34095 Montpellier Cedex 05, FRANCE

Tel.: 0033-67-14-33-01
FAX: 0033-67-52-39-08

INHALTSVERZEICHNIS/TABLE OF CONTENTS

	page
Teilnehmerliste/Scientific party	
Zusammenfassung	1
Executive Summary	3
Acknowledgements	5
1. Introduction and objectives	6
2. Chronology of the cruise	11
3. Hydrosweep swathmapping	13
3.1 General morphology	13
3.2 Ocean crust	17
3.3 The continental slope	23
4. Magnetic anomalies	31
4.1 Introduction	31
4.2 Magnetometer/Instrumentation	31
4.3 Data acquisition	33
4.4 Data reduction and preliminary processing	33
4.5 Diurnal removal and leveling of the lines	35
4.6 Data processing	43
4.7 Preliminary modeling and interpretation	43
4.8 Conclusions	61
5. Seismic reflection lines	63
5.1 Seismic acquisition	63
5.2 Seismic processing	73
6. Parasound	115
6.1 Instrument	115
6.2 Selected Records	115
7. Geologic Investigations	123
7.1 Sediment sampling from cores	123
7.2 Rocks recovered by dredging	127
7.3 Foraminifers of core and dredge samples	138
7.4 Siliceous microfossils of core samples and calcareous nannofossils of dredge samples	145
8. Appendices	
Appendix 1: Geographic names in this report	151
Appendix 2: Kapitnsbericht	152
Appendix 3: Stations	169

ZUSAMMENFASSUNG

Das marine Geoforschungsprojekt CONDOR wurde vom 23. März bis zum 8. Mai 1995 während der Reise SO101 mit dem FS SONNE vor der Küste Valparaisos, Chile durchgeführt. Die Gruppe der an CONDOR teilnehmenden Wissenschaftler setzt sich international aus deutschen, chilenischen, dänischen, französischen, spanischen und amerikanischen Forschern. Ziele des Projektes sind das Verständnis von Naturkatastrophen und des tektonischen Systems des konvergenten chilenischen Kontinentalgrabens. Hierzu werden erstmals geophysikalische Aufnahmen tektonischer Strukturen an den Stellen durchgeführt, an denen der chilenische Kontinentalrand durch die Kollision des Juan Fernandez Rückens geformt wird. Dort, wo der Rücken unter den kontinentalen Rand subduziert ist, befindet sich das nördliche Ende der zentralen vulkanischen Zone, die gleichzeitig mit einer wesentlichen Veränderung der Benioffzone verbunden ist. Eine Verbindung mit dem Juan Fernandez Rücken ist bekannt, aber noch nicht verstanden. Die Geologie des Kontinentalrandes ist durch Material aus Dredgen und Sedimentkernen beschrieben. Die Kernproben wurden unter anderem genommen, um den Sedimenttransport und die Palaeoumgebung zu verstehen. In dem Projekt sind mit der Geophysik, der Geochemie und der Palaeontologie Disziplinen aus weiten Teilen der Geowissenschaften vertreten. Neben der Hauptförderung durch das "Bundesministerium für Bildung, Wissenschaft, Forschung und Technologie" (BMBF) hat jede beteiligte Institution einen finanziellen und sachlichen Beitrag geleistet.

Die multidisziplinäre Forschung wurde in drei aufeinanderfolgenden Abschnitten durchgeführt. Während des ersten Teils sind Hydrosweep und magnetische Anomalien entlang systematisch verteilter Kurse vermessen worden. Größere morphologische Strukturen in großer Tiefe wurden mit Reflexionsseismik und Parasound während des zweiten Abschnitts untersucht. Aus den akustischen Daten wurden Stellen für die Probennahme mit Dredge und Kerngerät während des dritten Abschnitts ausgewählt. Diese normale Abfolge der Untersuchungssequenzen konnte nur durch das sofortige Prozessing der Meßdaten an Bord ermöglicht werden. Nur dann kann die Planung des folgenden Abschnitts auf die Ergebnisse der vorigen Meßreihe zurückgreifen und die hier gewonnenen neuen Erfahrungen sofort in die aktuelle Untersuchung einbauen. Um dies zu ermöglichen, wurde auf dem FS SONNE eine leistungsfähige Workstationumgebung aufgebaut. Mit diesen Anlagen konnten die Hydrosweepdaten prozessiert werden und in Karten und perspektivischen Diagrammen aufbereitet und dargestellt werden. Weiterhin wurden die magnetischen Meßwerte mit den üblichen Reduktionen versehen und in Karten dargestellt. Ebenso wurden die Profile der Mehrkanalseismik prozessiert und geplottet. In begrenztem Umfang konnte eine "real time" Palaeontologie während der Probennahmen durchgeführt werden und damit zu einer Optimierung der Probenlokationen während der fortschreitenden Messungen beitragen. Eine der großen Leistungen des CONDOR Projektes liegt in der Verarbeitung der Meßwerte an Bord, die üblicherweise erst später als ein Jahr nach den Forschungsreisen vorliegen. Die vorläufigen

Ergebnisse der an Bord durchgeführten Datensynthese deuten bereits die zu erwartenden inhaltsreichen Ergebnisse einer weitergeführten und laborgestützten Datenanalyse an.

Die hochauflösende Darstellung der Morphologie (Abbildung) offenbart eine Vielzahl von Bruchstellen, kleinen Vulkankegeln und größeren extrusiven Merkmalen entlang des Juan Fernandez Rücken. Magnetische Anomalien zeigen, daß diese Strukturen der normalen ozeanischen Kruste überprägt wurden. Dort, wo der Rücken in den chilenischen Tiefseeegraben eintritt bildet er eine Barriere von 2,5 km Höhe. Hinter diesem Hindernis ist die Grabenachse auf 30 km Länge mit Sediment gefüllt. Die achsiale Füllung nördlich dieser Rückenbarriere ist deutlich geringer. Dieser Unterschied im Eintrag in die Subduktionszone ist verbunden mit tektonischen Unterschieden entlang des unteren und mittleren Kontinentalhanges. Im Süden, dort wo der Sedimenteintrag am größten ist, bilden die für Faltungen in Akkretionskeilen typischen längeren Rücken den unteren Teil des Hanges. Der mittlere Teil des Hanges scheint mehr dem kontinentalen Typ zu entsprechen und besteht aus Gesteinen, die für den zugehörigen Küstenabschnitt typisch sind. Über dem subduzierten Rücken sind in der Grabenachse deutlich weniger Sedimente abgelagert. Hier zeigt der untere Teil des Hanges älteres kontinentales Gestein und ist von nicht anlagernden Typus. Im mittleren Teil befindet sich an dieser Stelle das Valparaiso Becken, das größte bekannte "Fore-Arc" Becken südlich der peruanischen Grenze. Seismische Daten zeigen in der nördlichen Hälfte stark deformierte Sedimente, die gegen einen diagonal verlaufenden Rücken ausgerichtet sind. Dieser Rücken scheint sich über dem subduzierten Juan Fernandez Rücken gebildet zu haben. Im nördlichen Gebiet befindet sich eine Einbuchtung im Kontinentalhang, deren Morphologie einen tektonischen Einbruch nahelegt. In den aufgenommenen Daten wird ein enger Zusammenhang zwischen der Morphologie der subduzierten Platte und den tektonischen Prozessen in der oberen Platte gesehen.

Durch den, an der Mündung des von Santiago kommenden Rio Maipo beginnenden, unterseeischen San Antonio Canyon wird der Sedimenttransport vom Land über den Kontinentalrand geleitet. Flüsse nördlich dieses Bereiches enden bereits im Valparaiso Fore-Arc Becken. Dieses Transportschema definiert die Grenzgebiete für den Transport anthropogenen Materials von der Küste. Die rauhe Topographie der Canyons und der landwärtigen Seite des Valparaiso Beckens sind als Zielgebiete für weitere Arbeiten der Fischereibiologen ausgewählt worden.

Das Projekt CONDOR wird mit der Reise SO103 des FS SONNE fortgesetzt. Basierend auf den an Bord erzielten Ergebnissen werden OBH Refraktionsdaten in Verbindung mit einem landgestützten Array aufgenommen. Die Ergebnisse sollten weitere Aussagen über die Beiträge der tektonische Umgebung zur Generierung von Erdbeben in diesem stark bevölkerten Gebiet Chiles ermöglichen.

EXECUTIVE SUMMARY

The CONDOR marine geoscience investigation offshore Valparaiso Chile was accomplished during RV SONNE cruise 101, from 23 March to 8 May, 1995. The CONDOR investigators are international including German, Chilean, Danish, French, Spanish, and US scientists. Objectives of the project are to understand natural hazards and the tectonic system of the Chile convergent margin through a geophysical assessment of tectonic structures where the Chilean margin is impacted by the colliding Juan Fernandez Ridge. Where the ridge has subducted beneath the continental margin is the northern end of the central volcanic zone and also a fundamental change in the Benioff zone. The association with the Juan Fernandez Ridge collision of these first order features is recognised but not understood. The margin geology was characterise with rock samples recovered by dredging, and sediment cores. Cores were taken to help understand sediment transport and the paleoenvironment. The geosciences represented in the project include geophysics, petrology, geochemistry, and paleontology. Although principal funding and direction is from the BMBF (Bundesministerium für Bildung, Wissenschaft, Forschung und Technologie) most participating institution contributed financially to the project.

The multidisciplinary scientific investigations were accomplished on three successive legs. During the first leg, Hydrosweep and a magnetic anomaly data were collected on a systematic pattern of tracks. Major morphological features were investigated in greater depth during the second leg with the seismic reflection and Parasound instrument systems. The acoustic data were used to locate sampling sites which were cored and dredged on the third leg. This normal sequence of investigation could be accomplished on one cruise only if the data could be processed during shipboard acquisition so that each leg could plan on the information of the leg which preceded it. Therefore a powerful workstation environment was constructed on SONNE to process Hydrosweep data for maps and perspective diagrams, to reduce and make maps of the magnetic anomalies, and to process lines from the multichannel seismic data. Limited "real time" paleontology was accomplished during the sampling leg to optimise site location as the leg progressed. A major accomplishment of CONDOR is the onboard processing of data which brought geophysical data to a status normally not realised until a year after a cruise. The preliminary onboard synthesis of the data that follows indicates the potential results of a more deliberate shorebased data analysis.

High resolution morphology reveals many fractures, small volcanic cones, and larger extrusive features along the Juan Fernandez Ridge. Magnetic anomalies show that these features were superimposed on normal oceanic crust. Where the ridge enters the Chile Trench, it forms a barrier 2.5 km high behind which a sediment body 30 km wide fills the trench axis. The axial sediment north of the ridge barrier is much less. This different input to the subduction zone is associated with tectonic differences along the lower and middle continental slope. In the south where the sediment input is greatest, longer ridges typical of the folds in an accretionary prism form the lower slope. The middle slope appears to have a continental affinity and is covered by

sediment typical of the adjacent coastal area. Over the subducted ridge where the axis has little trench sediment fill, the lower slope exposes older continental rock and this segment of the margin is fundamentally non-accretionary. The Middle slope here contains the Valparaiso Basin, the largest forearc basin known south of the Peruvian border. Seismic data reveal highly deformed sediment in the northern half of the basin against a diagonal ridge inferred to have formed above the subducted Juan Fernandez Ridge. The area north of the ridge contains an embayment in the continental slope in which the morphology suggests tectonic collapse. A close correspondence between the morphology of the subducting plate and the tectonic processes in the upper plate is observed in the data.

Sediment transport from the land is directed across the margin to the trench in San Antonio submarine canyon which begins at the mouth of the Rio Maipo, draining Santiago. Rivers north of this area end in the Valparaiso forearc basin. This transport pattern identifies the terminal areas for anthropogenic materials carried from the coasts. The rugged topography of the canyons and the landward side of Valparaiso Basin are identified as sites for further work by fisheries biologists.

The CONDOR project continues on RV SONNE cruise S0103 which is based on these shipboard results. OBS refraction data extending into an on-shore recording network will be acquired. The results should add constraints on the tectonic environment of earthquake generation in this populated central part of Chile.

CONCERNING THIS REPORT

The scientific party of the CONDOR project is multinational and the project is of interest to an international audience. Therefore the language is English. The report is informal and its purpose is to consolidate a data base for reference, serve as an initial report for the BMBF, and as an aid for further study by interested investigators. The text that follows was principally prepared at sea and ideas will undoubtedly be modified as the result of further work onshore.

ACKNOWLEDGEMENTS

Preparations for the CONDOR cruise, the work at sea, and post-cruise activities involved many persons and we are thankful for assistance from many un-named persons in Europe, Chile, and the US. The able assistance of Frau Michaela K uchler, first secretary and council of the German Embassy, Santiago, is gratefully acknowledged. Our particular gratitude is extended to Captains Andresen, Bruns, and the crew of the SONNE for excellent performance and help at sea. Administrative tasks of the granting institution were handled by A. Wempe at BEO, Warnem nde, Germany. Principal funding for the cruise and scientific support was extended to GEOMAR by the Bundesministeriums f ur Bildung, Wissenschaft, Forschung und Technologie (BMBF) whose continued support of marine research with an outstanding platform like the SONNE is most laudable.

1.0 Introduction and Objectives

(R. von Huene)

The history of marine geological exploration along the Chilean margin goes back to the time of Darwin, but not much was known about the tectonic structure until the great Chilean earthquake of 1960 stimulated interest in the structure of this margin. The 1960 earthquake along South-central Chile had a moment magnitude (M_W) of 9.5, killing more than 1,000 persons in Chile. Massive destruction along coastal Chile was amplified by an additional 200 fatalities and the 500 structures damaged in Japan and Hawaii.

Along the northern Chile margin, bathymetric profiles of the early 1960's showed a steep continental slope dropping from a narrow continental shelf to 7 km depths in the trench axis (Hays, 1966). In 1967, the first reflection seismic survey by the USNS Davis (Scholl et al., 1970) showed that the Chilean margin did not conform to the general model of a convergent margin. Bathymetric work during the Nazca Plate Project (Schweller et al., 1980) (Figure 1.0) provided the first comprehensive morphology along Peru and Chile. The instruments available during these early studies were unable to image critical structures that fail during great earthquakes but the visible tectonic structure was inconsistent with the 1960's plate tectonic concepts of an accretionary margin.

One of the Davis seismic lines indicated an unusual forearc basin near Valparaiso which corresponded to a bathymetric terrace (Schweller et al., 1980), informally named the Valparaiso Basin (Figure 1.0). It is located directly east of O'Higgins Seamount, a part of the Juan Fernandez Ridge extending some 900 km west from the Chilean coast. The ridge is comprised of 11 major submarine volcanoes, three of which rise above sea level to form the islands of Alexander Selkirk, Robinson Crusoe, and Santa Clara (Mammerickx et al., 1975). The western end is the youngest seamount and O'Higgins, at the eastern end, is the oldest of these volcanoes which are probably a hot spot chain dating back at least to the Miocene (Stoffers et al., 1992). Satellite gravity mapping (Sandwell and Smith, 1992) (Figure 1.1) shows how the ridge is being subducted beneath the Chilean margin in the area of Valparaiso Basin. This is also an area of repeated great earthquakes the last of which occurred in 1985 (Figure 1.1). These earthquakes have been occurring every 82 ± 6 years along rupture planes extending about 150 km along the margin (Barrientos and Kausel, 1990). The nature of asperities nucleating these earthquakes is poorly known but perhaps they are part of the subducted Juan Fernandez Ridge. Interestingly, on land in the Andes, the northern end of the southern volcanic belt is found at the same latitude as the Juan Fernandez collision zone.

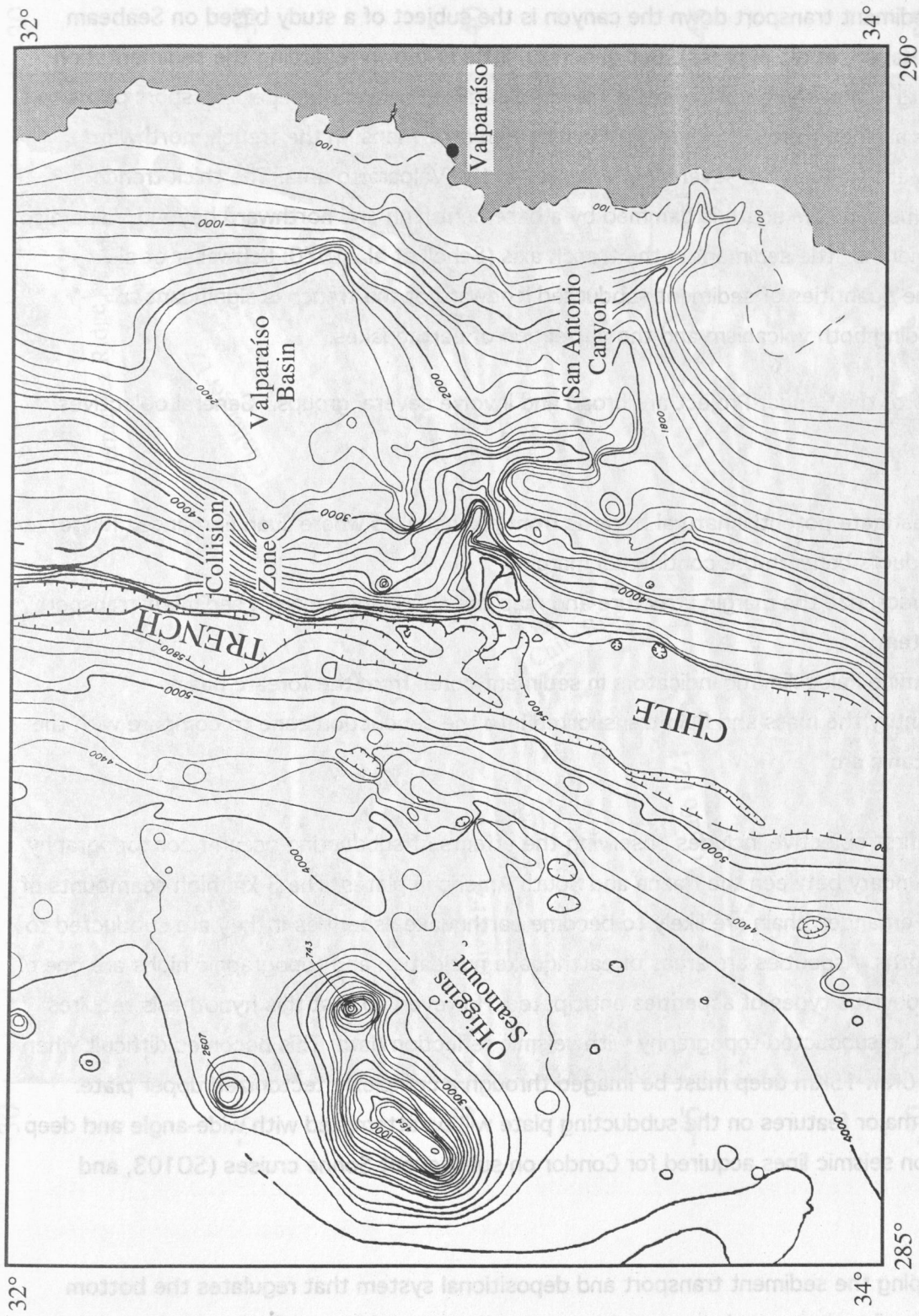


Figure 1.1 Conventional bathymetry in the Condor project survey, area from the map of Schweller and Prince, (1980).

Another striking feature of the margin is the San Antonio Canyon which borders the southern flank of Valparaiso Basin (Figure 1.1). This submarine canyon heads at the mouth of the Maipo River and its path with sharply right angle bends appears to be tectonically controlled. Because of erosion, the canyon walls may expose some of the deeper rocks of the margin. Sediment transport down the canyon is the subject of a study based on Seabeam mapping (Hagen, et al., in press). But generally, little is known regarding the sedimentation of this margin. The source of sediment filling Valparaiso Basin and deeper transport paths to the trench are not apparent in conventional bathymetric maps. In the trench, northward axial sediment transport is severely interrupted in the Valparaiso area. The thick trench filling sediment to the south is dammed by a basement high and northward beyond Valparaiso to Arica there is little sediment in the trench axis (Scholl et al., 1970; Schweller et al., 1981). The quantities of sediment subducted landward of the trench is significant to understanding both volcanism and the nucleation of earthquakes.

Objectives of the Condor Project are broad and involve several groups. General objectives are:

1. investigate potential natural hazards from earthquakes where Juan Fernandez Ridge subducts beneath the continental margin
2. characterize the margin structure and map the continental margin sediment transport system
3. examine Paleoclimatic indicators in sediment cores from the forearc basins
4. quantify the mass and fluid transported into the subduction zone to compare with the volcanic arc

The first objective includes observing the effects of subducting ocean floor topography on the boundary between the Nazca and South American plates. The 3 km high seamounts of the Juan Fernandez chain are likely to become earthquake asperities if they are subducted to 15 km depths. Asperities are areas of earthquake nucleation and topographic highs are one of the most obvious types of asperities anticipated. However, to test this hypothesis requires resolving the subducted topography with seismic reflection data. This becomes difficult when a target 10Km-15Km deep must be imaged through a complexly tectonized upper plate. Resolving major features on the subducting plate will be attempted with wide-angle and deep penetration seismic lines acquired for Condor on subsequent Sonne cruises (SO103, and SO104).

Mapping the sediment transport and depositional system that regulates the bottom distribution of anthropogenic waste addresses environmental issues. Such questions will be

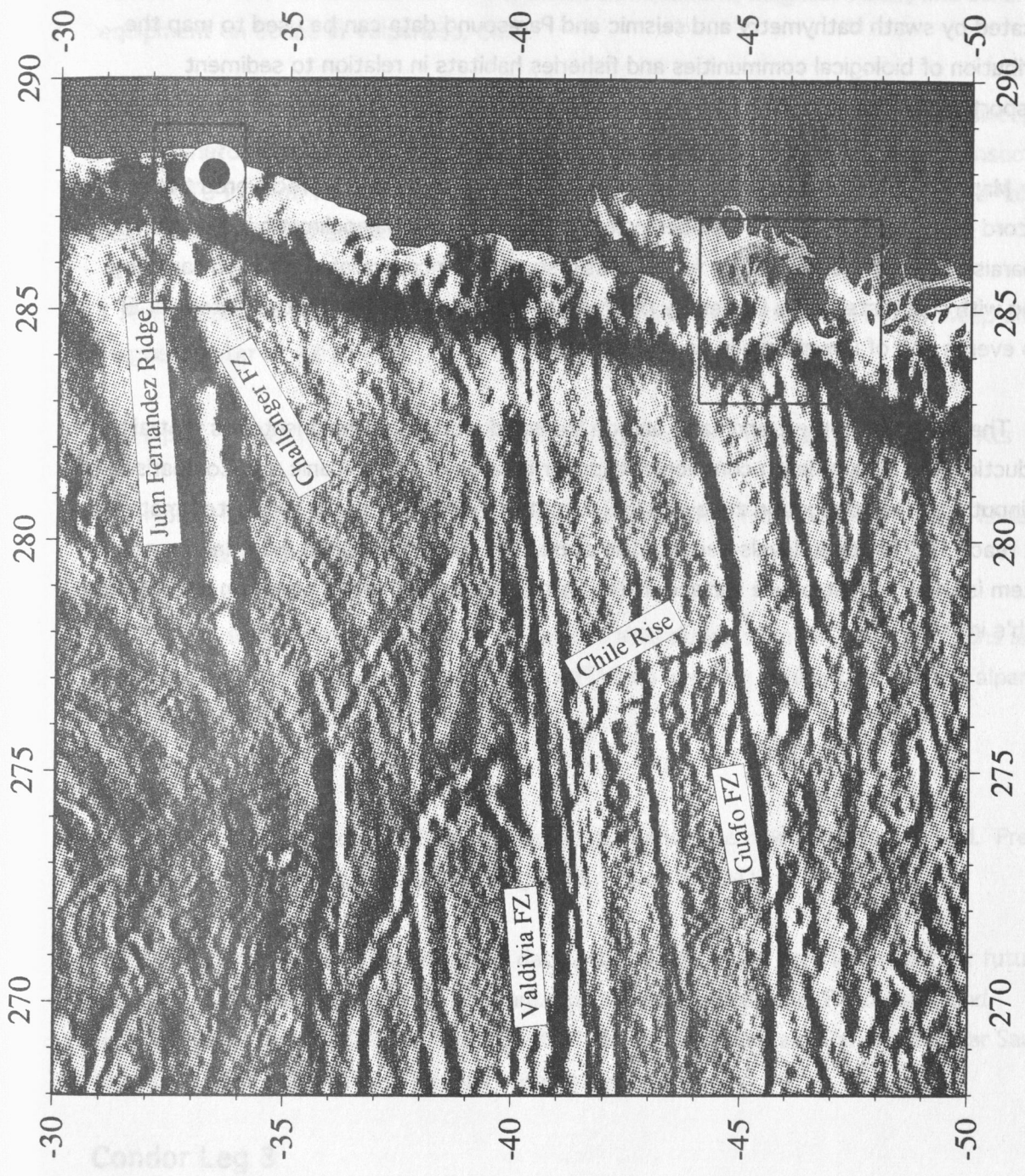


Figure 1.2 Satellite gravity map of the Pacific ocean area off Chile south of 30°S. The circle marks the aftershock area of the Ms 7.8 central Chile earthquake of 1985.

studied with high resolution bathymetry and sub-bottom imaging in basins and the canyons along which sediment is transported across the shelf. How long does the sediment reside on the shelf and in local basins? The sediment transport framework is fundamental in the program of ongoing pollution monitoring by Chilean agencies. The character of the bottom indicated by swath bathymetry and seismic and Parasound data can be used to map the distribution of biological communities and fisheries habitats in relation to sediment transport and sediment sinks.

Mapping of sedimentary basins locates areas where cores can be recovered that contain a record of sedimentation and includes paleoceanography and paleoclimatic indicators. Valparaiso Basin is the first major forearc basin south of Arica available for such sampling. Along with scientists at the University of Bremen, questions concerning the history of El Niño events and of upwelling can be addressed.

The sediment in the trench axis and on the subducting plate hold isotopes that after subduction to 100 km depth commonly reappear in lavas of the volcanic arc. Comparison of the input into the subduction zone and the output of volcanoes tracks subducted materials that reach 100 km deep levels beneath the crust. The subduction zone material transport system is known to introduce surface materials to deep crustal levels or return them to the earth's interior.

2.0 Chronology of the Cruise

Condor Leg 1

23 March, 1995 Unload container and install workstations, magnetometer, and other equipment on Sonne in Valparaiso, Chile.

24-31 March Depart Valparaiso at 0730 and conduct transit profile with Hydrosweep and magnetometer at 12 Kts to northern part of coarse grid. Begin east-west transects and take a CTD in 4 km water for sound velocity. Continue systematic transects to the halfway point near O'Higgins Guyot at WP 44.

1 April Conduct a 12 hr. detailed grid over O'Higgins Guyot area with Hydrosweep and magnetometer at 12 Kts

1-6 April Finish transects to WP 77 with Hydrosweep and magnetometer at 12 Kts

6-9 April Fill gaps between the main lines with short lines from south to north. Ended in severe storm to force 8

9-10 April Run line at northern end of mapped area during storm in both directions and head into seas transiting south to fill gaps left when avoiding fishing boats near Valparaiso. Run into port at 2000.

Condor Leg 2

11 April Port day to load and set up seismic gear and take new persons onboard. Press conference and briefing for Navy Hydrographic Office (SHOA)

12-23 April Acquire seismic reflection data and process those lines important for future sampling and wide-angle seismic program. Concurrent Hydrosweep, Parasound, and magnetic data recorded. Finish this leg with 1 day Hydrosweep and Parasound near San Antonio Canyon. Run to port for late evening docking.

Condor Leg 3

24-29 April Completed 6 core and 6 dredge stations. After station 6 the ship transited to O'Higgins Guyot to begin work in that area.

30 April-4 May Complete dredging and coring in O'Higgins area and return to the trench axis area to dredge the mouth of San Antonio Canyon and take the box-core station C-9 in the trench axis.

4-7 May Dredging continued in the Papudo area and the cruise was finished with dredges in upper San Antonio Canyon to tie the lower slope stratigraphy with that on land.

3.0 Hydrosweep Swathmapping

(R. von Huene, W. Weinrebe, S. Dominguez)

During leg 1, Hydrosweep measurements were made along 8,300 Nautical miles of ships track (Figure 3.0). Most of the area was covered 100% by soundings except in shallow waters above O'Higgins Guyot and near the shelf. All sweeps were edited at sea for the maps and diagrams in this cruise report using the mbsystem software (Authors D.W. Caress and D.N. Chayes) and the GMT software (Wessel and Smith, 1991). Permission to conduct scientific measurements were granted by Chilean authorities beyond the 12 nm line from the coast.

3.1 General morphology

A chart showing the detail inherent in these data is larger than can be included in this report but a smaller map (Figure 3.1a) and a perspective diagram (Figure 3.1b) are used to illustrate the principal morphological features. Names given to major features are shown in Appendix 1.

The oceanic crust can be divided into 3 larger morpho-tectonic elements. 1) The normal ocean crust generated from a northwest trending spreading ridge is cut by northeast trending fractures paralleling the Challenger Fracture Zone (Candy and Haxby, 1991). 2) A N70°E trending zone marking the Juan Fernandez Ridge that contains the O'Higgins group of volcanos (O'Higgins Guyot, O'Higgins Seamount and 2 larger seamounts). 3) Where the ocean crust is flexed into the trench it is broken by extensional faulting mostly parallel to the trench axis. These 3 morphotectonic elements on the oceanic crust are little modified by sedimentation. Only in the trench axis are sediment ponds indicated by the flat morphology.

The continental slope is more complex but is also divisible into three discrete morphotectonic provinces. In the north the base of the slope is steep and has a sinuous trace unlike most accretionary prisms. Pta. Salinas embayment in the north interrupts a generally steep continental slope. Valparaiso Basin is also in an embayment of the upper slope and forms an unusually large forearc basin bounded on the south by San Antonio Canyon. South of the canyon the slope drops from a narrow shelf to a moderately dipping middle slope and then to the steep lower slope. At the base of the slope is a series of ridges typical of accretionary terrains.

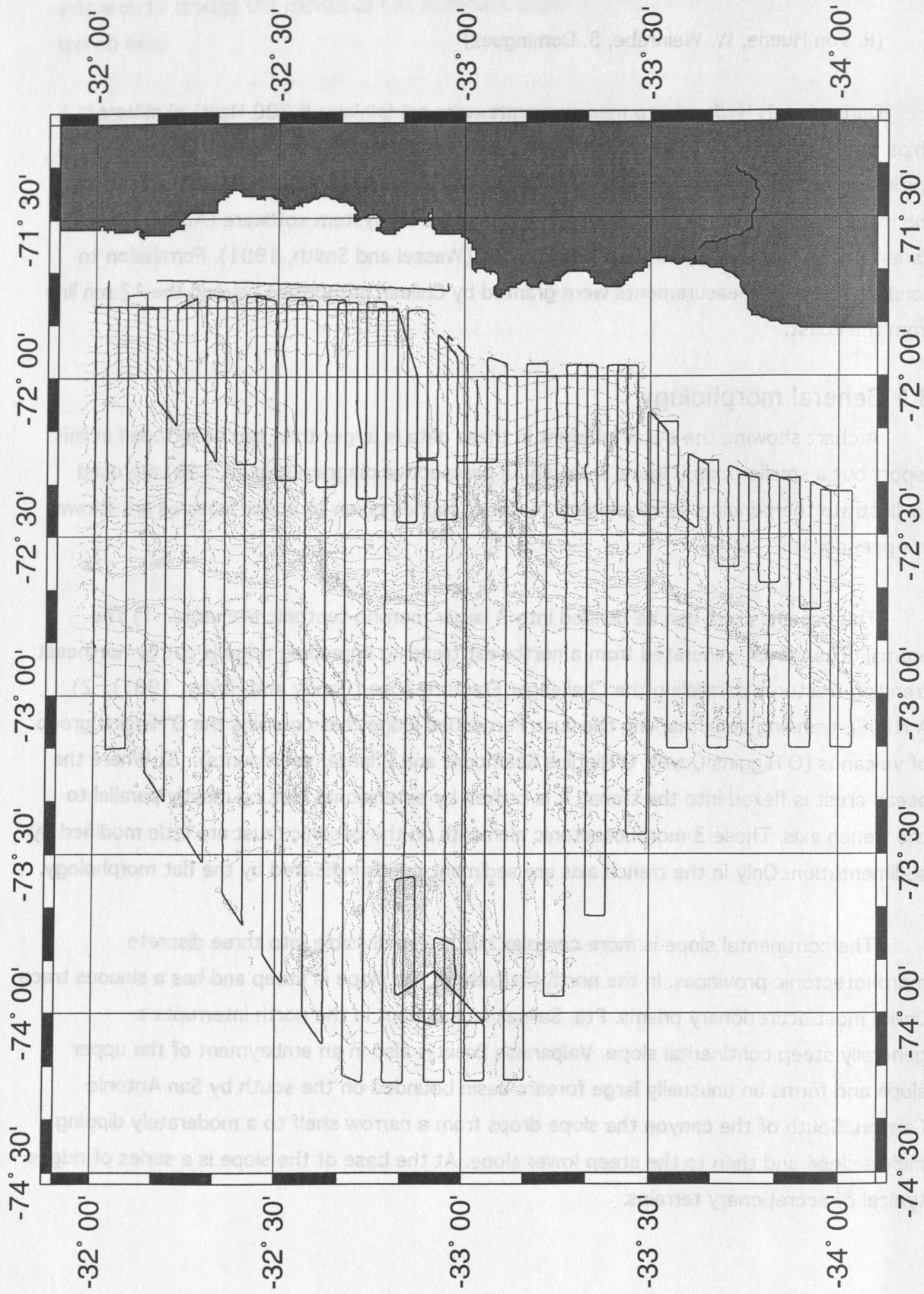


Figure 3.0 Ship's tracks comprising the Hydrosweep and magnetic survey on Leg 1, SO101 cruise

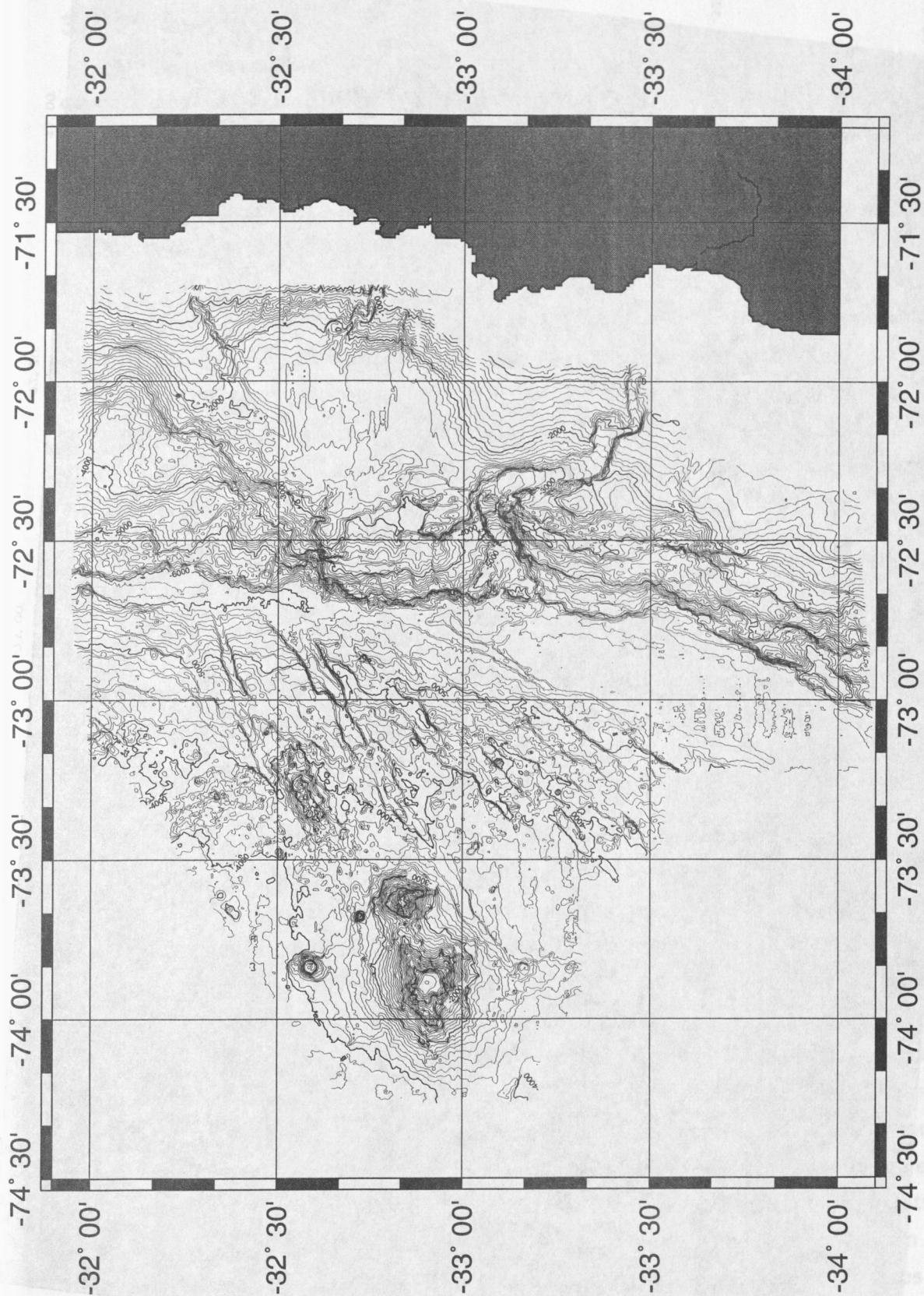
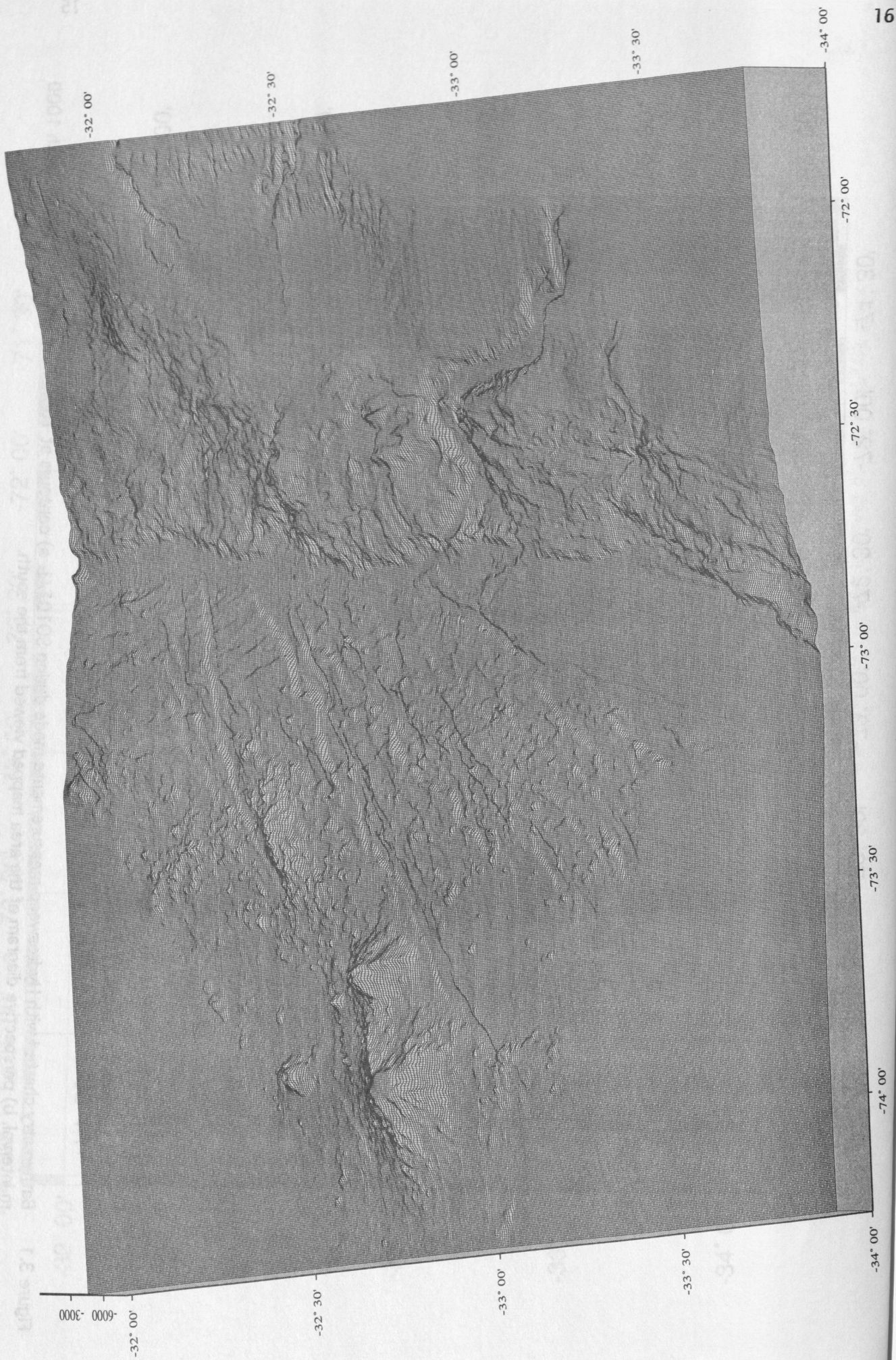


Figure 3.1 Bathymetry charted with Hydrosweep measurements made during SO101/1. a) contours at 100m intervals with bold lines each 1000 m interval. b) perspective diagram of the area mapped viewed from the south.



3.2 Ocean crust

In the north and south parts of the mapped area smooth oceanic crust is flexed downward into the trench axis in the 35 km seaward of the trench axis. On the typical crust is a low northwest trending ridge composed of many small volcanic cones, which parallels the magnetic anomalies (Figure 3.2a). It terminates southeast against an orthogonal trending reactivated fracture discernible as a long narrow northeast trending graben. Cutting these orthogonal ridge and fracture trends are normal faults with sinuous traces sub parallel to the trench axis. Some faults near fractures turn parallel to them whereas others cross the fracture trend or end at fractures. Almost none of the normal faulting is parallel to the structural grain of the oceanic crust (parallel to the magnetic anomalies) except in one area between fractures. Apparently the trench parallel axis of flexure is at an angle greater than that which favors failure along the inherited directions of weakness parallel to the magnetic fabric. Vertical displacements on normal faults reach 300 m and no lateral shifts are observed. This faulted morphology disappears beneath the sediment ponded in the trench axis except over the crest of Juan Fernandez Ridge.

The ocean floor south of O'Higgins Guyot has a smooth morphology (Figure 3.2b). Near the trench axis, normal faults trend 10° to the trench which here swings west as does the regional trend of the margin. These faults also trend 10° to the zone of fractures. They begin to break the crust about 60 km from the base of the slope which is twice the distance as in the north.

Zone of fracturing and Juan Fernandez Ridge. Between the northern and southern tracts of less deformed ocean crust is a zone of fractures trending $N60^\circ E \pm 10^\circ$ diagonal to the north-south trench axis named the O'Higgins zone of fractures (Figure 3.3). The fractures parallel an ocean crustal trend observed in Satellite gravity maps (Figure 1.2) that characterizes crust subducting north of the Valdivia Fracture zone and east of Selkirk Rise (Cande and Haxby, 1991). The fracture pattern angles across the trend of the Juan Fernandez Ridge and is perpendicular to the major magnetic anomalies. The magnetic anomalies perpendicular to the zone of fractures show little lateral displacement across them (see section 4). Morphologically the zone of fractures is expressed by scarps and narrow graben of 60 to 150 km extent. A typical fracture graben is illustrated in Figure 3.2. Scarps are highest near the trench axis and indicate the reactivation of inherited trends as the ocean crust is flexed into the axial area. Some scarps reach heights of 1,000 m although most are between 200 m-400 m high. Where the O'Higgins zone of fractures (OZF) crosses the projection of the Juan Fernandez Ridge in the trench axis, little axial sediment is observed as noted previously (c.f. Schweller et al., 1981).

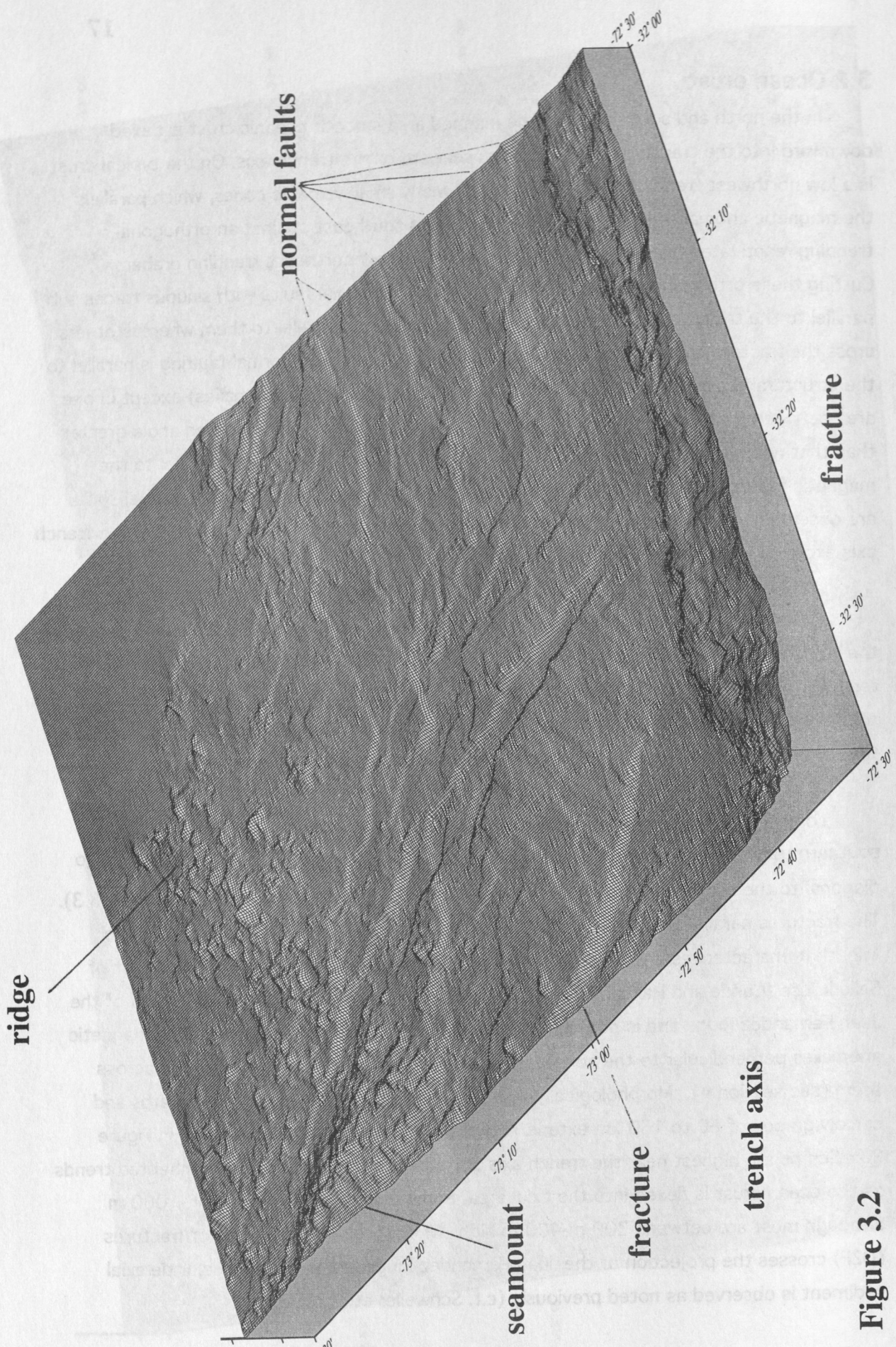


Figure 3.2

Perspective diagrams showing ocean crust which is normally faulted as it flexes down into the trench axis. a) area north of the zone of fractures, b) looking east across the trench axis from San Antonio Canyon

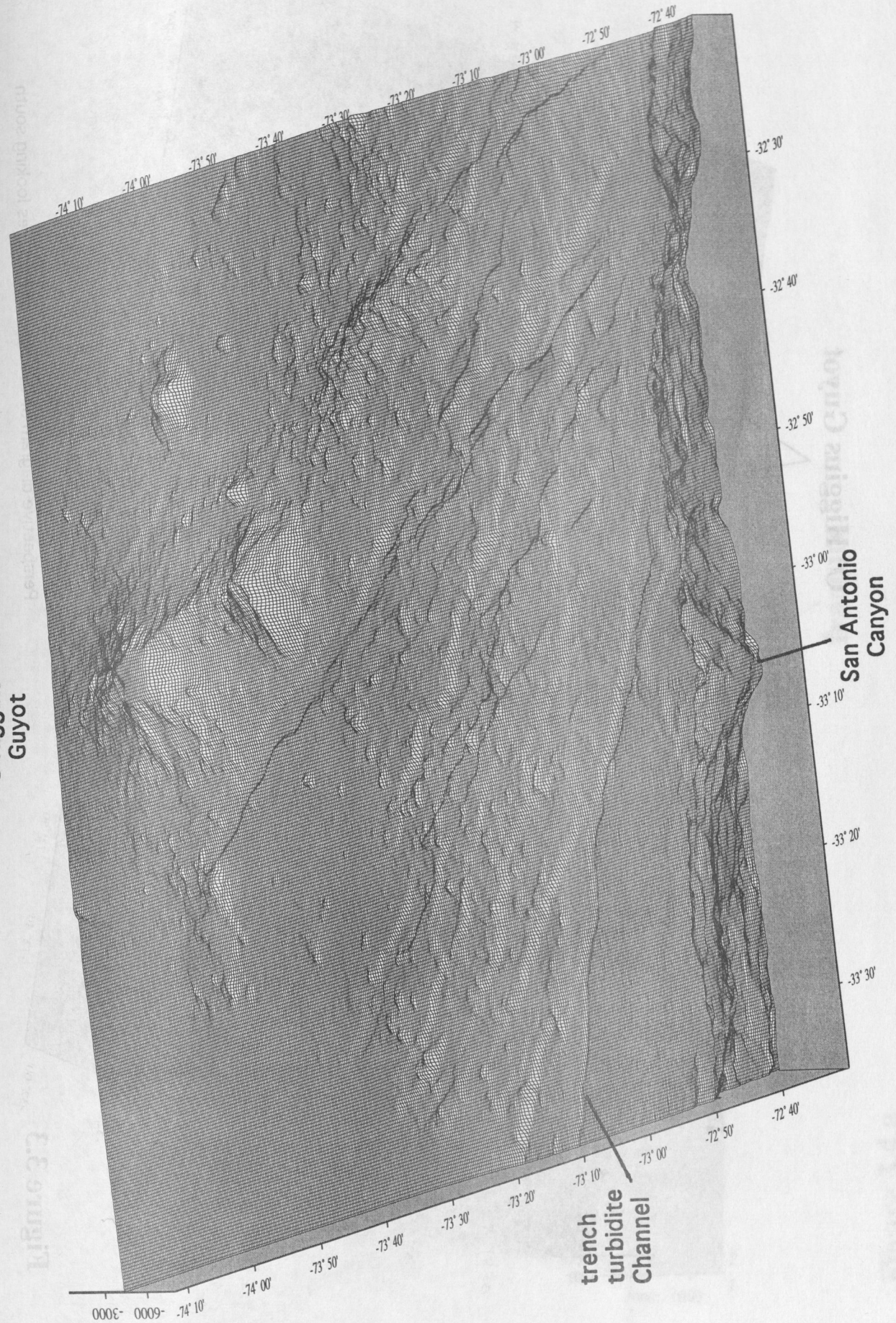
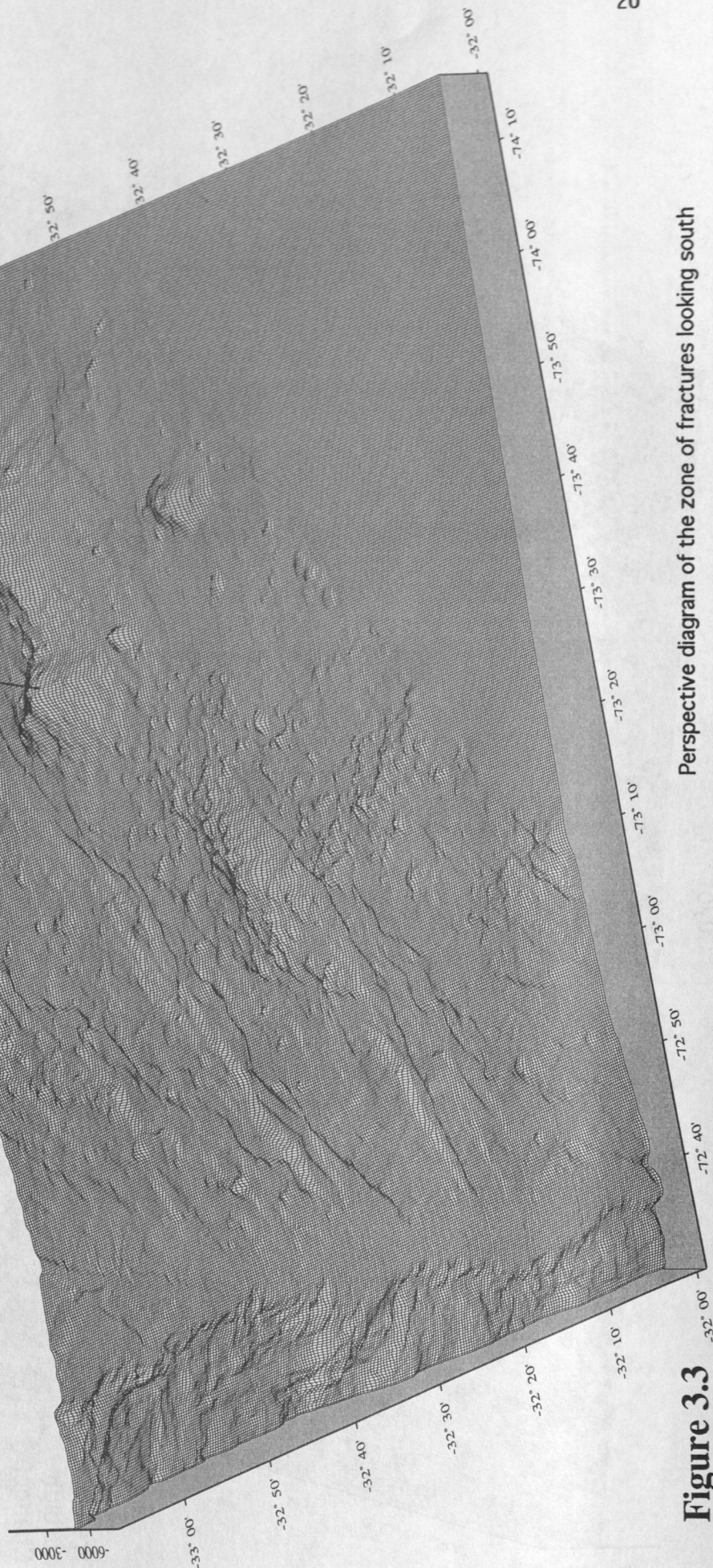


Figure 3.4. Bathymetric map of the Guyot region showing the trench turbidite channel and San Antonio Canyon. The map is overlaid with a grid of latitude and longitude coordinates. The map is titled "Guyot".

O' Higgins Guyot

fracture

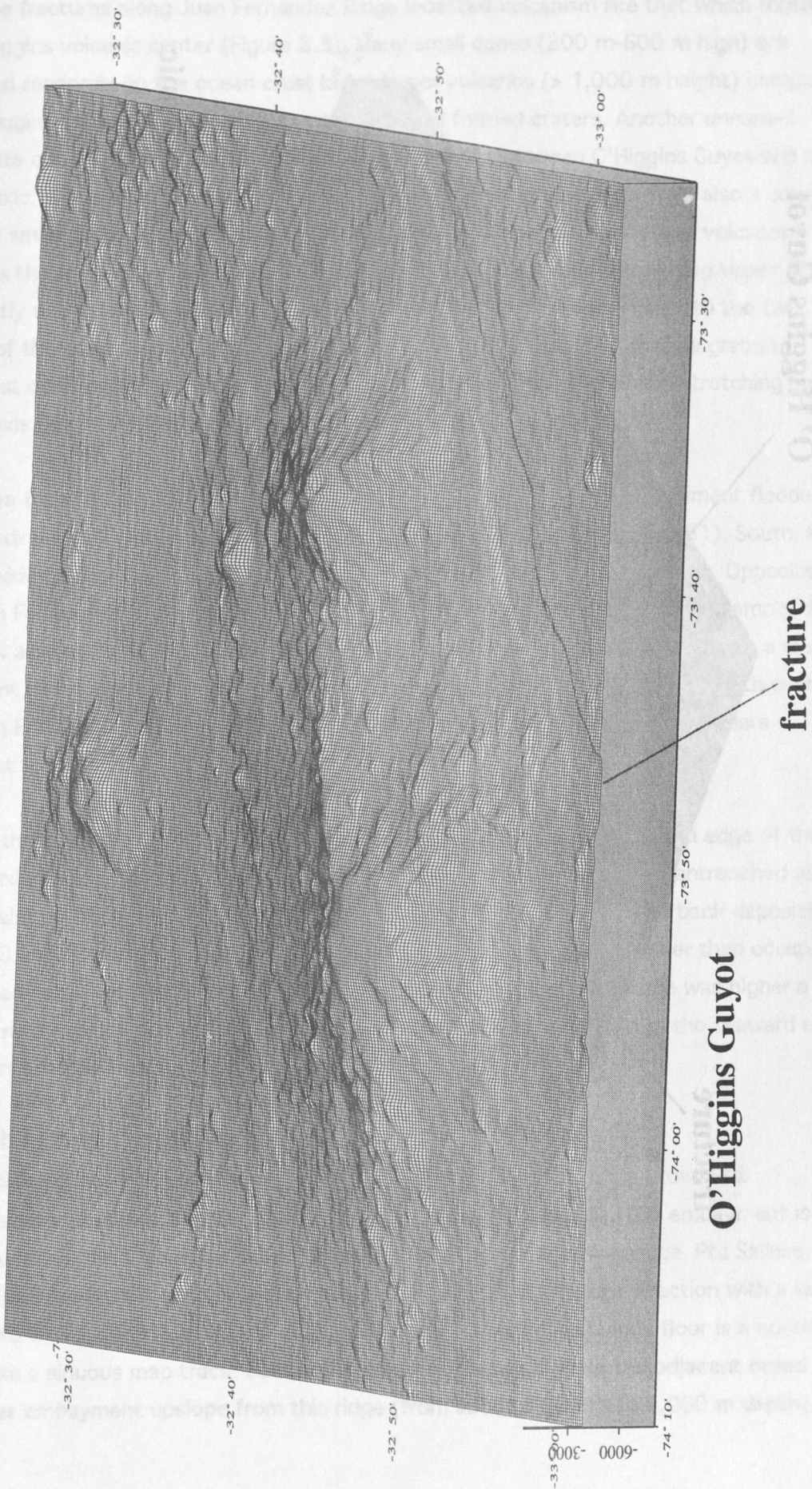
trench
axis



Perspective diagram of the zone of fractures looking south

Figure 3.3

single volcanic



cone

O'Higgins Guyot

fracture

Figure 3.4.a

a) View northward of O'Higgins Guyot at 1.5X vertical exaggeration b) View southward of O'Higgins Guyot. The overlap of outer beams from two adjacent tracks are visible as east-west stripes and indicate the maximum data noise level in flat areas

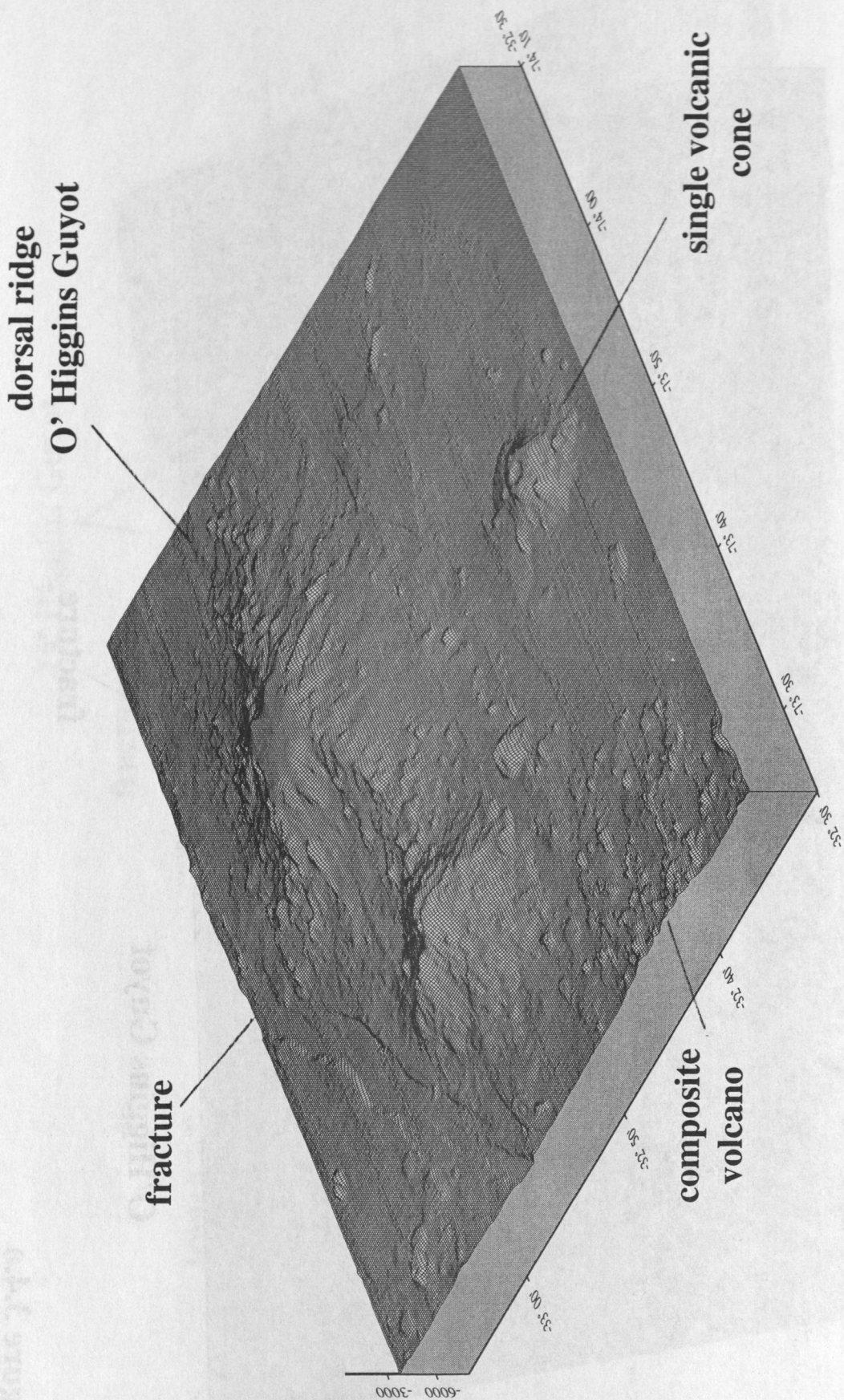


Figure 3.4.b

The fractures along Juan Fernandez Ridge localized volcanism like that which forms the O'Higgins volcanic center (Figure 3.3). Many small cones (200 m-600 m high) are scattered randomly on the ocean crust but 4 larger volcanos (> 1,000 m height) comprise the O'Higgins center. Two are single cones with well formed craters. Another unnamed composite cone elongate parallel to the fracture trend is between O'Higgins Guyot and the trench axis. The two volcanos comprising O'Higgins Guyot and Seamount are also composed of many small cones (Figure 3.4a and 3.4b). The dorsal ridge joining the two volcanos indicates the fracture which localized erupting lava. On the Guyot a very steep upper slopes and gently undulating tilted flat top suggest an earlier insular history similar to the two islands of the younger eastern part of the Juan Fernandez Ridge. The shallow graben southeast of O'Higgins is part of a long fracture with a seafloor expression stretching to the trench axis (Figures 3.3 and 3.4a).

The trench axis. The mapped area includes the barrier between a sediment flooded and a sediment starved trench axis (Scholl et al., 1970; Schweller et al., 1981). South, the 30 km wide trench floor (Figure 3.1b) results from the 2 km thick axial wedge. Opposite the Juan Fernandez Ridge the sediment essentially disappears and the trench is empty. North a narrow axial sediment body is ponded behind a constriction in the axis caused by a small seamount in the trench (~32°S). The axial profile drops from 5,400 m in the south over the Juan Fernandez Ridge intersection to more than 6,000 m. The gradient appears sufficient to keep the trench axis clean of sediment.

In the south a prominent axial turbidite channel runs along the seaward edge of the trench axis floor. Northward toward the Juan Fernandez Ridge it becomes entrenched and has eroded almost 200 m into the trench fill rather than nourished it with overbank deposits (Figure 3.1b). The area in front of San Antonio Canyon is also eroded rather than occupied with a sediment fan. Apparently the barrier over the Juan Fernandez Ridge was higher a short time ago since the turbidite channel has not migrated very far from the seaward edge of the trench floor toward the base of the slope.

3.3 The Continental Slope

Northern continental slope. North of the Valparaiso Basin is the broad Pta. Salinas embayment which encompasses a lower terrace (Figure 3.5). The embayment is separated from the Valparaiso Basin by a diagonal northeast trending ridge, Pta Salinas Ridge. The seaward descending slope has a strong northeast fracture direction with a lessor conjugate trend. The lower 400 m -500 m of the slope along the trench floor is a continuous ridge with a sinuous map trace. Behind this ridge are closed lows. In the adjacent broad triangular embayment upslope from this ridge (from about 5,500 m to 4,000 m depth) the

diagonal ridge



Valparaíso
Basin

lower slope
ridge

trench
axis

Figure 3.5

Looking east at the northern continental slope showing the northern embayment. Track overlap stripes have not been smoothed from the data to give maximum resolution. Note the push up ridge at the base of the slope causing closed basins. Congugate shear directions oriented diagonally to convergence direction are indicated in the small scaled morphology.

relatively gentle slope has a highly disordered topography similar to the area of land-sliding off northern Peru (Bourgois et al., 1988; von Huene et al., 1989). A small local terrace occurs at about 3,500 m depth.

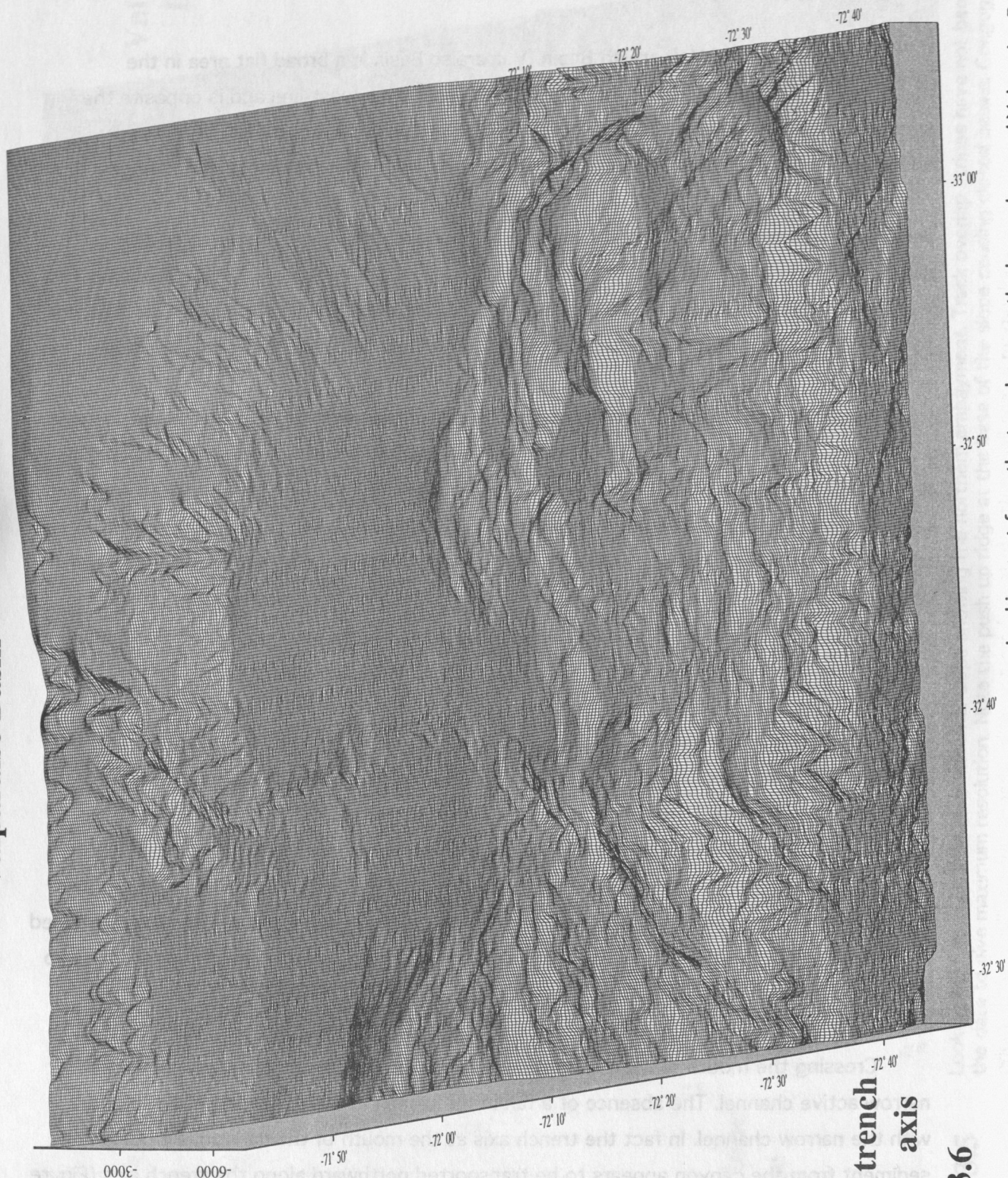
Middle slope and Valparaiso Basin. Valparaiso Basin is a broad flat area in the middle slope. The basin fills an embayment in the shelf and coast-line and is opposite the subducting Juan Fernandez Ridge (Figure 3.6). Its landward flank dips relatively steeply and is cut by two large and numerous small canyons. A transverse almost buried ridge midway between the north and south basin flanks divides the basin into a northern and southern part (see seismic records, chapt. 5) The seaward flank is a broad complexly structured ridge that closes most of the basin. From the basin the lower slope descends to a very steep lower-most 500 m high sinuous slope which locally suggests a low ridge adjacent to the trench axis. Short scarps parallel to the trench axis form steps in the lower slope.

Two areas stand high on the seaward flanking ridge, one in the north near the seaward end of the Pta. Salinas ridge and the other on both sides of lower San Antonio Canyon. The latter consists of a series of north trending ridges. The northern high is associated with the buried circular Papudo magnetic anomaly (see Magnetics). This segment of the margin is bounded by two large triangular indentations. The northern is not as large as the southern one which is the lower part of San Antonio Canyon. The wide v-shaped mouths of the indentations are typical of features made by subducting topographic highs on the oceanic crust.

San Antonio Canyon. The sharp right angular course of San Antonio Canyon suggests a structurally controlled path (Figure 3.7). More than one-third of the canyon runs sub-parallel to the regional trend. Steep canyon walls reach heights of more than 1 km. The canyon mouth empties into the trench axis at a triangular breach in the lower slope about 20 km on a side. The origin of the triangular mouth and transverse lower course is suspected to be from a subducting positive feature on the oceanic crust. The broad U-shaped valley crossing the upper slope suggests a canyon sculptured more by erosion than those to the north.

Crossing the mouth of the Canyon is an irregular ridge breached by a surprisingly narrow active channel. The absence of a fan in the trench axis is surprising but consistent with the narrow channel. In fact the trench axis at the mouth of the canyon is eroding and sediment from the canyon appears to be transported northward along the trench axis (Figure 3.7).

Valparaiso Basin



trench axis

Looking east from the trench across the lower slope and Valparaiso Basin

Figure 3.6

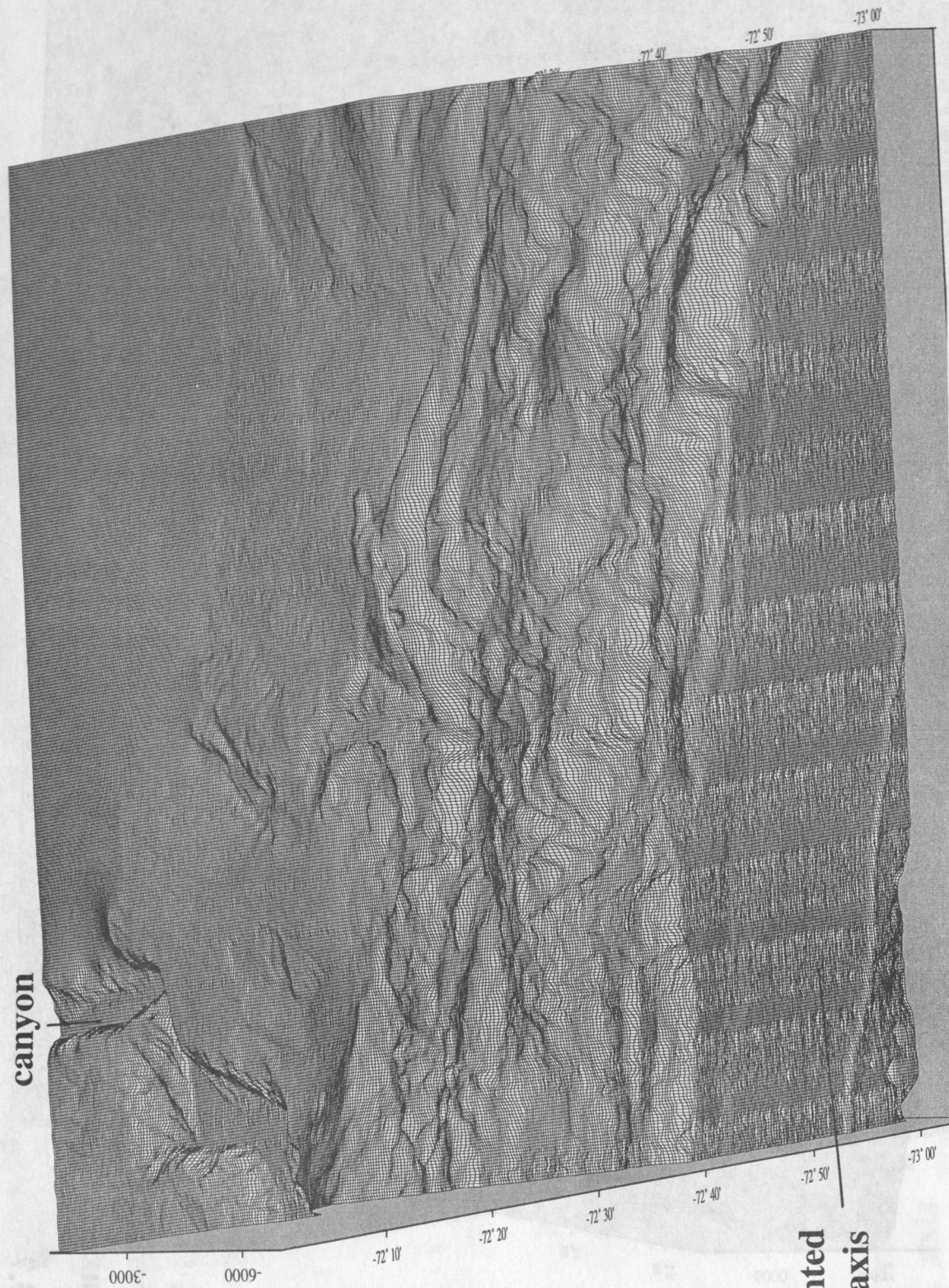
San Antonio canyon



Figure 3.7

The San Antonio Canyon preliminary figure

**San Antonio
canyon**



**sedimented
trench axis**

Figure 3.8

The southern continental slope adjacent to the sediment filled trench axis. Differences in depths along overlapping outer beams from two adjacent traces are very noticeable in the flat trench axis and are reduced up slope in shallower areas.

Southern slope. South of San Antonio Canyon the continental slope and trench axis swing from a north-south to a north 25°E trend. The trench floor widens to about 30 km - 35 km because of thick ponded turbidites (Scholl et al., 1970; Schweller et al., 1981). The active axial channel runs along the seaward side of the trench axis and is entrenched from erosion whereas an abandon channel runs along the landward side (Figure 3.8). At the foot of the slope are elongate ridges some in a rough en'echelon pattern. Behind the ridges the lower slope is generally as steep as that to the north opposite Valparaiso Basin. In the middle slope are 2 canyons that become disrupted in the lower slope indicating recent tectonism. Above about 3,000 m depth to the edge of the shelf the morphology of the slope smoothens. The morphological contrast between the lower tectonized and upper little disturbed slopes is a clear indication of where deformation is most active.

REFERENCES CITED

- Bourgeois, J., B. Pautot, T. Bandy, T. Boinet, P. Chotin, P. Huchon, B. Mercier de Lepinay, F. Monge, J. Monlau, B. Pelletier, M. Sosson, and R. von Huene, 1988, Seabeam and seismic-reflection imaging of the tectonic regime of the Andean continental margin off Peru (4°S to 10°S), *Earth and Planetary Letters*, 87, 111-126
- Barrientos, S.E. and Kausel, E., 1990, Rupture processes of the 1985 central Chile earthquake, *Revista de Geofisica*, v.46, p 3-18
- Cande, S.C. and W.F.Haxby, 1991, Eocene propagating rifts in the southwest Pacific and their conjugate features on the Nazca Plate; *Jour. Geophys. Res.* v.96, P 19,609-19,622
- Hagen, R., H. vergara, and D. Naar, 1995, Morphology of San Antonio Canyon on the central Chile forearc, (Submitted, *Marine Geology*)
- Hayes, D.E. 1966, A geophysical investigaion of the Peru-Chile Trench: *Marine Geology*, v4, p.309-351
- Mammerickx, J., R.N. Anderson, H.W. Menard, and S.M. Smith, 1975, Morphology and Tectonic Evolution of the East-Central Pacific, *Geological Society of America Bulletin*, 86, 111-118
- Scholl, D.W., M.N. Christensen, R. von Huene, and M.S. Marlow, 1970, Peru-Chile Trench sediments and sea-floor spreading: *Geological Society of America Bulletin*, v. 81, p. 1339-1360

Schweller, W.J., L.D. Kulm, and R.A. Prince, 1981, Tectonics, structure, and sedimentary framework of the Peru-Chile Trench, *in* L.D. Kulm et al., eds., Nazca Plate: crustal formation and Andean convergence: Geological Society of America Memoir 154, p. 323-349

Stoffers, P., Hekinian, R. et al., 1992, Cruise Report SONNE 80a-Midplate III Oceanic Vulkanism in the Southpacific, Valparaiso - Easter Island, Berichte - Reports geol.-Palaont. Inst. Univ. Kiel, Nr. 58, 128S., November 1992 ISSN 0175-9302 Christian-Albrechts-Universitat Kiel Germany

Schweller W.J. and R.A. Prince, 1980, Bathymetry of the Peru-Chile Trench and continental margin, Latitude 31°-36° south: Geol. Soc. Am. sheet MC-34

Schweller, W.J., L.D. Kulm, and R.A. Prince, 1981, Tectonics, structure, and sedimentary framework of the Peru-Chile Trench, Geol. Soc. Am. Memoir 154, 323-349

von Huene, R. J. Bourgois, J. Miller, and G. Pautot, 1989, A large tsunamogenic landslide and debris flow along the Peru Trench, J. Geophys. Res. 94, B2, 1703-1714

Wessel, P. and W.H.F. Smith, 1991, Free software helps map and display data, EOS Trans. Amer. Geophys. U., Vol. 72, 441, 445-446.

4.0 Magnetic Survey: Instrumentation, Data Acquisition, Processing, Modeling and Interpretation

(G. Yañez, C. R. Ranero, J. Díaz)

4.1 Introduction

During the CONDOR cruise the total intensity of the Earth's magnetic field was measured with a systematic coverage of the survey region (see in Figure 1 the tracks of the survey lines). The survey consisted of a set of E-W tracks with a line spacing of 6 km to the west of the trench axis and 3 km over the continental slope region. In addition 4 lines at 3 km cross the O'Higgins Seamount region. In total, the survey covered a surface of $\sim 300,000 \text{ km}^2$ with 12,000 line km of ship's track where magnetic signal at a sampling rate of 6 seconds was recorded.

In the following sections we describe the field work considering the acquisition, data processing and reduction, preliminary modeling, and interpretation of the main features.

4.2 Magnetometer/Instrumentation

During the CONDOR cruise (SO-101) the total intensity of the Earth's magnetic field was measured with a proton precession magnetometer G-811 from EG&G Geometrics loaned from the US Geological Survey (USGS). The two components of the G-811 are the magnetic sensor and the control unit which are connected via a cable.

The sensor consists of a non-magnetic container, filled with a hydrogen-rich liquid (e.g. petrol) in which a coil is immersed. During the polarization cycle an electric current generates a strong magnetic field in the coil and forces the magnetic moments of the protons to be aligned parallel to the excited field. During the following measuring cycle, i.e. when the excited field is removed, the protons realign themselves with the Earth's magnetic field. According to the moment preservation law, this happens by precession of the protons with a certain frequency which is directly proportional to the intensity of the Earth's magnetic field. This frequency is measured as AC electric current created by magnetic induction in the coil, amplified, counted and transformed to magnetic field intensity values (measuring unit : $10^{-9} \text{ Tesla} = 1 \text{ nT}$), which are recorded.

To minimize the influence of the ship's hull, the sensor is towed at three times the ship's length behind the ship for a resolution of about 1 nT. In our experiment, the cable connecting the sensor with the recording unit was installed at the rear end of the

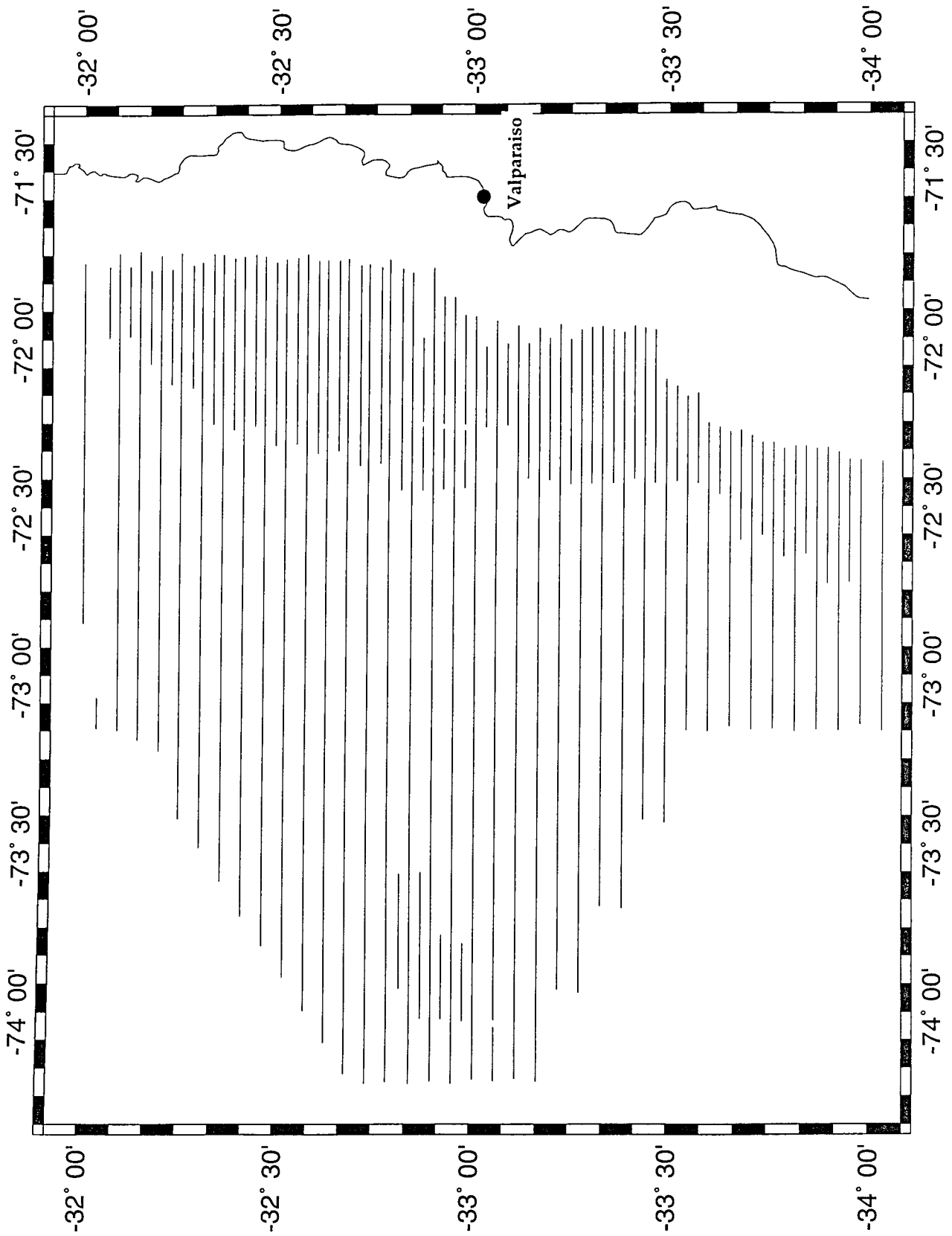


Figura 1. Track lines.

ship and had a length of about 300-315 meter whereas the length of the R/V SONNE is 95 m. Therefore, the sensor was towed at a distance outside the ships magnetic field.

The control unit was connected via the RS-232 interface to a computer for digital recording and storage of the raw magnetic data in ASCII files. The data files consist of date and time (from the PC) and field readings of the absolute values of the Earth's magnetic field.

4.3 Data Acquisition

At the beginning of the SONNE-101 cruise several problems delayed the recording of the data. The first problem was damage of the recording unit during the transport which was repaired onboard. A second problem was that interface software to the PC was unavailable. A BASIC-coded program was written onboard for recording and storage of data.

For marine acquisition, where recording is carried out at relatively low speed (10 to 12 knots), a sampling rate of 6 seconds was considered sufficient to process data and record long wavelength variation of the magnetic field (typically 5 to 20 km).

During recording of the first data, isolated spikes occurred in the otherwise smooth magnetic field. Eventually the number of bad readings became larger than the good readings. The sensor was opened and 1-2 liters of water were found in the fluid. The water was removed and replenished with petrol. Thereafter, recordings were smooth without detectable noise.

4.4 Data Reduction and Preliminary Processing

Quality control, data processing and presentation were done onboard. In order to process the magnetic data, ASCII files of raw data were transferred to a Sun workstation network installed by GEOMAR. Processing consisted of despiking of the data obtained before the refilling of the liquid of the sensor, filtering, resampling and merging of the magnetic data with the GPS navigation from the ship. Subsequently, the IGRF (International Geomagnetic Reference Field) from 1990 (EOS, 1991) was subtracted (subroutine provided by P. Sloutweg), the anomalies were plotted along track, gridded, and contour maps were produced.

The processing software was written onboard using UNIX shell scripts, GMT programs and FORTRAN code. The processing steps (Figure 2) were:

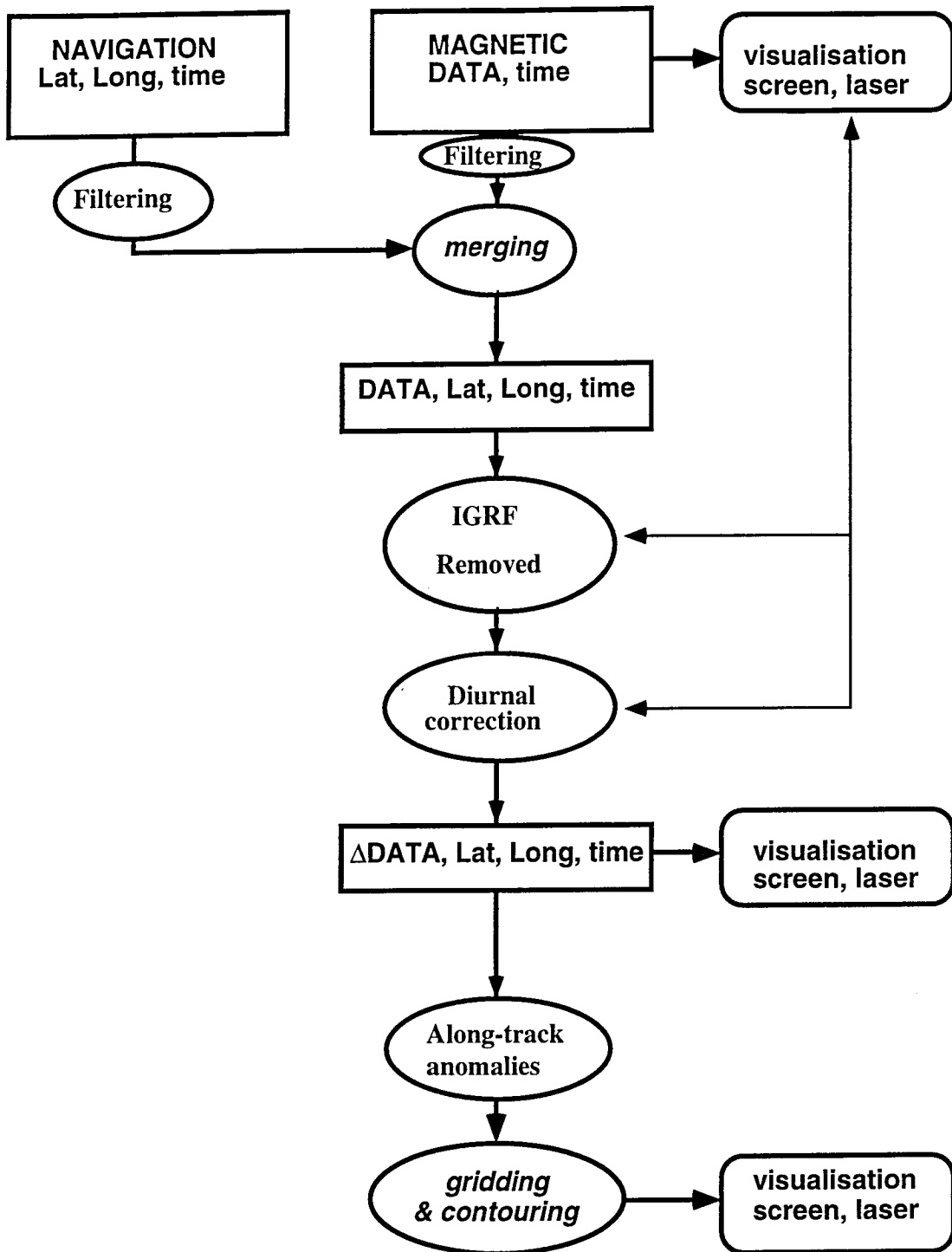


Figure 2 Flow chart for magnetic data processing

Raw data were processed daily and then filtered and decimated. The optimal smoothing was achieved with a median filter 240 s long and resampling of the data from 6 s interval to 60 s interval. The GPS navigation also contained spikes and was smoothed by filtering. Ships tracks with magnetic data are shown in Figure 1.

After filtering the navigation (data values every 30 s after median filtering), the magnetic and navigation data were merged. Then the International Geomagnetic Reference Field of 1990 (IGRF-90) was subtracted from the total intensity measurements. Subsequently, the whole data set could be shown as along-track magnetic anomalies. In the next section we will discuss the process of diurnal variation removal and final leveling of the magnetic data set.

Contour map (Figure 3) and track coverage (Figure 1) were taken together for comparison and possible correlation with the simultaneously acquired swathmapping bathymetry.

In order to obtain some quantitative information of the quality of gridded data we made several comparisons. First we compared the data recorded along two lines (profiles 26-27 and 42-43 in Figure 4) with the anomalies extracted from the gridded data. The match between observed and gridded anomaly can be observed in Figure 4 in panels a and b. The fit between observed (dashed line) and gridded data (continuous line) is good, with only small differences due to the loss of the highest frequencies inherent in the process of gridding.

Second, we extracted data from the grid along synthetic tracks perpendicular to the NW-SE trending seafloor spreading magnetic anomalies observed in the gridded data (profiles 1 and 2 in Figure 1 and panels c and d in Figure 5). The purpose is twofold, to compare the synthetic profiles with the recorded anomalies and to facilitate the identification of the spreading anomalies. The shape of the magnetic anomalies along the synthetic track is very similar to the shape observed in the along track anomalies (profiles 26-27, 42-43), allowing for the change in strike.

4.5 Diurnal removal and leveling of the lines

Diurnal effects are evident in the raw contour map (Figure 3), especially in the eastern side of the survey region where the intensity of the anomalies is small (mostly continental sources, see in section 5 further details on the nature of these anomalies). Given the importance of this region for the ocean-continent plate

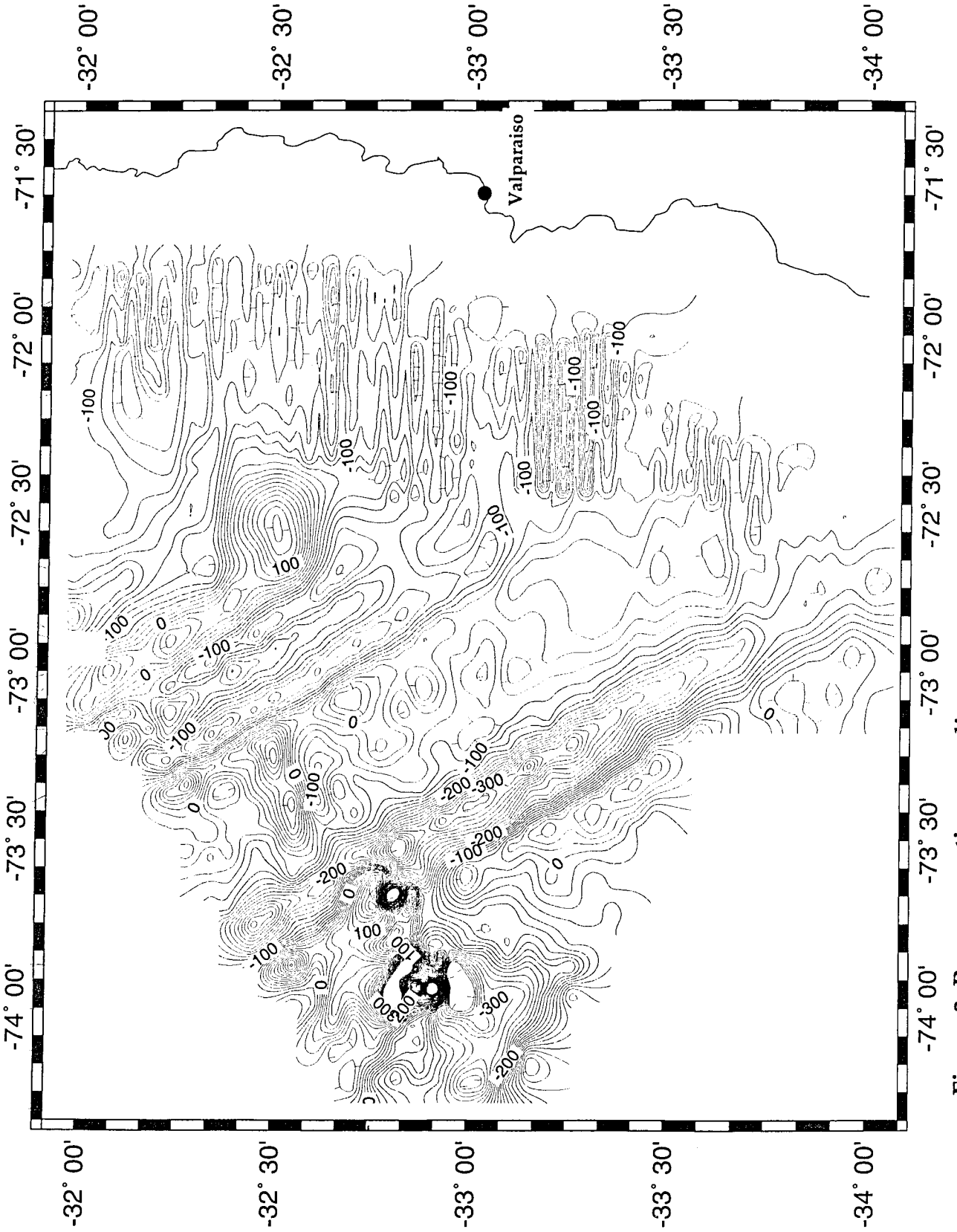


Figure 3. Raw magnetic anomalies

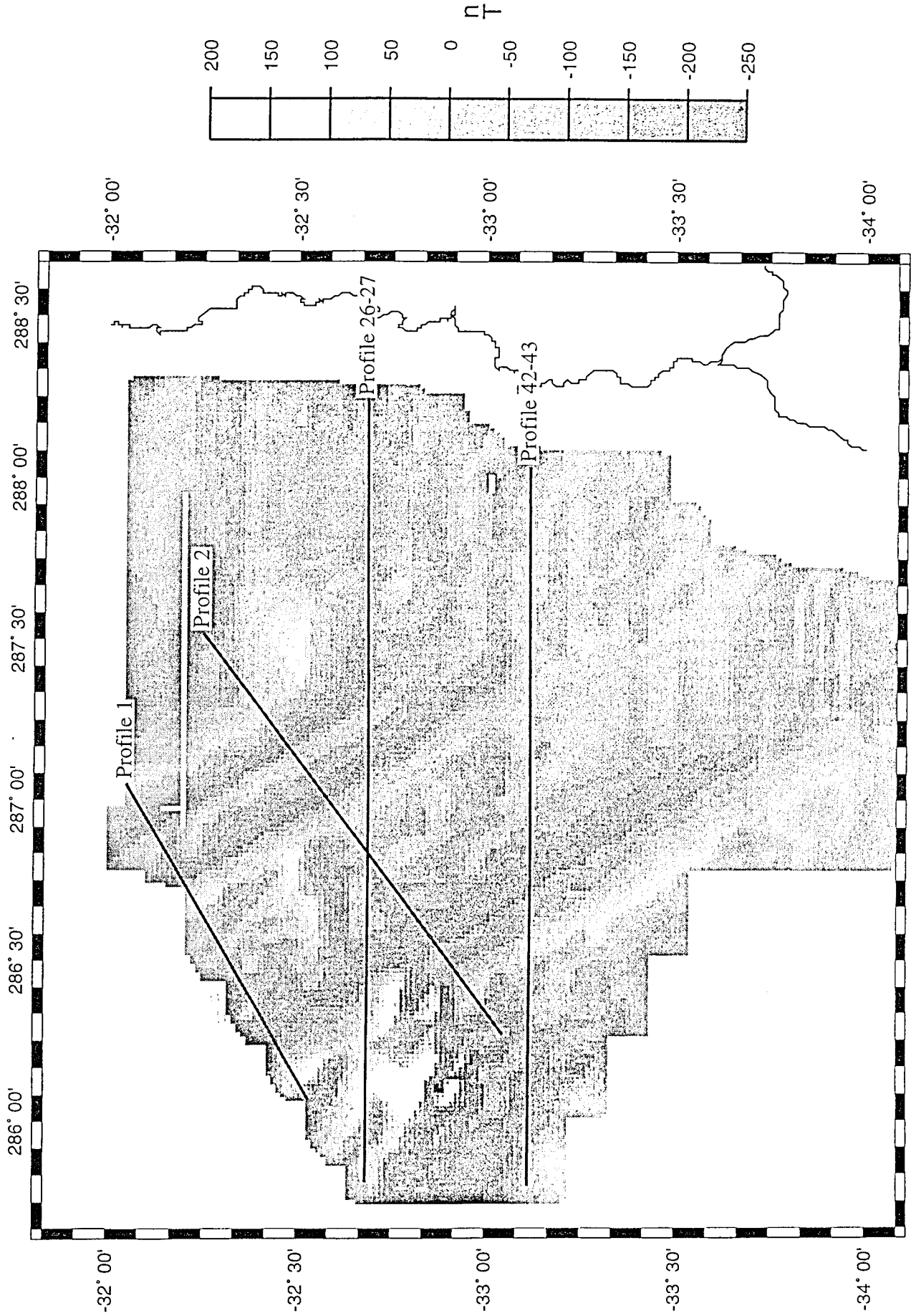


Figure 4. Magnetic anomalies offshore Valparaíso (Chile). Contours every 25 nT. Artificial illumination from the NE.

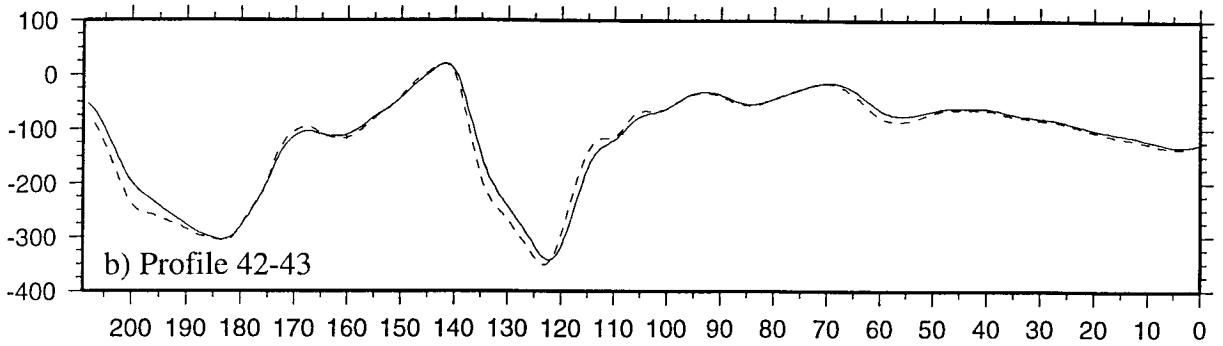
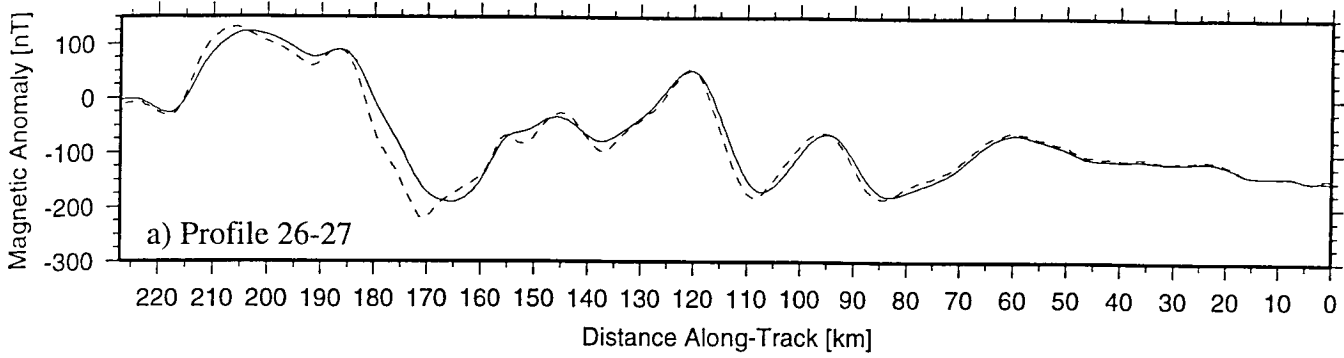


Figure 4. a) and b) Observed along track magnetic anomalies (dashed lines) and calculated from the grid (continuous lines).

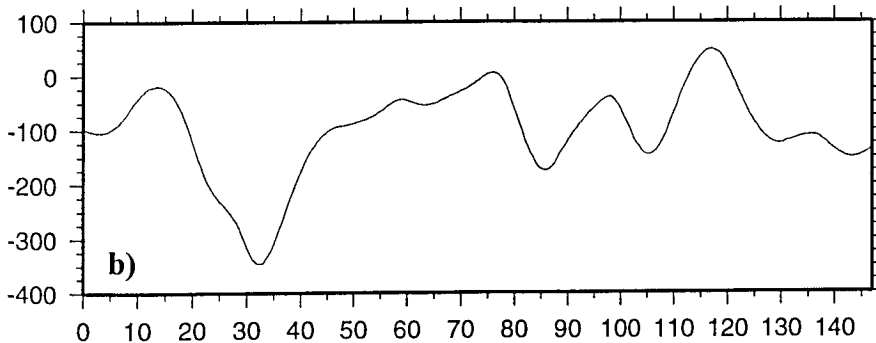
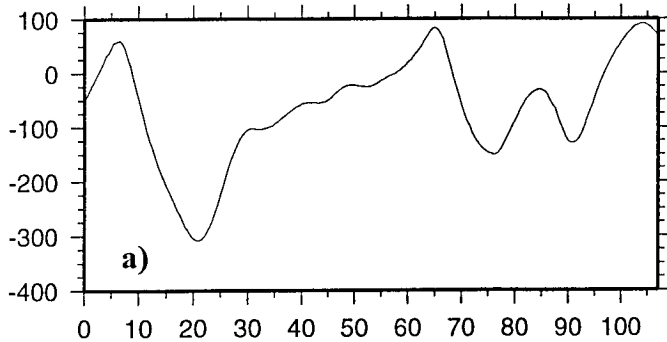


Figure 5. a) and b) are synthetic profiles extracted from the gridded data. See figure 1 for location.

interaction, a thorough effort of removal of these long wavelength components was carried out.

For logistical reasons, a base station was setup near Santiago (~ 70°30' W/ 33°30' S), using a total magnetic field digital instrument (Geometrics G-866) loaned from GEODATOS. The diurnal record is shown in Figure 6 as a function of time in terms of Julian days. Unfortunately, during the time span of April 1st to April 6th (Julian day 91-96) we couldn't get a continuous magnetic record due to an unpredictable requirement of the instrument by GEODATOS. During that time, a manual record of the magnetic field was recorded during work hours only. For the remaining days, a similar digital instrument (G-866) was loaned from Mantos Blancos Mining Company. Therefore two main problems hampered a fully successful diurnal removal: a) the distance from the survey area; and b) the lack and/or not totally reliable base station magnetic information. The distance from the survey area becomes even more important considering the pattern of the magnetic time series at the base station. In general the magnetic signal was not quiet, and probably we recorded the effects of a magnetic storm, specially noticeable during March 26th (Julian day 85) and April 7th (Julian day 97), and probably in the poorly recorded April 2nd day (Figure 6). In such a stormy environment, inductive effects of a good conductor, such as the ocean layer, certainly induces a near field transient effect over the steady crustal signal.

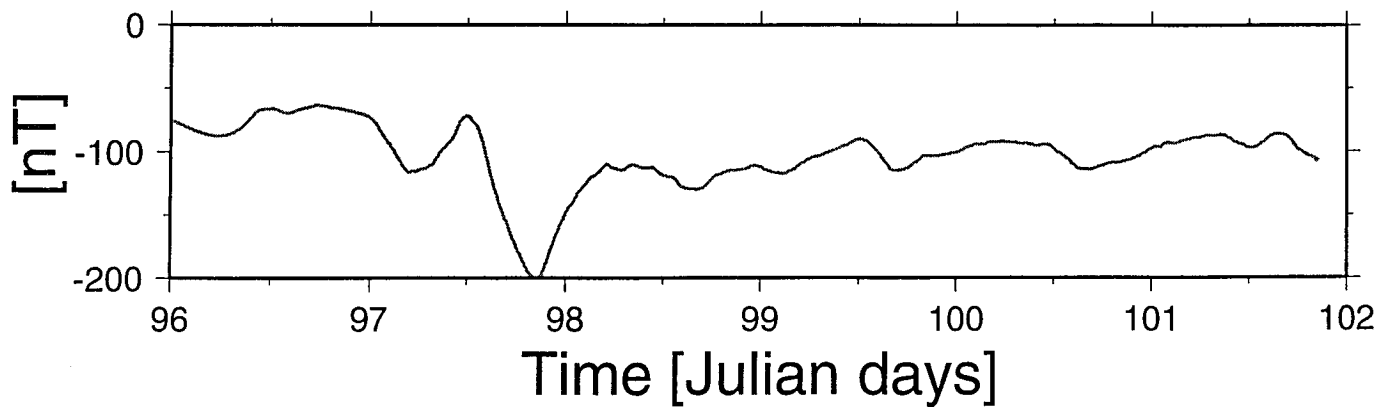
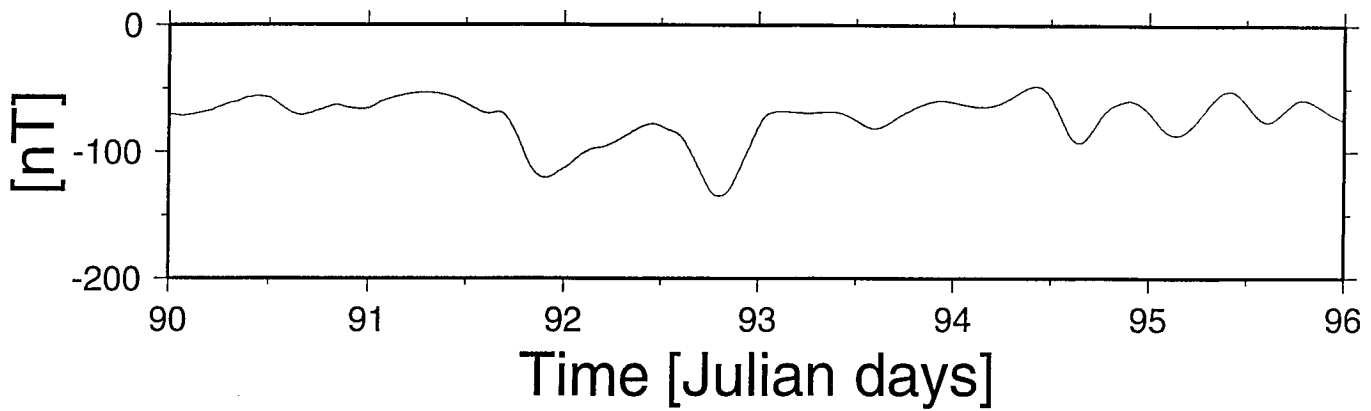
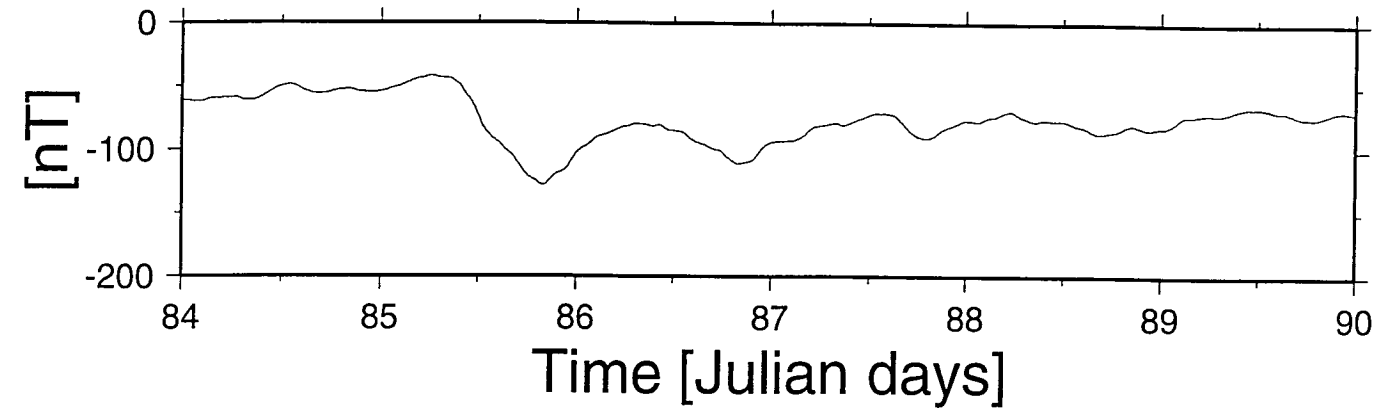
For all these reasons a very careful diurnal correction was performed including the following steps:

a) Low-pass filtering of the diurnal variation with a moving average window of 4 hours, reducing in this way most of the high frequency signal associated with near-field effects. These near-field effects cannot be extrapolated from the base station to the survey region.

b) Removal of the filtered diurnal variation from the production lines.

The resulting leveled grid is shown in Figure 7, where we can appreciate the improvement over the raw data set (Figure 3). However it is clear that some linear E-W trends are still present in the signal, mostly due to a poorly resolved diurnal correction on some days. In fact looking at the worst cases, the correlation between the bad leveling and those "stormy" days is very high. In order to remove all these artifacts from the magnetic signal, we developed on board a robust technique that was able to account with most of these effects. The procedure includes a gridding with GMT software at a coarse interval (~0.05-0.08 degrees) such that only the main trends

Figure 6 Base Magnetic Station



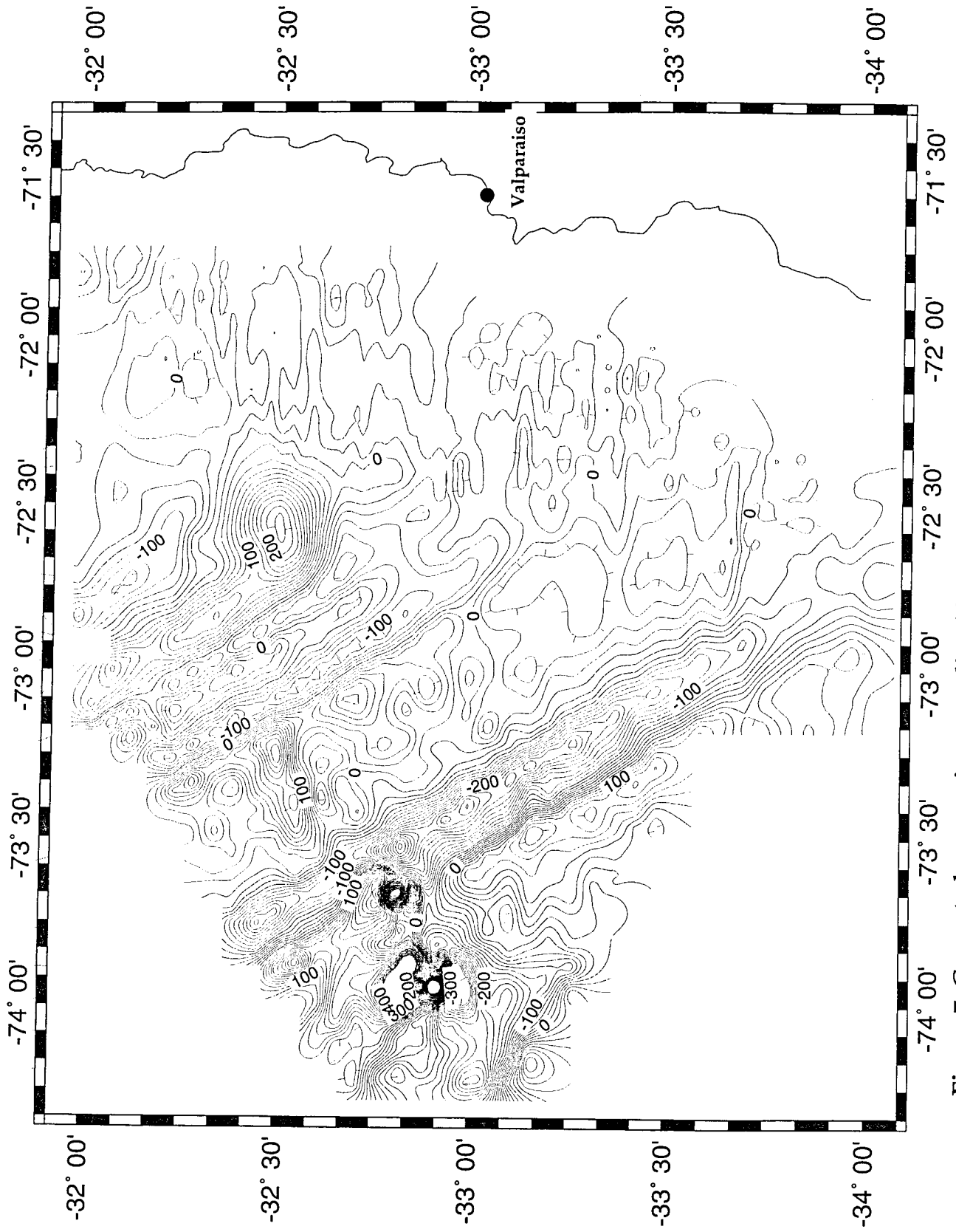


Figure 7. Corrected magnetic anomalies (diurnal variation removed only).

are preserved. From this "coarse" grid we interpolated the regional field into every data point of the survey, taking the difference with the actual reading in each case. A low pass filter or a moving average of this time series would provide an estimate of the transient regional that has to be removed from the data. In practice we take a gaussian filter with a window of 8 hours, the resulting trend is then removed from the data and a new coarse grid is recomputed. We applied this procedure iteratively until no further differences between one grid and the next was achieved.

The previous robust approach is probably good enough for relatively quiet regions, whereas in regions of highly varying magnetic field it would carry some valuable signal. Therefore we took a step further, restricting the leveling estimates to the areas not severely contaminated with high intensity magnetic anomalies, specifically the region to the east of the trench axis (see in section 6 a likely explanation for this low magnetic signal). Then we computed the departure from every point in this segment of the line, adding the average of the whole set of residium to the diurnal variation of the entire line (D.C. shift). This approach proves to be very successful but in the O'Higgins seamount region which corresponds to a time of unreliable diurnal correction and presumably under stormy conditions (Julian day 92 in Figure 6). Lucky, the O'Higgins seamount region presents a strong magnetic signal in which case leveling effects in the order of tens of nanoteslas [nT] does not affect a signal of a couple hundreds of nT.

Finally some minor leveling problems were resolved taking some lines out of the gridding data set, computing the grid without the "shifted" line and removing the average level from the line (second D.C. shifting), and incorporating again the corrected line to the gridding data set.

The final grid is shown in its contouring form in Figure 8. The grid was computed considering a grid interval of 0.01 degrees (~ 1.1 km) and a tension factor of 0.3. We can appreciate the real improvement comparing the final map with the raw data map (Figure 3). We are very confident in the quality of the final product although it is clear that some high frequency signal inherent to a local diurnal variation is probably still present in the data, but at levels lower than 10 nT. In Figure 9 we present a comparison between the magnetic signal of crustal origin and the signal finally removed from the data. From the figure it is clear that we only introduced very long wavelength components and D.C. effects on the magnetic signal. Besides, comparing Figure 9 with the original diurnal variation of Figure 6, we identify some departures especially in the already mentioned stormy days.

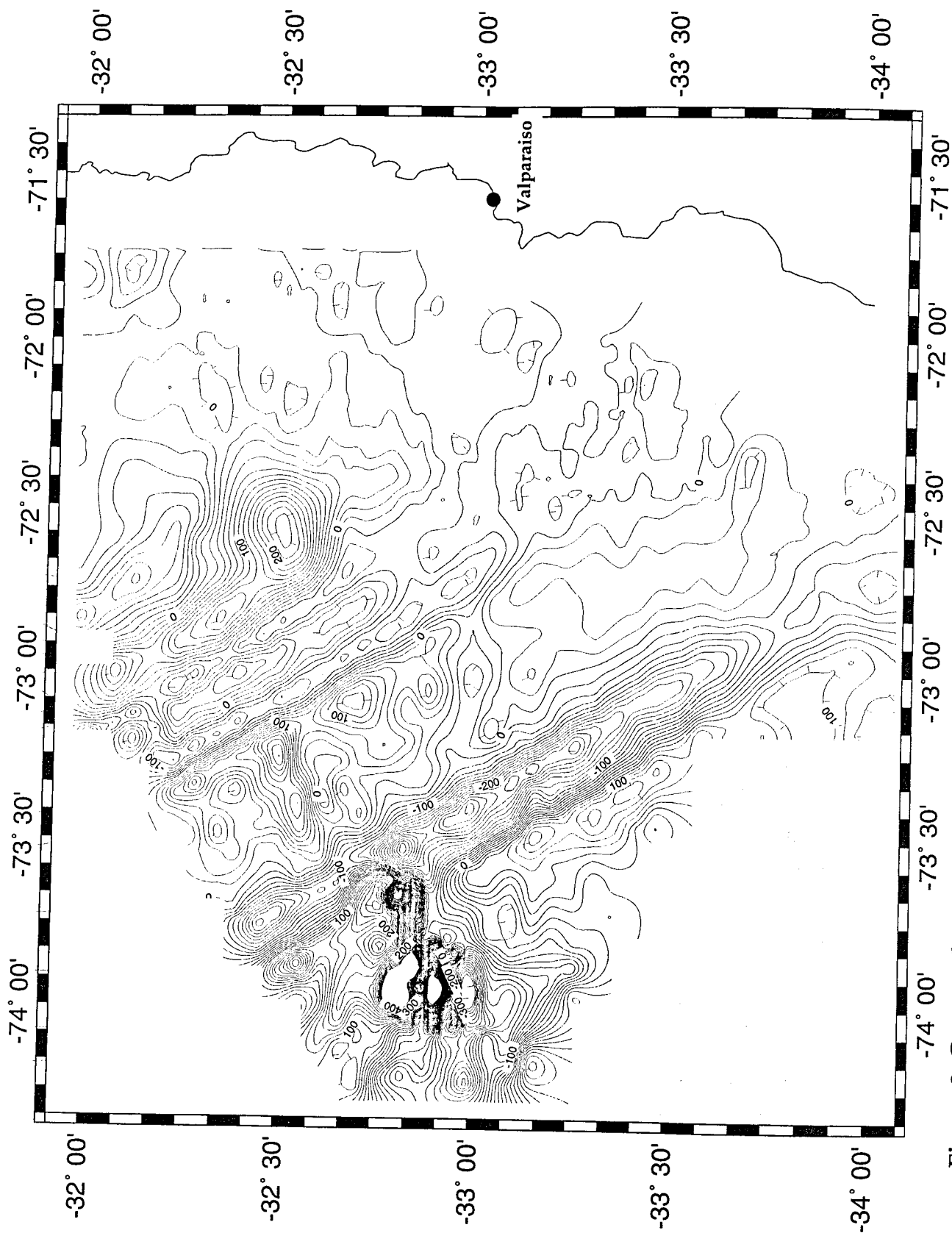


Figure 8. Corrected magnetic anomalies (diurnal variation removed plus robust component).

4.6 Data Processing

After the data reduction a series of sub-products of the original data set were produced, providing in this way a better visualization of all the magnetic features present in the survey area. The process includes the following products:

- Reduction to the pole (Figure 10)
- Analytical signal (Figure 11)
- Projected profiles along the tracks "wiggles" (Figure 12)

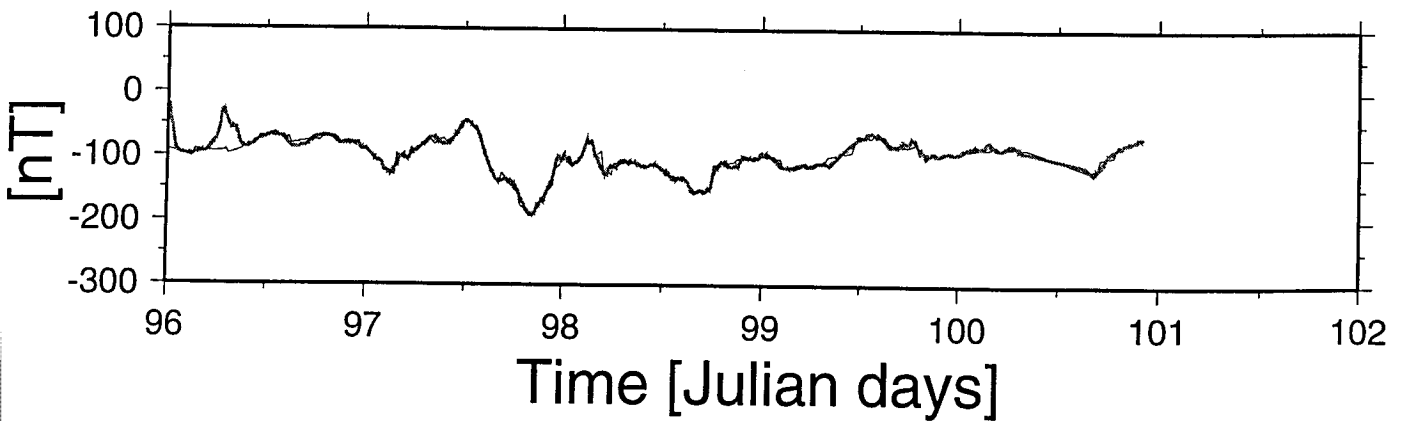
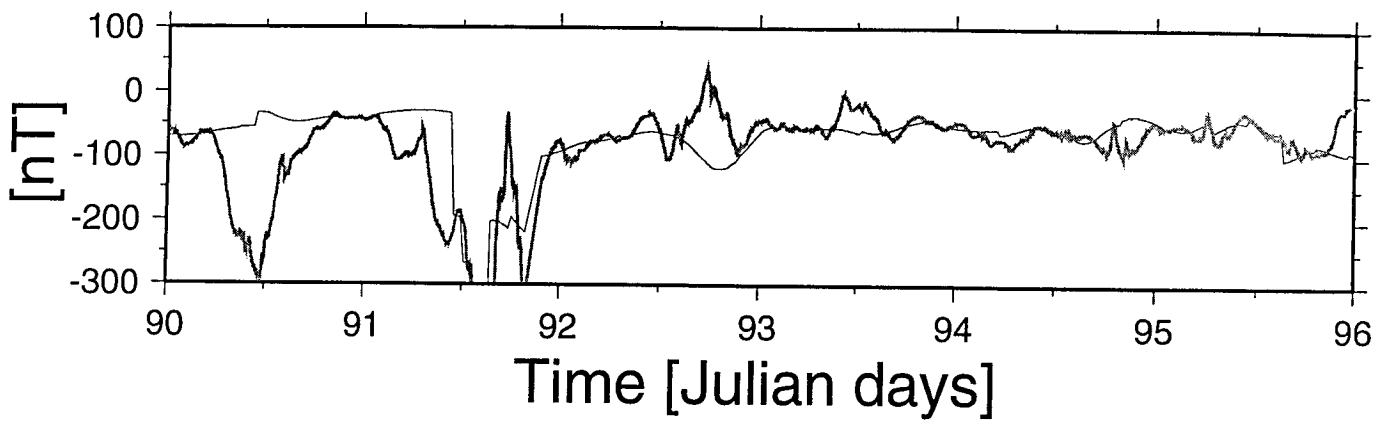
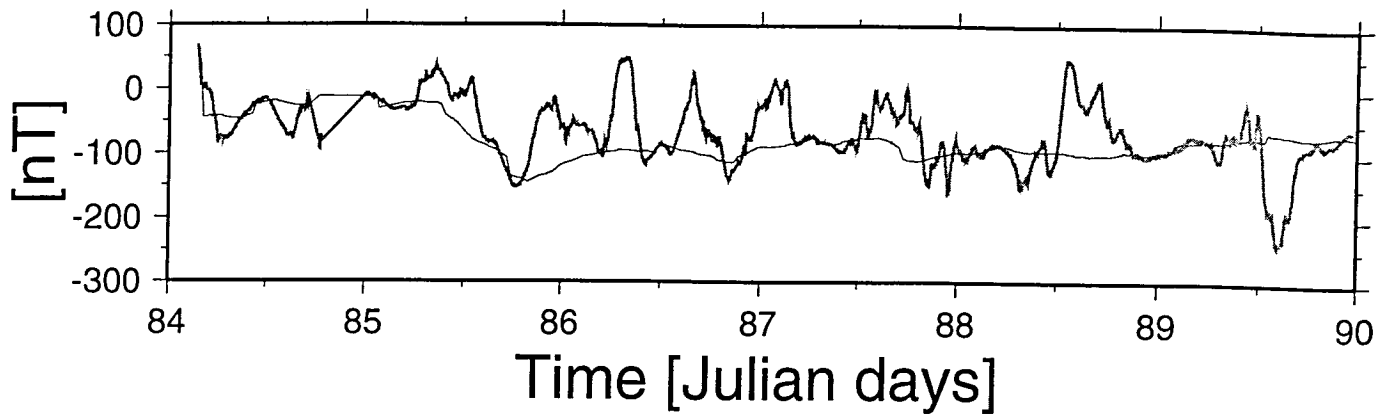
The reduction to the pole and analytical signal products were produced using the spectral analysis package of the Servicio Nacional de Geología y Minería (SERNAGEOMIN), Chile. The aim of these products is to reduce the skewness of the magnetic signal at low-to-intermediate geomagnetic latitudes. Reduction to the pole is a conventional technique in which the spectrum of the potential field is multiplied and divided by the spectrum of the cosine vectors at the pole and equator respectively. Providing that we know the direction of the main field and the magnetization of the magnetic body, this procedure eliminates the disturbance of the magnetic inclination, forcing a vertical magnetization that locates the anomaly right on top the causative body. However in oceanic crust with a sequence of normal and reverse magnetic field this procedure could be ambiguous because we are unable to fix a single direction of remanence and inductive effects. On the other hand the analytical signal technique is insensitive to the geometrical factors associated with the vectorial magnetic field in a complicate magnetized environment. Essentially what is represented in the analytical signal product corresponds to the absolute value of the modulus of the three gradient components of the total magnetic field. In general terms, a combined use of both techniques has proved to be the most efficient way to handle the interpretation task.

Projected anomalies along the tracks is performed using the GMT program called pswiggle. This representation of the magnetic anomalies provides a better view of tiny features that are normally missed in the gridding procedure.

4.7 Preliminary Modeling and Interpretation

Descriptive analysis and interpretation. In order to get a better understanding of the nature of the magnetic field in the region we assembled a composite map, including the information on the adjacent land. This data set belongs to SERNAGEOMIN and it is part of the regular mapping program of the institution. The composite map is presented in Figure 13, and no leveling or any kind of analytical continuation has been applied to any of the two data sets. Because the continental

Figure 9 Magnetic Raw Data and TotalCorrection



information was acquired at 600 hundred meters above the surface, the transition from continent to ocean should be relatively smooth and good enough for a general, regional interpretation of the main features. The two data sets have an almost equivalent line spacing, and thus the spectral content is roughly the same. From an analysis of this composite map (Figure 13), from the subproducts of the present survey (reduction to the pole, analytical signal, and along-track magnetic data) (Figures 10, 11 and 12 respectively), and the bathymetric map of the region (Figure 14), we identified four different magnetic domains which are described in Figure 15. Each one of these units has a characteristic magnetic fabric described in terms of the shape, wavelength and intensity of the magnetic anomalies and the principal trends or magnetic lineation. The domains and their main characteristics are the following:

Oceanic crust domain. Located to the west of the trench axis, it is characterized by lineated anomalies with a dominant trend of NW-SE direction which is particularly prominent to the north of approximately $-33^{\circ}15'$ and west of $287^{\circ}30'$, but rapidly vanishes toward the east. The sudden attenuation of the magnetic anomalies a few km east of the trench axis beneath the continental plate could be interpreted as a steeply dipping subducting oceanic lithosphere. Ocean spreading anomalies are completely attenuated about 30 km from the trench axis. These lineated anomalies are seafloor-spreading anomalies that delineate the strike of the spreading center at which this ocean crust was formed. According to previous studies (i.e. Cande and Haxby, 1991), this piece of oceanic crust belongs to the Eocene sequence. According to our preliminary analysis described in the following subsection (6.2 Magnetic Modeling), the oceanic crust would represent a repeated section of anomaly 16 with a ridge jump towards the west (~ 80 km), during a normal period within anomaly 16 (~ 37.4 Ma). The spatial location of this eventual ridge jump is roughly coincident with a series of small volcanic centers aligned parallel to the magnetic trend (see Chapter 3 for a better visualization of the seafloor imaging).

This magnetic domain is crossed by the O'Higgins magnetic trend at an almost right angle with respect to the seafloor spreading lineations and sub parallel and bounded by the O'Higgins zone of fracture (OZF). This major trend is clearer noticeable in the analytical signal map (Figure 11), where it becomes evident that the cross section wavelength of this prominent feature is much wider than the high topographic relief represented by the O'Higgins seamount and guyot. These later features are characterized by rounded anomalies of very high intensity. Reduction to the pole and analytical signal representations (Figures 10 and 11), locate the source of these anomalies right on top of the prominent topographic features. A forward

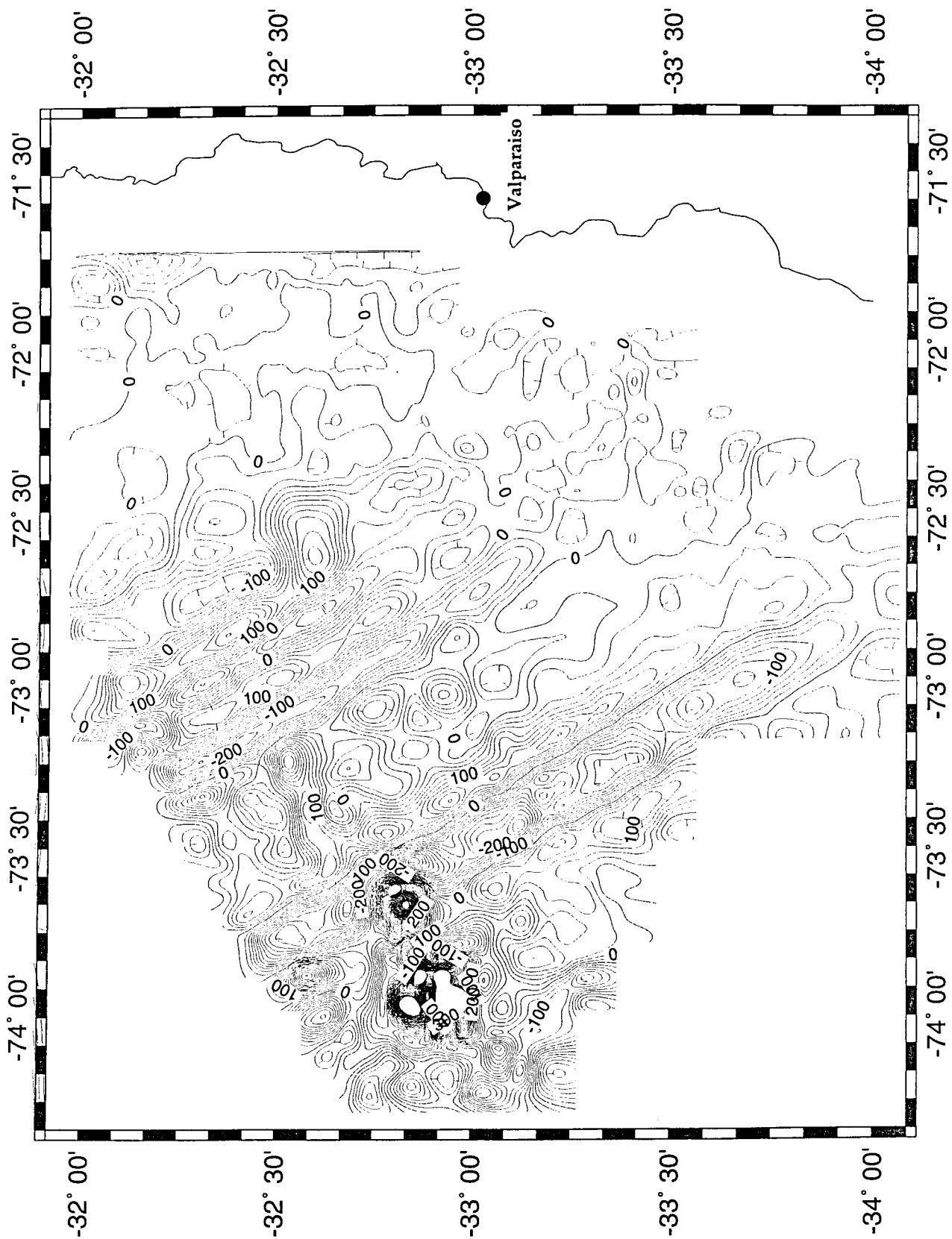


Figure 10. Reduction to the pole.

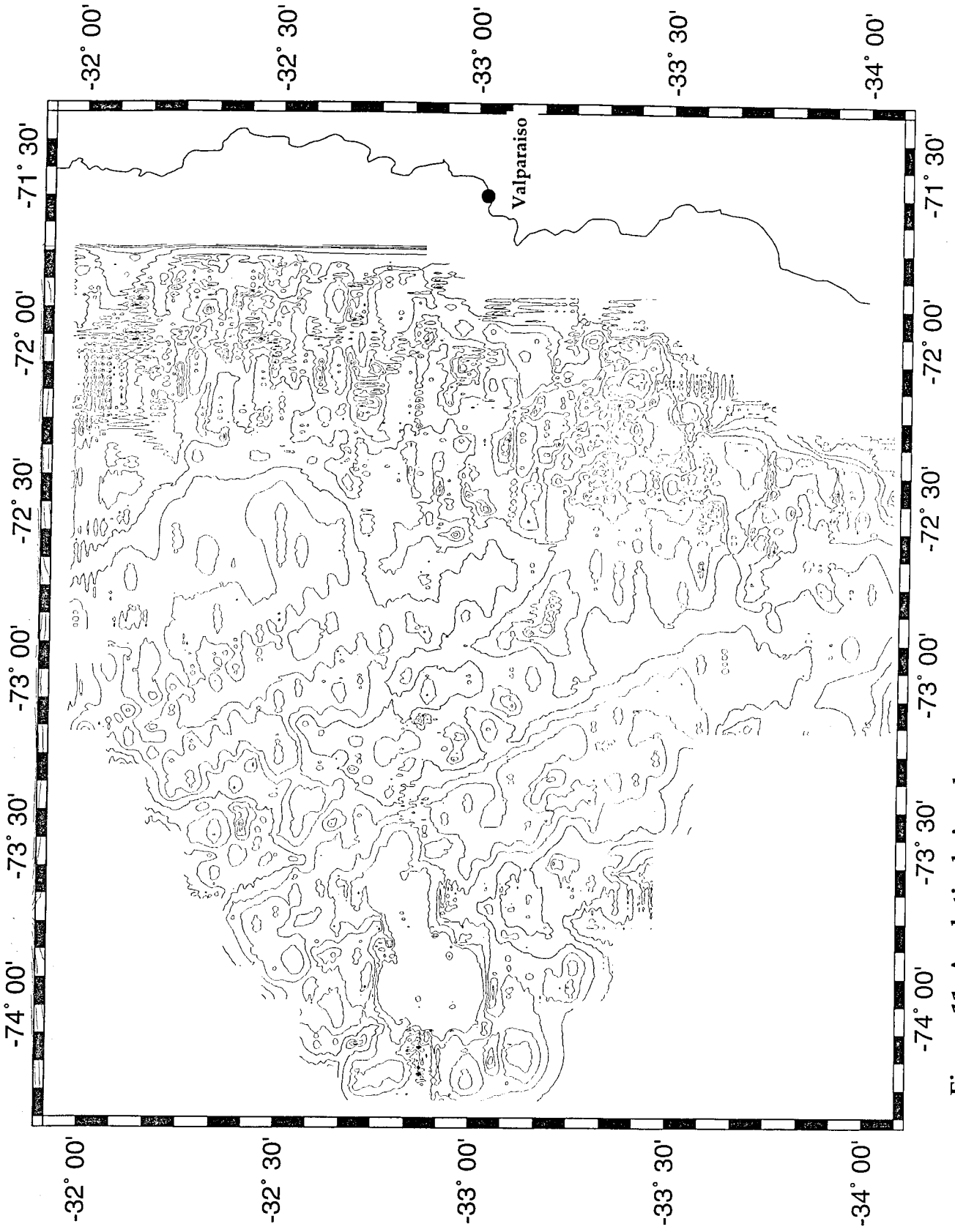


Figure 11. Analytical signal.

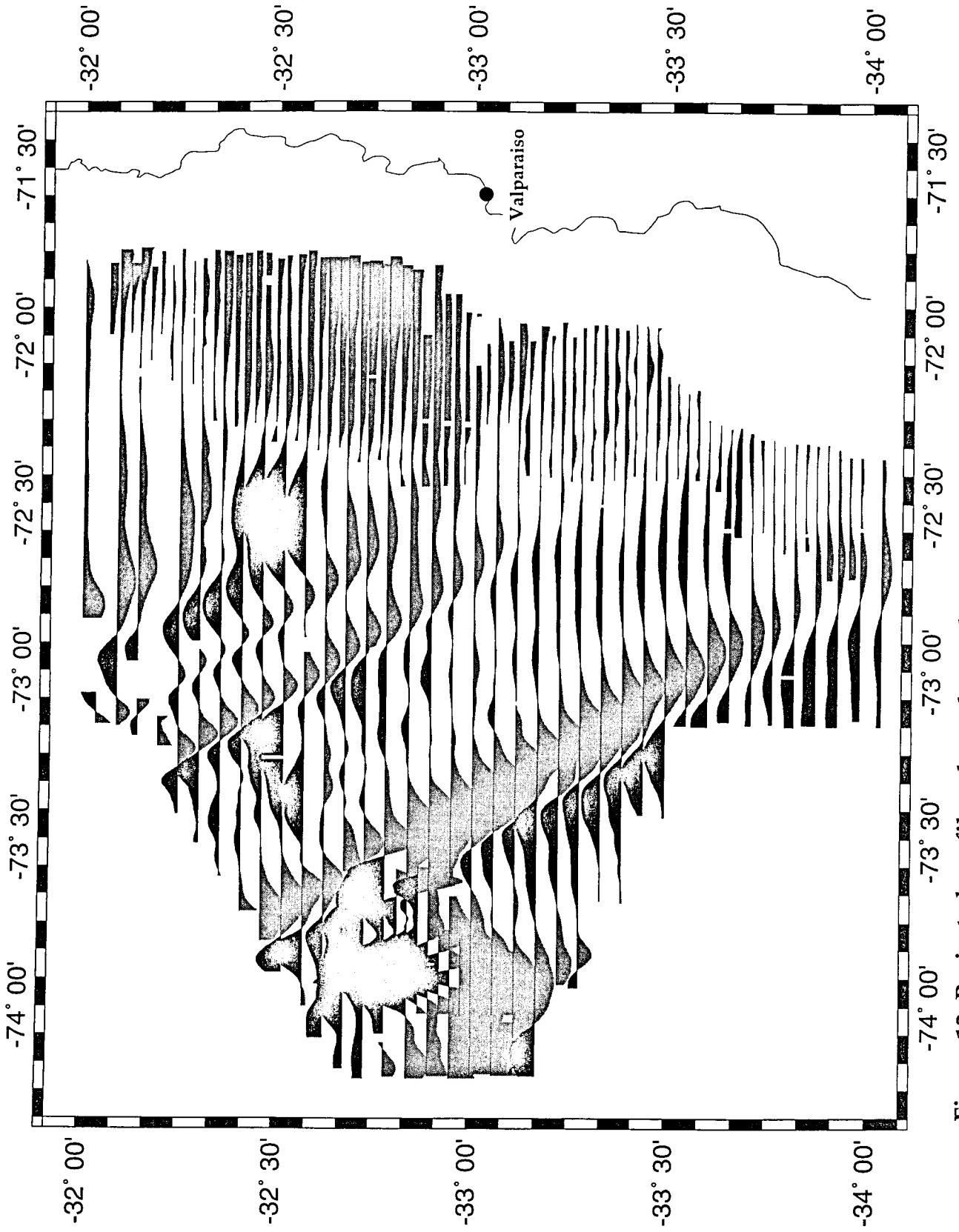


Figure 12. Projected profiles along the tracks.



Figure 13. Composite magnetic map offshore continent.

modeling of these anomalies (see next sub-section) shows that they corresponds to a highly magnetized source of basaltic origin and are very close to the surface. According to the model effort the O'Higgins seamount would be formed in two steps a first and broad building process during a period of normal polarity of the magnetic field followed by a final stage in which the cooling of the magma occurred while the magnetic field was reversed. The section of the volcanic edifice affected by this remanent process is located in the upper sections of the northern flank. Probably coeval with this late pulse of the O'Higgins Seamount, the O'Higgins Guyot was formed because in both cases a remanent magnetization is required to explain the magnetic pattern. Reinforcing this argument, the bathymetric map of the region (Figure 14) shows that the northern flank of the O'Higgins Seamount and the O'Higgins Guyot are connected by a lineated feature that may correspond to some sort of weaker lineament that would allow the magma to reach the seafloor.

Continental crust domain. Located in the eastern flank of the region, it is characterized by magnetic anomalies of low intensity and without a clear pattern or trend. But if we expand the view to include the continental information (Figure 13), some of the most conspicuous E-W trends in the continental region have a clear extension in the continental platform with some bending towards the north. Also representative of this domain is a lineated sequence of rounded anomalies that follows an almost N-S trend in the middle of the magnetic domain, some of them seem to follow the upper course of San Antonio Canyon. The pattern and orientation of this trend can be correlated with the well known magnetic signature observed at the roots of the Middle to Late Cretaceous arc in the eastern flank of the Coastal Cordillera (Parra & Yañez, 1988), which is shown at 71°W in Figure 13. If the analogy is correct, these magnetic sources could represent the location of an abandoned arc of probably Early Jurassic or Late Triassic time, given the fact that the intrusives at the coastal region are Mesozoic in age and the migration of the arc has been mostly eastward since at least Middle Jurassic time (Mpodozis and Ramos, 1989). That intrusive chain is probably associated with the Topocalma Knoll which is an uplifted region in the seismic records (see in chapter 5.1 of this report the discussion of the seismic results). All the elements considered in the previous paragraph are consistent with a continental origin of these magnetic anomalies, supporting in this way the interpreted tectonic domains.

Deep source domain. This magnetic domain is located to the north and west of the Continental Domain and it is characterized by a very mild and long wavelength magnetic signature. Both are first order characteristics of deep source magnetic anomalies. This inference is consistent with the multichannel seismic imaging of the

Valparaiso Basin, north and south respectively, in which the only prominent features are the Punta Salinas Ridge and the positive relief underneath the Montemar Canyon. Those features are clearly observed in the magnetic signal as a set of SW-NE and E-W trends respectively, probably representing the uplift of basement rocks.

Deformation front domain. Located in between the Oceanic Crust and Deep source domain. Magnetic anomalies in this domain are of intermediate to high intensity, long wavelength and rounded form. The most prominent anomaly in the domain is located at $-32^{\circ}30'/287^{\circ}25'$. Considering the pattern and intensity of the continental anomalies (low intensity and small size), this anomaly is probably of oceanic origin and therefore it occurs beneath the upper plate. The spatial association of the other two local anomalies (O'Higgins magnetic trend) to volcanic edifices and the presence in the upper slope of uplifted topography and a retreat of the plate boundary (see Chapter 3), indicates the presence of a subducted seamount. The location of the seamount is not exactly at the location of the magnetic maxima since some skewness can be observed in the other two local anomalies. In fact the reduction to the pole of this region (Figure 10) shows a shift towards the south. Interestingly the same representation of the analytical signal presents a body composed by two independent bodies a couple of kilometers apart. The projection of these lines towards the trench are coincident with two zones of retreat in the plate boundary (see Figure 14 and Chapter 3). Considering a highly likely volcanic nature of this body and also its affinity to the magnetic anomalies associated with the O'Higgins magnetic trend, we modeled this anomaly considering the same parameters that allowed us to model the other well exposed source in the O'Higgins magnetic trend (see details in the next subsection). Using this approach we had a chance to better constrain the depth to the top of this magnetic source. Putting some constraints in the depth to the bottom of the body at the dipping subducting slab surface ($\sim 8-9$ km at a distance of 10 km from the trench with a dipping angle of 30 degrees), we ended up with a causative body at a depth of 6-7 km from the surface. We also computed the same model considering its top surface at a greater depth. We use this approach in order to constraint a potential volcanic edifice that could be associated with the 1985 earthquake event with an epicenter located further south and eastward, in the Crustal Domain specifically. At that location, the top of the magnetic body would be located at a minimum depth of 10 km. In that case, a broad magnetic anomaly of less than 20 nT and more than 30 km of wavelength would show up, however, in the magnetic map (Figure 8) a feature with this pattern is not evident, although we have to consider that a body with these characteristics is at the limit of detectability.

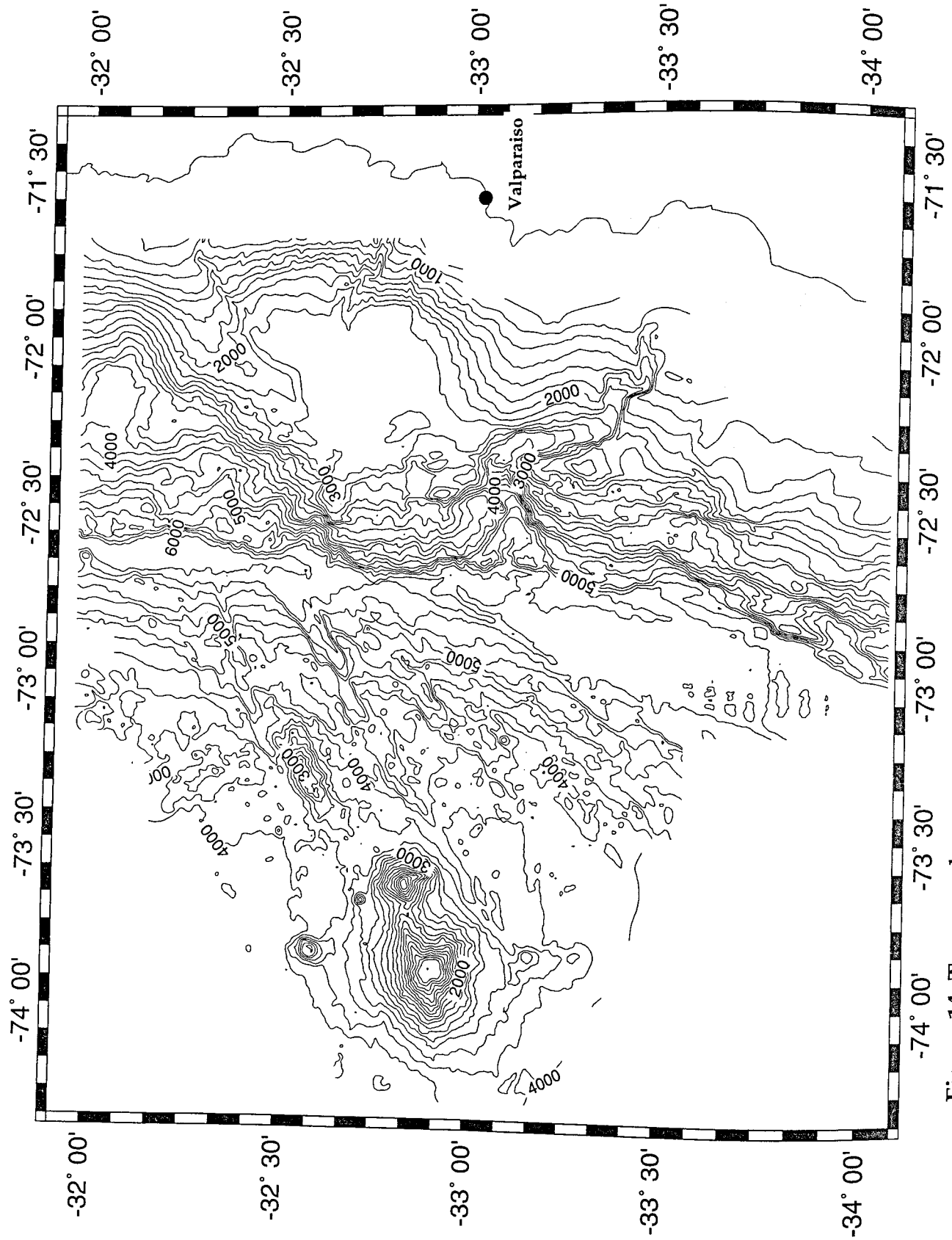


Figure 14. Topography

Preliminary magnetic modeling. As mentioned in the previous section, we run a set of forward models in order to get a better understanding of the main magnetic anomalies observed in the survey area. The modeling effort can be separated in two sections: a) Magnetic modeling of the seafloor spreading sequence and b) Magnetic modeling of localized volcanic centers (i.e. O'Higgins Seamount, Papudo Anomaly). Therefore, in the following paragraphs we will describe the technical aspects of this modeling effort, providing in this way a quantitative support to the conclusions of the previous sub-section and the overall interpretation of the magnetic data set.

Seafloor spreading anomalies. Seafloor spreading magnetic anomalies in this section of the Nazca plate are part of the Eocene sequence (i.e., Cande and Haxby, 1991). In the sparse coverage of the seafloor spreading magnetic anomalies identified along the margin to the south and north of Challenger Fracture Zone, we find a range from anomaly 16 to 18 (~ 36-38 Ma). According to Cande and Haxby (1991), the seafloor spreading velocity for the Nazca plate at that position and time was about 63 mm/yr. Therefore our first attempt to identify the magnetic sequence observed in the area was to construct a magnetic sequence between anomaly 16 and 18 in which the size of every body is controlled by the velocity of the plate. We used standard parameters for the magnetization of the oceanic crust sequence: a layer 2a of 0.5 km thickness at a depth of 4.5 km, a magnetization of 0.005 emu/cc; and remanent inclination of -70° and 0° of declination (axial magnetic dipole assumption). We run the experiment using a Talwani 2-D model implemented in the SERNAGEOMIN geophysical package. The resulting forward model is shown in Figure 16. In the same figure we plot a profile interpolated from the magnetic grid in the northern part and perpendicular to the magnetic sequence. From the figure we can see that the correlation is not very good, either correlating the synthetic anomaly located at 37.5 Ma with the first anomaly in the left hand side of the data (~ 30 km), or in the following sequence (~ 70 km). We concluded that a standard section of seafloor magnetic anomalies in the Eocene sequence does not match the observations. However, Cande and Haxby (1991) had suggested the presence of a ridge jump to the west at the time of anomaly 16. Looking at the magnetic sequence we found that the only chance to get a repeated sequence in anomaly 16 is provided by a ridge jump during a period of normal polarity in which a tiny reversal is included (between 37.2 and 37.7 Ma in Figure 16). Then we fix the required width of the symmetric anomaly to fit the observations, displacing the remaining part of anomaly 16 at a convenient place to fit the rest of the magnetic sequence to the west, but always keeping in mind the constraint imposed by the seafloor spreading velocity and timing. The resulting product of this model is presented in Figure 17, along with the profile of the previous

figure. In this case we put a more realistic shape of the oceanic plate, bending downwards as it collides with the trench. As it becomes evident from the figure, the first order correlation between the observed anomalies and the predictions of the model are considerably better than in the previous case. A characteristic feature of the anomaly associated with the ridge jump is a small but broad positive peak followed by a relative negative and a much larger positive. This sequence is observed in almost all the profiles of the oceanic sequence, especially noticeable in the along track representation of the survey (Figure 12).

From this analysis we concluded that the age of the oceanic plate in the region lies in the range of 37-39 Ma, with a likely ridge jump of 60 km to the west at 37.4 Ma.

3-D magnetic modeling of seamounts bodies. The other prominent feature in the magnetic anomaly map corresponds to the anomalies associated with positive relief bodies like the O'Higgins seamount and the Papudo seamount of the O'Higgins Magnetic Trend (Figure 15). In the first set of models we compute the forward model of the more simple and evident case of the O'Higgins Seamount and Guyot. Once the parameters used to fit the first set of anomalies were well constrained, we then kept the same parameters to fit the depth to the source in the less obvious magnetic sources in the Deforming Front and Continental Crust Domains. This rationale is based on the assumption that all those rounded bodies would share a common origin at the hotspot of the Juan Fernandez Chain. If that is true, then a common magnetic signature is a good starting point for their interpretation.

In terms of the modeling procedure, we used a 3-D forward modeling under the assumption of prismatic bodies of horizontal surface at the top and bottom of the body (Pluoff, 1975). The algorithm has been implemented in the SERNAGEOMIN package for an interactive procedure.

For the O'Higgins Seamount and Guyot, the shape and position of the body is constrained by the bathymetry of the region (Figure 14). The magnetization is then fixed by the required amplitude of the anomalies, to a number of 0.0026 emu/c.c. which is almost a 50 % of the magnetization used in the seafloor spreading anomalies (section 6.2a). This somehow lower magnetization value is the mixed response of a lower geomagnetic intensity at the paleolatitude of magnetic acquisition at the time of cooling below the Curie point (more equatorial than the oceanic crust of the host rock), and probably a little bit more silicic magmatic source than a MORB basalt. This kind of "intermediate" geochemistry is not unusual in other well studied seamount chains and

Figure 15: Magnetic Domains and Lineations

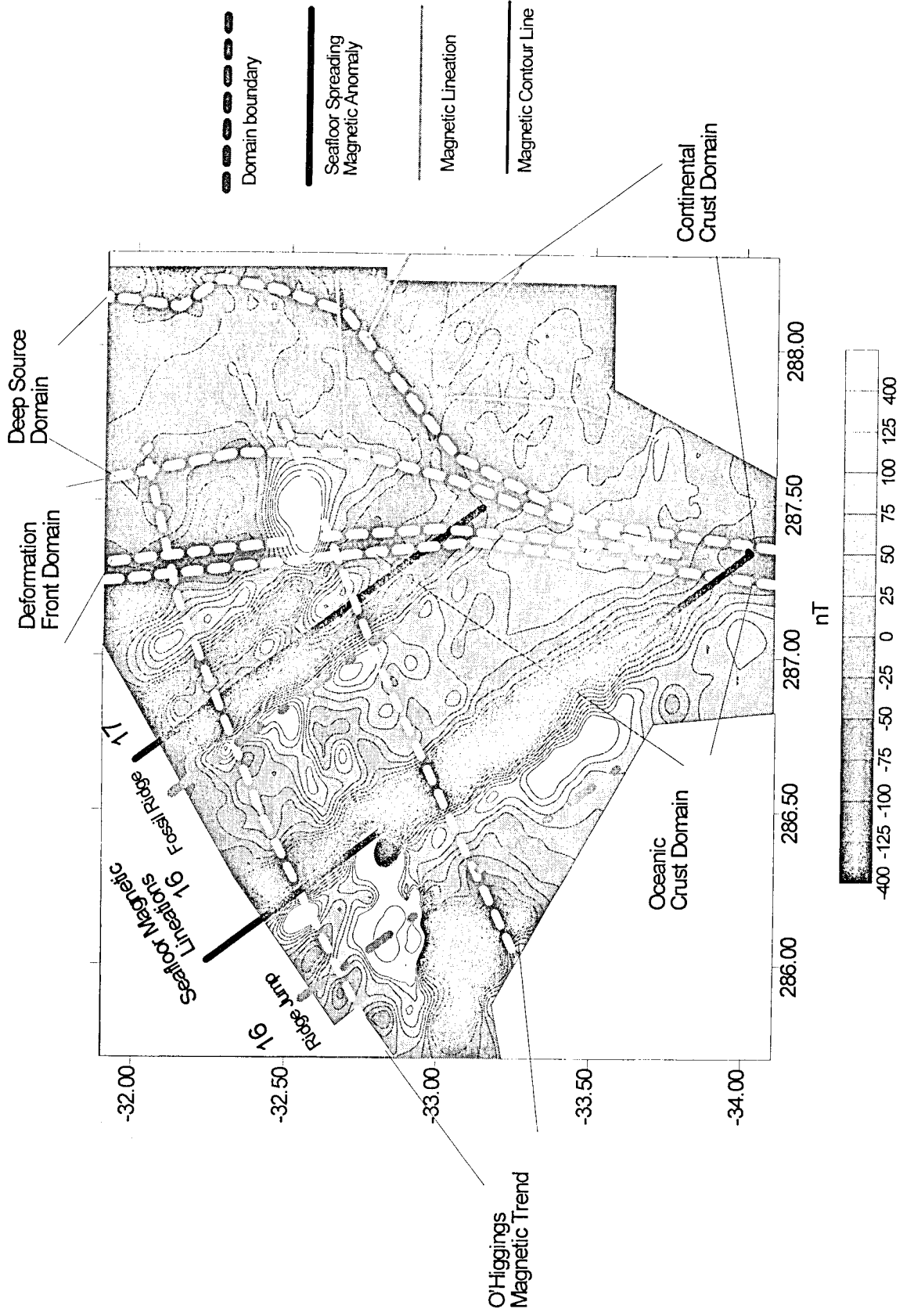
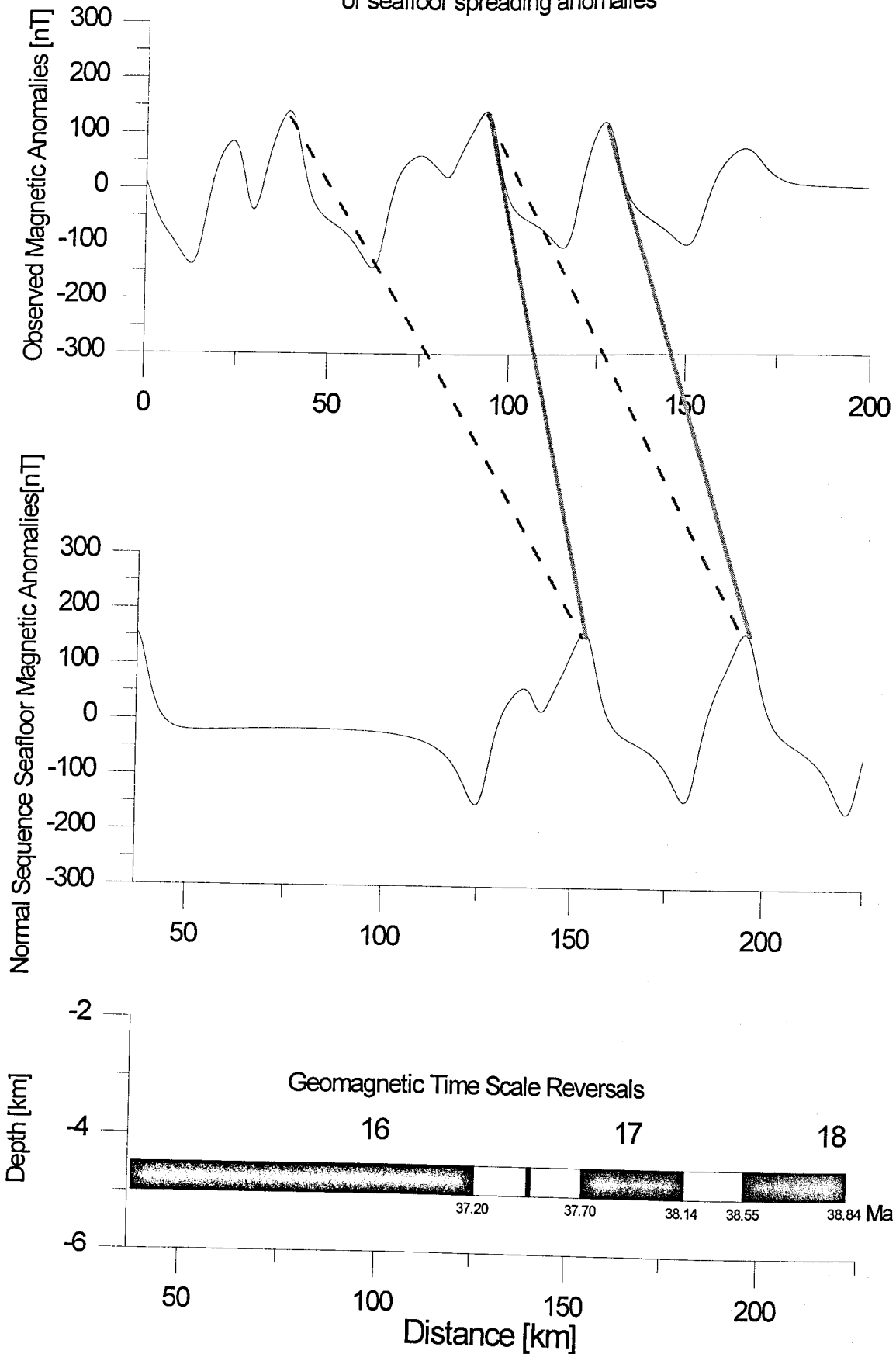


Figure 16: 2-D Magnetic model of the normal Eocene sequence of seafloor spreading anomalies



hotspot areas (i.e. Fullerton et al., 1989). In Figure 18, we present a preliminary forward model for the magnetic effect of O'Higgins Seamount and O'Higgins Guyot. The O'Higgins seamount is modeled with three bodies, a larger one of 3.0 km thickness over which two smaller bodies of 2.5 km thickness represent the upper and steeper section of the volcanic edifice (see in Figure 18 the plant view of the bodies). Interestingly, the northern small body requires a reversal magnetization to fit the anomaly data (also shown in the right hand side of the figure). On the other hand, the much smaller O'Higgins seamount is modeled in terms of a single body resting at 0.8 km from the surface and with a thickness of 2.2 km. Again the characteristic shape of the anomaly, with a broad negative flanked by minor positives in the northern and southern edge, required a negative polarity in order to fit the data (see in section 6.1 the discussion of the likely connection in the timing of the magmatic events that generated the seamount chain).

Having made a quantitative estimate in the parameters required to fit the well exposed seamount bodies of the O'Higgins magnetic trend we turn our attention to the more difficult task of determining the depth to the source in some suspected seamount underneath the overriding plate. Specifically we tried to model the Papudo Anomaly in the Deforming Zone Magnetic Domain. Using an estimate of 30° for the dip angle of subduction (Kirby, in prep.) we set up a tentative depth of 9 km for the bottom of the Papudo Anomaly, coincident with the Benioff plane at a distance of 10-15 km from the trench axis. Considering a thickness of 3 km, we obtained a reasonable fit of the observed anomaly (Figure 19). This result means that the top of the "subducted seamount" is probably at a depth of 6 km from the sea surface and then 1-2 km from the continental slope surface or seafloor. A better constraint of the top of the body should be clear from the seismic record. In Figure 19, we also modeled the same body but at a depth of 13 km from the surface. We try this model as a way to quantify the magnetic effect of others seamounts of the same nature that would be further in land and at greater depth on the descending plate. We see that the amplitude of the anomaly is severely attenuated and the wavelength content is translated to the longer domain. A quick look at the magnetic pattern in the Continental Crust Domain does not show any other seamounts, although we have to consider that these kinds of features are at the limits of detection in the present experiment. In order to make a more reliable estimate we need a set of N-S lines with a very good diurnal control in a coastal position.

Figure 17: 2-D Magnetic model of a repeated sequence of anomaly 16 in the Eocene seafloor spreading magnetic anomalies

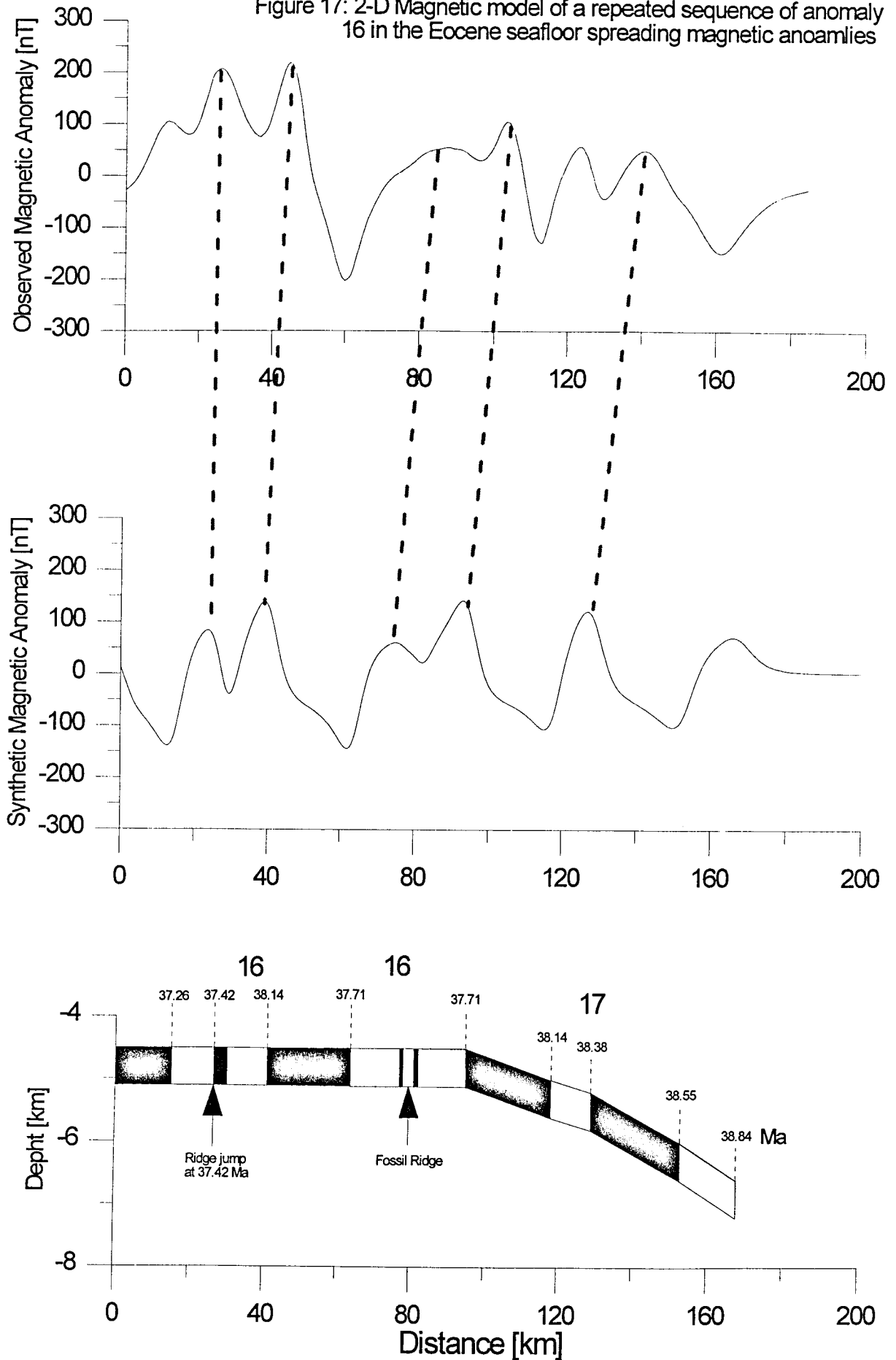
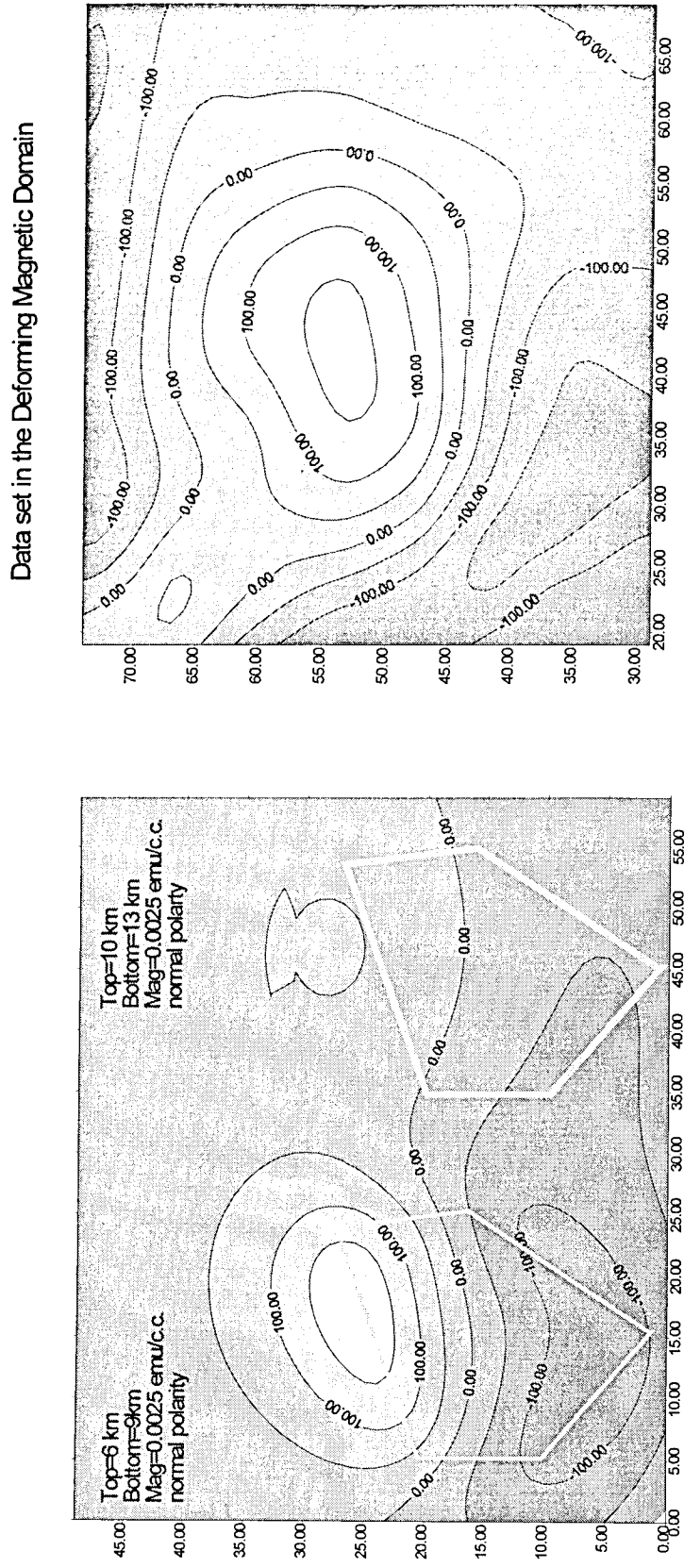


Figure 19: 3-D Magnetic Model of a seamount under the continental shelf



4.8 Conclusions

From the previous discussion we want to highlight the following conclusions:

- A high quality magnetic survey was obtained during the Condor survey which was post processed over a grid of 0.01 degree and 5 nT of envelope error.

- A composite offshore onshore magnetic map was also produced joining this survey with an aeromagnetic survey of SERNAGEOMIN. The joint map provides a better understanding of the interaction between the oceanic and continental plates.

- From the magnetic maps, their sub products, the bathymetry and the seismic information we were able to define different magnetic domains within the survey area. These domains are characterized by distinctive trends and features which can be interpreted in terms of the main morphotectonic units of the region. Relevant to the continental geology is the continuity of major old structures trending E-W, that represent inherited weaker domains probably reactivated during later tectonism.

- One conclusion from these magnetic domains regards the almost right angle intersection of the Juan Fernandez chain with the trend of the Cenozoic seafloor spreading anomalies. This relation indicates a bend between the western younger and eastern older parts of the Juan Fernandez Ridge. Also relevant to the understanding of the collision process is the fact that the interaction between the continental plate and the oceanic rough topography comprises a much broader region than the isolated volcanic edifices.

- The modeling of seafloor spreading anomalies in the survey area show a likely ridge jump during anomaly 16 at 37.4 Ma. This ridge jump implies that a 60 km wide lithospheric plate was transferred from the Pacific to the Nazca plate. The overall range of ages in the oceanic plate of the area ranges between 36-38 Ma.

- 3-D modeling of the of the O'Higgins Seamount and Guyot required a combination of normal and reversed magnetized bodies, with magnetizations a small amount less those from a MORB basaltic source. The bodies magnetized during a reversal of the magnetic field appear to be coeval, post-dating the emplacement of the normally magnetized larger body. A similar kind of a rounded body but emplaced at a greater depth (~ 6 km below the surface) is probably responsible for the broad magnetic Papudo anomaly observed in the Deforming Magnetic Domain. Putting the body at the expected depth of an asperity potentially related with 1985 earthquake is essentially beyond the resolution of the present survey.

REFERENCES CITED

Cande, S.C. and W. F. Haxby, 1991, Eocene Propagating Rifts in the Southwest Pacific and their Conjugate Features on the Nazca Plate, *J. Geophys. Res.*, 96, 19609-19622.

Fullerton, L.G., H.V. Frey, J.R. Roark, and H.H. Thomas, 1989, Evidence for a remanent contribution in Magsat data from the Cretaceous Quiet Zone in the South Atlantic, *Geophys. Res. Letts.*, 16, 1085-1088.

Mpodosis, C. & V. Ramos, 1989, The Andes of Chile and Argentina, *in* *Geology of the Andes and its Relations to Hydrocarbon and Mineral Resources*, G. E. Ericksen, M. T. Cañas Pinochet, and J. A. Reinemund, eds., Houston, Texas, Circum - Pacific Council for Energy and Mineral Resources Earth Science Series, Vol.11.

Parra, J.C. and G. Yáñez, 1988, Provincias Magnéticas del Chile Central, *Revista Geológica de Chile*, V.15, 2, 101-117.

Pluoff, D., 1975, Prismatic modeling of magnetic and gravimetric bodies, *Geophysics*.

5.0 Seismic Reflection

(J. Korstgard, P. Trinhammer, J. Laursen, R. von Huene)

5.1 Seismic acquisition

Instrumentation. The seismic acquisition equipment consists of an acquisition unit with two tape decks, a trigger control unit, sleeve guns, and a streamer.

Acquisition unit (Geometrics ES 2420):

15 bit ADC (4 gain bit IFF); Gain 30.1 dB; Lowcut 15 Hz 18 dB/octave; Anti-alias filter 180 Hz 55 dB/octave; Sample interval 1 ms

Tape deck (STC 2925):

Tape density 6250 BPI. 100 IPS; Tape length 2400 ft; Tape format SEG-D, DeMux

Trigger control unit:

Custom made unit which controls triggering and shooting interval of sleeve guns and acquisition unit.

Sleeve guns (SG-I 40 cubic inch):

4 in a cluster, distance between each gun 40 cm

Synchronized by timing coil, delay 12 ms

Streamer:

24 channels (3 active sections, 50 m each); Channel interval 6.25 m; Group length 3.125 m, 7 hydrophones in each group

Setting up. The container was onboard the ship at about 11.04.95, 1200.

Acquisition unit, tape decks, trigger control unit and neartrace plotting was set up in the GEOLAB on deck 4 (main working deck). Streamer winch and gun umbilical winches were mounted at the rear of the vessel on the main working deck. This work was completed at 2100 hours.

The first profile was a 14-km-long tune-up line running east to west along latitude 33°30' S (Figure 5.1.1). The set-up of airguns, streamer etc. can be seen from Figure 5.1.2.

The recording parameters on the acquisition unit were in general:

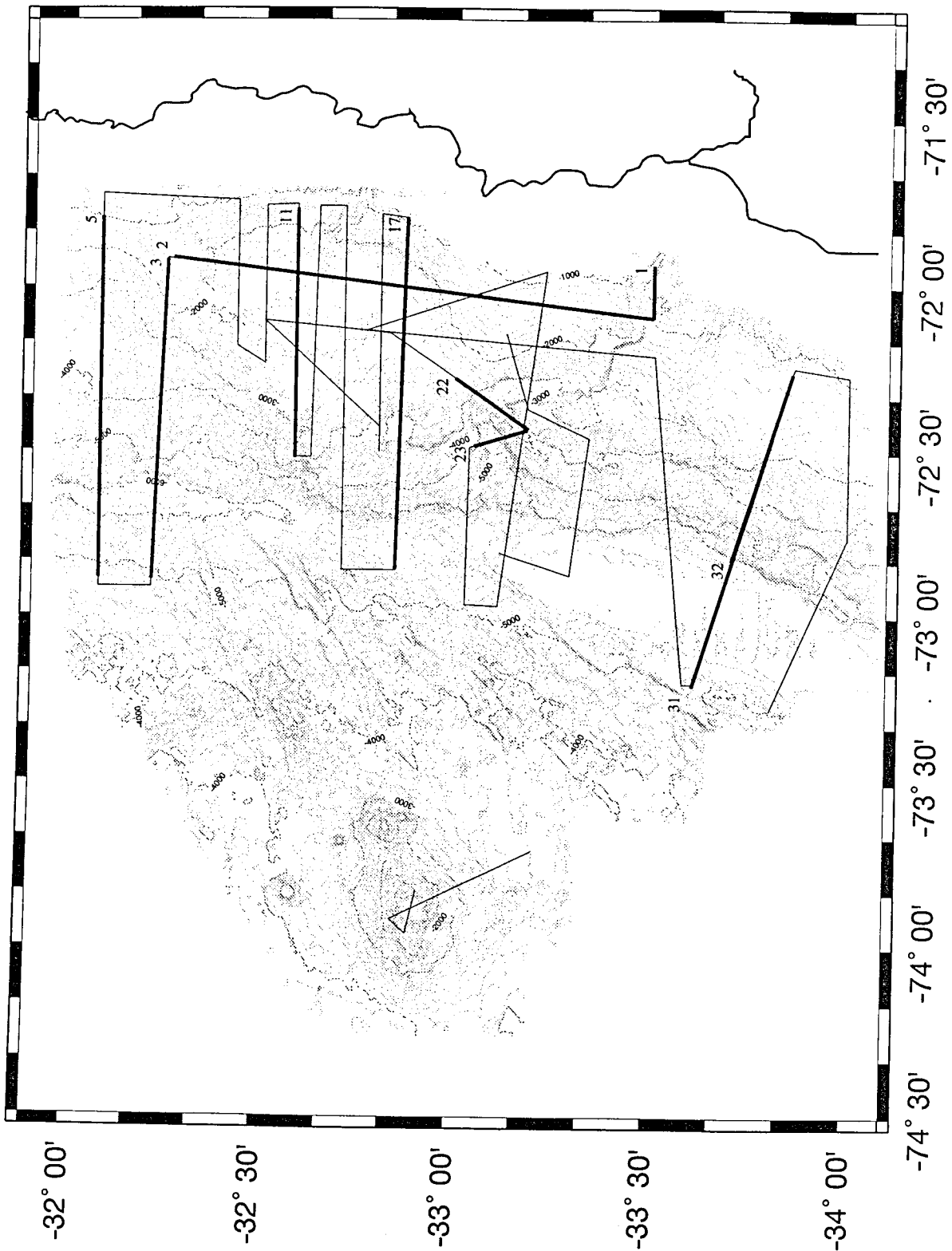


Figure 5.1.1: Location map showing seismic lines

Water depth		DSP	Delay	Rec. length
meter	milliseconds	seconds	milliseconds	milliseconds
<1,500	<2,000	7.5	700	5,000
1,500-3,000	2,000-4,000	10	2,000	5,000
3,000-4,500	4,000-6,000	10	3,500	4,500
>4,500	>6,000	12.5	6,000	4,500

Recording parameters were set according to depths in a HydroSweep profile.

The tune-up line was positioned along the southern slope of San Antonio Canyon and the image was therefore obscured in the neartrace plot. However, all the equipment functioned properly although the streamer was towing too deep at the far end. The streamer was towed from the starboard side of the stern and the air-guns were towed from the center. This close towing position would often bring them together during turns and occasionally they would cross.

During the cruise there were problems keeping the streamer balanced at the proper depth and it was taken onboard several times for weight adjustment. Its position in the water appeared to depend on weather conditions, ship's heading in relation to swell direction, and possibly current. During rough sea two umbilical airhoses broke and had to be repaired. The trigger connection to one gun also had to be repaired twice.

About 2,000 km of seismic reflection profiles were shot along the lines shown in figure 5.1.1. Lines were positioned for good coverage of the Valparaiso Basin, San Antonio Canyon and the lower trench slope. Two lines were also shot across O'Higgins Guyot and the adjacent oceanic crust.

A number of reflection profiles were processed onboard (see section 5.2) allowing more detailed interpretation. The following description is based on both neartrace plots and processed profiles. To avoid duplicating figures, we will refer to some figures in section 5.2.

The Valparaiso Basin is separated into Northern Valparaiso Basin and Southern Valparaiso Basin by an east-west central (basement?) ridge (Figures 5.2.8 and 5.2.9). In addition, both the northern and the southern basin can be separated into outer (western) and inner (eastern) parts (Figures 5.2.24 and 5.2.25) by a roughly north-south trending basement high.

SHIP: <u>SONNE</u> WIND (M/S): _____ SHIP SPEED: <u>4.8 knots</u> DATE: _____ PARTY CHIEF: <u>Von Harne</u> CLIENT: <u>GEOMAR</u> PROSPECT: <u>CO11DOR</u> LINE: <u>120-121-</u>	MARINE SURVEY GENERAL INFORMATION	WIND (M/S): _____ DATE: _____ LINE: <u>120-121-</u>																
SKETCH OF SHOTPOINT - GEOMETRY SHOTPOINT DISTANCE: _____ M. _____ % COVERAGE																		
SEISMIC INSTRUMENTS: TYPE: <u>ES 2420</u> FILTERS: <u>15-180</u> GAIN SETTING: <u>30.1 dB</u> RECORD TIME: _____ SAMPLE RATE: <u>1 ms</u> LINEPROFILER _____ TRACE NO <u>13</u> EVERY <u>1</u> SHOTS	NAVIGATION: <u>Datum WGS-84</u> GPS: <u>Ashtech XII</u> DECCA: _____ LORAN C: _____ DOPPLER SONAR: _____ DIGITAL RECORDING: _____	STREAMER: TYPE OF CABLE: <u>TELEDYNE</u> CABLE LENGTH: <u>143.75</u> M NO OF LIVE SECTIONS: <u>24</u> TOWING CABLE LENGTH: <u>80</u> M SECTION INTERVALS: <u>6.25</u> M HYDROPHONES IN SECTION: <u>7</u>																
SEISMIC ENERGY SOURCE: <table border="1" style="width:100%; border-collapse: collapse;"> <thead> <tr> <th>GUN SER. NO</th> <th>NO</th> <th>CU. IN.</th> </tr> </thead> <tbody> <tr> <td><u>C-3081</u></td> <td><u>1</u></td> <td><u>40</u></td> </tr> <tr> <td><u>C-3070</u></td> <td><u>2</u></td> <td><u>-</u></td> </tr> <tr> <td><u>C-3058</u></td> <td><u>3</u></td> <td><u>-</u></td> </tr> <tr> <td><u>C-3289</u></td> <td><u>4</u></td> <td><u>-</u></td> </tr> </tbody> </table> AIRGUN PRESSURE: <u>100 bar</u> DEPTH AIRGUN: <u>2-3</u> M		GUN SER. NO	NO	CU. IN.	<u>C-3081</u>	<u>1</u>	<u>40</u>	<u>C-3070</u>	<u>2</u>	<u>-</u>	<u>C-3058</u>	<u>3</u>	<u>-</u>	<u>C-3289</u>	<u>4</u>	<u>-</u>	GUN CONFIGURATION 	REMARKS: <u>Gun delay 12 ms</u>
GUN SER. NO	NO	CU. IN.																
<u>C-3081</u>	<u>1</u>	<u>40</u>																
<u>C-3070</u>	<u>2</u>	<u>-</u>																
<u>C-3058</u>	<u>3</u>	<u>-</u>																
<u>C-3289</u>	<u>4</u>	<u>-</u>																
GEOMAR GEOLGISK INSTITUTT AARHUS UNIVERSITET																		

Figure 5.1.2: Configuration of seismic instrument system

Northern Valparaiso Basin has an upper sedimentary unit that can be traced from the inner to the outer basin across the north-south trending basement high (Figures 5.2.24 and 5.2.25). The upper sedimentary unit is about 200 ms thick in the outer basin and 400 ms thick in the inner basin and is separated from the lower sedimentary unit of the basins by a pronounced unconformity. The deeper sedimentary unit of the outer basin occurs in what appears to be half-grabens tilted toward the east. Basement is about 4,000 ms deep in the outer basin. Below the unconformity the deeper sedimentary unit of the inner basin is much thicker than in the outer basin (Figure 5.2.25). Thickness of the deeper sedimentary unit is about 1,500 ms and basement occurs at about 5,500 ms or deeper. Towards the east the basement rises towards the steep slope and on the shallower lower part of the slope the development of a lobe or fan radiating from the steep slope can be seen in the upper sedimentary unit (Figure 5.2.26)

In Southern Valparaiso Basin the outer part of the basin is wider than in the north (Figure 5.1.3). The deeper sedimentary unit appears to be deposited in a number of east tilted half-grabens. The graben furthest to the west is more than 1,000 ms deep. Generally the basement is located at about 3,800 ms. The upper sedimentary unit is continuous from outer to inner Southern Valparaiso Basin and has a thickness of about 200 ms. The deeper sedimentary unit of the inner basin is saucer shaped and basement is deep (ca.4,300 ms). The three dimensional geometry of this basin has not yet been established but it holds the key to tectonic history and origin.

In the southernmost part of Southern Valparaiso Basin separation of outer and inner basin becomes less clear and the unconformity between upper and lower sediments is less pronounced (Figures 5.1.4, 5.2.29 and 5.2.30).

The Punta Salinas Embayment contains a small basin in the northernmost part of the area but further down the slope than the Valparaiso Basin. However, like the Valparaiso Basin, it has a fairly flat-lying upper unit separated from a lower unit by an unconformity. Sediments in the lower unit occur in what appears to be half-grabens (Figure 5.2.20)

The Topocalma Knoll is bounded to the north by the Valparaiso Basin and to the west and south by the San Antonio Canyon. From the Valparaiso Basin and southwards toward the Knoll the basement rises from about 6,000 ms to about 2,500 ms. The basement surface appears highly irregular. On the easternmost profile (Figures 5.2.7, 5.2.6 and 5.2.5)) the deeper sedimentary unit of the inner Southern Valparaiso Basin appears to continue up over the top of the Topocalma Knoll where it reaches the surface, is eroded, and thins out

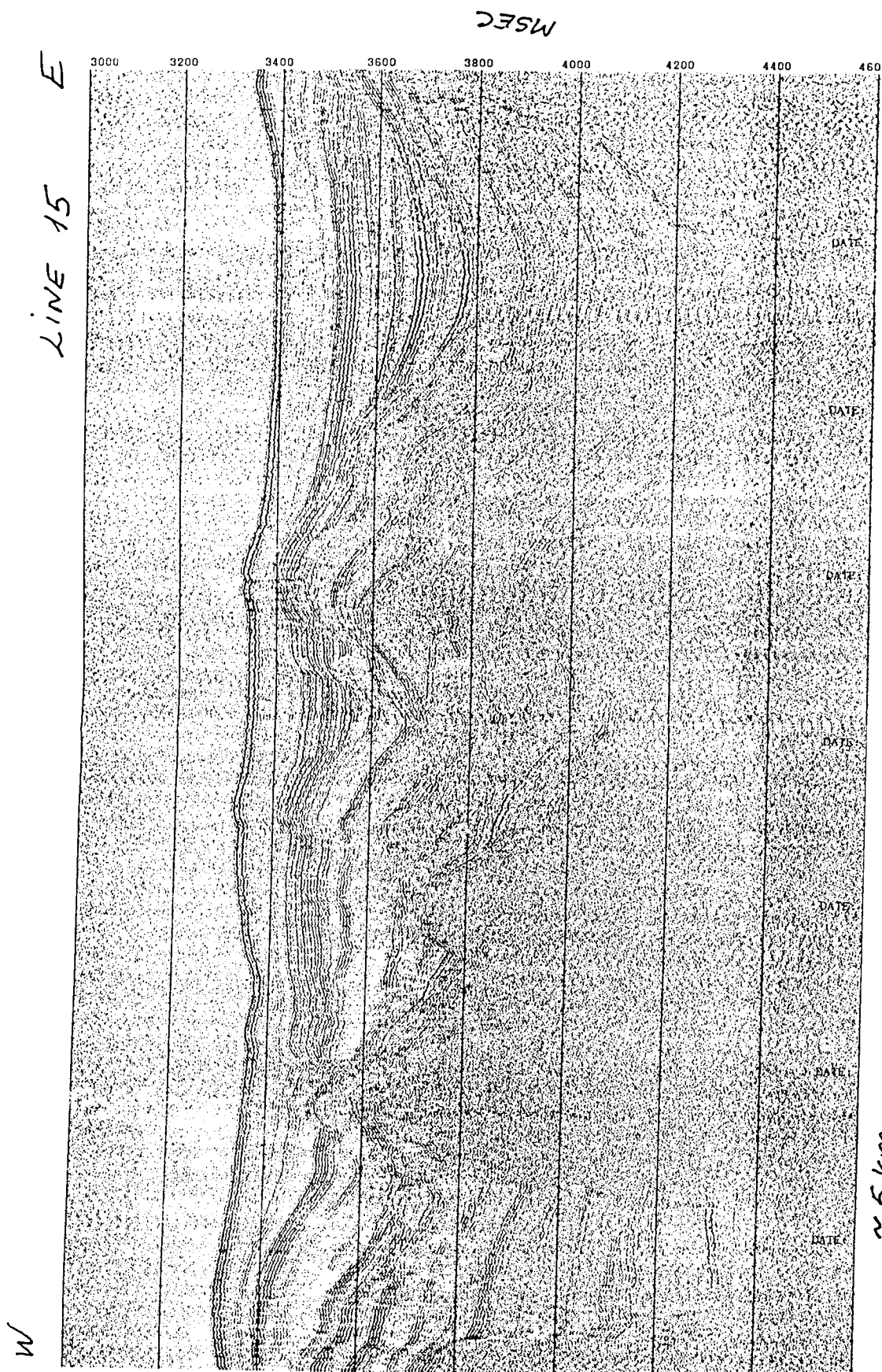


Figure 5.1.3: Monitor record line 15

~ 5 km

from about 1,500 ms in the basin to about 600 ms over the knoll. Further to the south, towards San Antonio Canyon (Figures 5.2.5 and 5.2.4), the basement drops somewhat and the sediments traced from the deep Valparaiso Basin thin more. However, on top of these sediments younger sediments occur in the area between the top of the Topocalma Knoll and the San Antonio Canyon. These younger sediments are very thin near the top of the Knoll and thicken to about 500 ms near San Antonio Canyon. The two sediment packages are separated by a pronounced unconformity.

Westward from the top of the knoll the younger sediments can be followed down the slope. They appear to thicken downslope (Figure 5.1.5) where they are eroded and cut-off by the San Antonio Canyon. The older sedimentary unit cannot be traced on the neartrace plot. The younger sediments appear to onlap the older sediments upslope.

The survey includes 9 lines that cross the trench axis. At least one line from each of the three structural regions was stacked (lines 3, 5, 17, and 31-32). In the north the lines cross onto the oceanic crust where they image normal faults as the oceanic plate is flexed into the trench axis. The lower continental slope in all records is obscured by diffraction's and little structural information can be seen in the highly exaggerated monitor records. The stacked sections are also highly obscured but locally the seismic images show the less deformed sediment.

On the oceanic crust the stack of line 3 (Figures 5.2.15, 5.2.16) shows a uniformly thick pelagic layer resting on basement. Normal faults dipping both landward and seaward form horst and graben and this structure can be followed beneath the trench axis fill. A third dimension is given by the topography (chapter 3, Figure 3.2). Small ponds of presumed hemipelagic turbidites fill some of the graben. The pelagic sediment and extensional structure is more obscure in line 5 (Figure 5.2.28).

The trench axis is narrow and deep in the northern part of the area becoming very narrow and shallow opposite the Juan Fernandez Ridge. This is in contrast to the wide trench axis south of the ridge (Figure 5.1.1)

The northern trench axis ranges from 5 to 8 km wide and its sediment fill is between 600 and 1,000 ms thick. On the two northernmost profiles (Figures 5.2.15 and 5.2.18) a small proto-thrust dipping to the east can be seen. The oceanic crust can be followed beneath the trench sediments and the continental crust.

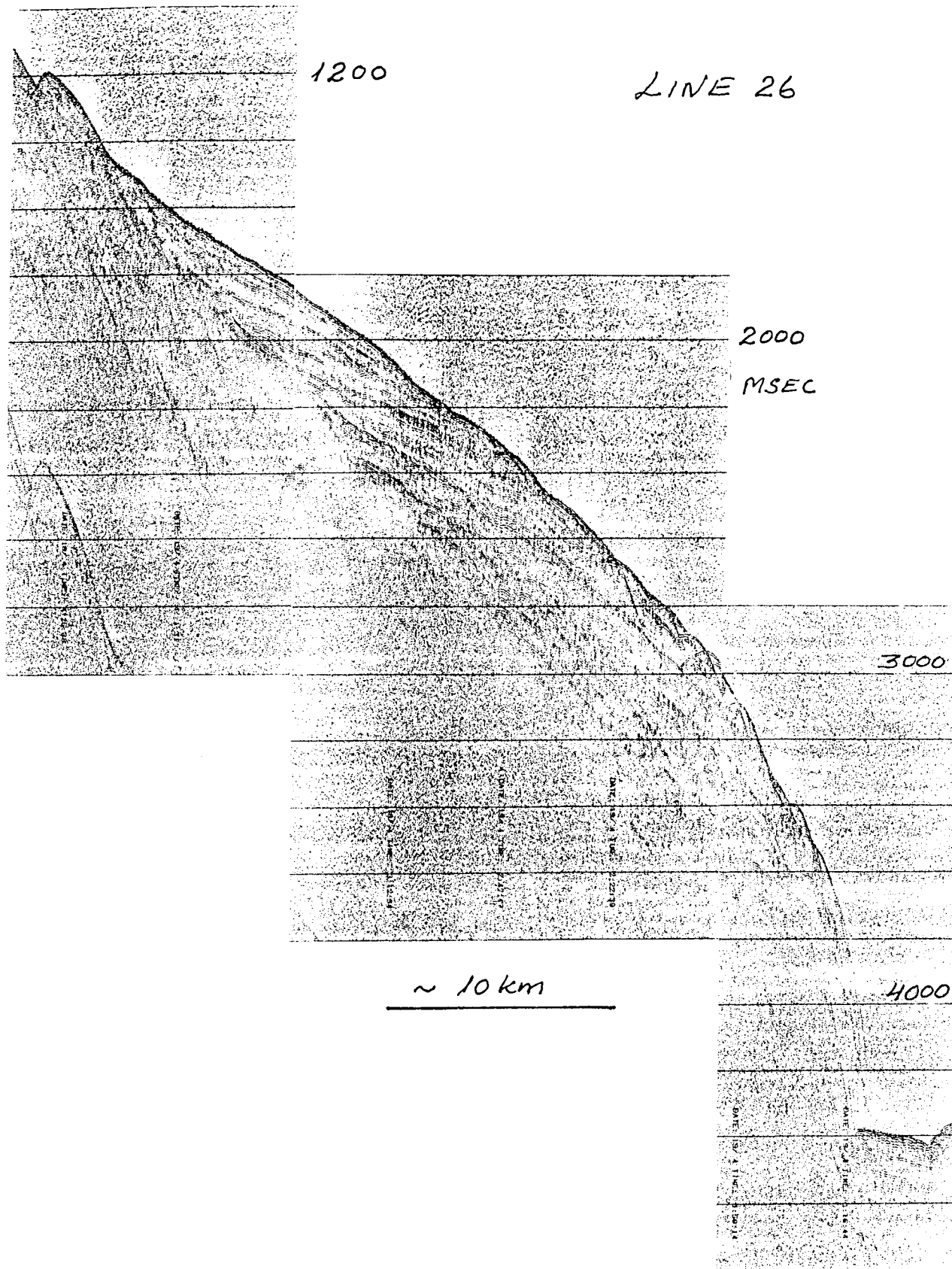


Figure 5.1.5: Monitor record line 26

Opposite the Juan Fernandez Ridge the trench axis narrows and is less than 5 km wide where crossed by the seismic line. The sediment thickness is less than 500 ms and no signs of thrusting are detected (Figure 5.2.27).

In the south the trench widens to more than 25 km where crossed by the seismic line (Figures 5.2.34, 5.2.35 and 5.2.36). Imaged sediment appear to be more than 2,000 ms thick. On the eastern continental side of the trench a thrust-fold is clearly imaged (Figure 5.2.36). On the western oceanic side is a narrow channel eroded about 200-300 ms (150m) deep (Figure 5.2.34).

On the continental slope the deformed lower and less deformed upper slope seen in the trench landward slope morphology is also seen in the stacked seismic images. The upper slope is covered by well stratified sediment up to a second deep in the southern sections (line 31-32, Figures 5.2.37 to 5.2.40) whereas in the northern sections the sediment cover has less stratal continuity and clarity of image (Figures 5.2.11, 5.2.12). In the north much more fracturing breaks the section (Figures 5.2.20, 5.2.21) as also seen in perspective diagrams of the swath morphology whereas in the south greater continuity of the slope cover sediment is observed. The central area opposite the Juan Fernandez Ridge has two basins with back-rotated sections indicating normal faulting (Figure 5.2.29).

The lower slope is different from north to south but not much can be constrained from the data in their present form. They mimic the morphology and are obscured by diffraction's. The slope is sediment covered but few basement reflections are clearly imaged. In the north, slope sediment is about 0.5 sec thick whereas in the south it appears thicker. Local flat areas show ponded or dipping slope sediment. The lowest ridges in the south appear composed mainly of deformed stratified material. In the north the seismic data also indicate deformed stratified material in the first fold but locally acoustic basement is observed further landward.

5.2. Seismic Processing

(D. Kläschen and C. R. Ranero)

Processing hardware and software. The hardware facilities onboard the SONNE included 2 GEOMAR SUN[®] workstations (Sparc 10/40 and IPC) with a total disk capacity of 7-8 Gygabytes and one tape drive. GEOSYS (PRAKLA-SEISMOS) was used as seismic processing software.

Data analysis and processing. The onboard processing of the reflection data was a trade off between rapid results and good imaging. A first objective was to quickly obtain record sections showing the internal structure of the margin for quality control and to help the planning of the ongoing seismic acquisition. Another goal was to obtain images from the deepest structures recorded in the data. The basic processing flow is shown in Figure 5.2.1.

The first step in processing was to copy the raw data to disk. The relative shot location geometry was calculated from the shots time information and an assumed constant ship speed. Time delays applied during recording were also included. The geometry, time delays (obtained from the observer logs), and data quality were checked with near trace plots.

Due to the large amount of data collected, fast processing required resampling from 1 to 2 ms before stacking. Also the common-mid -point (CMP) bin was increased from 3.125 to 6.25 m during stacking. The fold depends on the shot point distance and changes from 4 to 6 and to 8 for shot point distances of 12.5 s (31.25 m), 10 s (25 m) and 7.5 s (18.75 m) respectively.

Improvement of the deepest recorded structures was attempted by means of a gentle 3 trace mixing in the shot gather domain. The operators were 0.2, 0.6, 0.2 in order to preserve the original amplitudes. This dip filter should improve the signal to noise ratio and the continuity of deep reflections. Improvement of the deep image has probably also been obtained by enlarging the CMP bin.

In addition to these processing steps, the processing flow included a notch filter to reject a strong 50 Hz noise observed in the data

Velocity models were constructed following the geological structure observed in the single channel sections. The velocity model were basically 3 layers, water, sediments (up to 2 layers if they are thick), and basement.

Volume of data processed onboard. The 10 seismic lines processed onboard totaled 668 km (Figure 5.2.2) and is unimpressive when compared to most multichannel data. However, at a 6.25 m bin size this amounts to 108800 CMPs and a total raw data volume of about 36 Gigabytes. The seismic data is shown in Figures 5.2.3 to 5.2.40 in many small parts because longer record sections could not be included in the cruise report.

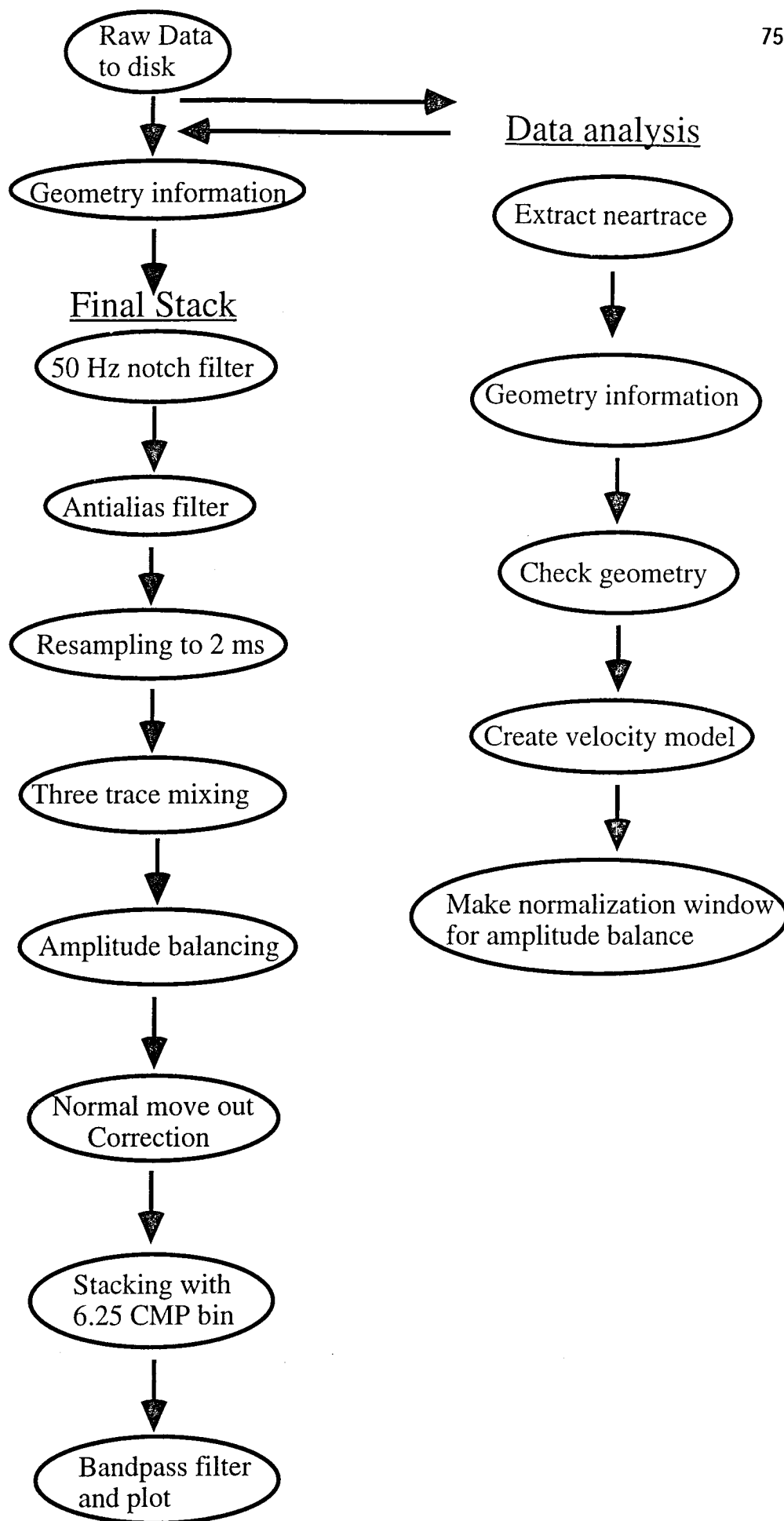


Figure 5.2.1. Seismic processing flow

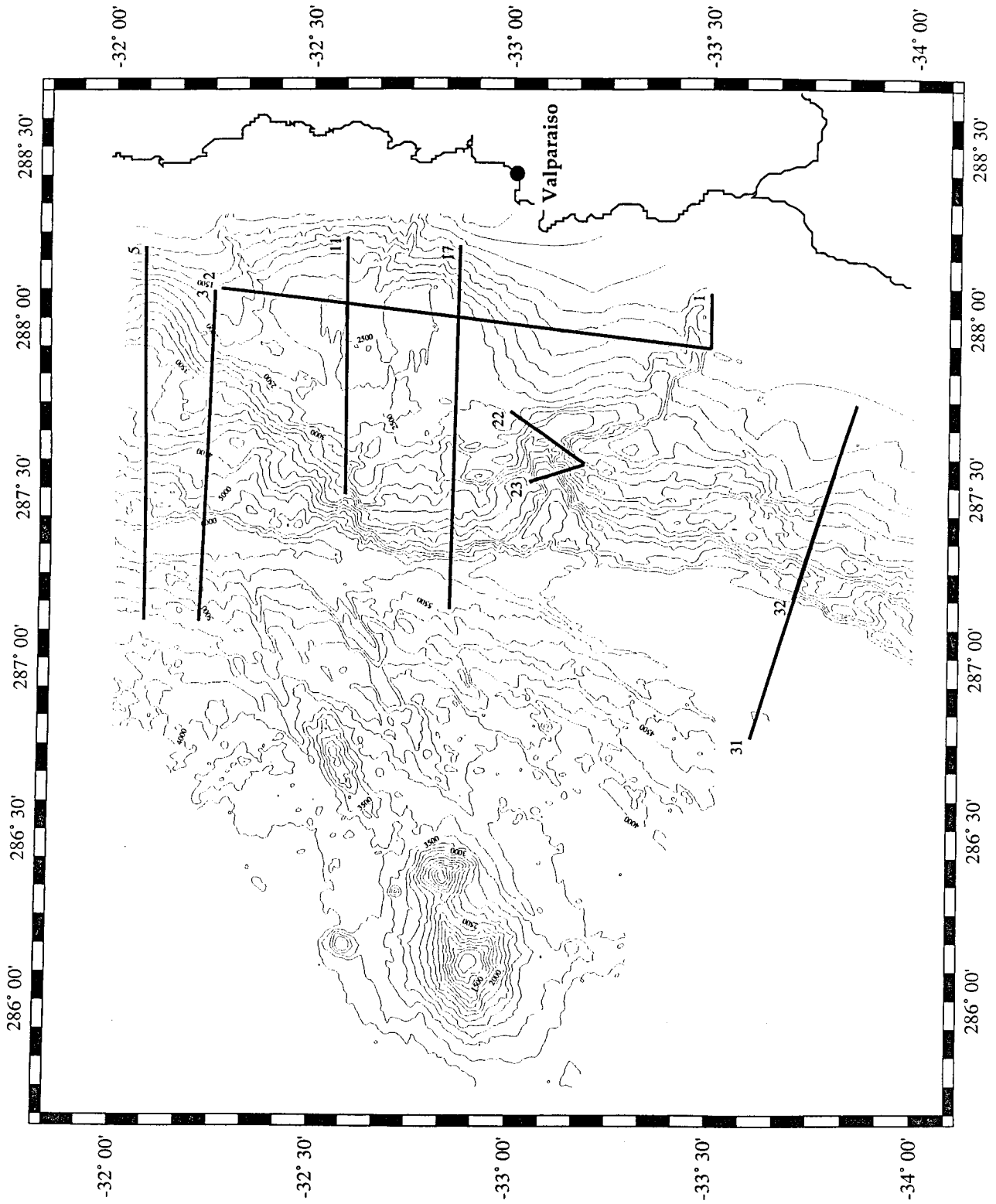
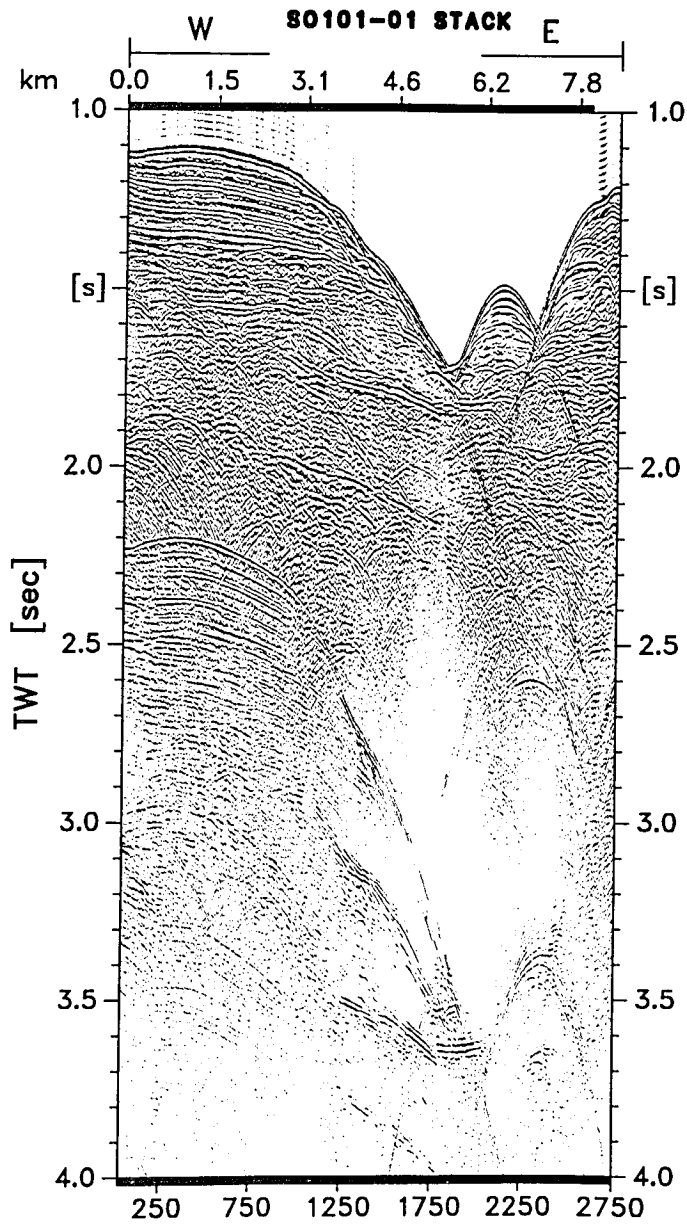


Figure 5.2.2. Seismic tracks of onboard processed data on bathymetry.

Figure 5.2.3



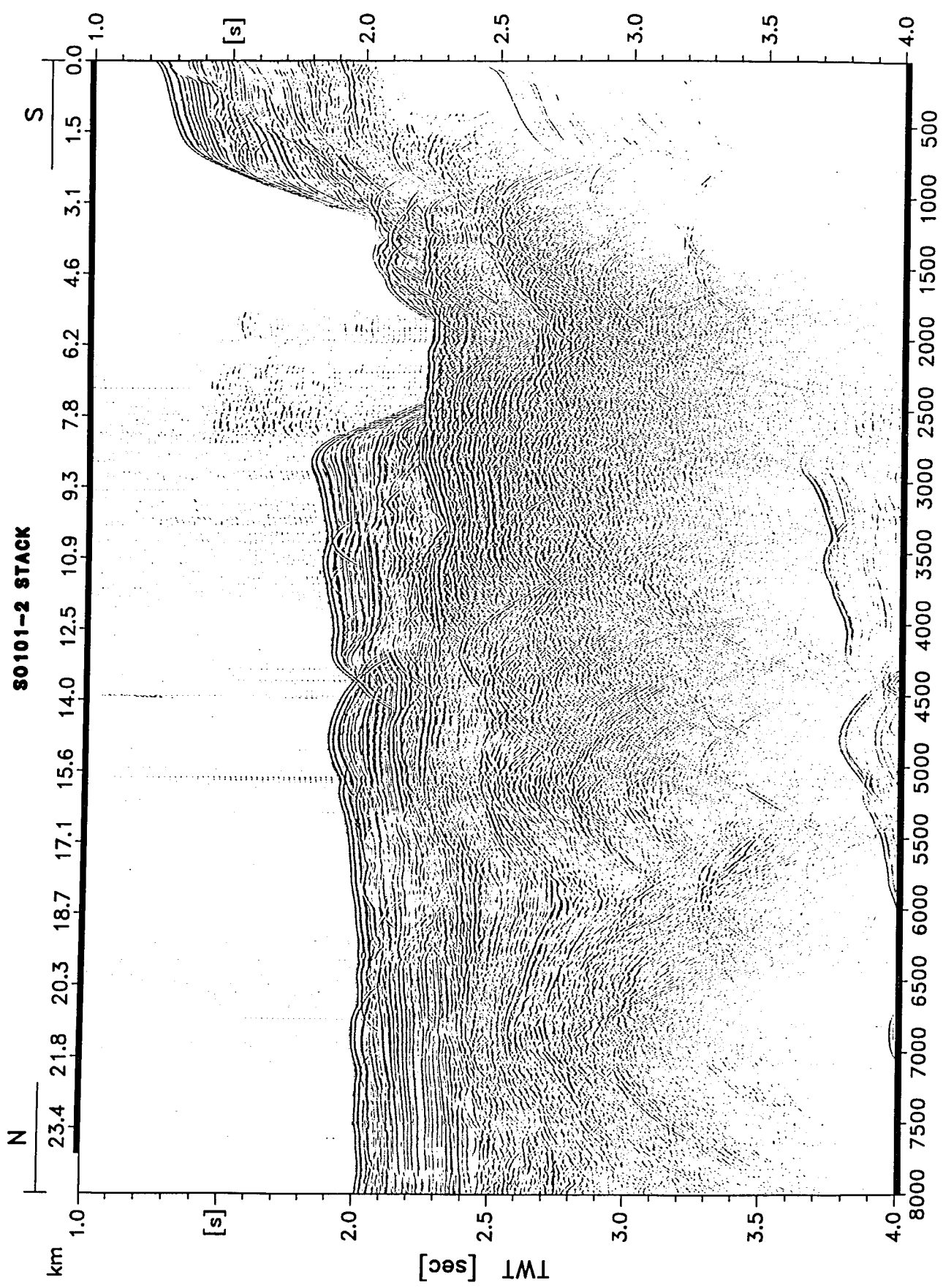


Figure 5.2.4: San Antonio Canyon

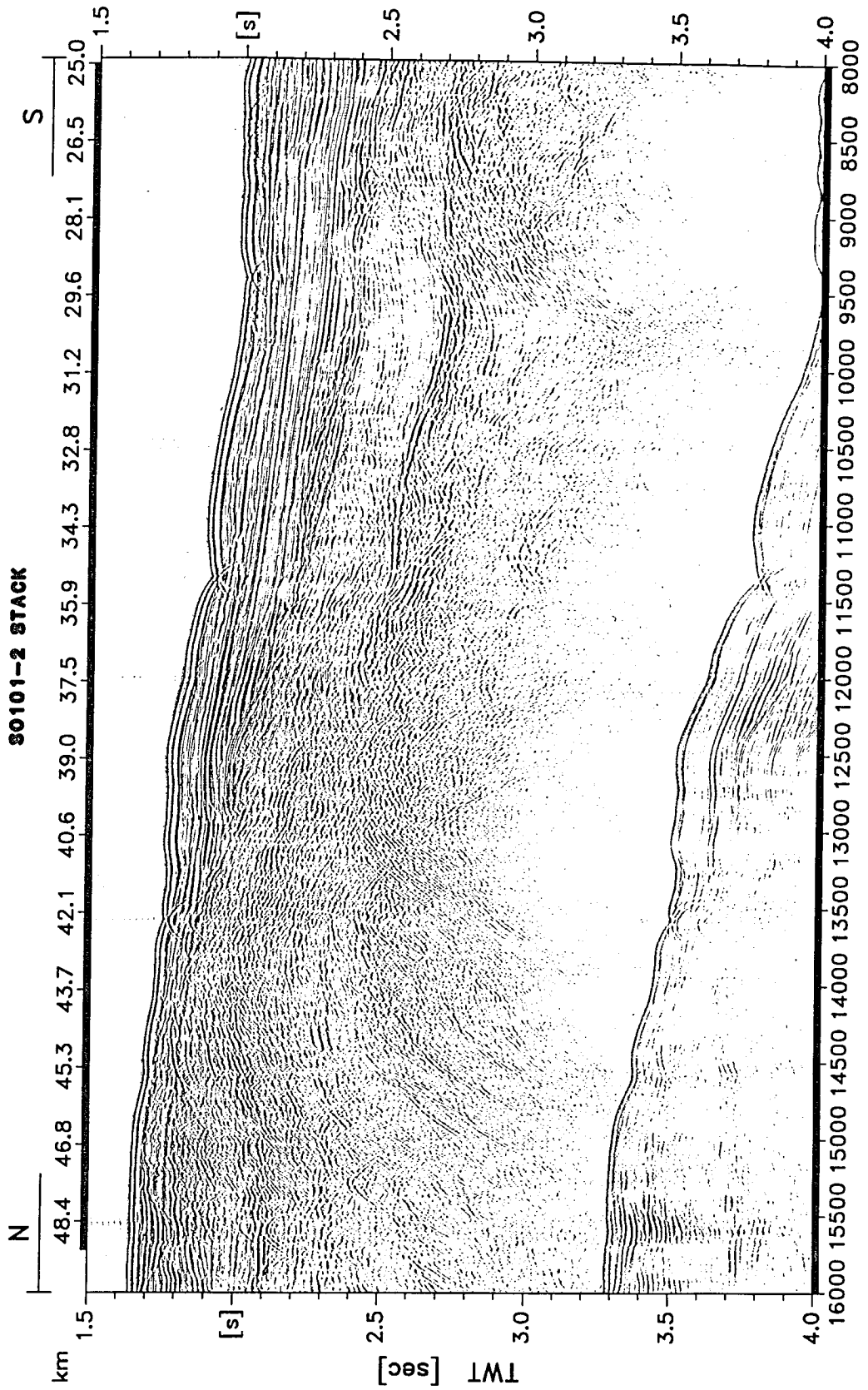


Figure 5.2.5: Topocalma Knoll

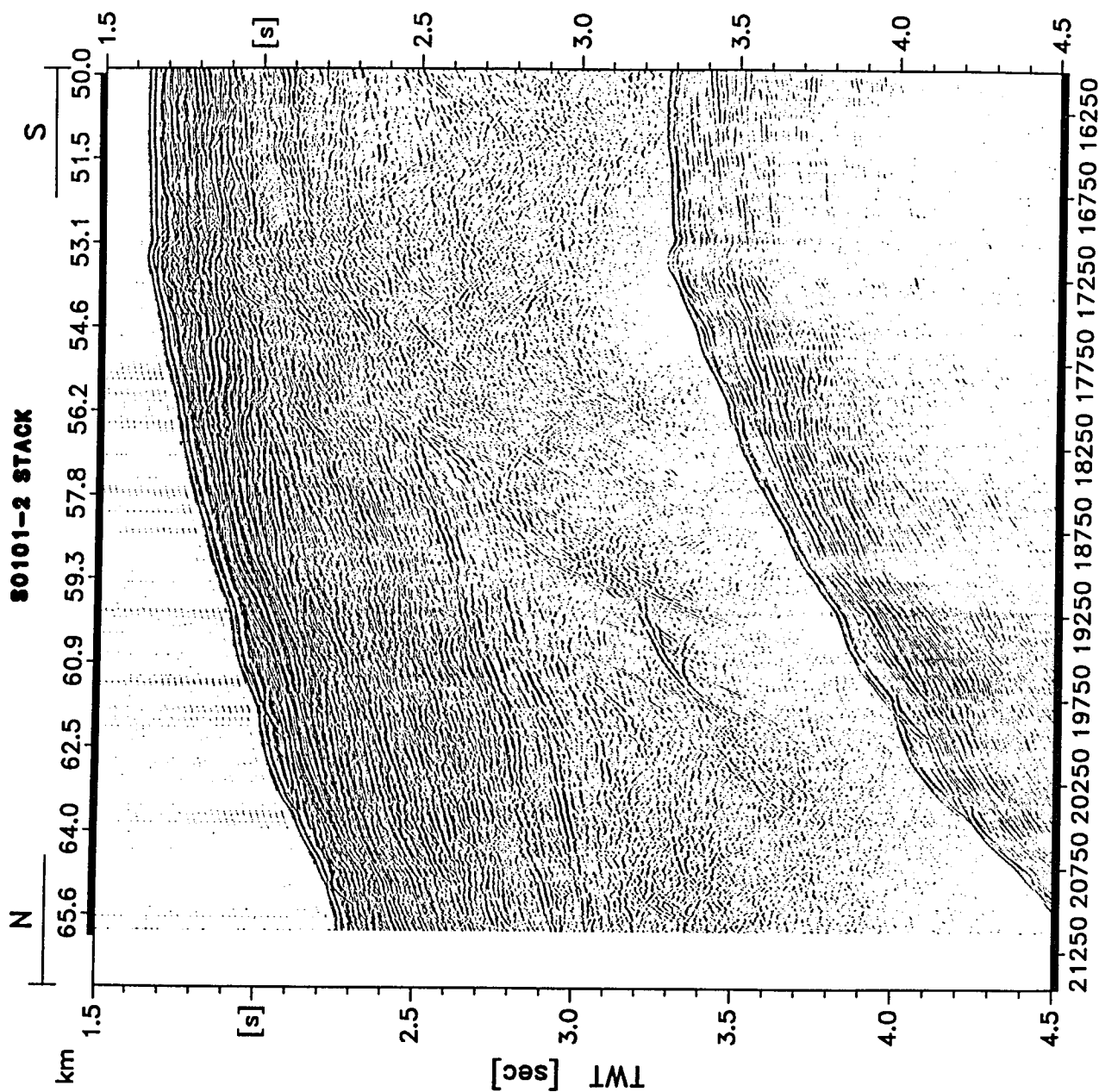
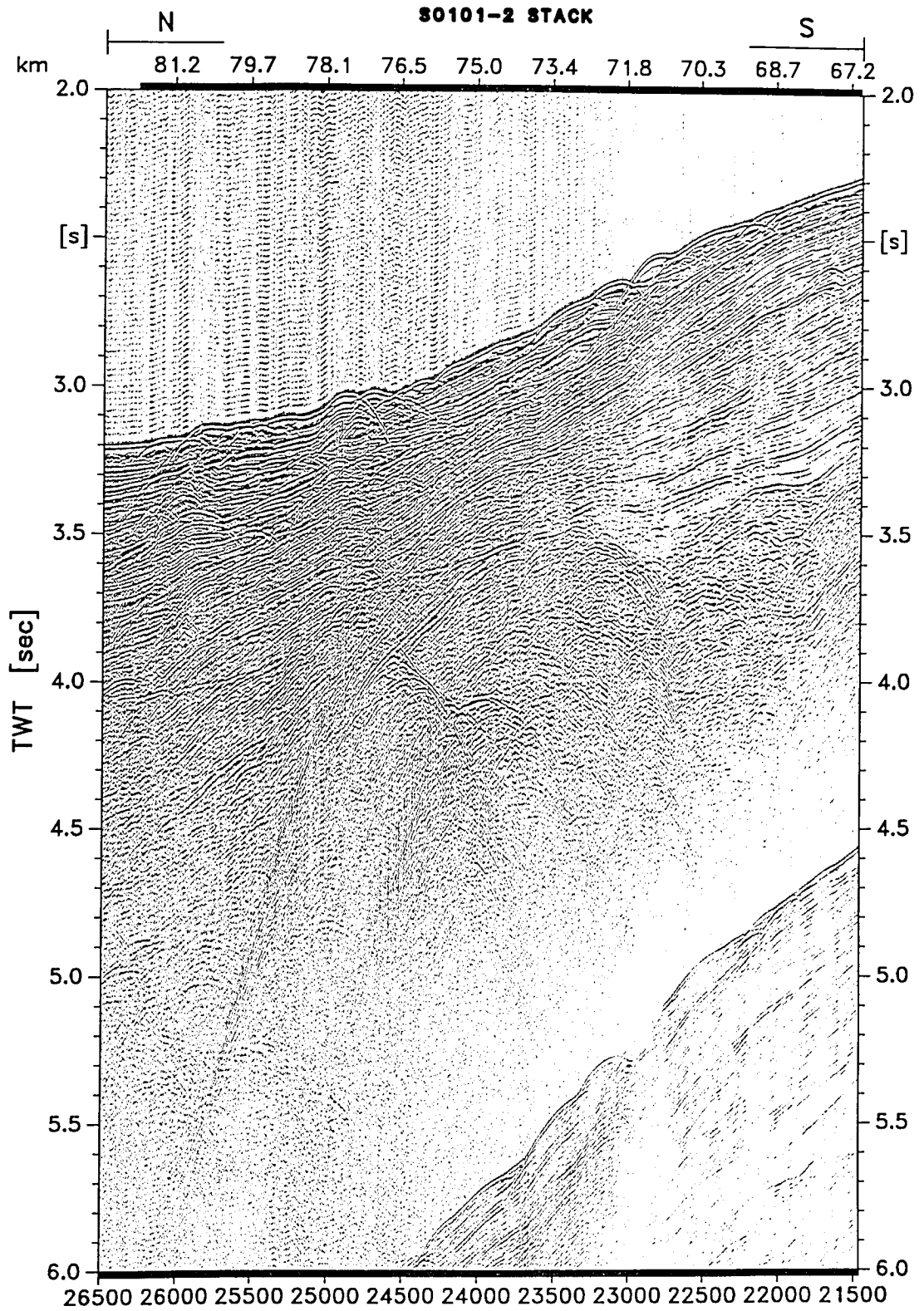


Figure 5.2.6: Topocalma Knoll

Figure 5.2.7



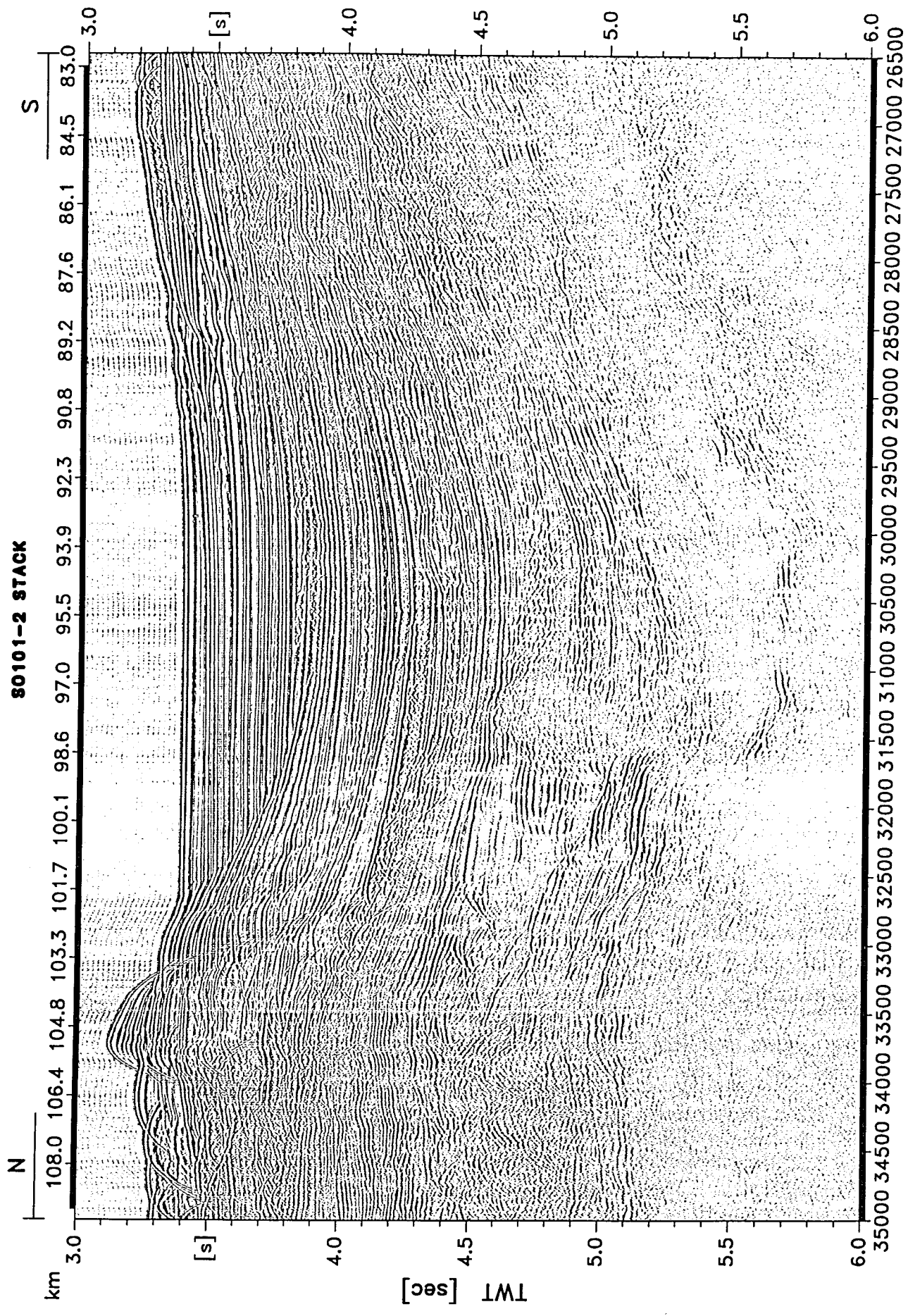


Figure 5.2.8: Southern Valparaíso Basin

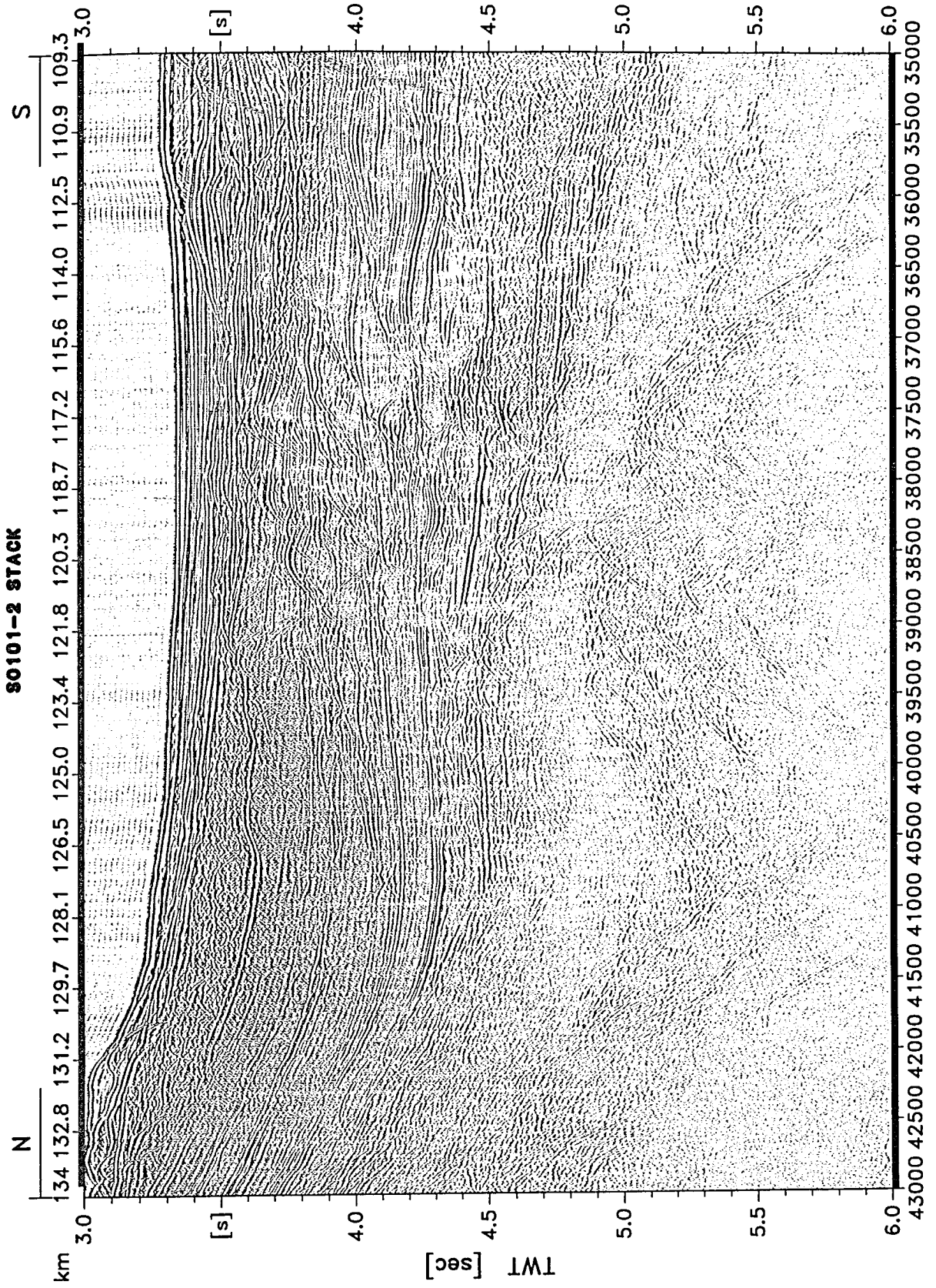


Figure 5.2.9: Northern Valparaiso Basin

Figure 5.2.10

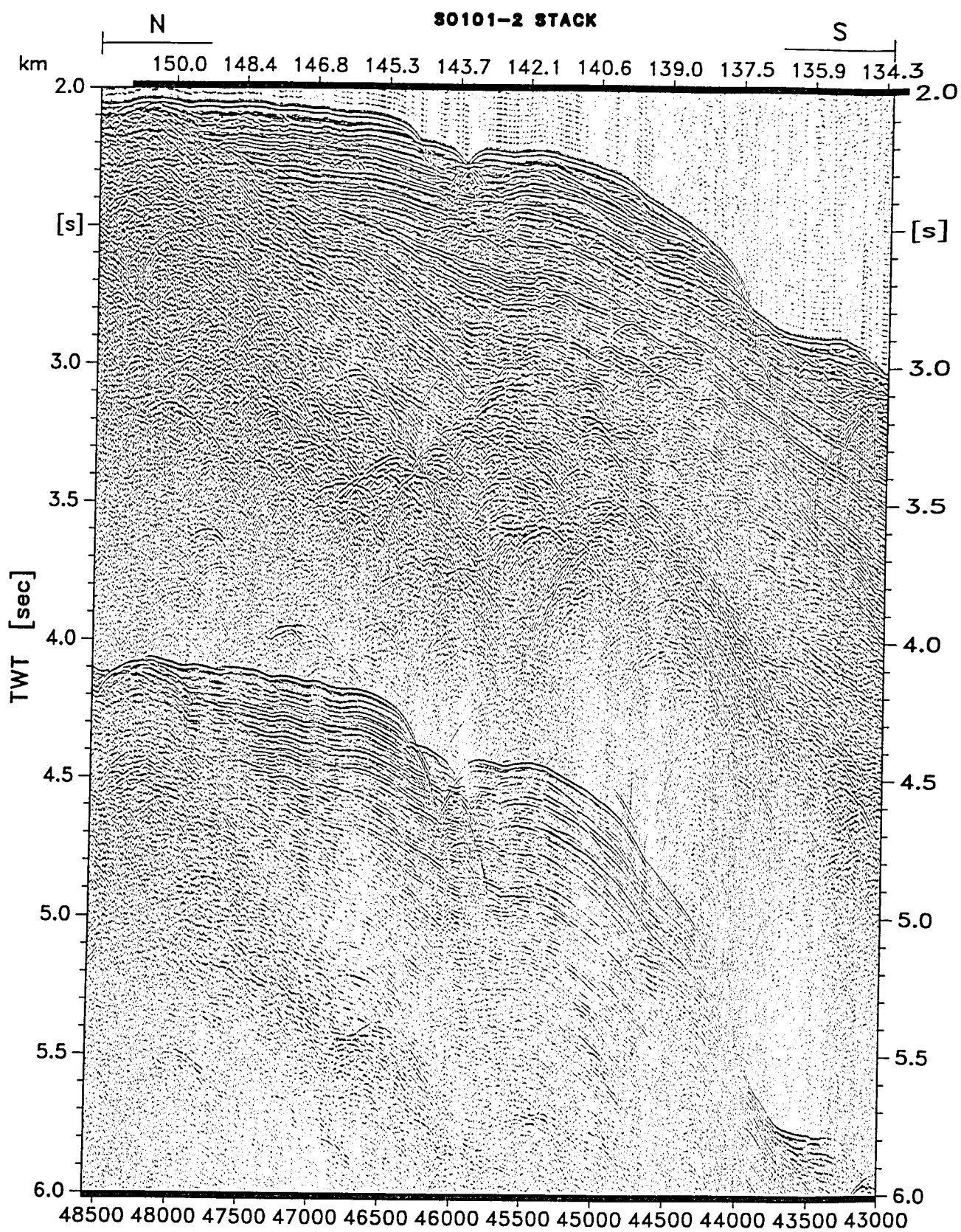


Figure 5.2.11

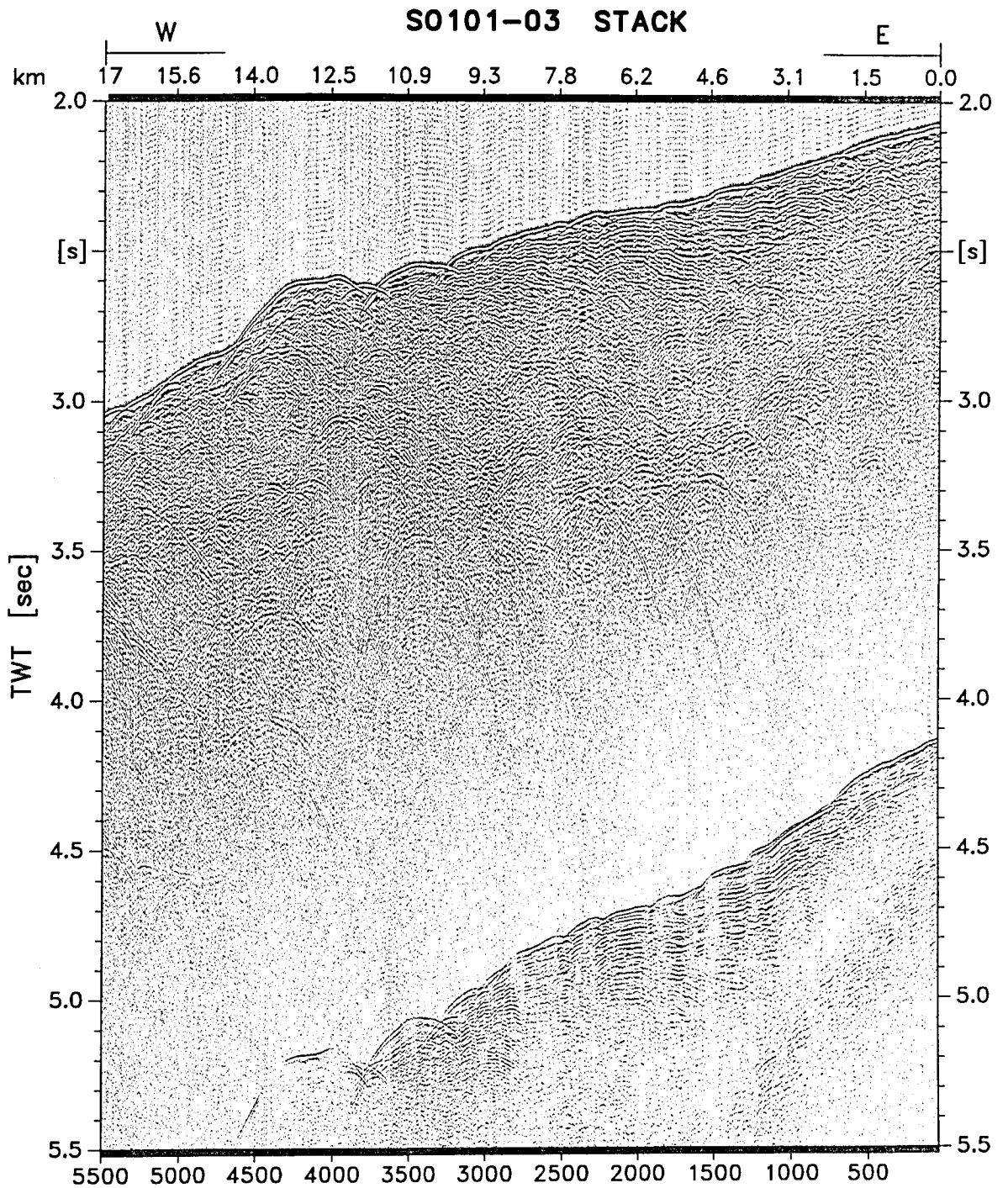


Figure 5.2.12

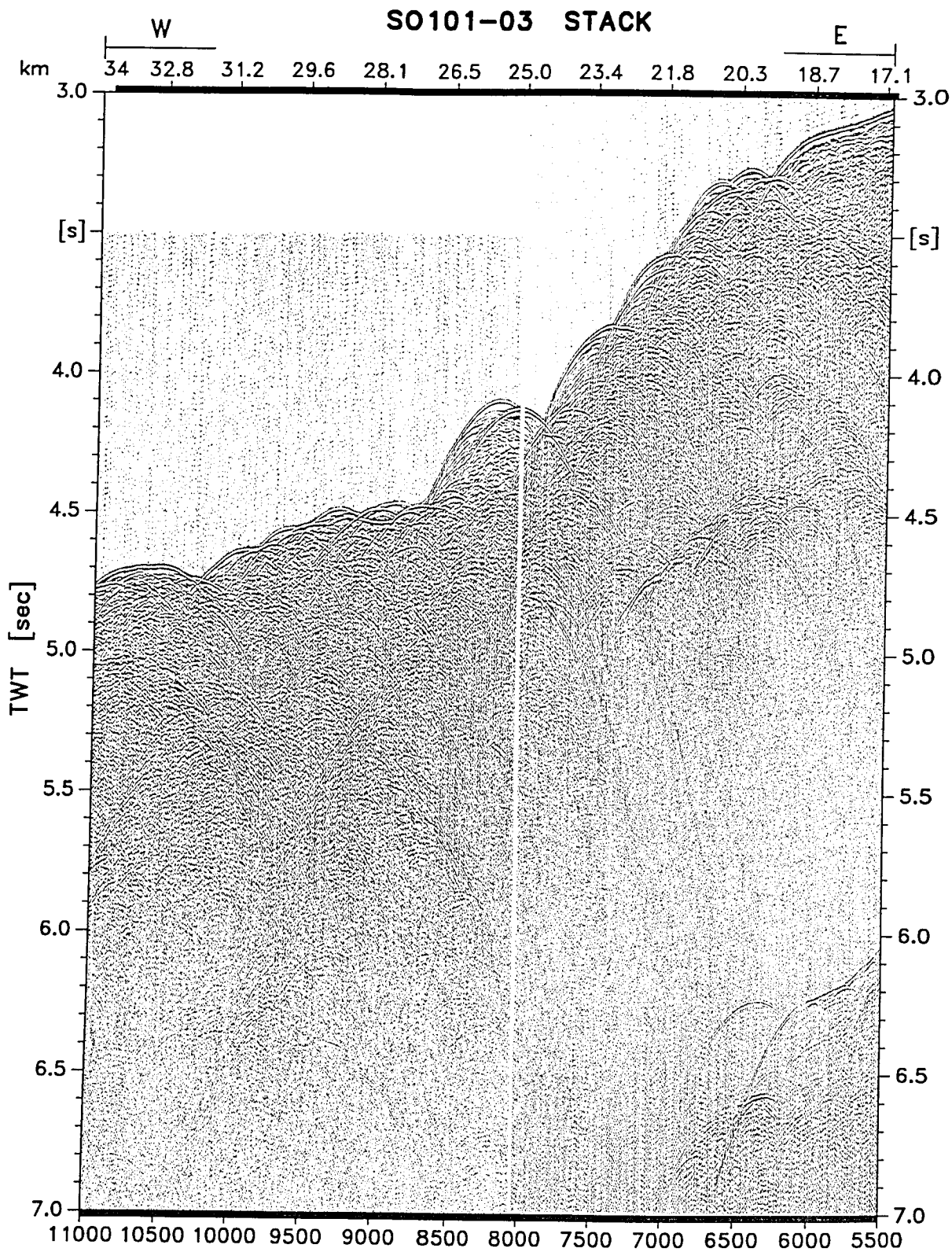


Figure 5.2.13

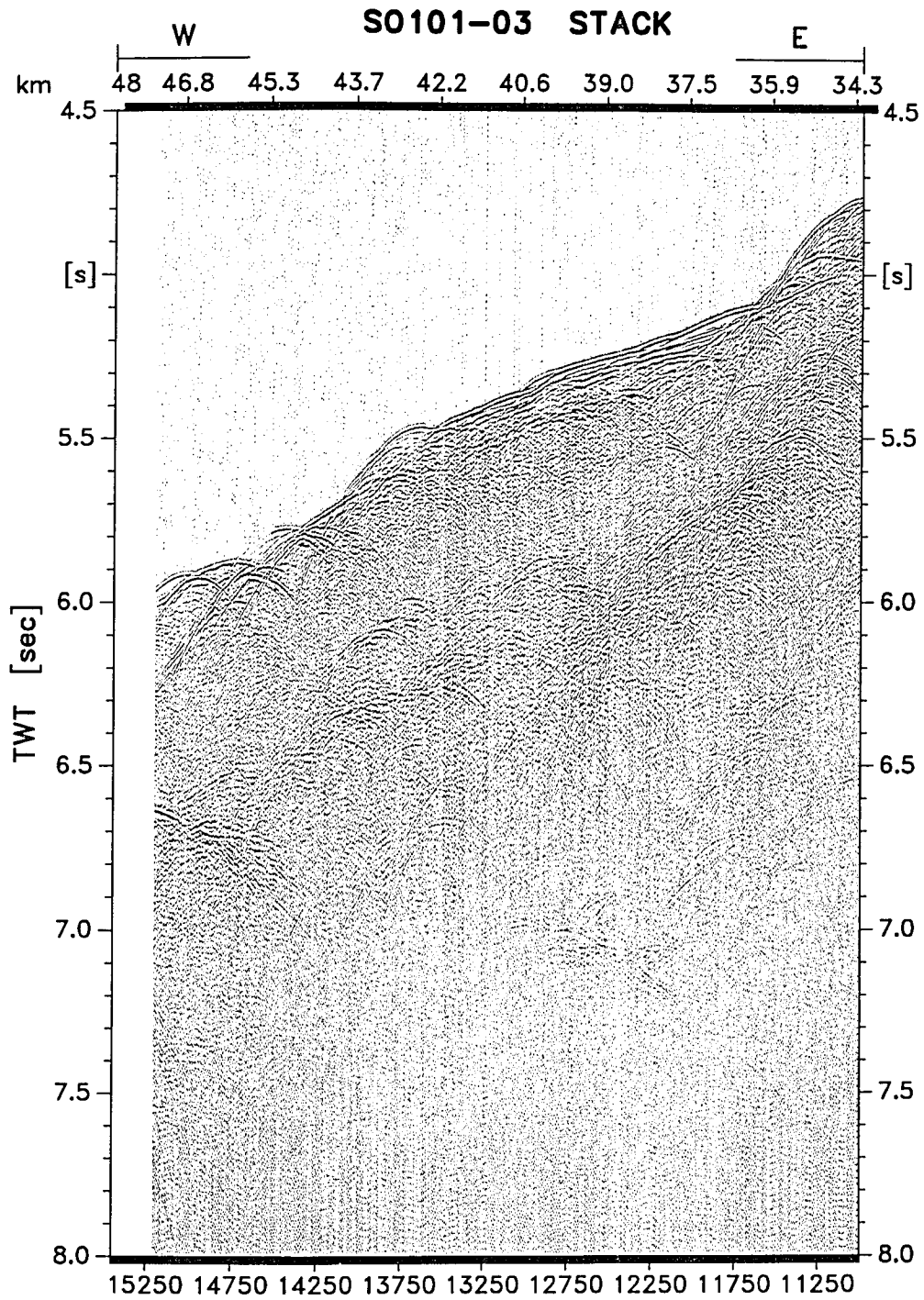
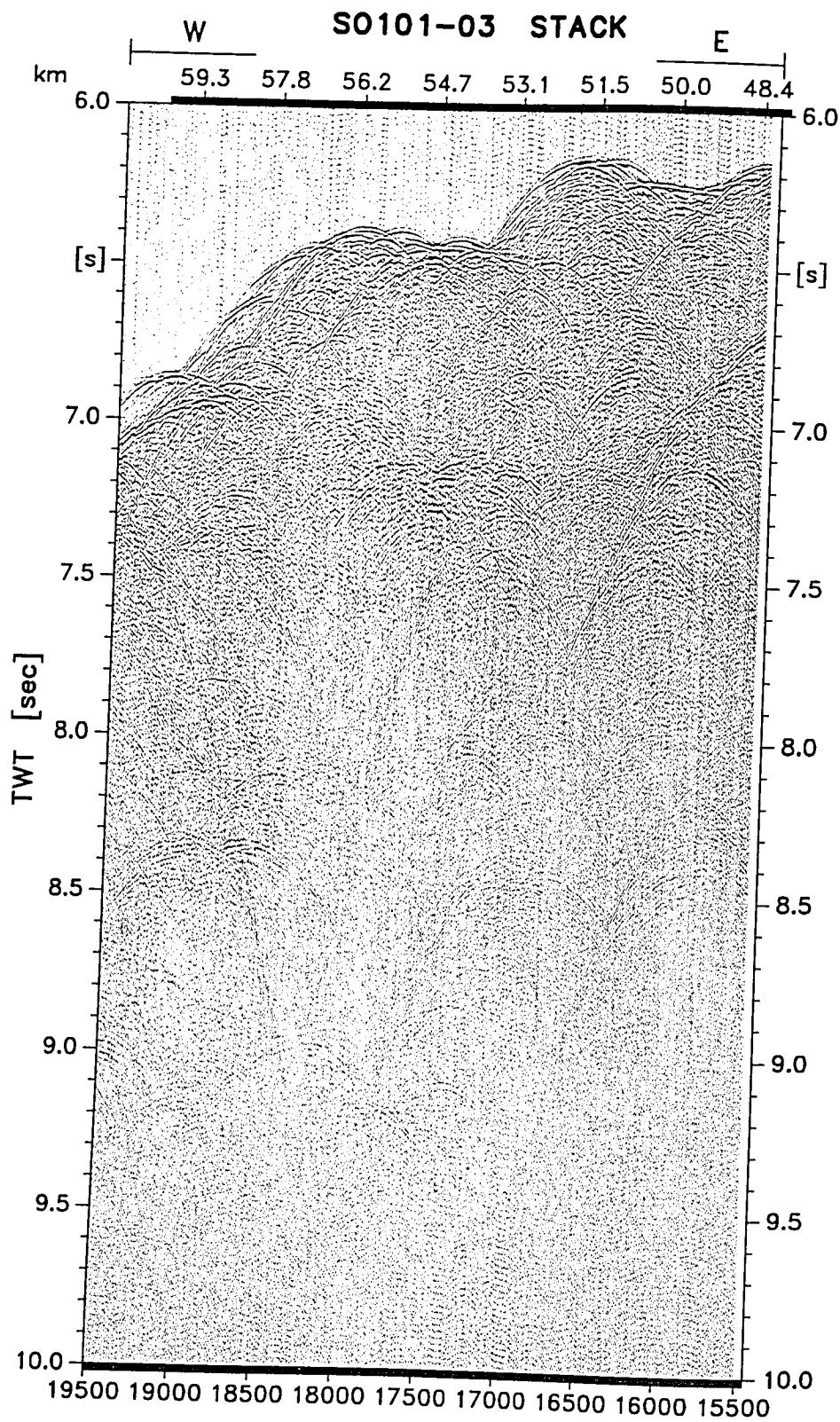


Figure 5.2.14



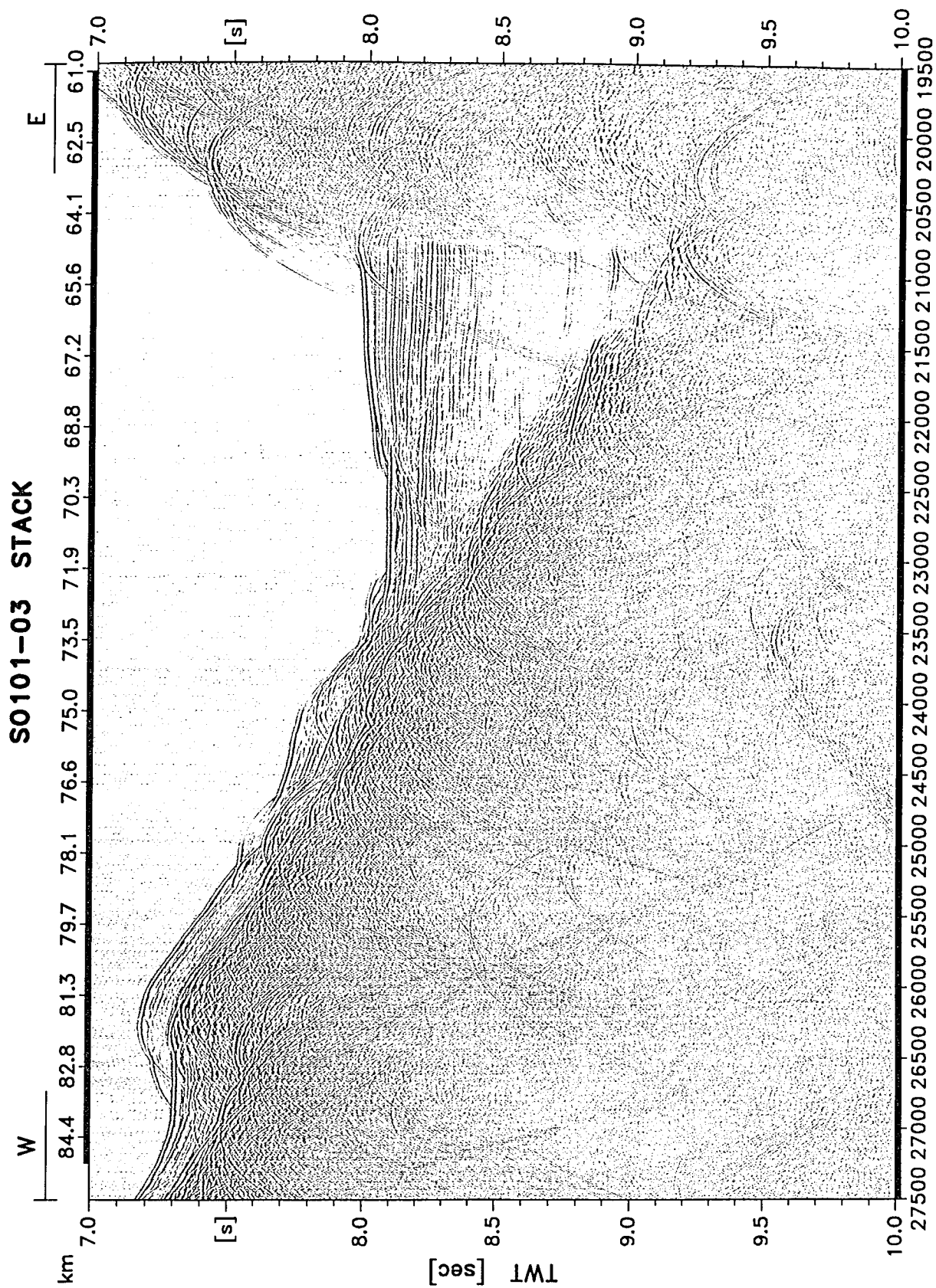


Figure 5.2.15: Northern Trench

Figure 5.2.16

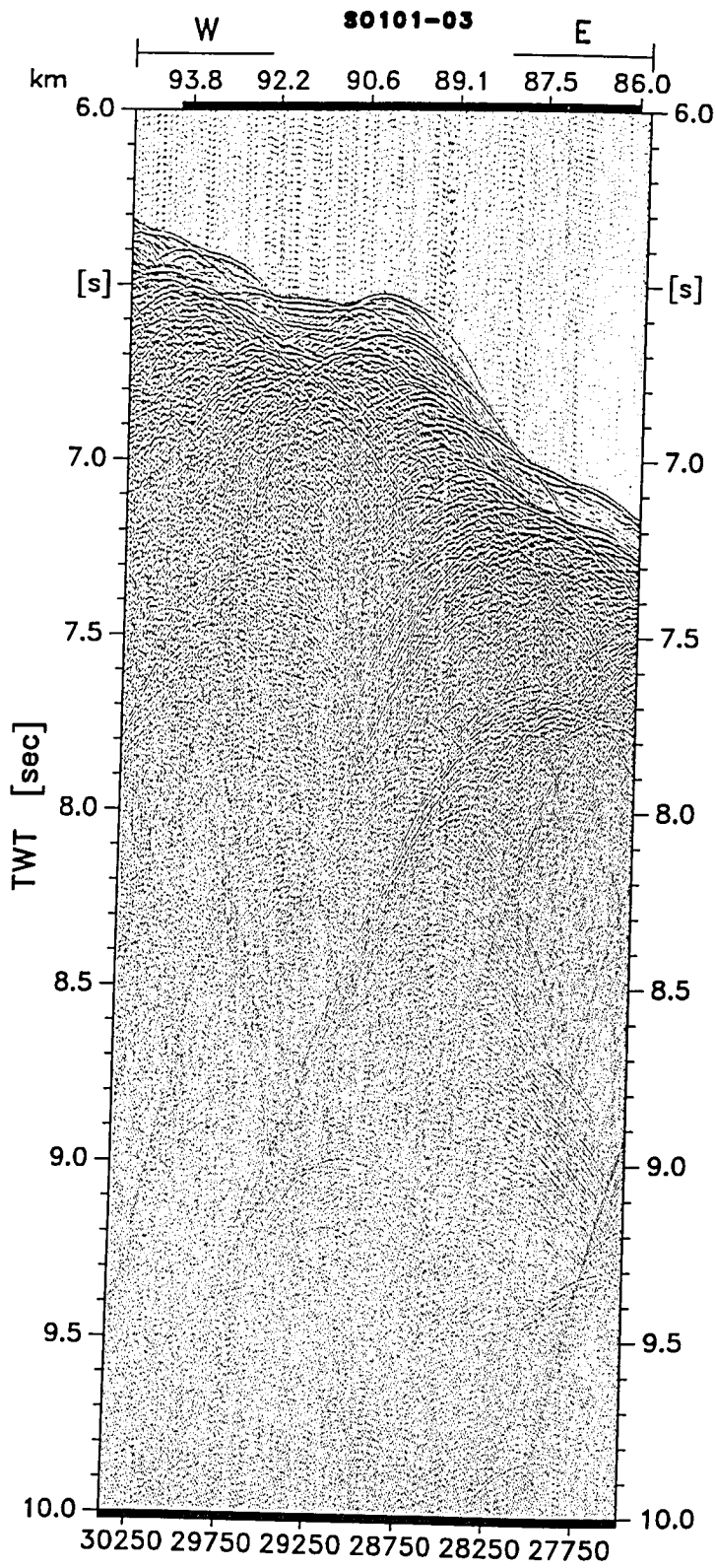
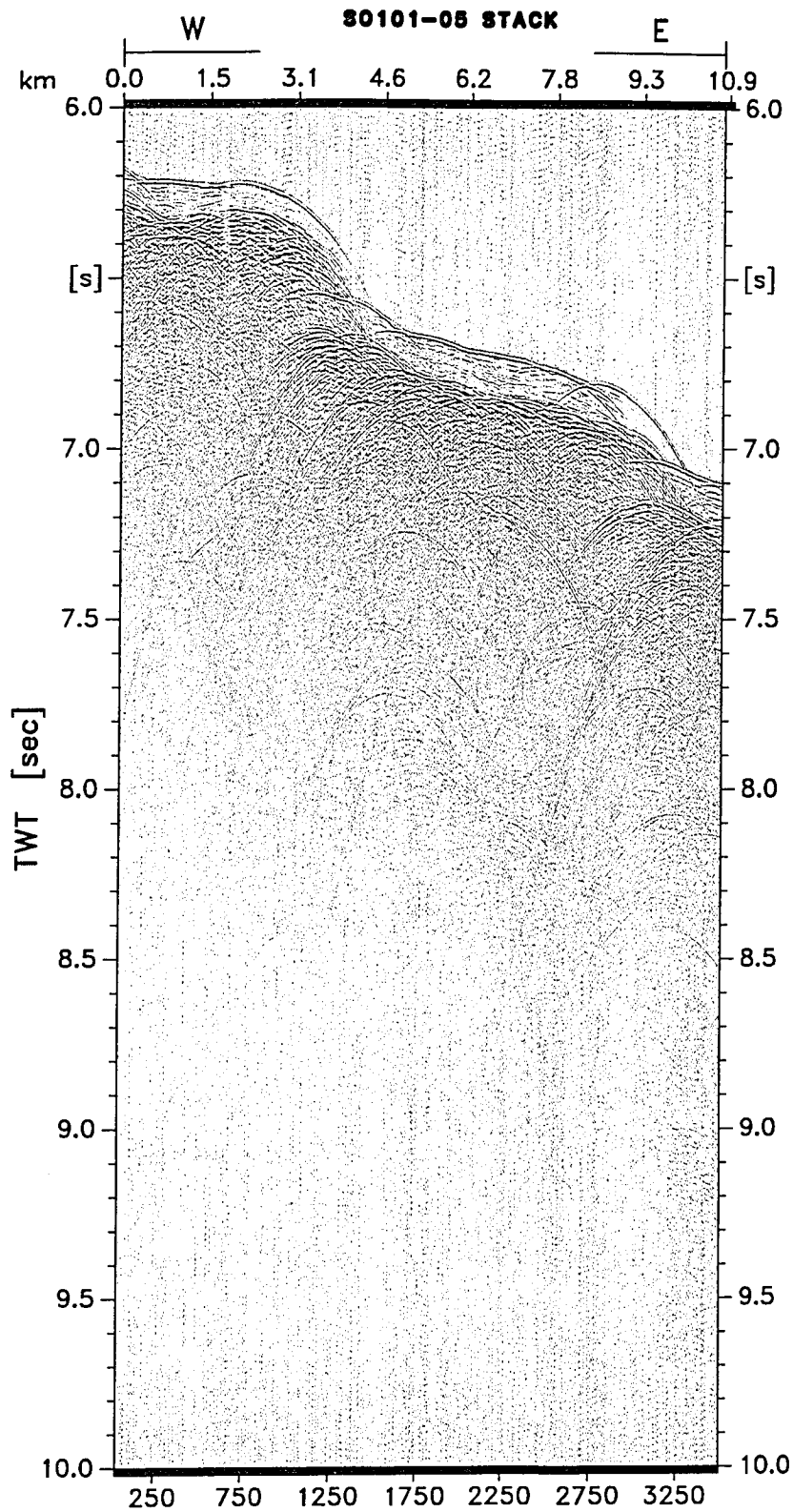


Figure 5.2.17



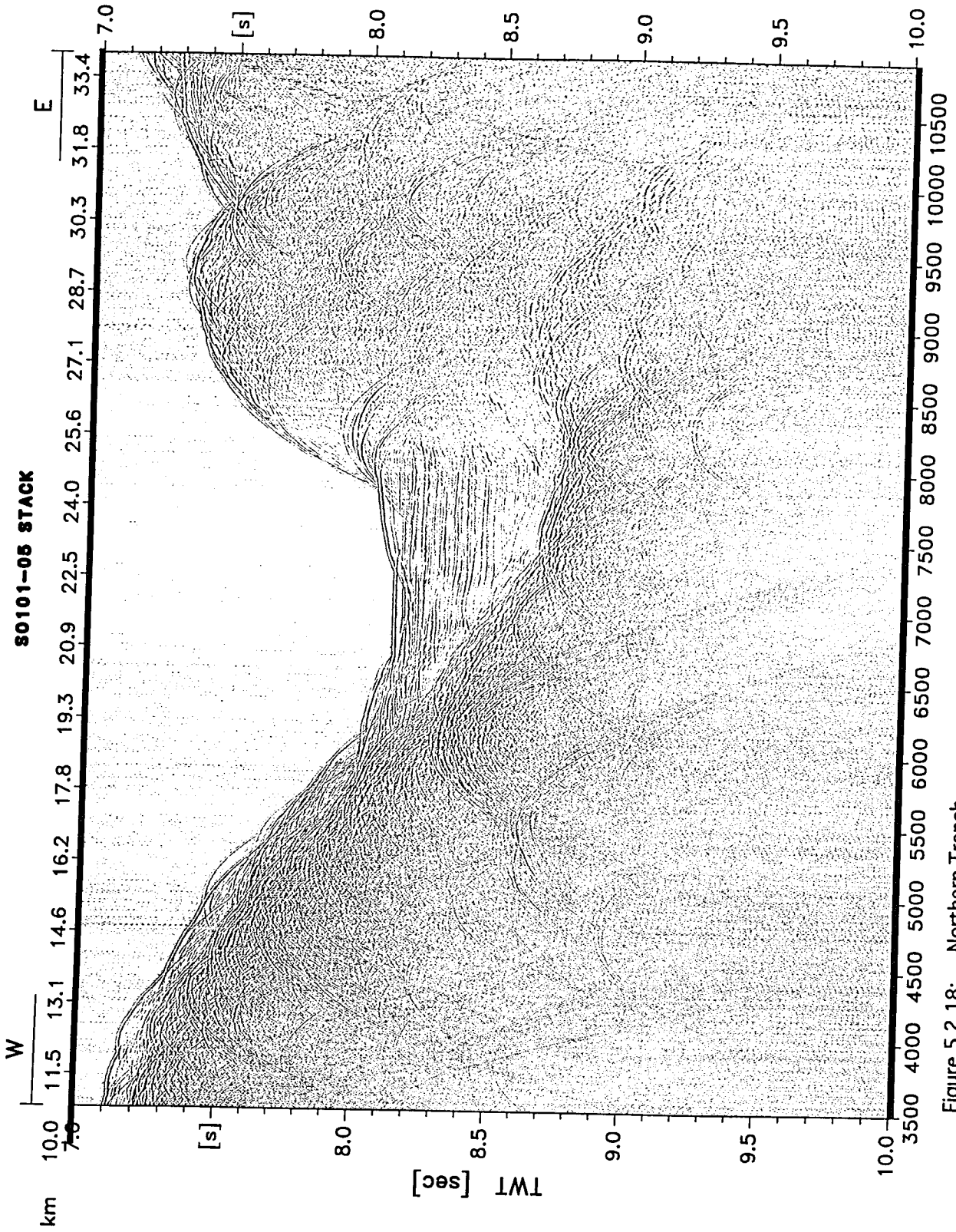
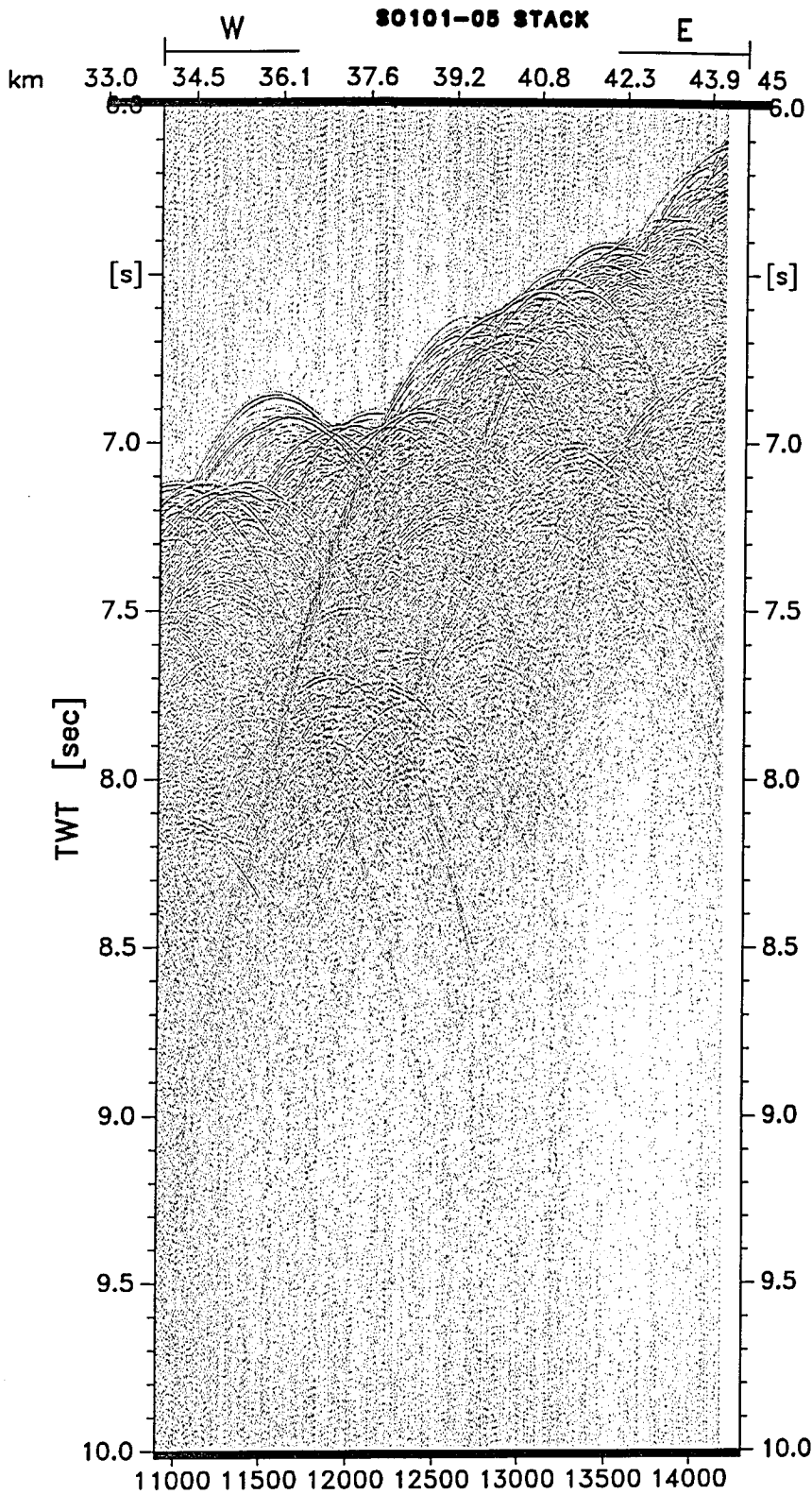


Figure 5.2.18: Northern Trench

Figure 5.2.19



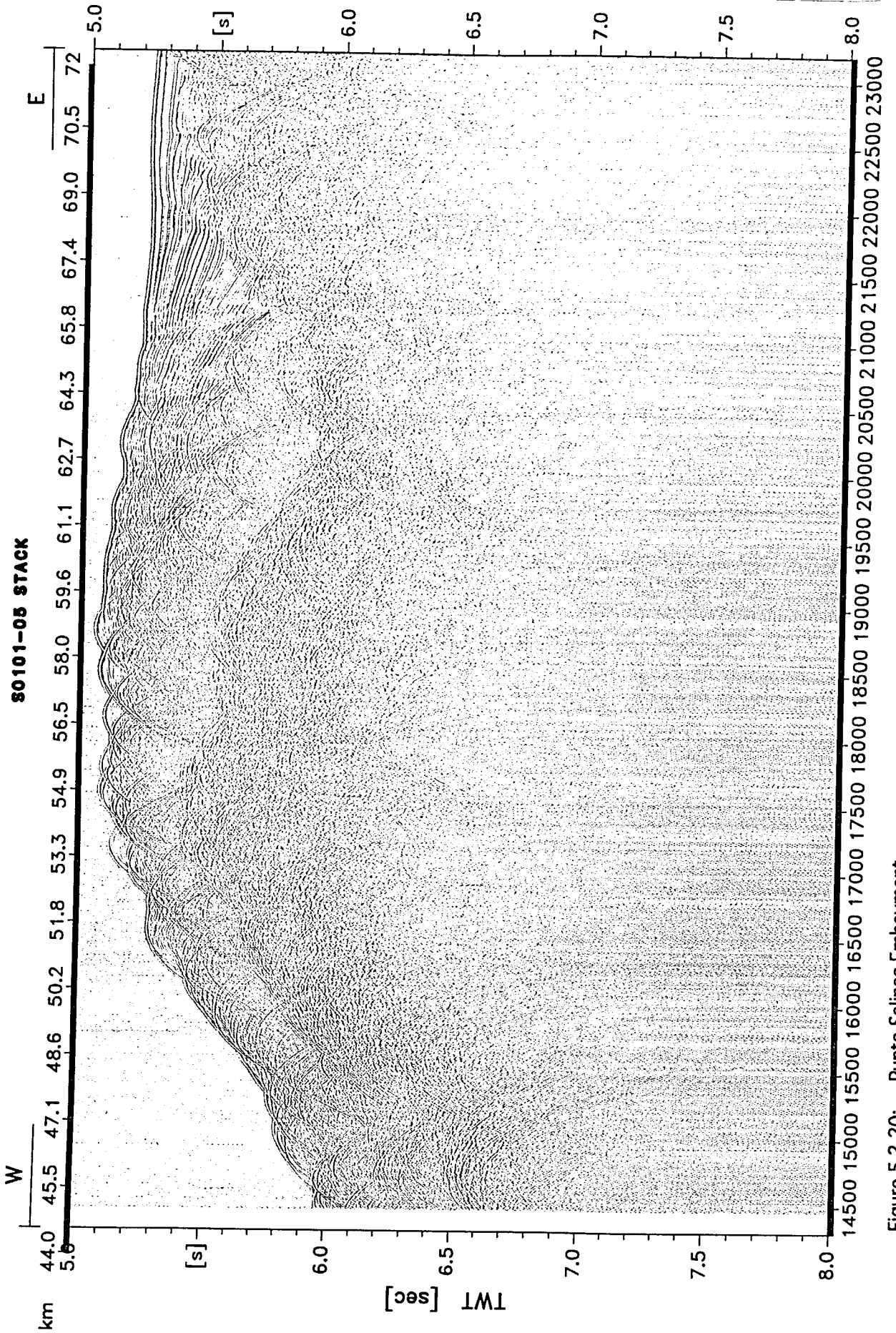


Figure 5.2.20: Punta Salinas Embayment

Figure 5.2.21

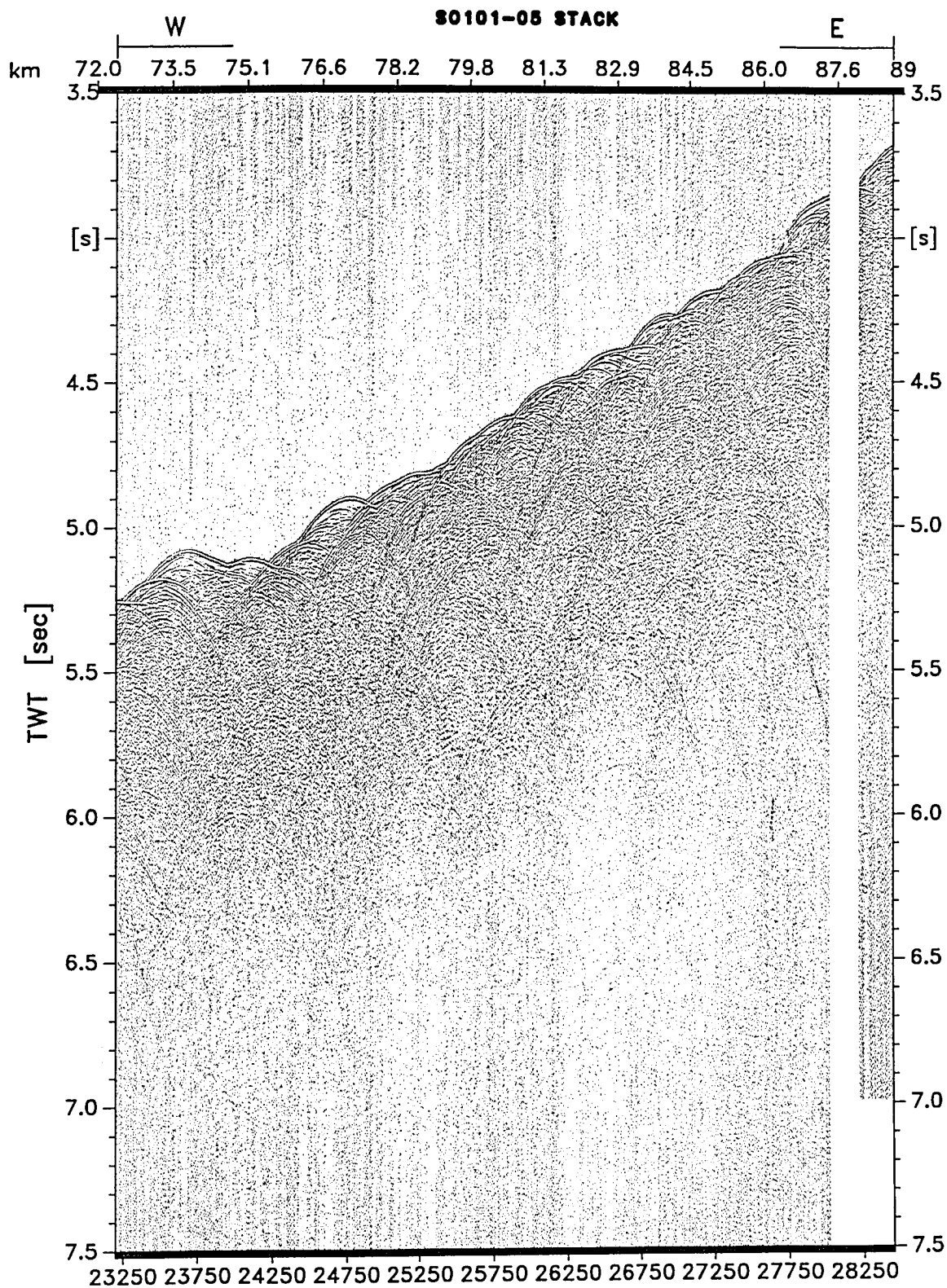
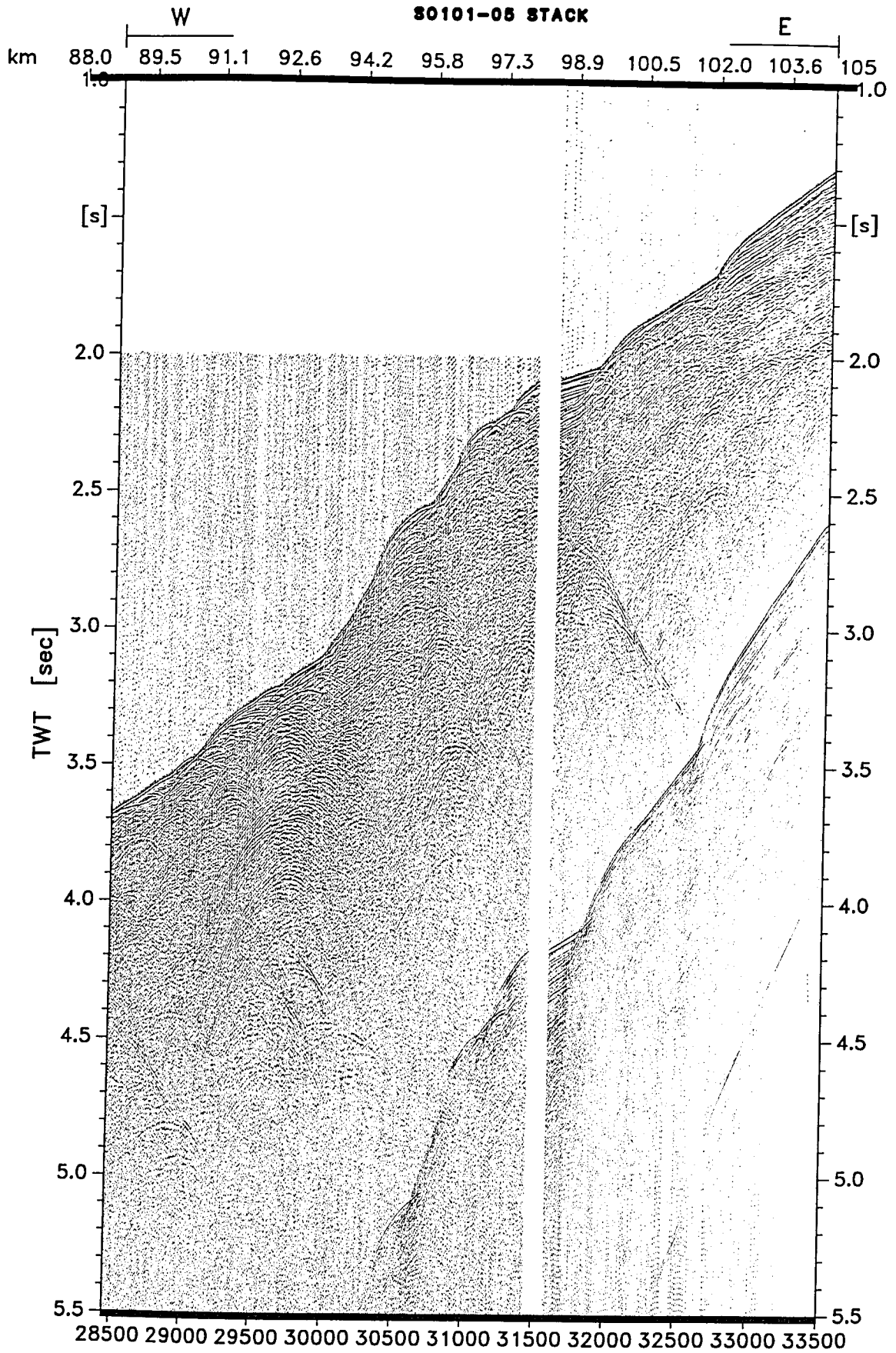


Figure 5.2.22



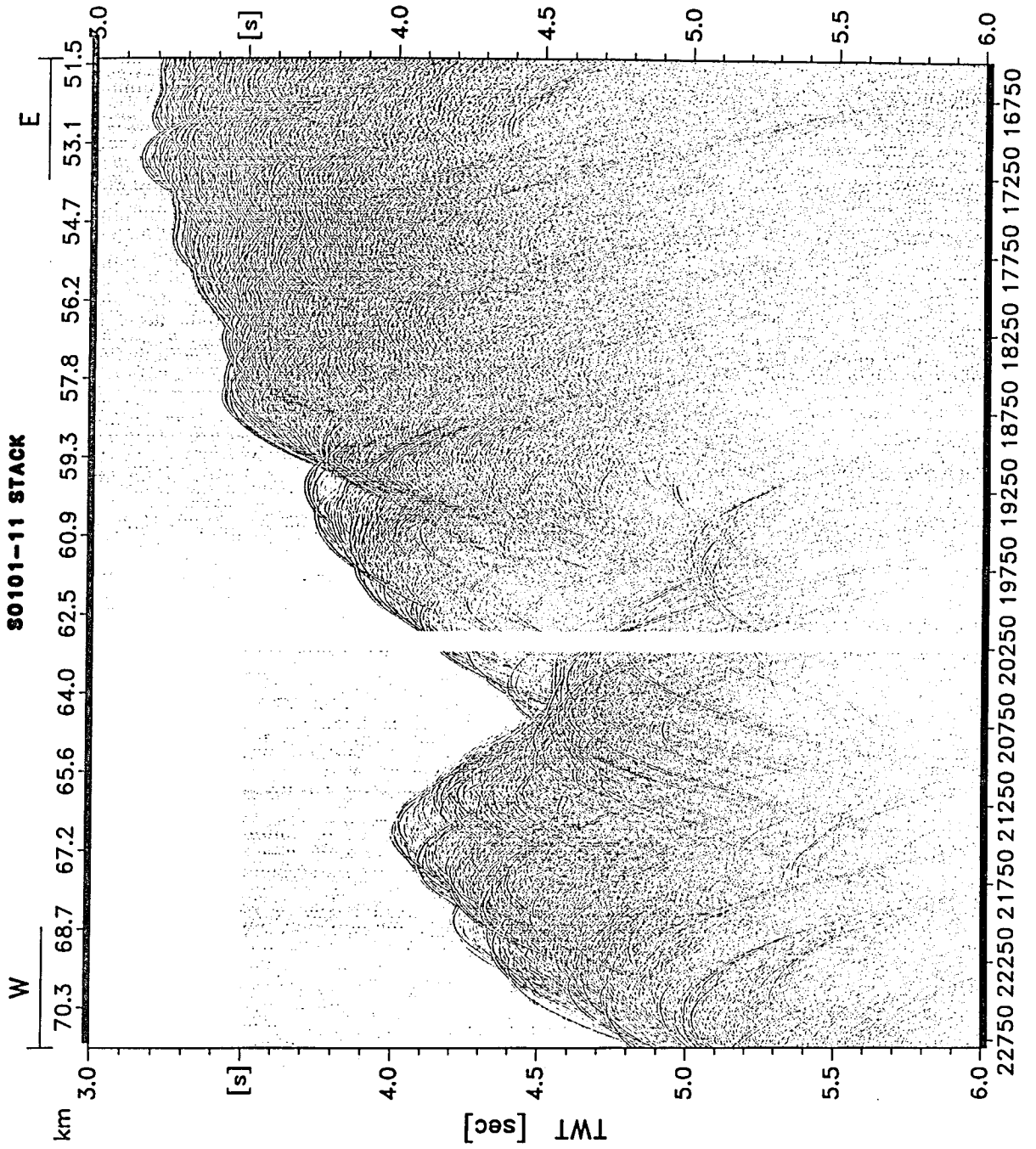


Figure 5.2.23

Figure 5.2.24: Outer northern Valparaíso Basin

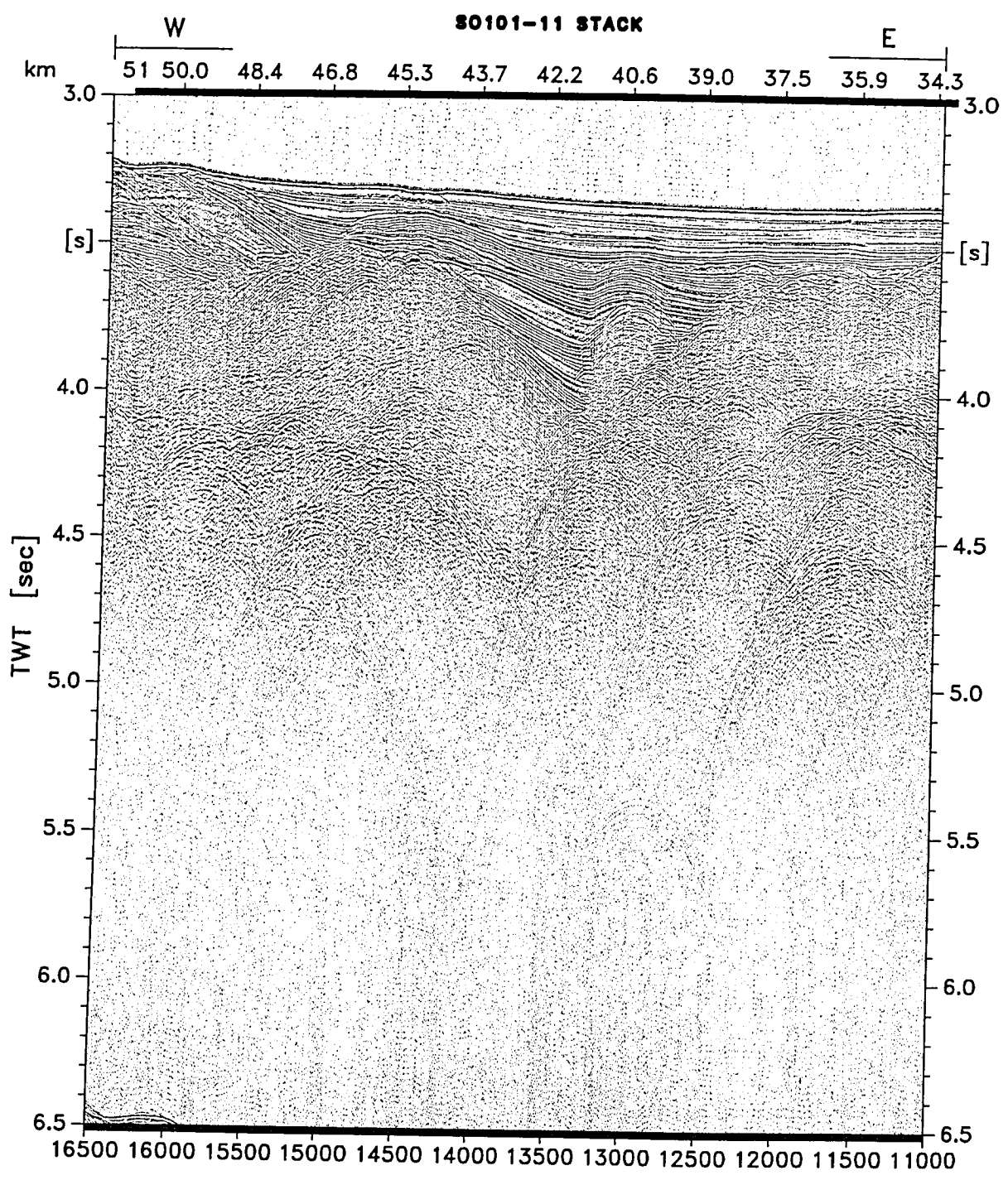


Figure 5.2.25: Inner northern Valparaíso Basin

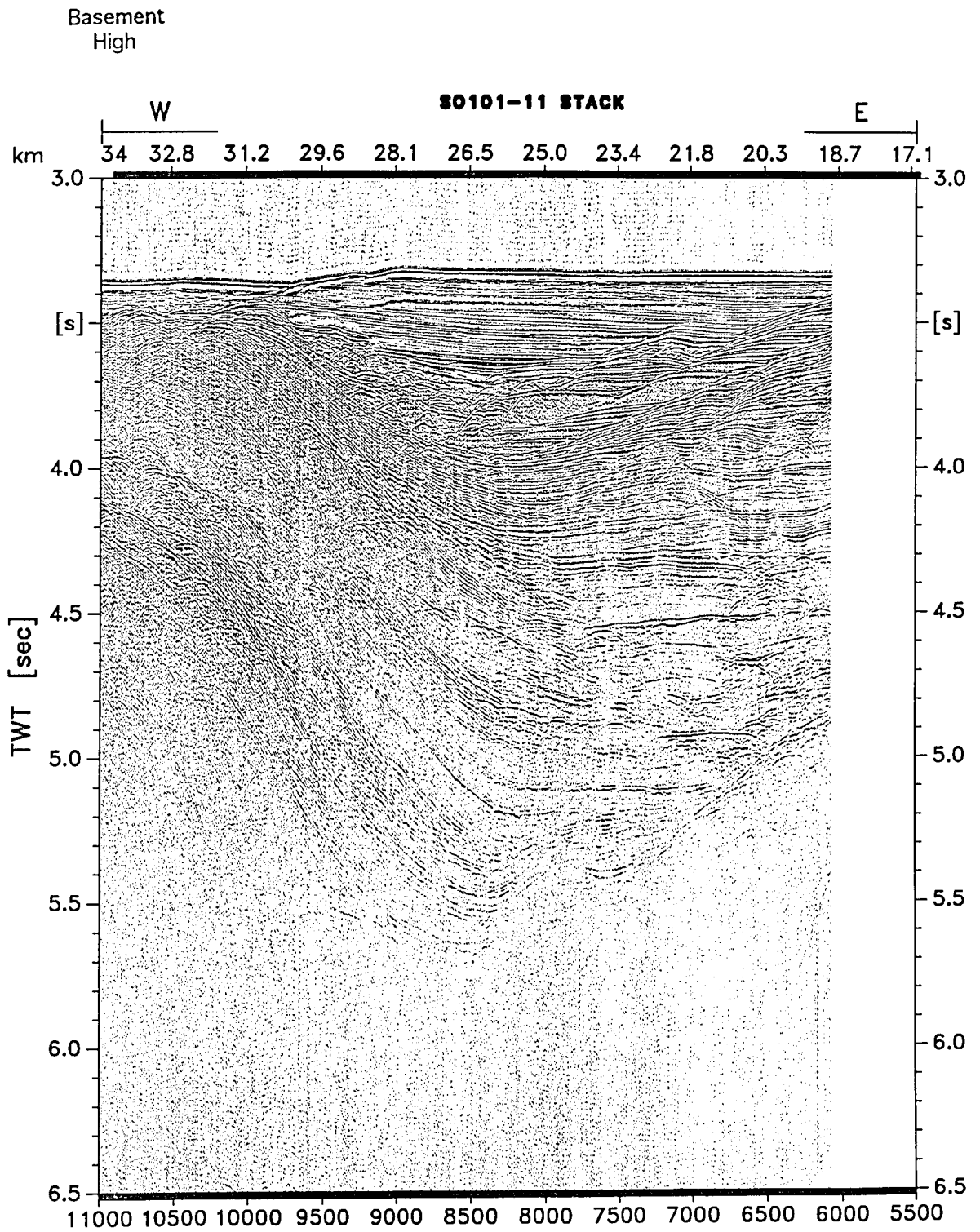


Figure 5.2.26

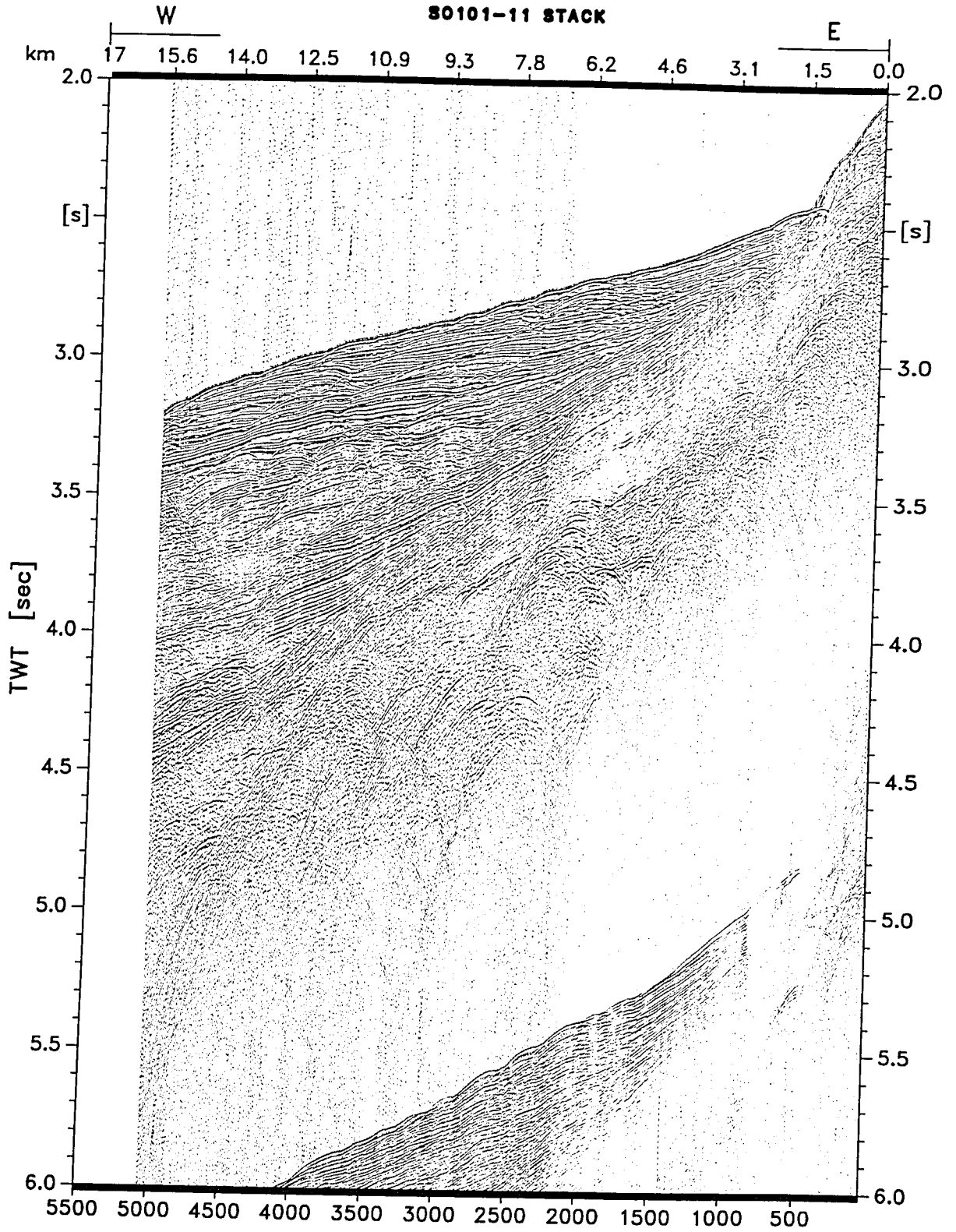
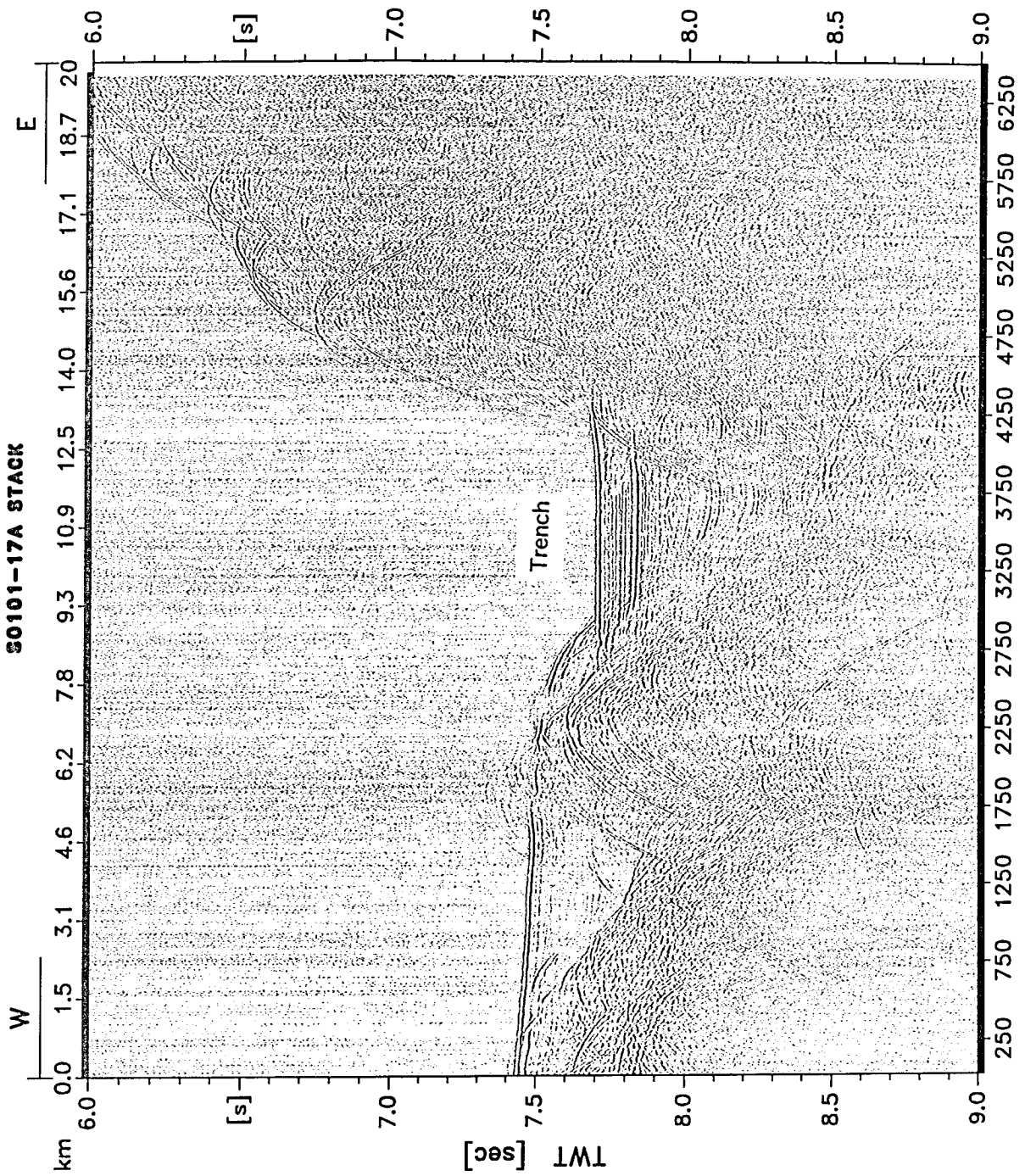


Figure 5.2.27



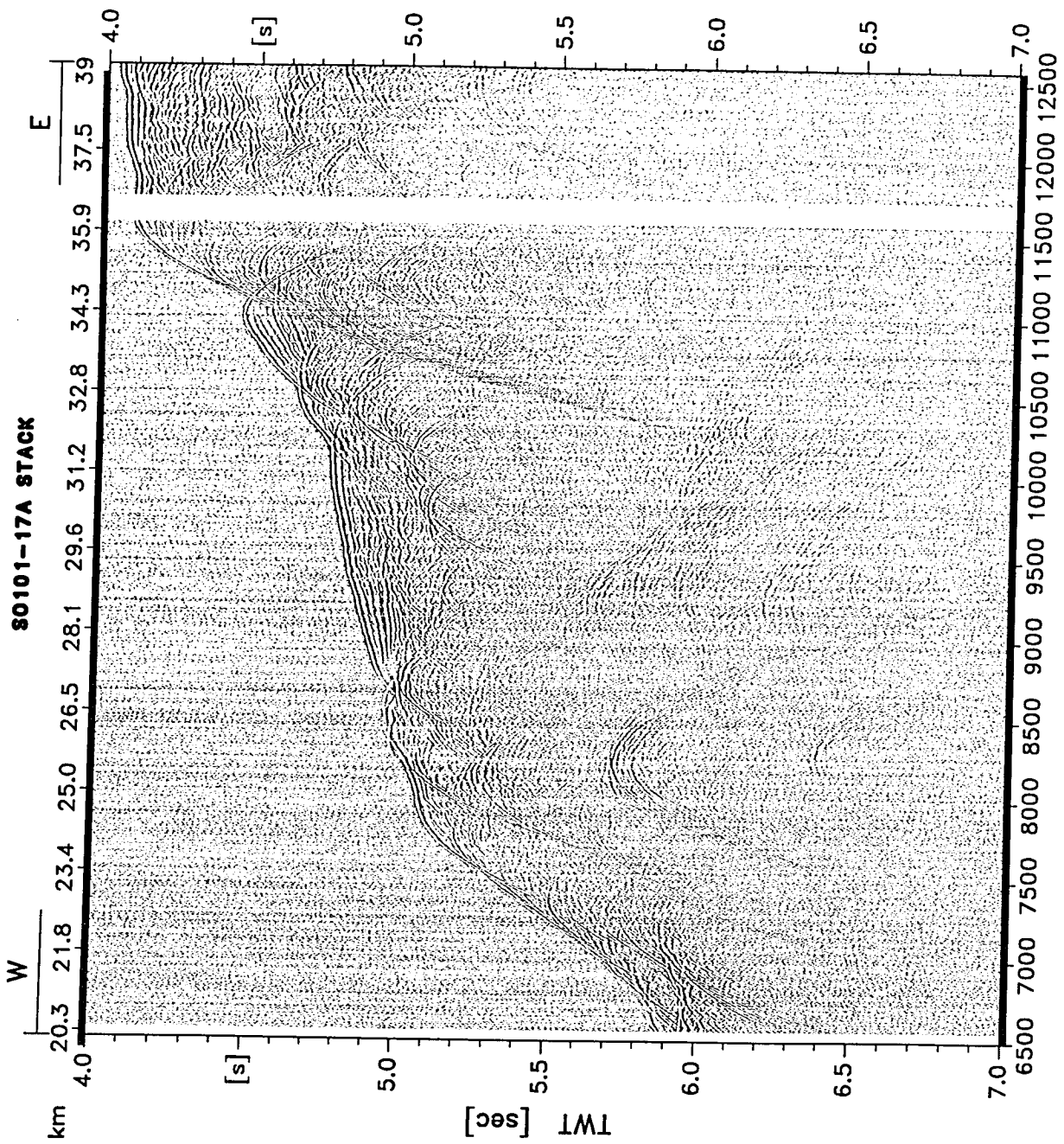


Figure 5.2.28

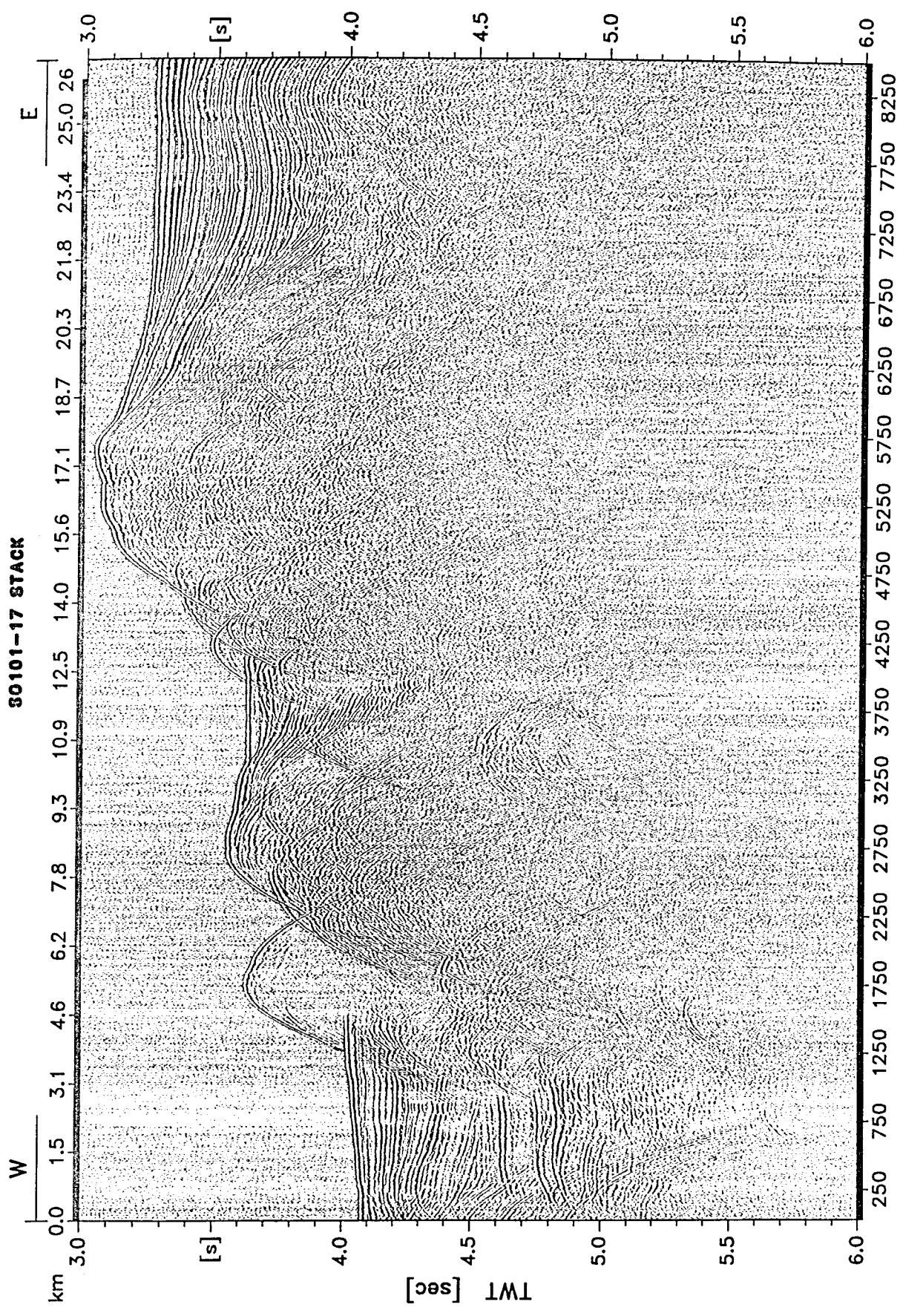


Figure 5.2.29

Figure 5.2.30

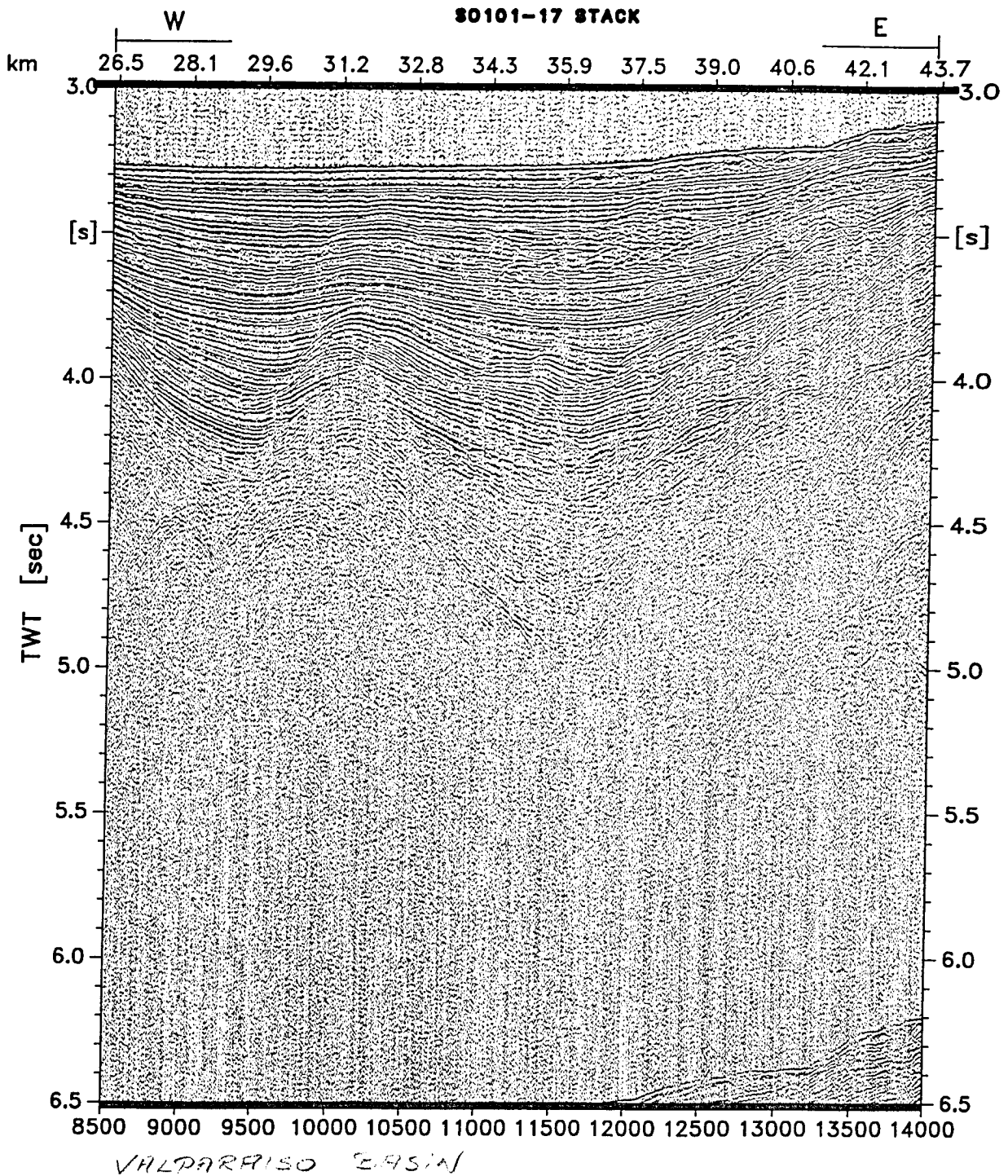
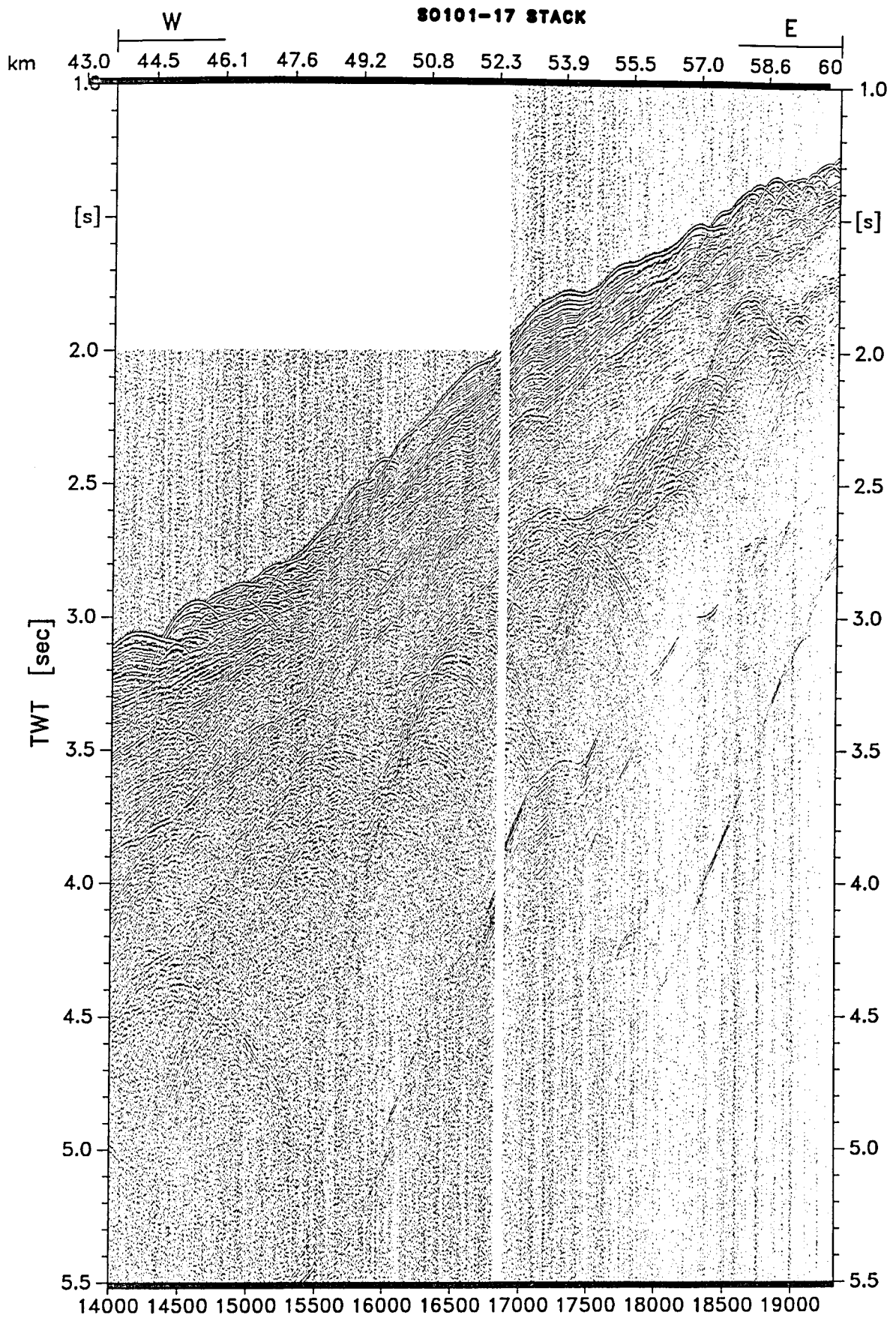


Figure 5.2.31



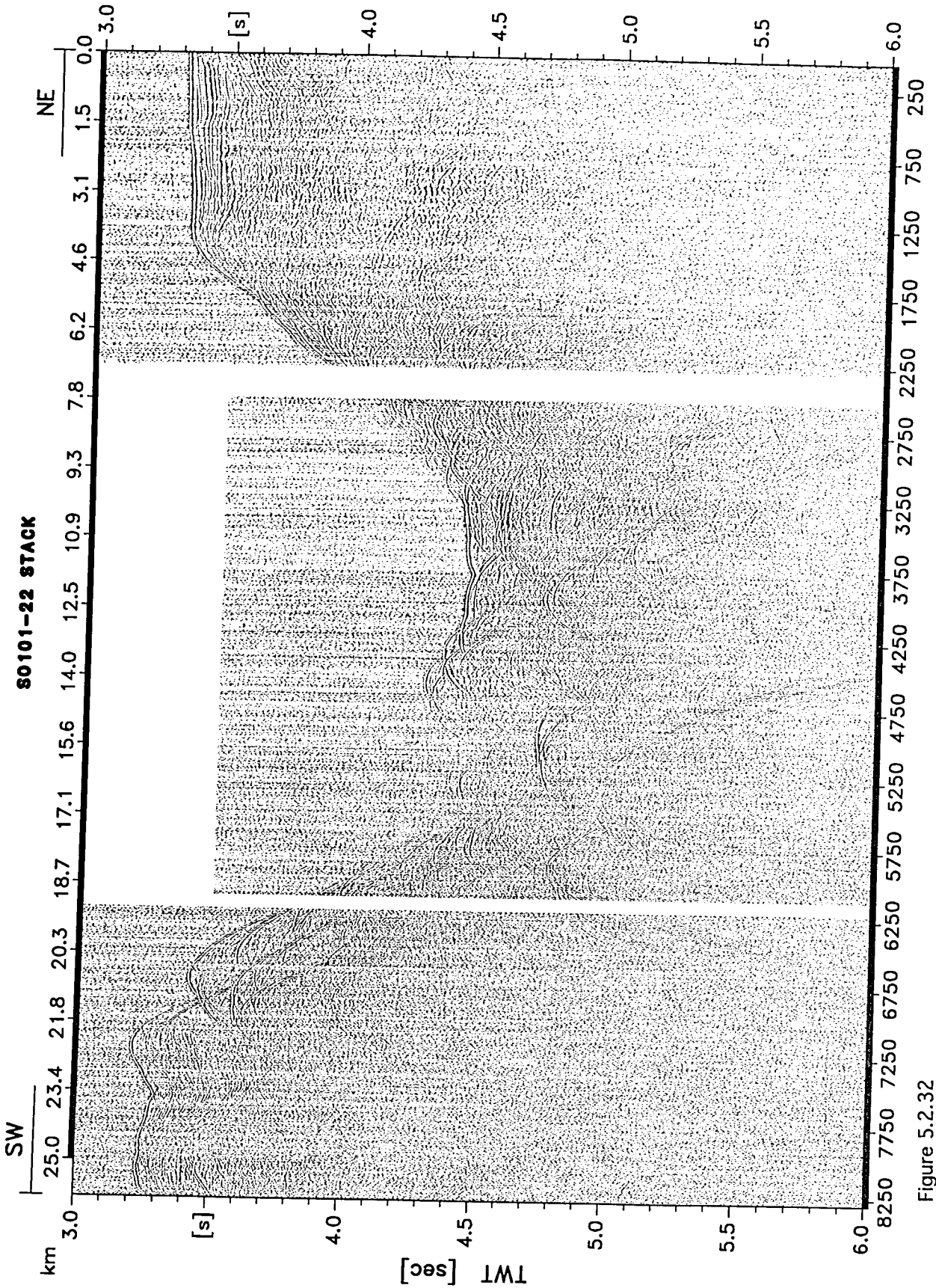


Figure 5.2.32

Figure 5.2.33

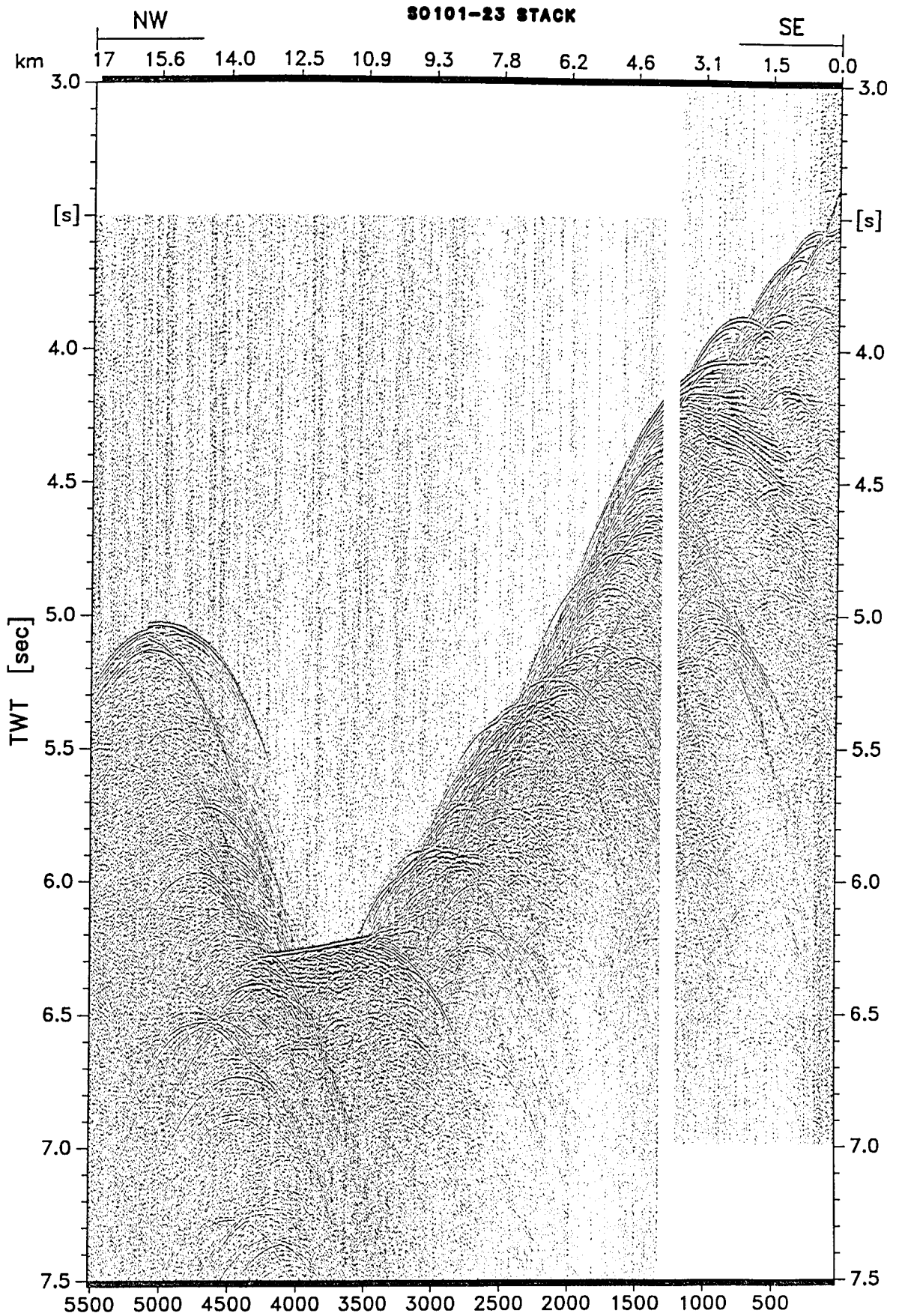


Figure 5.2.34

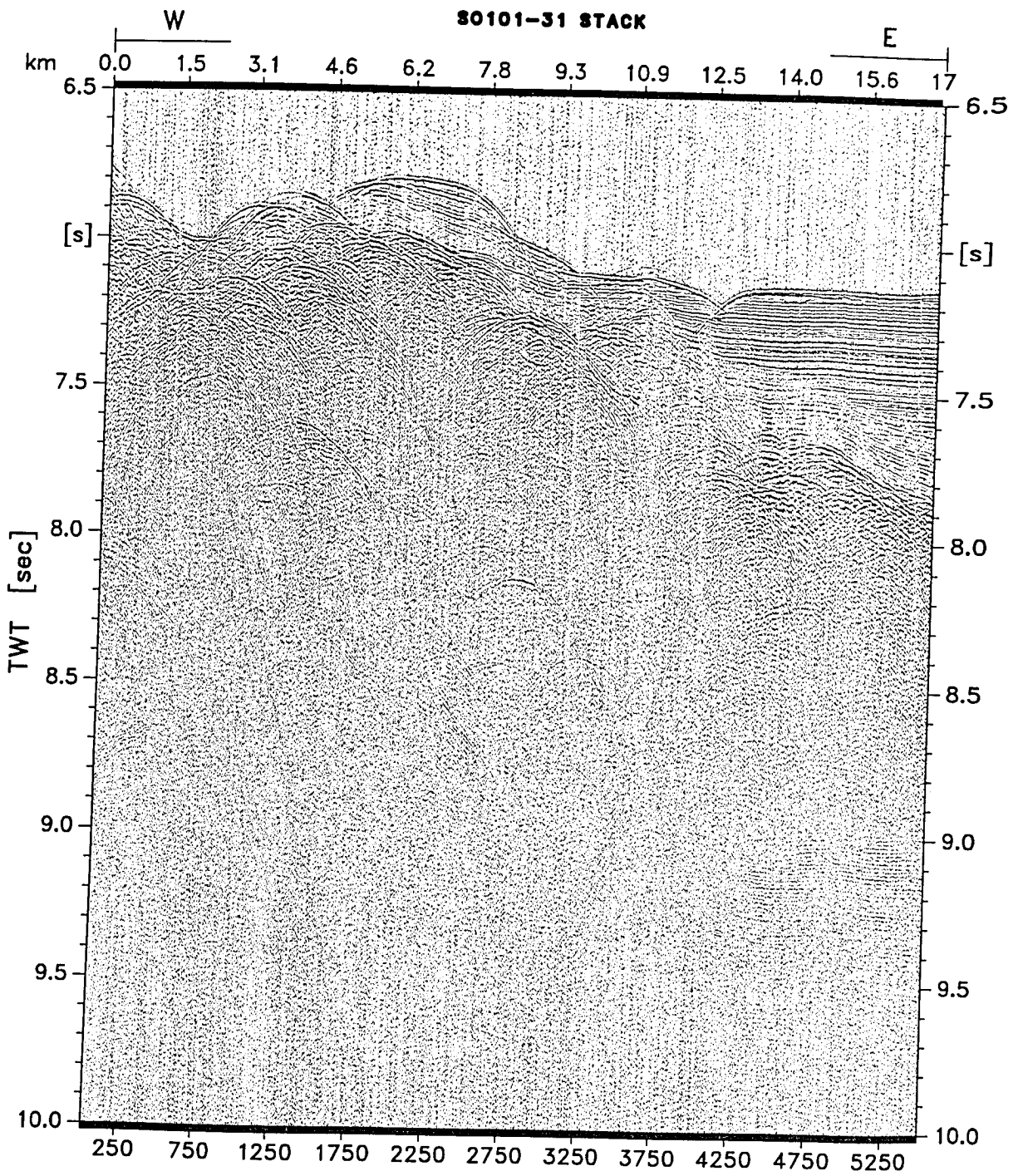


Figure 5.2.35

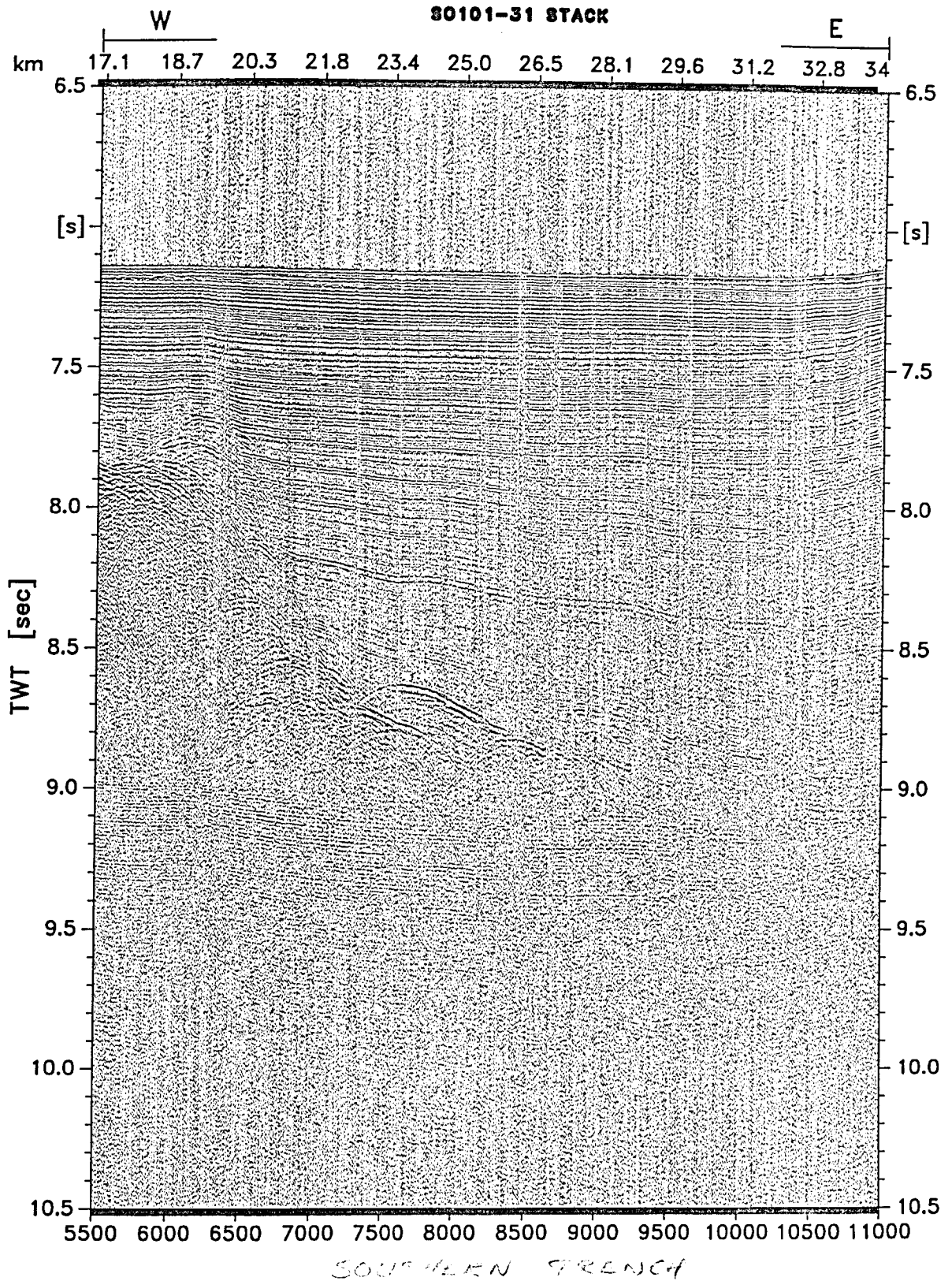


Figure 5.2.36

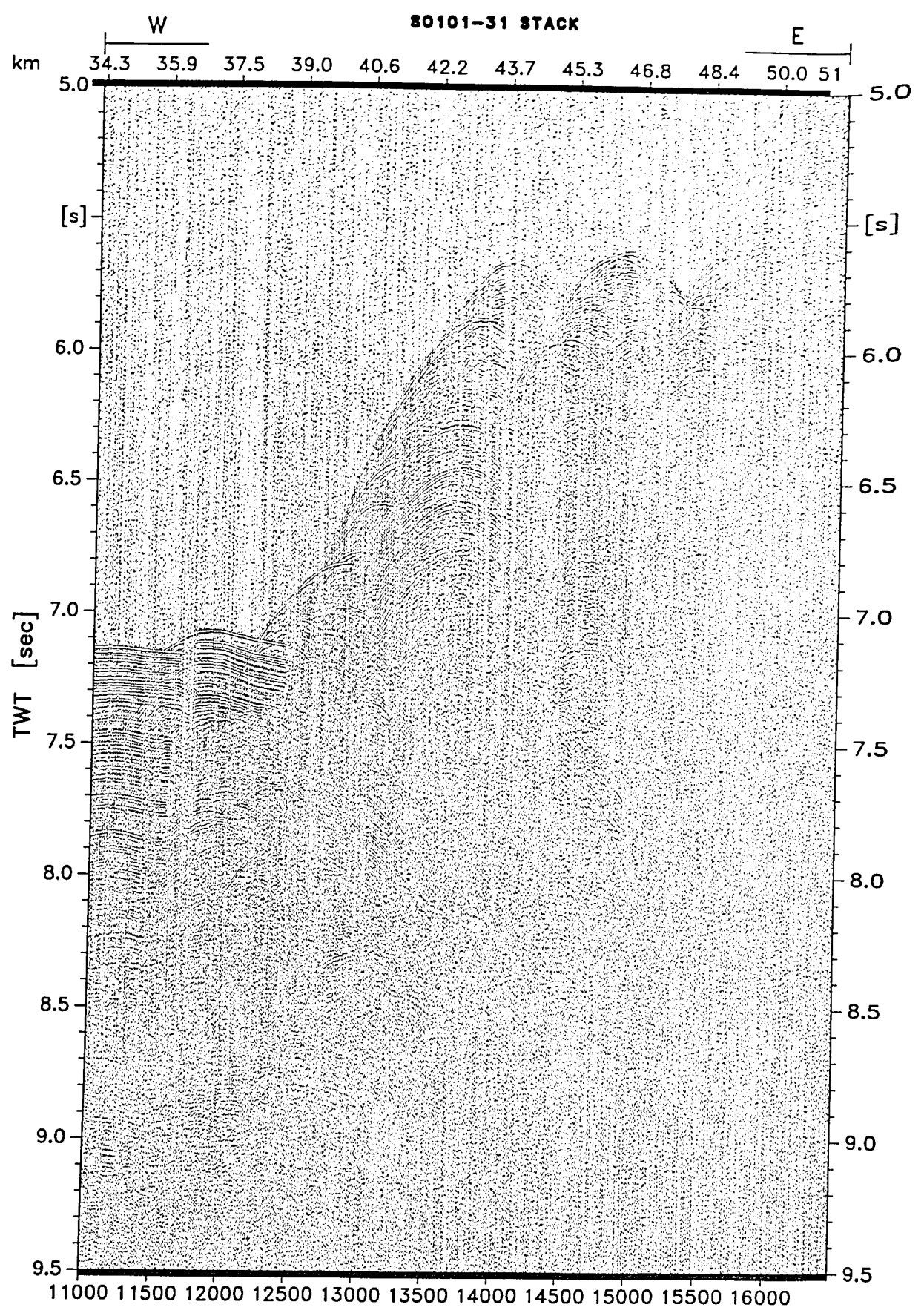


Figure 5.2.37

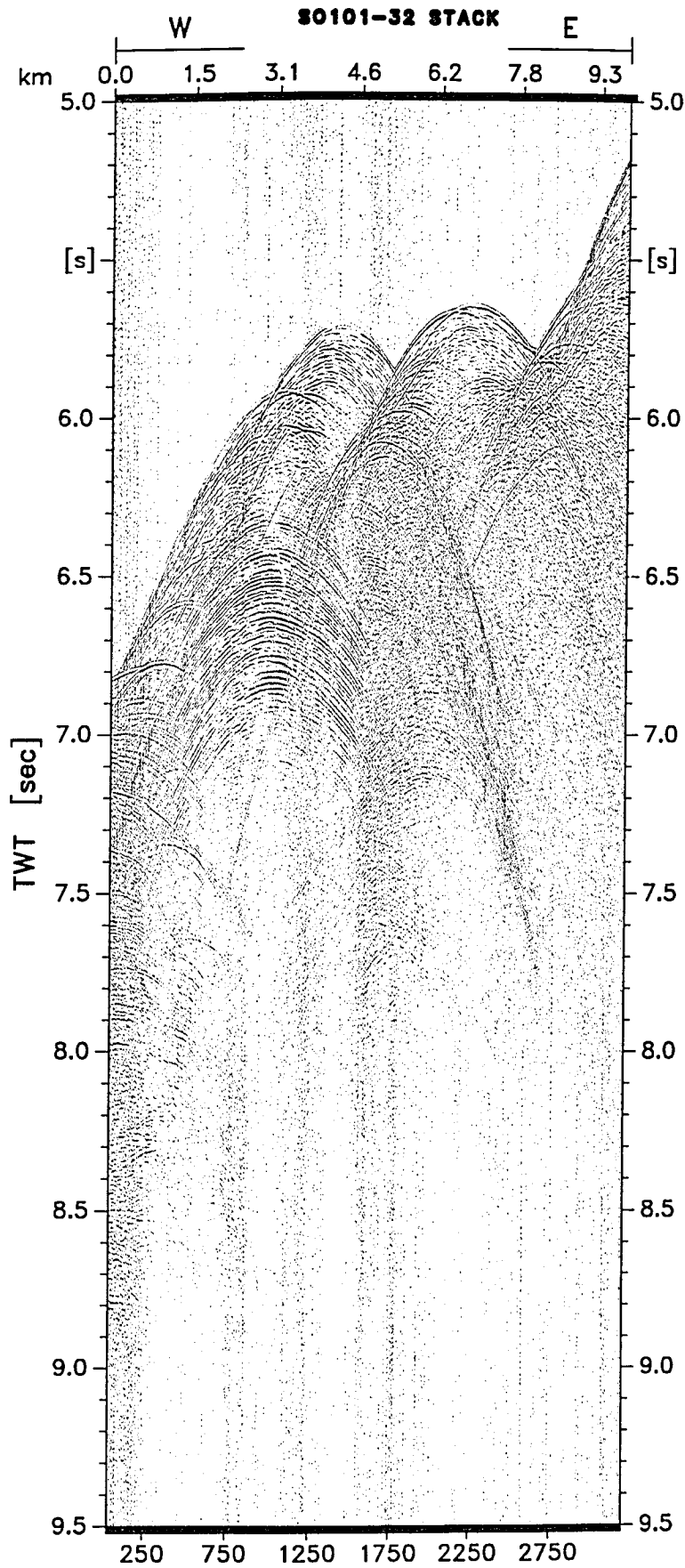


Figure 5.2.38

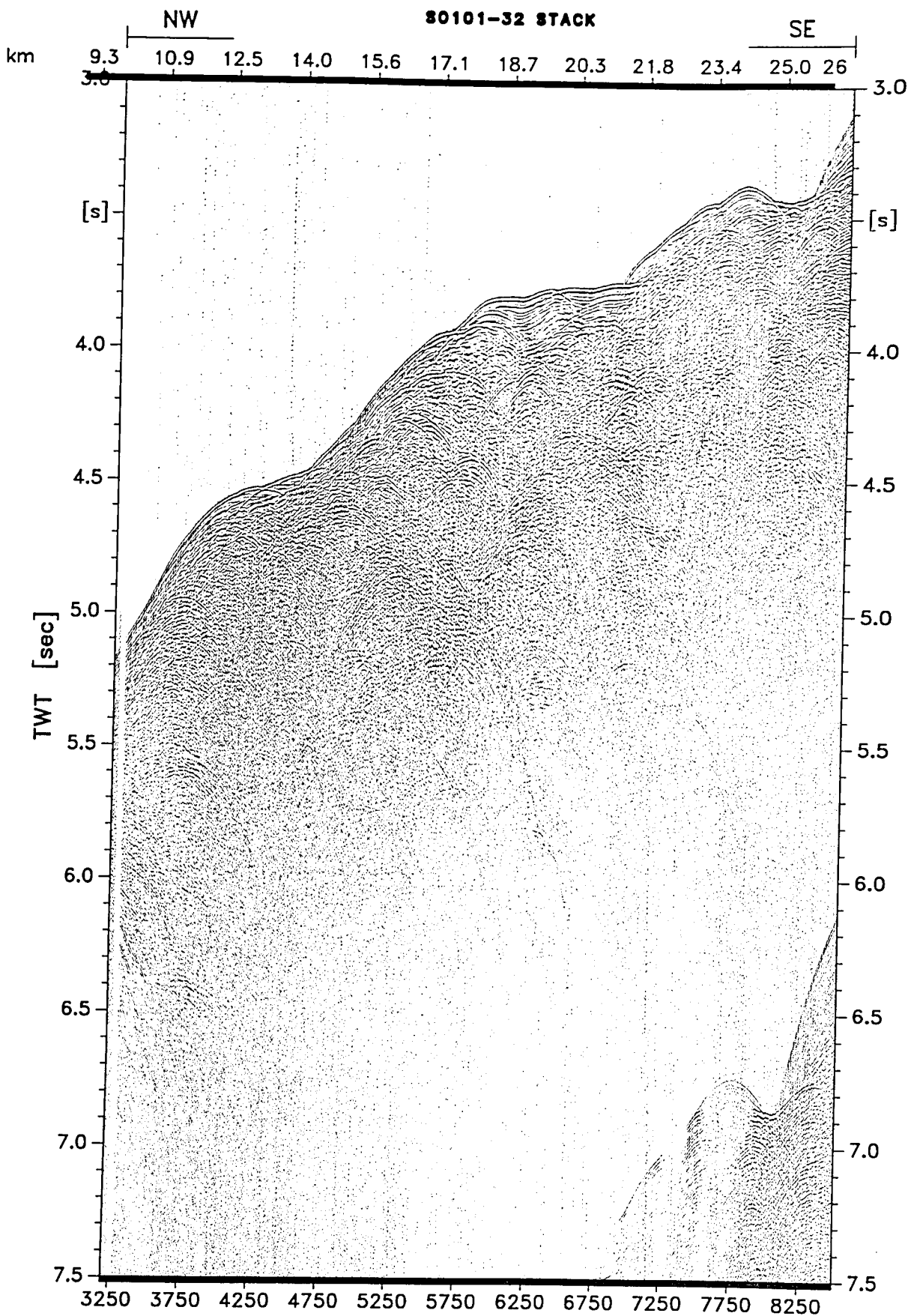


Figure 5.2.39

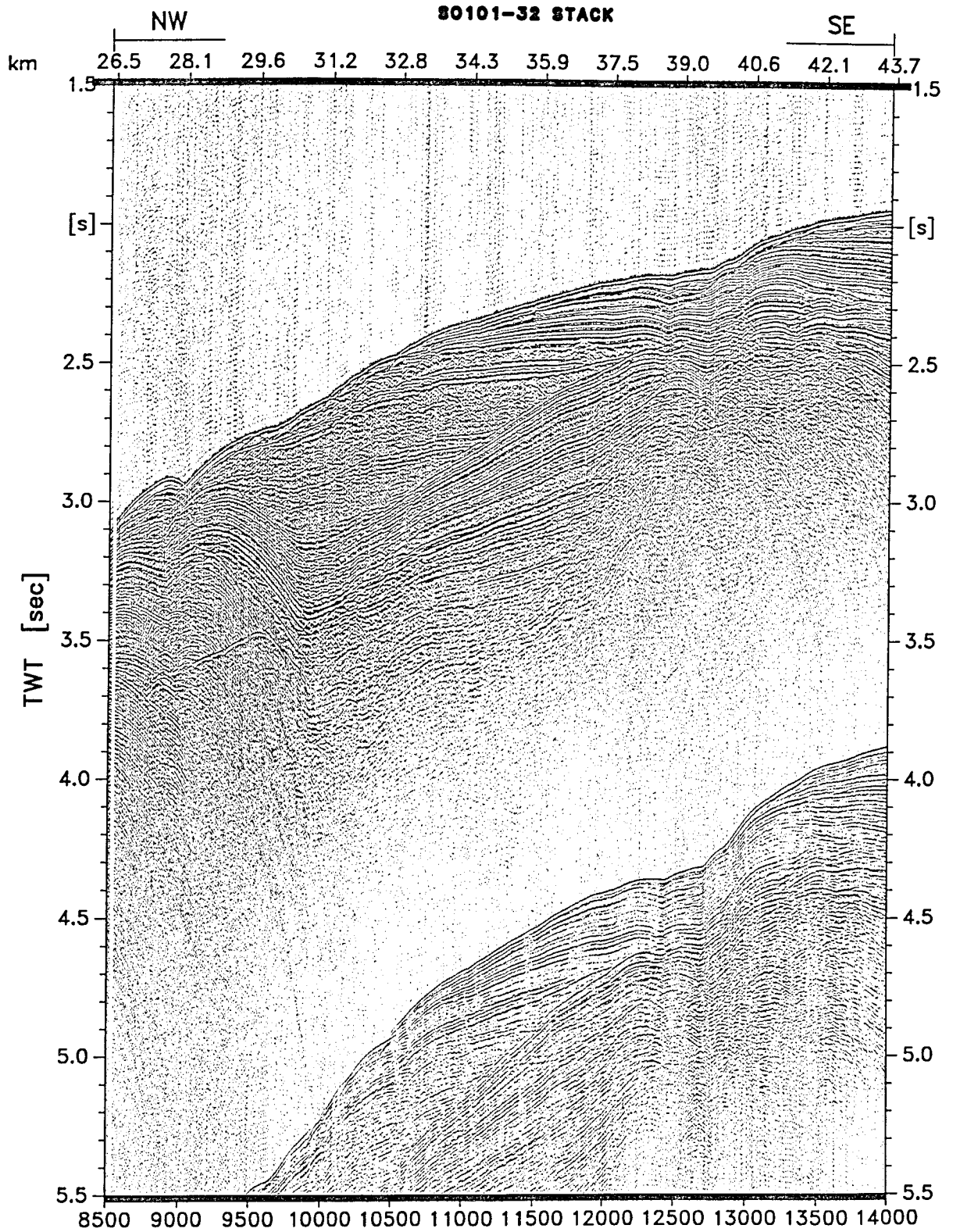
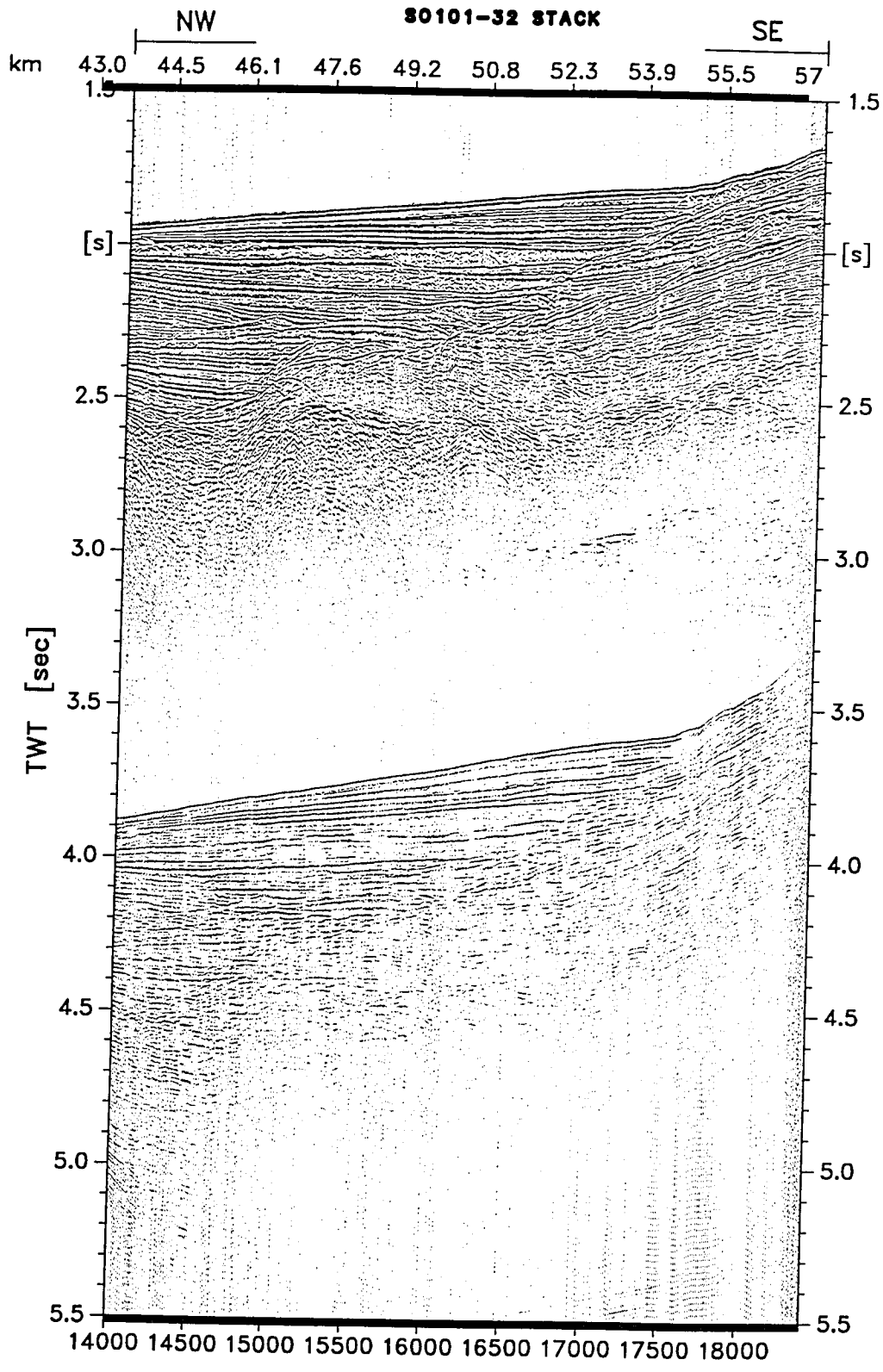


Figure 5.2.40



6.0 Parasound

(G. Harms, R. von Huene)

The Parasound instrument rarely records much on slopes that dip more than 2°. Record quality and resolution also depends considerably on ship's speed. Thus it was not employed during the hydrosweep measurements because little information is recorded at 12 kts. It was used continuously during the seismic acquisition run at 4.5 kts and it was used at all core stations. Quality records were made in basinal area, along the trench axis, on the smooth oceanic crust, and over the top of O'Higgins Guyot.

6.1 Instrument

A detailed record of the upper most sediment layers was recorded locally with Parasound, a shallow penetration transducer instrument generally employed to locate optimum sites for core sampling. The signal is generated in a parametric mode which allows frequencies to be varied between 2.5 and 5.5 kHz. By emitting one signal at 18 kHz and a variable signal between 20.5 and 23.5 kHz with proper phase delay a lower frequency signal can be generated. The signal has a nominal 4° beam angle so that the insonified area is about 7% of the water depth. The reflected signal received is processed and displayed on a screen with color indicating the relative returned amplitude. The signal can also be recorded digitally on another system named Paradigma that allows post processing of the data.

6.2 Selected Records

O'Higgins Guyot. Two seismic and Parasound lines were acquired across the summit of O'Higgins Guyot. The seismic records showed a thin sediment cover and one small basin. Parasound (Figure 6.1a and b) imaged a uniform 10 m thick pelagic sediment layer with little internal structure save a thin bed at the base. The strong basement reflector and transparent nature of the image indicates little absorption of the transducer signal. This was confirmed by the pelagic limestone dredged at station 8. Coring was attempted only once because it resulted in a bent the core barrel presumed to be caused by impact into an indurated material.

Interesting in the summit area are small ridges which might be reefal build-ups or volcanic promontories (Figure 6.1a). Only the summit area at 355 m - 360 m shows topographic roughness whereas the rest of the low relief summit is smooth.

Nazca abyssal plain. Parasound penetrated 100 m or through the complete pelagic section that was also imaged in the seismic records across the smooth abyssal plain south of O'Higgins Guyot (Figure 6.2). As also seen in the seismic records, the section is divided into a well stratified upper and a more transparent lower section. Stratification is uniformly parallel. The basement is characteristically uneven and magnetic anomalies indicate an age of about 35 Ma (see chapter 4).

Chile Trench. In the Parasound records the sediment filled trench axis south of the Juan Fernandez Ridge has a reflective northern part with little penetration and a well stratified southern part. Gravity coring was unsuccessful in the northern part and a box core in the intermediate area recovered 3 sharply defined sand layers. Sand near the surface could thus be a reason for the coring failure. Maximum Parasound penetration in the trench axis is about 40 m (Figure 6.3). The section is deformed near the landward slope and surface folding in the Parasound record is also seen in the seismic images. The high vertical exaggeration of the Parasound record obscures the vergence of this structure. The upper 10 m of the sediment have parallel strata but the underlying strata thicken toward the eroded turbidite channel on the western side of the axial fill.

Valparaiso Basin. Parasound was generally good in imaging the upper most layers in the Valparaiso Basin. An example (Figure 6.4) shows a series of steps increasing in displacement toward the south that are highly diffracted. Despite a 15 times vertical exaggeration, vergence appears to be southward indicating basinward dipping faults. The 40 m imaged section sloping toward the basin is transgressed by the 20% thicker section in the middle of the basin. This transgression is clearer in seismic records (see chapter 5). The excellent penetration and clear imaging of strata suggest a soft upper sediment sequence.

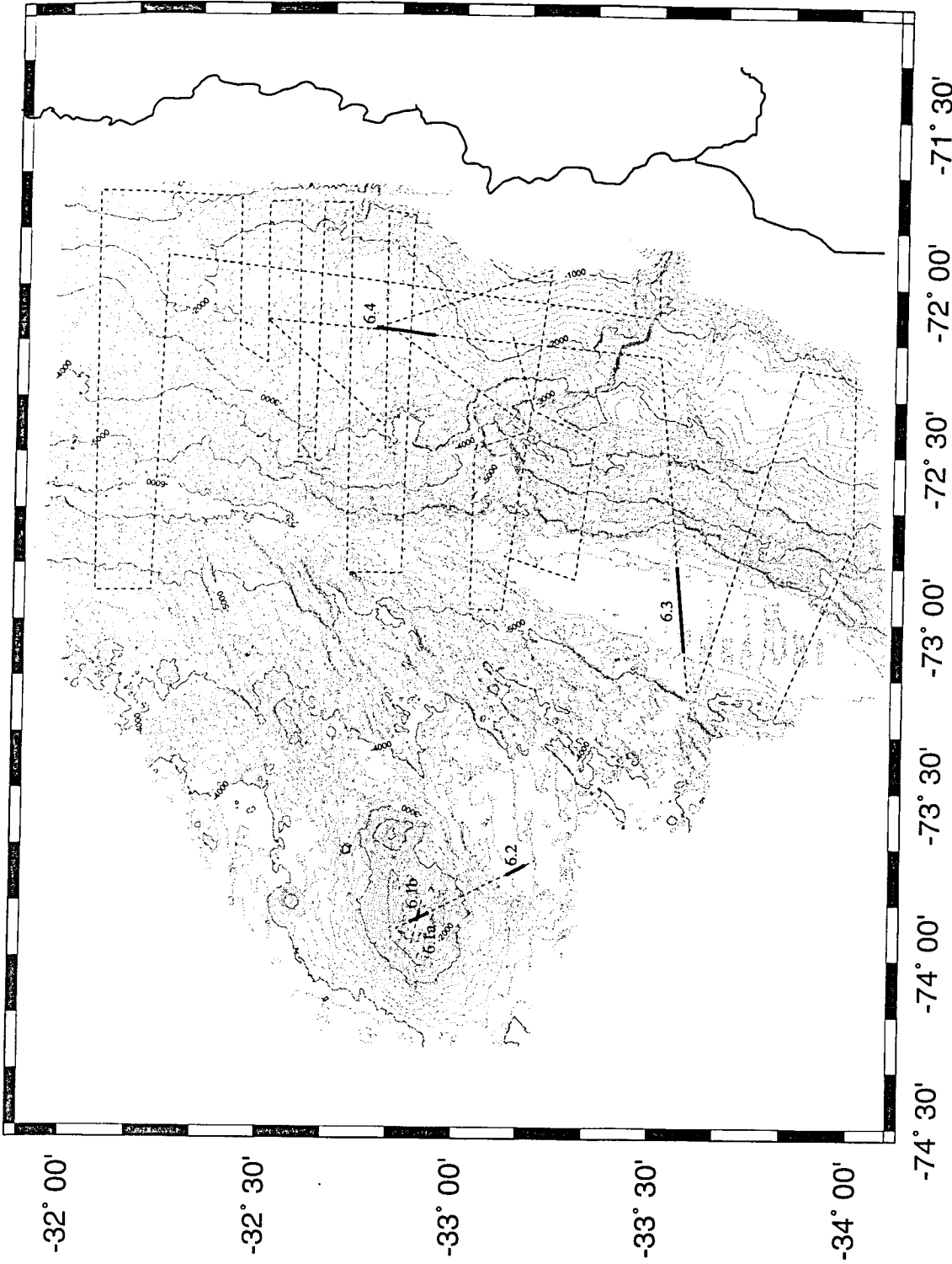
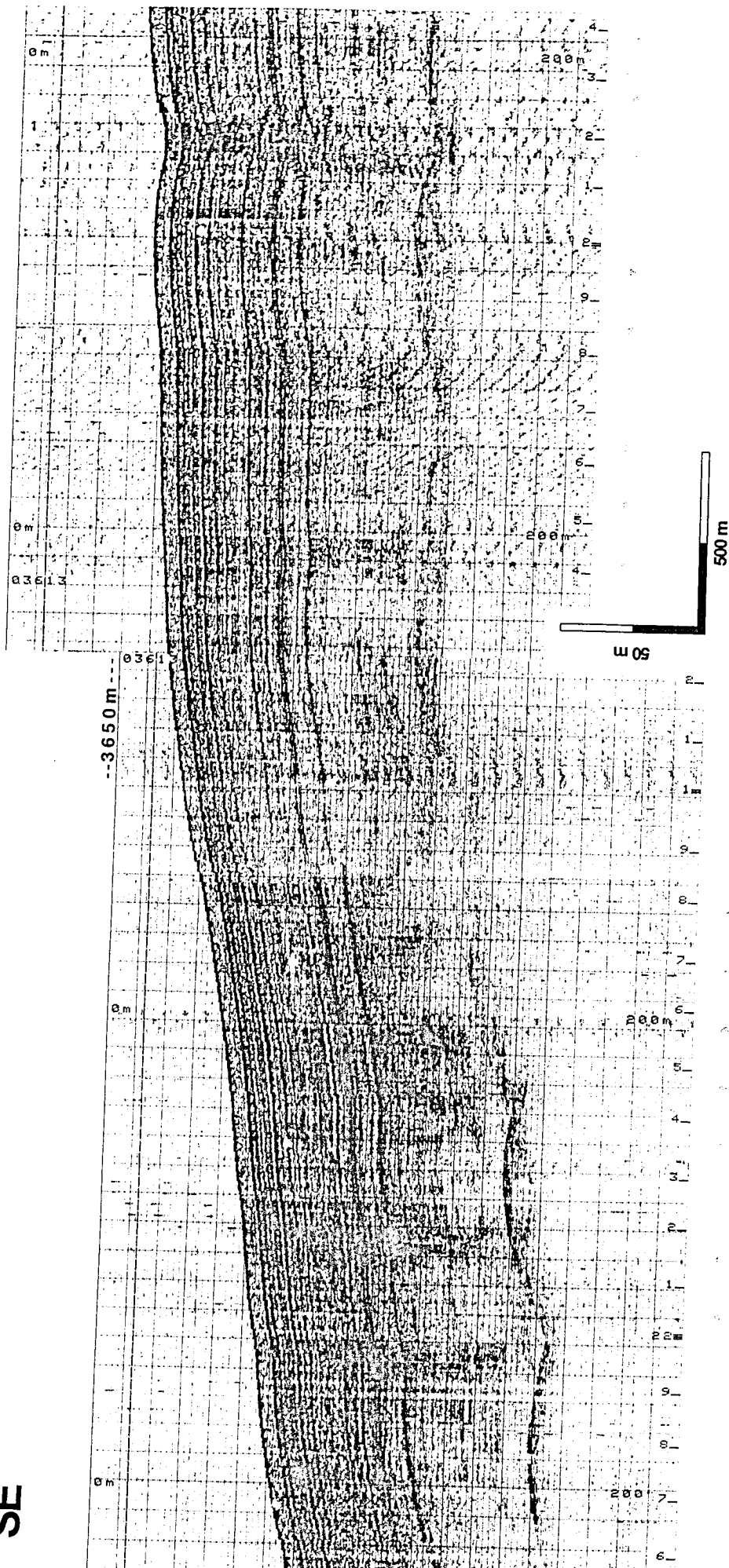


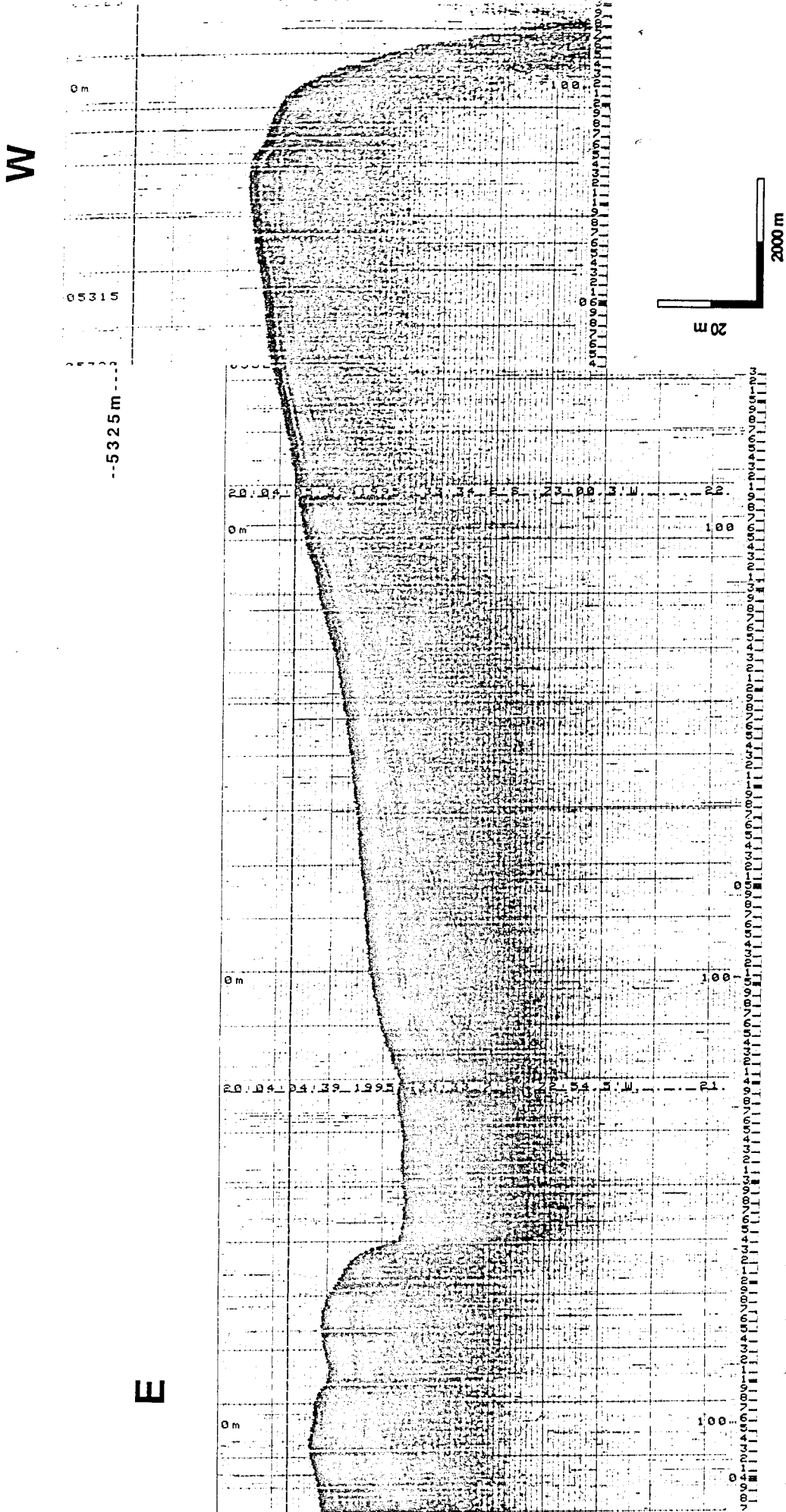
Figure 6.0 Location map showing parasound tracks. Bold sections indicate locations of figures as noted.

NW

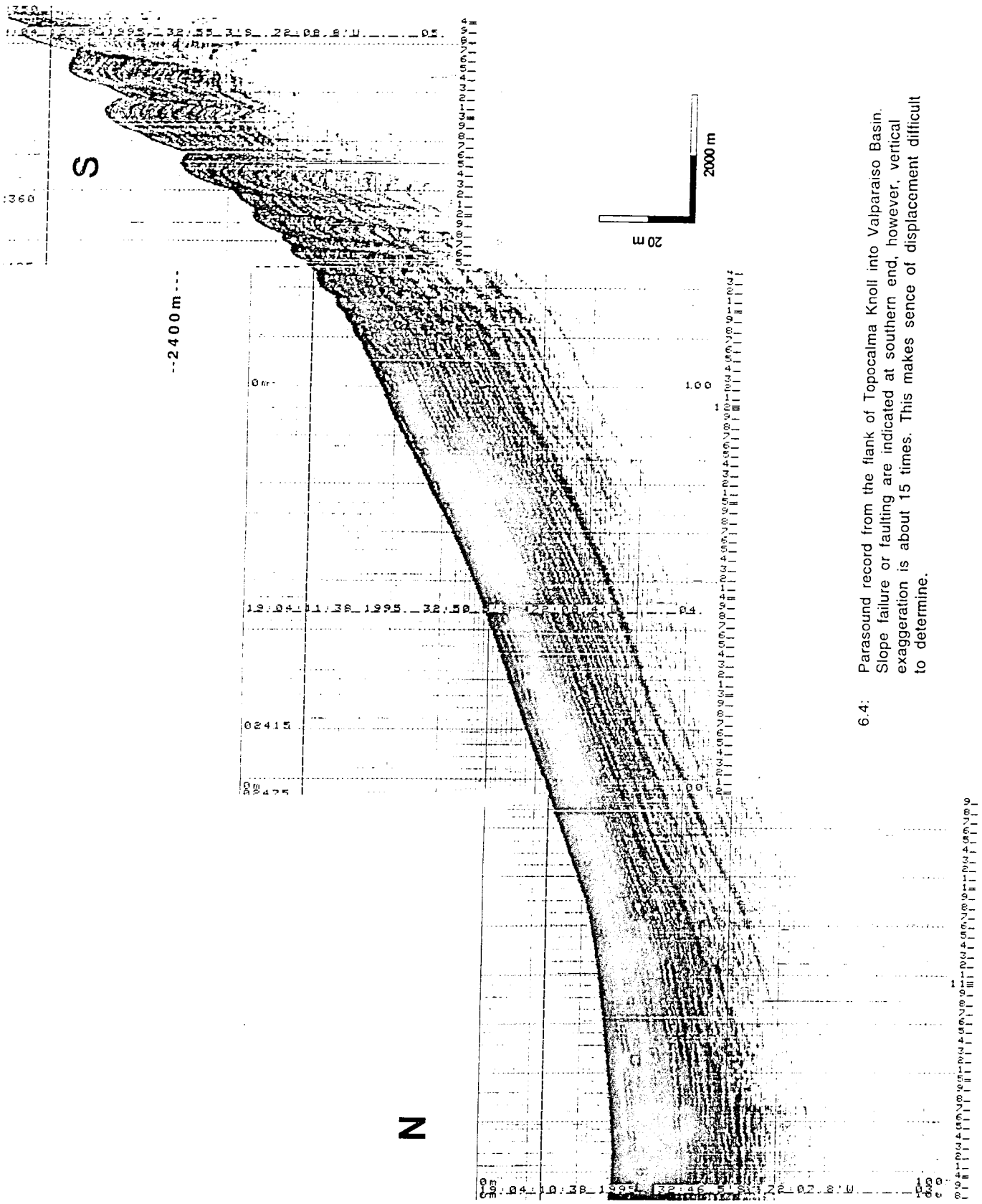
SE



6.2: Parasound record across a smooth section of the Nazca abyssal plain. Penetration reaches basement ca. 100 m.



6.3: Parasound record across the Chile Trench axis in southern area where the trench is sediment flooded. Western end shown is one bank of the eroded axial channel. Wedging beds open toward the channel indicating episodes of overbank deposition.



6.4: Parasound record from the flank of Topocalma Knoll into Valparaiso Basin. Slope failure or faulting are indicated at southern end, however, vertical exaggeration is about 15 times. This makes sense of displacement difficult to determine.

7.0 Geologic Investigations

Since studies of paleoceanography in the CONDOR project area were planned for a subsequent cruise by the University of Bremen, the two projects were coordinated so that the full range of studies originally planned for CONDOR could draw on the expertise of all interested groups. The geological program also included dredging for hard rock to characterize the provenance and history of marine rock units and correlate them with geologic mapping and stratigraphy onshore. Sampling was planned based on the results of the previous CONDOR legs and the distribution of cores and dredge stations occupied during CONDOR Leg 3 are located on swathmapped bathymetry in Figure 7.0.

7.1. Sediment sampling from cores

(D. Beese, N. Biebow, F. Lamy, S. Locker, M. Segl, and D. Spiegler)

During the CONDOR Cruise Sonne 101/3, sediment was sampled with a gravity corer, a multicorer and Reineck-corer at eleven sites off Valpariso between 472 m and 5,412 m of water depth. Figure 7.0 shows the location of Core Stations C-1 to C-11. The geographical position, the waterdepth, and the recovery of cores are documented in Table 7.1.

The multicorer was the main tool for the sampling of complete undisturbed sediment surfaces and the overlying bottom water. It is equipped with 8 large tubes of 10 cm diameter and 4 smaller tubes of 6 cm diameter. At all sites we retrieved usable samples, but as the weather became rough, some of the tubes released prematurely and were filled with clear water.

The multicorer tubes were usually sampled as follows:

- Three large cores for investigations of foraminifers and for measurements of stable oxygen and carbon isotopes of the carbonate were cut into 1 cm slices. The surface sample was stained with a solution of rose bengal in ethanol (Geol. Bremen).
- One large core for organic geochemical analysis was cut into 1 cm slices and frozen (Geol. Bremen).

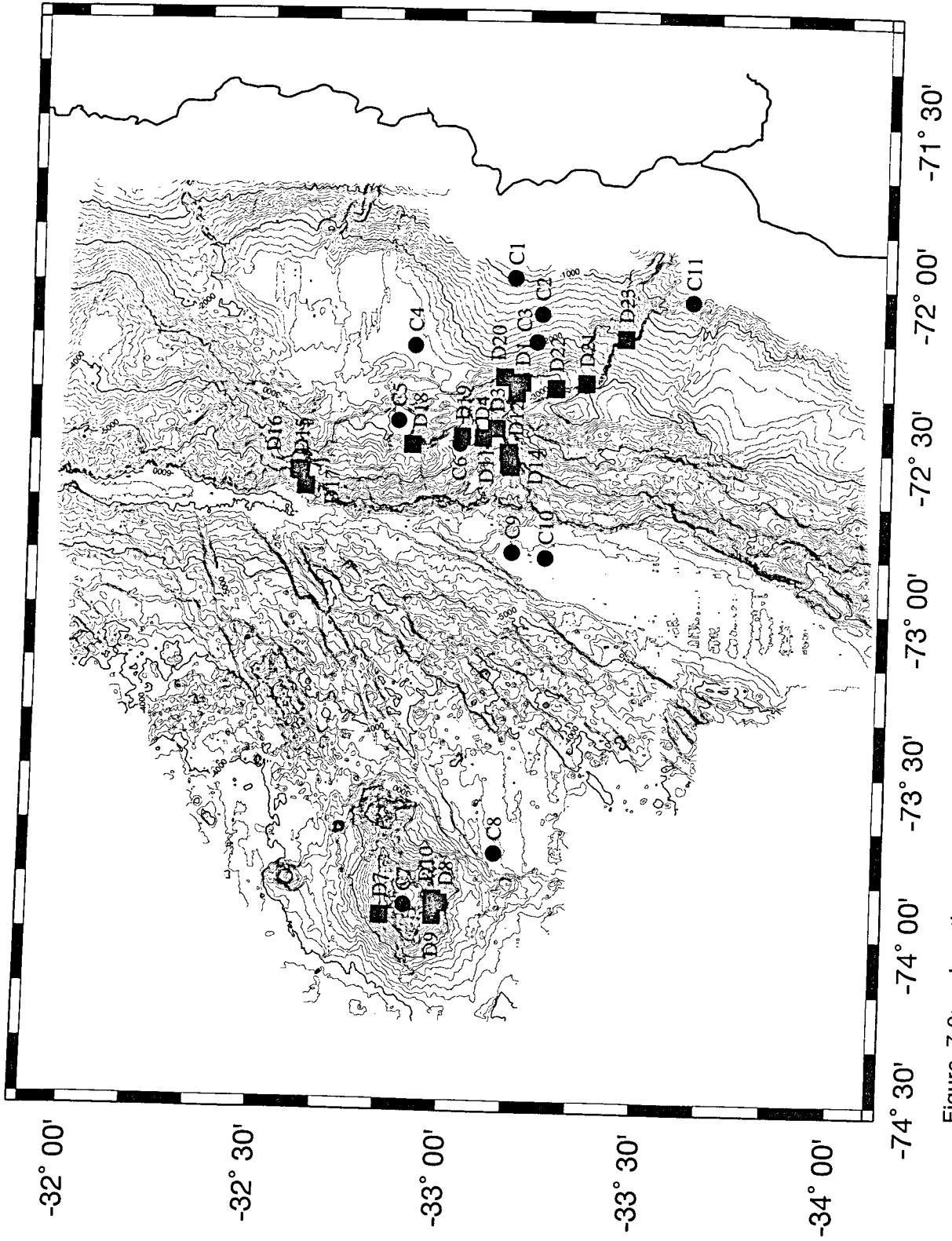


Figure 7.0: Location map of core and dredge sites.

Core Station	Latitude	Longitude	Waterdepth	Recovery
C 1-MUC	33°08,8' S	71°58,9' W	917 m	27 cm
C 1-SL			974 m	466 cm
C 2-MUC	33°13,1' S	72°05,2' W	1502 m	24 cm
C 2-SL			1497 m	412 cm
C 3-MUC	33°12,4' S	72°10,5' W	1983 m	27 cm
C 3-SL			1984 m	389 cm
C 4-MUC	32°53,4' S	72°11,5' W	2413 m	25 cm
C 4-SL			2411 m	917 cm
C 5-MUC	32°51,1' S	72°25,4' W	3029 m	30 cm
C 5-SL			3028 m	424 cm
C 6-SL	33°00,9' S	72°29,5' W	4077 m	538 cm
C 7-SL	32°53,9' S	73°54,6' W	432 m	0 cm
C 8-MUC	33°07,9' S	73°44,9' W	3620 m	12 cm
C 8-SL			3621 m	1025 cm
C 10-RC	33°07,9' S	72°50,3' W	5412 m	36 cm
C 11-SL	33°36,5' S	72°02,8' W	472 m	385 cm

Table 7.1

- One large core for foraminifers was cut into 1 cm slices. The surface was stained with bengal rose (GEOMAR, Spiegler).
- One small core for siliceous micro- and nannofossils was cut into 1 cm slices (GEOMAR, Locker).
- One large core for the investigation of dinoflagellate cysts was cut into 1 cm slices and refrigerated (GEOMAR, Biebow).
- One large and one small tube were frozen as archive cores (Geol. Bremen).
- From one of the large tubes the bottom water was sampled for stable isotope measurements (Geol. Bremen).

Water samples for stable isotope measurements were taken with the rosette at Station C 4 and C 6 (C14 Laboratory Kiel, Erlenkeuser).

The Reineck box-corer was used successfully at only one site (Site C 10) on the Chile Trench where the PARASOUND showed a 5 m thick hard reflector, indicative of a coarse sand layer. After a failed core, the box-corer recovered 36 cm of sediment with four 3 - 5 cm thick layers of coarse, dark sand.

The gravity-corer was used to obtain long sediment cores. Depending on the PARASOUND signal, a 6 m or a 12 m core barrel was used. The sediment cores were opened during the next leg by members of the Department of Marine Geology from the University of Bremen.

The sediment cores and the surface sediment samples recovered during CONDOR were acquired in a cooperative program related to the next leg, SONNE 102 (CHIPAL). The aim of the CHIPAL program is to reconstruct the paleoproductivity of the Chile/Peru Current during the late Quaternary. The relationship between this high-productivity area and global productivity changes during glacial to interglacial periods shall be investigated.

7.2 Rocks Recovered By Dredging

(E. Valenzuela, J. Corvalán, E. Morales, S. Kay)

Twenty-three dredge stations were occupied of which sixteen were in the San Antonio Canyon (D 1 - D 6A, D 11 - D 14, and D 18 - D 23). Four dredges (D 7 - D 10) were taken around the flanks of O'Higgins Guyot, and three dredges were made near the Papudo Magnetic Anomaly (D 15 - D 17). A map of the dredge station locations is shown in Figure 7.0. Coordinates and water depths at the dredge sites, and the recovery, are documented in Table 7.2 and in the Captain's Report (Appendix 2). Results of dredge recoveries are summarized in Table 7.3.

Dredge Station D-1

Recovery: Thirty-three well rounded Pliocene (Recent) clasts showing moderate sphericity. Six of them have tabular shapes. The fragments are:

1 clast of volcanic liharenite	3 %
20 clasts of porphyritic andesite	61 %
5 clasts of volcanic andesitic breccias	15 %
3 clasts of hornfels	9 %
3 clasts of diorite	9 %
1 clast of olivine basalt	3 %
Total 33 fragments	100 %

There are two size populations: big cobbles (25X21X11 cm) and smaller clasts (12X97 cm). All of them show very good roundness and moderate sphericity. The source area of the cobbles is presently found about 140 km eastward from the sample site. This means about 70 km inland of the coastal zone. Their most probable source are Mesozoic volcanic-sedimentary formations of Jurassic and/or Cretaceous age. Most cobbles have iron oxides on their surfaces, which suggests that there was no reworking along the canyon. The olivine basalt could be the only fragment of Tertiary age. These clasts were probably all from the floor of San Antonio Canyon.

Dredge Station D-2

Recovery: No clasts; only residuals of soft silty sand stuck on the dredge's teeth. The sandy fraction greater than $62,5 \mu$ is a quartz-feldspar (Oligoclase n 1.54) flaky sand with grains of angular shape. This suggests a relatively nearby source area of plutonic origin. The sand is Holocene in age and it contains forams (planktonic>benthic), other calcareous remains (echinoderm spines), arenaceous

Location of dredge samples, SO101-3

Dredge	From		To		Depth [m]		Duration
	Station	Latitude	Longitude	Latitude	Longitude	From	
D 1	33°10.3'	72°18.0'	33°10.6'	72°22.1'	3357	2400	2h 17min
D 2	33°09.5'	72°20.0'	33°09.8'	72°21.7'	3480	2480	1h 23min
D 3	33°06.5'	72°26.6'	33°07.1'	72°25.5'	4110	3197	1h 23min
D 4	33°04.5'	72°28.3'	33°03.1'	72°28.6'	4689	3776	1h 29min
D 5	33°08.7'	72°33.3'	33°09.9'	72°32.5'	5020	3849	1h 52min
D 6	33°08.9'	72°33.6'	33°08.9'	72°33.5'	4955	4902	1h 50min
D 6A	33°08.9'	72°33.6'	33°03.8'	72°32.2'	4685	3842	1h 30min
D 7	32°50.2'	73°56.6'	32°50.1'	73°56.8'	1889	2234	1h 50min
D 8	32°59.5'	73°54.1'	32°59.6'	73°54.3'	2124	2025	2h 00min
D 9	32°58.5'	73°56.5'	32°58.7'	73°56.4'	1975	2100	1h 36min
D 10	32°58.5'	73°53.5'	32°58.0'	73°53.7'	1935	1587	4h 16min
D 11	33°08.6'	72°31.4'	33°09.9'	72°32.5'	4887	3860	2h 20min
D 12	33°08.4'	72°31.0'	33°09.8'	72°31.6'	4903	3800	2h 20min
D 13	33°08.6'	72°33.3'	33°09.7'	72°32.3'	5073	3901	1h 50min
D 14	33°08.6'	72°33.3'	33°09.6'	72°32.5'	5026	3967	1h 25min
D 15	32°35.9'	72°35.0'	32°37.8'	72°33.5'	4961	3372	2h 24min
D 16	32°35.6'	72°34.7'	32°37.2'	72°33.2'	4974	3680	3h 00min
D 17	32°36.8'	72°37.7'	32°37.6'	72°36.8'	5210	4951	2h 30min
D 18	32°53.4'	72°29.8'	32°53.6'	72°28.2'	3424	2579	1h 23min
D 19	33°01.2'	72°28.2'	33°01.0'	72°25.3'	3999	2865	1h 56min
D 20	33°07.6'	72°17.1'	33°06.9'	72°16.1'	3282	2519	1h 18min
D 21	33°20.2'	72°18.0'	33°21.2'	72°19.0'	2411	1988	1h 29min
D 22	33°15.5'	72°19.0'	33°16.5'	72°19.6'	2811	2417	1h 20min
D 23	33°26.2'	72°09.7'	33°26.1'	72°10.7'	2049	1365	0h 48min

Table 7.2

Sample ID	Minerals & Rocks														Comments					
	Feldspar	Mica	Quartz	Amphibol	Pyroxene	Magnetite	Glass	Ash	Pellets	Mn & FeO coating	Sed. Breccia	Soft sediments	Hard Sediments	Volc. Breccia		Basalt	Andesite	Plutonic Rocks	Horofels	Organic & carbon
D 1														18	3	61	6	6		Rounded rock cobbles
D 2	A	A	F	S	R		A			R		A							S	Dredge's scraps of fine sand
D 3 gray	A	A	S	F					A			A	A		R					3 fragments of silty sand; barren
D 3 brown	F	A	S	F					A			A	A							Clayish silt; barren
D 4 gray	F	A	S		R	A			A				A							Silty sand
D 4 brown	F	A	S	S	R	A			A				A							Clayish silt
D 5 brown								85	A				A							Barren clayish silt
D 5 gray	R	A			5			75	F				A							Silty sand
D 6						A							A							Barren clayish silt
D 6 A	A	A	S	R				85					A							Silty sand & clyish silt
D 7													A							Silty sand & clyish silt
D 8							10				100									No sample in dredge
D 9										A					100					Indurated foram & ashy Ooze
D 10					F		15		A	a					80	a				Olivine basalt w/Mn coating
D 11	A	F			A	F	F		F										S	30 large rocks & lithic sand
D 12																				Dredge's scraps of silty sandstone
D 13	A	A			F	A	F	40					A							No sample in dredge
D 14 brown	A	A			A			85				100								A Silty sand & clyish silt
D 14 gray	R	A			A			70				100								Barren clayish siltstone
D 15												A								Sandy siltstone
D 16													A							A 32 sandy siltstone fragments
D 17		A								A			A							8 frags. very fine silty sandstone
D 18	A	A								A										A 89 frgmts. silty sandstone & clayish siltstone
D 19	A	A								A			A							Dredge's scraps of sand
D 20																				A Silty sandstone
D 21														A						No sample in dredge
D 22														A						60 hard rock cobbles
D 23														A						50 hard rock cobbles
																				A 250 kg, indurated silty sandstone

Table 7.3

species, diatoms and siliceous spines. Abundant nannofossils were observed on smear slide sections preserved in Canada balsam. The assemblage suggests a CCD below 3,300 m and upwelling currents chanelized along the submarine canyon.

Dredge Station D-3

Recovery: Three dark gray siltstone fragments with maximum long axis of 20 cm moderately rounded and slightly indurated.

The sandy fraction greater than $62,5 \mu$ consists of angular grains of feldspar (Oligoclase $n=1.54$), quartz and mica flakes. This mineralogic and textural pattern suggest a relatively nearby source rock of plutonic origin.

No microfossils were found on smear slides or in washed and sieved preparations. This lithology is quite similar to the basal layers of the Navidad Formation (middle to uppermost Miocene), described by Darwin (1843) at Los Goterones cliff, exposed along the coastal range south of San Antonio.

Dredge Station D-4

Recovery: Several fragments of two types of sediments: very dark gray siltstones and dark gray to brownish gray mudstones. Degree 7 compaction. The siltstone fragments show cleavage, slicken-slides and evidence of shearing. The mudstones are finely laminated and contain abundant Teredo-type boreholes, 1 to 8 mm in diameter, worm tracks, and sand filled worm tubes.

The sandy fraction greater than $62,5 \mu$ consists of angular grains of feldspar (Oligoclase $n=1.54$), quartz and mica flakes including rare glassy and basaltic grains plus pellet-like clusters of rhyolitic ash and pumice ($n<\text{balsam}$). The brownish sediment is a clayish silt made of $>80\%$ biotite rich ash, on agnetite and very few forams. The dark sediment is a silty sand of plutonic origin, with abundant dark minerals (biotite, magnetite, anfibol) and few light colored minerals (feldspat and quartz). This lithology is similar to that of the sediments recovered at the previous dredge station (D-3).

Dredge Station D-5

Recovery: Nine fragments with an average thickness of 5 cm and the following size data in cm for six of them: 5X12X15 - 5X12X7 - 3X6X7 - 3X4X8 - 3X5X8 - 3X5X7. The other three are smaller size fragments. They are dark gray and brown siltstones, with rather abundant mica and some glass. The sandy fraction greater than $62,5 \mu$, consists of angular grains of feldspar (Oligoclase $n=1.54$), quartz, mica flakes and magnetite including rare glassy and basaltic grains plus pellet-like clusters of rhyolitic ash and pumice ($n<\text{balsam}$). Both types of sediment were recovered in previous dredge stations (brown clayish silt and silty sand). The

mixing of these two components generate a third sandy ash type of sediment that in smear slides show rare radiolaria, diatoms, and abundant nannofossils, but do not contain foraminifera.

Dredge Station D-6

Recovery: Thirty fragments of indurated dark gray siltstones showing rounded and tabular shapes. The largest one is about 22 cm long and is pervaded by worm tubes up to 10 cm long and 0.6 cm in diameter. There was no sediment infilling the tubes. Other fragments are moderately rounded, with long and short axis of 11-8, 9-7, 8-5 and 8-4.5 cm. The remaining clasts are smaller. Most of them show an outer brown crust of approximately 5 cm in thickness and an inner gray core including sand size clasts (common), pyrite (frequent), rather abundant with mica, and a few pumice fragments.

The sandy fraction is similar to that of the sediments recovered in dredges D-4 and D-5. The brown clayish silt is barren but the silty sand includes several benthic and planktonic forams.

Dredge Station D-6A

Recovery: Eight fragments of sandy siltstone, dark gray in the center (core), becoming brownish to gray reddish outwards. Center probably contains more organic material. The larger fragments measure as follows: 17X13X4 cm - 17X9,5X3,5 cm - 7,5X4X3 cm - 18,5X11X4 cm and 10X7X4 cm. The general shape is therefore elongate and planar, suggesting a derivation from sedimentary beds, 4 to 3,5 cm thick, fractured and weathered to form incipient concretions.

The sandy fraction is similar to that of the sediments recovered in dredges D-4, D-5 and D-6. The brown clayish silt is barren but the silty sand includes several benthic and planktonic forams.

Dredge Station D-7

Recovery: No recovery.

Dredge Station D-8

Recovery: Three large fragments of white color, moderately indurated sediments, with the following dimensions: 30X15X13 cm - 55X15X18 cm - 25X14X10 cm; also two light gray to light greenish gray fragments measuring 9X8X4.5 cm and 7X4,5X3,5 cm. All the materials collected are composed of a moderately indurated foramineferal ooze. Some polychaete tubes up to 14 cm long and 2.5 cm in diameter also occur.

Petrographically, two types of sediments were recognized: Calcareous ooze and ash ooze. The former shows 100% planktonic and benthic forams, some of them coated with Mn or mixed with Mn micronodules. *Discoasteridae* on smear slides indicate a Pliocene age. The ash ooze consists of rhyolite volcanic ash (n<balsam), and abundant planktonic forams.

Dredge Station D-9

Recovery: Three fragments with the following dimensions: 15,8X9X12 cm - 8,5X5X3 cm and 10X9X4,5 cm. Correspond to a volcanic rock, probably a very altered basalt, gray-reddish color, with irregular manganese crust up to 0.4 cm thick. The core of the first fragment show fissility in 3 mm thick layers.

Dredge Station D-10

Recovery: About 30 large and smaller samples relatively fresh to altered.

1) A preliminary inspection of the materials collected allowed the identification of the following lithologies:

Obsidian vesicular black glass

Aphanitic lava showing fissility in 3 mm thick layers

Lava, altered rim 1,5 cm thick. Core with 20% phenocrysts 2 mm long

Sedimentary breccia: Sandy matrix containing abundant bryozoa and other shell fragments; larger clasts are angular fragments of vesicular, porphyritic lava (altered and fresh)

Vesicular lava with phosphatic(?) coating

Porphyritic olivine basalt

Vesicular scoriaceous lava

Mn coated porphyritic basalt

Fragments of possible pillows, with an outer Mn layer 2 mm thick and inner obsidian layer 6 mm thick. The porphyritic outer core is 7 cm thick and the inner scoriaceous core is 5 cm thick.

2) Further megascopic observations were made to identify and characterize each fragment. These were given correlative numbers. Most individual fragments were broken into smaller pieces for which the size was expressed according to the following scale:

very large	> 30 cm
large	> 20 cm
medium	> 10 cm
small	< 10 cm

3) Most rocks are massive to vesicular, porphyritic (olivine and plagioclase) mafic volcanic rocks. Limonite and very thin to 2 cm thick Mn coating are common. Vesicles fillings are Fe-oxide, hydroxide and zeolite.

4) Individual samples were preliminary identified as follows:

D10-1 highly altered porphyritic vesicular to slightly vesicular basalt coated with limonite; vesicle fillings (zeolitic) in upper part, 0.3 cm coating of Mg

25X18X10 cm - broken into 3 subequal pieces

D10-2 altered, porphyritic vesicular to massive basalt, relatively sharp boundary between massive and vesicular parts; vesicles filled in upper part; chilled margin; part of pillow

22X18X16 cm - broken into 3 subequal pieces

D10-3 variably altered to relatively fresh (?) massive mafic lava; limonite coating; in places Mn coating up to 0.25 cm thick

22X18X16 cm - broken into two larger and several smaller pieces

D10-4 altered vesicular basalt, could be a pillow; thin Mn coating; very large vesicles contain soft pelagic sediment

30X22X16 cm - broken into two large and two smaller pieces

D10-5 massive porphyritic (plagioclase and olivine - about 0.5 cm across, partially altered) basalt; Mn coating up to 1 cm, botryoidal in part. One of best samples for dating and chemistry.

26X14X14 cm - broken into two large and two medium size pieces

D10-6 altered vesicular basalt, vesicles partially filled

16X12X12 cm - broken into 2 large and 2 small pieces

D10-7 relatively fresh, massive (most of sample) to vesicular porphyritic (plagioclase and olivine, partially altered) basalt; Mn coating up to 1.5 to 2 cm thick and somewhat undulose due to large botryoids. One of the best samples for chemistry and dating

26X14X14 cm

D10-8 altered vesicular basaltic pillow; limonite coating

30X20X18 cm

D10-9 altered vesicular to massive porphyritic basalt with fine Mn coating; cavity containing botryoidal shaped forms, irregular limonite coating

20X10X10 cm

D10-10 irregularly altered vesicular to relatively massive porphyritic basalt; chilled margin; pillow fragment

28X15X10

D10-11 highly altered vesicular to somewhat massive basalt; some vesicles filled with limonite and zeolite

21X15X15 cm, broken into 1 medium and 3 small fragments

D10-12 altered porphyric vesicular to somewhat massive basalt; 1 to 2 mm coating of Mn

12X14X18

D10-13 very altered porphyric, amygdaloidal basalt; limonite coating in vesicle

14X6X6 cm, broken into 3 small pieces

D10-14 altered porphyric, basalt with large vesicles coated with limonite and zeolites; thick limonite coating

X15X16 cm

D10-15 very altered porphyric slightly vesicular basalt with thin Mn coating

18X12X10 cm

D10-16 altered porphyric vesicular to slightly vesicular basalt; zeolites in vesicles, irregular limonite coating

14X12X8 cm

D10-17 very altered porphyric vesicular basalt; limonite and patchy thin Mn coating

10X10X10 cm

D10-18 variably altered massive porphyric (partially altered plagioclase prominent) basalt, quite vitreous in one layer near rim; limonite and patchy 0.1 cm Mn coating

14X7X5 cm, broken into 3 small pieces

D10-19 altered porphyric (altered plagioclase) vesicular basalt, limonite coated

19X12X5 cm

D10-20 very altered, porphyric vesicular basalt, vesicles filled with zeolite

15X8X6 cm, broken into 4 pieces and assorted small fragments

D10-21 rounded massive porphyric basalt; 1 cm thick limonite coating

9X3X3 cm, broken into 3 small fragments

D10-22a to D10-22d altered porphyric vesicular to slightly vesicular basalt fragments; limonite in vesicles. Four macroscopically similar fragments from dredge basket

each about 10X5X5 cm

D10-23 Sedimentary breccia with carbonate and volcanic fragments; volcanic fragments are angular fresh basalt to more rounded highly oxidized, red vesicular basalt, up to 8 cm across; most are 2 to 5 cm across; matrix is light gray, pelagic(?) mud

30X10X18 cm to Chilean SERNAGEOMIN museum

D10-24 very altered basaltic block with limonite, irregular Mn coating

0X23X15 cm to Chilean SERNAGEOMIN museum

D10-25 altered porphyric massive basalt

10X6X5 cm

D10-26 three separate pieces of platy aphyric mafic volcanic rock

A - flat piece 12X7X1,5 cm

B - 8X3X3 cm

C - 3X2X2 cm

D10-27 altered porphyric vesicular basalt, limonite coating

6X6X4 cm

D10-28 altered porphyric vesicular basalt; large vesicles; limonite coating

7X4X4 cm

Dredge Station D-11

Recovery: Only a very small amount of very dark gray clay in the dredge

Dredge Station D-12

Recovery: No recovery

Dredge Station D-13

Recovery: Twenty-seven rounded fragments, very dark gray to medium brown. The larger, with major axis of 33, 22 & 18 cm are of very dark gray siltstone with frequent black, carbonaceous patches. Other fragments with longer axis of 13, 11, 11 and 12 cm, are very fine sandstone to sandy siltstone, light to medium brown, with abundant worm tubes. Both sediments have a degree of compaction of about 8 (7,5). They contain frequent grains of mica. The dark gray siltstone is fractured.

About 20 other smaller fragments are of both types of sediments. In some of them the contact between the two layers is well defined. One sample of the brownish very fine grained sandstones shows incipient tabular cross-lamination. The very dark gray siltstone contains small clast of the brownish sandstones previously recovered.

Dredge Station D-14

Recovery: One fragment of brownish sandy siltstone to very fine-grained sandstone, well indurated (compaction 8). Good stratification planes, separate one bed 2,8 cm thick. Size of the fragment: 18X15X4 cm. Another fragment of about 4 cm is a very dark gray siltstone with mica grains.

Dredge Station D-15

Recovery: Thirty rock fragments up to 12 cm diameter. They are of a) very dark gray siltstone, strongly fractured, with conchoidal fracture; b) fine- to medium-grained sandstone, medium gray to greenish gray; contact with siltstone planar; in

part channel sandstone; and c) very dark to gray siltstone with small carbonaceous (?) fragments.

Dredge Station D-16

Recovery: Eight rock samples. Very fine grained sandstone medium to dark gray, thin stratification, similar to that of Dredge D-15.

Dredge Station D-17

Recovery: Eighty-nine fragments up to 10-20 cm in diameter. About 80% of them are of fine to medium and medium- to coarse-grained, gray-greenish sandstones, the rest are brownish siltstones and one of volcanic rock (andesite ?) medium gray aphanitic groundmass with few small phenocrysts (whole rock dating ?). Sediments show thin stratification, diachlases, conchoidal fracture, abundant worm tubes and Mn and FeO coatings.

Dredge Station D-18

Recovery: Dredge teeth coated with brownish and greenish silt.

Dredge Station D-19

Recovery: Thirty-one fragments. Most of them are greenish dark silty sandstone to medium-grained sandstones, Mn and FeO coated, with worm tubes 1 cm Δ and 6,5 cm length.

2 clasts of medium gray aphanitic (volcanic ?) rock, strongly fractured (whole rock dating ?).

Dredge Station D-20

Recovery: No recovery.

Dredge Station D-21

Recovery: Sixty rock samples ranging in size from 21X12,5X6 cm to 6X4,5X2,5 cm (Rio Maipo Recent cobbles). All of them show very good roundness and moderate sphericity. Plutonic and volcanic cobbles of andesite, diorite volcanic breccia and Ocoite. Dredge also recovered reddish-brown muds, similar to Dredge 17.

Dredge Station D-22

Recovery: About 400 kg mostly of mud, with large blocks of sediments and 50 lithic clasts of the Maipo River that range in size from 20X13X11 cm to 4X3X2,5 cm. The predominant sediment is a medium brown to reddish mudstone (with microfossils). Some fragments are fractured and show slickensides. Also very dark gray mudstones.

Dredge Station D-23

Recovery: About 250 kg of slightly indurated sandstones in big slabs of 50X20X12 cm plus several smaller fragments (1 King crab).

7.3 Foraminifers of core and dredge samples

(D. Spiegler)

Planktonic foraminifers indicate the age of the sediment samples and the surface temperature of the former environment. Benthic foraminifers indicate the environment and sometimes also the age.

At each coring site two samples were analyzed: the surface sample, taken from the top of a the multicorer tube (MUC), and the core-catcher sample (CC) taken from the lowermost part of the sequence cored with the gravity corer (Table 7.4). Furthermore, all different dredged sediments were analyzed (Table 7.5).

The preparation methods used to obtain foraminifers were the standard techniques: briefly, the samples were soaked in diluted H₂O₂ solution, washed over a 63 nm screen, dried and the fossils were separated under the binocular microscope.

In the range charts the abundances are categorized as A = abundant, more than 25 specimens; C = common, 5-24 specimens; R = rare, less than 5; and B = barren. The state of preservation of foraminifers is described as follows: G = good; M = moderate, signs of fragmentation, overgrowth and/or dissolution; P = poor, severe fragmentation, heavy overgrowth and/or dissolution. The ratio of planktonic/benthic foraminifers were calculated.

A close relationship exists between the Recent faunal provinces of the plankton communities and the major hydrographic regions. The area under investigation lies in the Southern Transitional Zone, that separates the cold-water Subantarctic Planktonic Faunal Province from the warm-water Subtropical Region (Be, 1977). The dominant indigenous species of planktonic foraminifers of the Transitional Zone is *Globoconella inflata*.

Globoconella inflata is common in the core samples investigated, except the surface samples at Site C4, C5, C8, and C10. *Neogloboquadrina dutertrei*, *Globigerina apertura*, and *Globigerina bulloides* indicate together with the rare subtropical/tropical species *Globorotalia theyeri*, *Gl. tumida*, *Gl. hirsuta*, *Globigerinoides ruber*, *Globigerinella aequilateralis*, and *Globorotaloides hexagona* a distinct warm-water influence into the Planktonic Transitional Faunal Province.

Truncorotalia truncatulinoides is indicative for Quaternary sediments, *Truncorotalia tosaensis* for Pliocene sediments.

Table 7.4 shows the occurrence of selected planktonic foraminifers, abyssal benthic foraminifers, redeposited benthic shelf foraminifers, agglutinated foraminifers, and ostracods. All samples, except Sample SL C1-CC, are Quaternary in age and indicative for warm temperate surface temperatures. The Pliocene sediment may be reworked. Reworking is also observed in the surface samples of Sites C1, C2, and C3.

Table 7.5 documents the occurrence of planktonic and benthic foraminifers in the samples taken from the different dredge profiles. Dredge profile D 1 - D 6, and D 11 - D 23 were taken in the San Antonia Canyon. The samples of the Dredge profiles D 7 - D 10 comes from the O' Higgins Seamount.

Dredge D-1: No sediment was in the dredge.

Dredge D-2: Six samples of geyish silt were analyzed, taken from the teeth of the dredge. Two samples contain *Truncorotalia truncatulinoides* with the stratigraphical distribution of early Pleistocene to Recent. The occurrence of *Globorotalia theyeri* and *Pullenia primalis* indicate tropical/subtropical conditions. *Melonis pompilioides* is common in abyssal depths. The sample of brown silt was barren of foraminifers.

Dredge D-3: Two samples of siltstone were analyzed. Both contain no foraminifers.

Dredge D-4: Four samples were analyzed. Only one from the greyish siltstone contains rare foraminifers with poor preservation. Whereas *Globigerinita glutinata* has a stratigraphic range from Late Oligocene to Recent, the first occurrence of *Globorotalia scitula* indicates the base of Middle Miocene. Both taxa indicate temperate surface conditions. The benthic foraminifer *Cibicidoides trinitatensis* determined Miocene age and middle bathyal depth (Resig, 1990).

Dredge D-5: Five samples were analyzed, all barren in foraminifers.

Dredge D-6: Two samples were analyzed. Sample D 6 S1 came from the grey siltstone and contained common foraminifers. *Truncorotalia truncatulinoides* indicates early Pleistocene to Recent in age. *Melonis pompilioides* indicates lower

abyssal depth. The common occurrence of *Globoconella inflata* and the lack of *Neogloboquadrina dutertrei* indicate temperate surface-water.

Dredge D-6A: One sample of grey siltstone contains a poor assemblage of benthic foraminifers, indicating abyssal conditions. But *Buliminella elegantissima* and *Nonionella auris* are outer shelf species (Resig, 1990) and may be displaced. No age diagnostic taxa were observed.

Dredge D-7: No recovery

Dredge D-8: Three samples were analyzed, two from a white biogenic chalk, and one of a grey tuffite. The latter contains a poor assemblage with no age diagnostic taxa. The content of the other two samples is summarized in Table 7.4. The co-occurrence of *Globigerinoides ruber*, *G. extremus*, and *Globorotalia crassaformis* indicate Pliocene in subtropical conditions. Abyssal benthic taxa were not observed. Therefore, the chalk seems to be originated under subtropical neritic conditions.

Dredge D-9: No sediment

Dredge D-10: Three small samples of sediment, partly covering cavings in the volcanic rocks, were analyzed. *Truncorotalia tosaensis* together with *Globoconella inflata* indicate Upper Pliocene age. *Globoconella inflata* characterized Transitional watermasses. *Globorotaloides hexagonus* is typically in the tropical to subtropical Neogene Pacific. *Pullenia bulloides* indicates abyssal depth.

Dredge D-11: Two samples of grey silt were analyzed, taken from the teeth of the dredge. Both samples contain high amounts of crystalline material and volcanic glass. Foraminifers are rare and poor preserved. The small and juvenile planktonic foraminifers have no age diagnostic value. Most of the benthics are redeposited.

Dredge D-12: No recovery

Dredge D-13: Three samples of siltstone were analyzed. One was empty. The other two contained a small amount of non-age diagnostic foraminifers. *Cibicidoides wuellerstorfi* in Sample D13-S1 indicates abyssal depth, and an age younger than middle Miocene.

Dredge D-14: Two samples of grey and brown siltstone were analyzed. The brown siltstone was barren in foraminifers. The grey siltstone contained small numbers of juvenile *Globigerina* sp.

Dredge D-15: Five samples of lesser durated siltstones were analyzed. Samples D 15-S 1, -S 3, and -S 4 contained rare foraminifers. They are fragmented and heavily corroded, indicating slumping and reworking processes. Most of them are benthic shelf species Quaternary in age as *Nonionella auris*, *Buliminella elegantissima*, *Bulimina pulchella*, *Elphidium* sp., *Bucella peruviana*, *Bolivina costata*, and *Pyrgo* sp. *Orbulina universa* and small *Neogloboquadrina* sp. are the planktonic species. Sample D15-S 2 contains rare *Cassidulina laevigata* and *Globigerina* sp. in good preservation. Sample D 15-S 5 was barren in foraminifers.

Dredge D-16: The analyzed sample of brown siltstone was barren in foraminifers.

Dredge D-17: Two samples of brownish grey siltstones were analyzed. The abundance of foraminifers was rare and the preservation was poor. Small *Neogloboquadrina pachyderma* sinistral coiling form, and *Globorotalia crassaformis* were observed, indicating Quaternary in age and cold-temperate conditions.

Dredge D-18: The soft grey ooze of two samples was taken from the teeth of the dredge. The rich foraminiferal assemblages indicate Quaternary aged sediment in subtropical conditions. The third sample came from a brown siltstone and contains few *Neogloboquadrina pachyderma* dextral coiling form, indicative for Quaternary age in temperate condition.

Dredge D-19: Seven samples were analyzed; four (No 1 - 4) taken from the teeth of the dredge, and three (No 5 -7) taken from the dredge itself. The green clay of Sample D 19-S 1 contains a foraminiferal assemblage indicative for abyssal depth, and subtropical Quaternary age. The brown clay of Sample D 19-S 3 shows a poor fauna of abyssal Quaternary. Sample D 19-S 5 comes from a green-grey siltstone containing high amounts of different eruptiva, and only one specimen of *Globorotalia crassaformis*, indicative for Pliocene to Recent in age, and one juvenile *Globigerina* sp. The other samples contain no foraminifers.

Dredge D-20: No recovery

Dredge D-21: Silty mud contain a rich and well preserved foraminiferal association Quaternary in age and subtropical to warm-temperate condition.

Dredge D-22: Two samples of grey siltstone were analyzed. Both contain rich benthic associations typically for abyssal depth. The rare plankton foraminifers indicate Quaternary in age.

Dredge D-23: The dredged dark siltstone contain *Chilostomella ovoidea*, *Nodogenerina adolphina*. together with *Orthomorphina* cf. *consobrina* . Schönfeld & Spiegler (1995) described such an assemblage at ODP Site 141-861 (Chile Triple Junction) as *Orthomorphina* cf. *consobrina* Partial Range Zone. The age ranges from 1.2 Ma, early Quaternary to Pliocene.

SO 101/3 Core Samples	Abundance		PF%	Taxa																Age						
	P	G		<i>Truncorotalia truncatulinoides</i>	<i>Truncorotalia tosaensis</i>	<i>Neogloboquadrina dutertrei</i>	<i>Neogloboquadrina acostaensis</i>	<i>Orbulina universa</i>	<i>Globigerina apertura</i>	<i>Globorotalia scitula</i>	<i>Globorotalia theyeri</i>	<i>Globorotalia crassaformis</i>	<i>Globorotalia tumida</i>	<i>Globigerina bulloides</i>	<i>Globigerinoides ruber</i>	<i>Globocornella inflata</i>	<i>Globorotalia hirtuta</i>	<i>Globigerinita glutinata</i>	<i>Globigerinella aequilateralis</i>		<i>Globorotaloides hexagona</i>	Abyssal benthic foraminifers	Shelf benthic foraminifers	Ostracods	Agglutinated foraminifers	
MUC-C 1-surface	C	G	80	R		A	C	C	C		R	C		C		C		R				*		C	Quaternary	
SL-C 1-CC	C	G	80		(R)		C		R	R	R		C		C		R	R						R	Pliocene ?	
MUC-C 2-surface	A	G	50			A	C	R	R				R		C		R					*		R	Quaternary	
SL-C 2-CC	A	M	99	R		R	A	R	A	R		A	R		A		R	R						R	Quaternary	
MUC-C 3-surface	C	G	60			C	C	R				R	C		C						#	*		C	Quaternary	
SL-C 3-CC	C	G	80	R					C		R		C		C						#			R	C	Quaternary
MUC-C 4-surface	A	G	90	R		A	R	R	R	R	R	C		R			R				#			R	R	Quaternary
SL-C 4-CC	A	G	90	R				R	C	R					C						#			R	C	Quaternary
MUC-C 5-surface	C	G	90			A	R	R	R			R		R			R	R	R		#					Quaternary
SL-C 5-CC	C	G	90	R		R			C	R		R				A	R				#					Quaternary
SL-C 6-CC	A	G	99	R		A	C	C	C	R				C		C			R	R	#					Quaternary
SL-C 7-outside	C	G	95	R		C		R		R		R	R		R	R			R	R						Quaternary
SL-C 7-CC	A	G	99	R		A		R							R				R							Quaternary
MUC-C 8-surface	C	M	90			C	R	R		R		R		R		R					#			R		Quaternary
SL-C 8-CC	C	G	90			R		R	C	R		R		R		C					#					Quaternary
RC-C 10-surface	C	M	80			R		R	R	R				R							#					Quaternary
SL-C 11-CC	A	G	90			R	R	R	R	R				A		A								R		Quaternary

Table 7.4

7.4 Siliceous microfossils of core samples and calcareous nannofossils of dredge samples

(S. Locker)

The siliceous microfossil and calcareous nannofossil content was estimated both in core and dredge samples. Core samples were then studied for siliceous flagellates and radiolarians (Table 7.6) and dredge samples for calcareous nannofossils (Table 7.7).

Samples were examined on smear slides prepared from soft and indurated sediment. Group abundances were quantified as follows: T = traces, <1% of coverage per view field of the microscope; R = rare, 1-5% of coverage; F = few, 6-15%; C = common, 16-50%; A = >50%.

Species abundances of siliceous microfossils were indicated only by a cross in Table 7.6 because coarser particles are under represented in smear slides. Species abundances of calcareous nannofossils were estimated in relation to other species in Table 7.7 and indicated with the same letters as in groups. It should be noted that foraminifers are excluded from the smear slide analyses and they are reported in Chapter 7.3.

Core samples. Eighteen sediment samples from 11 core sites on the continental shelf, the O'Higgins Seamount area, and the Chile Trench (Fig. 7.0) were analyzed for microfossil content. Siliceous flagellates and radiolarians were used to indicate certain environmental conditions for the assemblages recovered. The results are summarized in Table 7.6.

The assemblages of siliceous flagellates contain only four taxa. The *Dictyocha* subspecies generally indicate warmer surface-water conditions, the *Actiniscus* and *Distephanus* species cooler conditions.

Several assemblages of radiolarians are characterized by a set of cool adapted deep-water taxa (Schroeder-Ritzrau, 1995), i.e. *Artostrobus annulatus*, *Botryostrobos auritus/astralis*, *Cornutella profunda*, and *Lirella* sp. Subpolar surface-water species are represented by *Actinomma* cf. *borealis*, *Lithomitra lineata* and *Spongotrochus glacialis*. Transitional to subtropical surface-water species are indicated by *Androcyclas* cf. *gamphonycha*, *Pterocorys zancleus*, *Rhopalodictyum* sp.,

and *Stylodictya* sp. The distinct co-occurrence of all these species points to the complex vertical structure of water masses in the area. The cool surface-water masses of the Chile Current along the continental shelf provided *Lithelius spiralis* (Molina-Cruz, 1977) and the subpolar species indicated. Sporadic incursions of warmer water masses carried transitional or subtropical species from the central Pacific toward the coast. Deep-water species settled from relatively cool deep-water layers.

Dredge samples. Fifty-three sediment samples from 23 dredge profiles over the continental slope, the San Antonio Canyon, and the flanks of the O'Higgins Guyot (Fig. 7.0) were analyzed for their microfossil content. Calcareous nannoplankton species were used to determine the age of sediment samples. Age determinations were based on the middle to high latitude nannoplankton zonation of Martini (NN-Zones, 1971) and the low to middle latitude zonation of Okada and Bukry (CN-Zones, 1980), respectively. The taxonomy and stratigraphic ranges of species follow mainly Perch-Nielsen (1980). The results are summarized in Table 7.7.

Siliceous microfossils such as diatoms, silicoflagellates, radiolarians, and sponge spicules are rare or very rare in dredge samples. Diatoms and radiolarians are predominantly present as fragments or corrosional remnants, seldom as valves or skeletons. Sponge spicules are mainly preserved as monaxonal fragments.

Dredge D-2: Seven samples of silty clay taken from the teeth of dredge were analyzed. Calcareous nannofossil assemblages are diverse and are probably all Quaternary in age. *Gephyrocapsa oceanica* indicates upper Zone NN19 of Martini (1971) or Zone CN14a of Okada and Bukry (1980), or a younger level. *Helicosphaera carteri* and some *Pontosphaera* species hint at temperate surface-water conditions.

Dredge D-3: Two samples of siltstone were checked. Only a few siliceous microfossils were found.

Dredge D-4: Five samples of siltstone were investigated. Two samples were barren of calcareous nannofossils, but three samples yielded Miocene nannofossil assemblages. *Cyclicargolithus floridanus* and *Calcidiscus macintyreii* indicate Zone NN6 or Zone CN5a, or an older level.

Dredge D-5: Four samples of siltstone were analyzed. Three samples contain rare siliceous microfossils but two also calcareous nannofossils of Quaternary age. Common specimens of small *Gephyrocapsa* species prove lower Zone NN19 or Zone

CN13, or an older level. *Helicosphaera kamptneri* and some *Pontosphaera* species indicate temperate surface-water conditions.

Dredge D-6 and D-6A: Two samples of siltstone were studied. Sample D6-S1 comprises rare siliceous microfossils but common calcareous nannofossils. Sample D6A-S1 contains rare siliceous as well as calcareous micro- and nannofossils. Both samples include *Gephyrocapsa oceanica*, which suggests upper Zone NN19 or Zone CN14a, or a younger level.

Dredge D-8: Two samples were analyzed, one from a white chalk and one from a grey tuffite. No biosiliceous particles were found but calcareous nannofossils are in great abundance. Calcareous nannofossil assemblages are composed of abundant specimens of small *Reticulofenestra* species and of several *Discoaster* species. *Discoaster asymmetricus*, *D. tamalis*, *D. triradiatus*, and *D. variabilis* indicate a Pliocene age, i.e. upper Zone NN15 to lower Zone NN16 or Zones CN11b/CN12a. The great number of *Discoaster* species is evidence for subtropical surface-water conditions.

Dredge D-10: Four samples of silty clay taken from cavities inside and outside the volcanic rocks were investigated. Two samples were barren of calcareous nannofossils but two samples yielded common to abundant specimens. Sample D10-S3 contains *Discoaster brouweri* and *D. decorus* and can thus be placed into Pliocene Zones NN15/NN16 or Zones CN11b/CN12a. Both these *Discoaster* species and *Helicosphaera kamptneri* suggest subtropical surface-water conditions. Sample D10-S4 contains *Gephyrocapsa oceanica*, which is diagnostic for upper Zone NN19 or Zone CN14a, or a younger Quaternary level.

Dredge D-11: Two samples of silty clay were studied. Calcareous nannofossil assemblages comprise *Gephyrocapsa oceanica*, which indicates upper Zone NN19 or Zone CN14a, or a younger Quaternary level.

Dredge D-13: One sample of siltstone was checked. Calcareous nannofossils include *Gephyrocapsa oceanica* and *Pseudoemiliania lacunosa*, which indicates upper Zone NN19 or Zone CN14a.

Dredge D-14: Two samples of siltstone were investigated. Sample D14-S1 contains rare calcareous nannofossils. Trace occurrences of small *Gephyrocapsa* species suggest lower Zone NN19 or Zone CN13, or an older level.

Dredge D-15: Five samples of siltstone were analyzed. All samples were barren of siliceous microfossils, but two samples yielded poor nannofossil assemblages. Trace occurrences of *Gephyrocapsa oceanica* indicate upper Zone NN19 or Zone CN14a, or a younger Quaternary level.

Dredge D-16: One sample of siltstone was checked. Traces of siliceous and calcareous micro- and nannofossils are recognized but enable only a rough age determination, i.e. Neogene to Quaternary.

Dredge D-17: Two samples of siltstone were studied. Sample D17-S2 contains rare but distinct occurrences of *Pseudoemiliana lacunosa*, which is diagnostic for Zone NN19 or Zone CN13/CN14a, or an older level.

Dredge D-18: Two samples of a grey ooze taken from the teeth of dredge provided abundant calcareous nannofossils. *Gephyrocapsa oceanica* indicates upper Zone NN19 or Zone CN14a, or a younger Quaternary level. Although *Reticulofenestra* cf. *minutula* has common occurrences, the co-occurrence of *Helicosphaera kamptneri* and *Pontosphaera* species probably indicate temperate surface-water conditions.

Dredge D-19: Two of three soft sediment samples taken from the teeth of dredge yielded calcareous nannofossils. Four samples of siltstone taken from inside the dredge remained barren of nannofossils. Occurrences of *Gephyrocapsa* species indicate a Quaternary age for both the above samples.

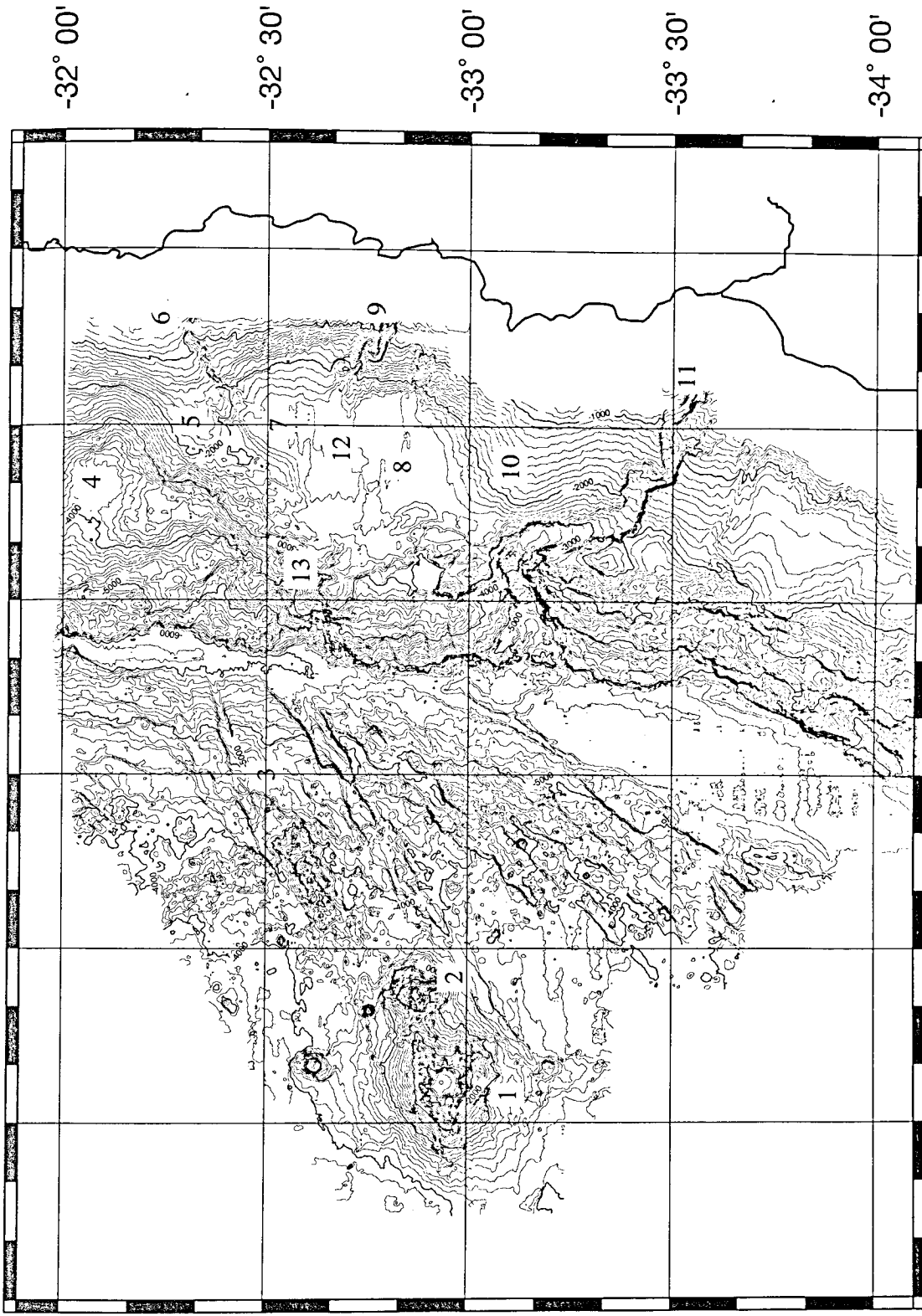
Dredge D-21: Two samples of silty clay were investigated. Both samples contain *Gephyrocapsa* species and can be placed into the Quaternary.

Dredge D-22: One sample of a grey siltstone was checked for nannofossils. Some poorly preserved coccoliths suggest a Quaternary age.

Dredge D-23: One sample of a siltstone provided abundant nannofossils. The distinct occurrence of *Gephyrocapsa oceanica* indicates upper Zone NN19 or Zone CN14a, or a younger Quaternary level.

APPENDICES

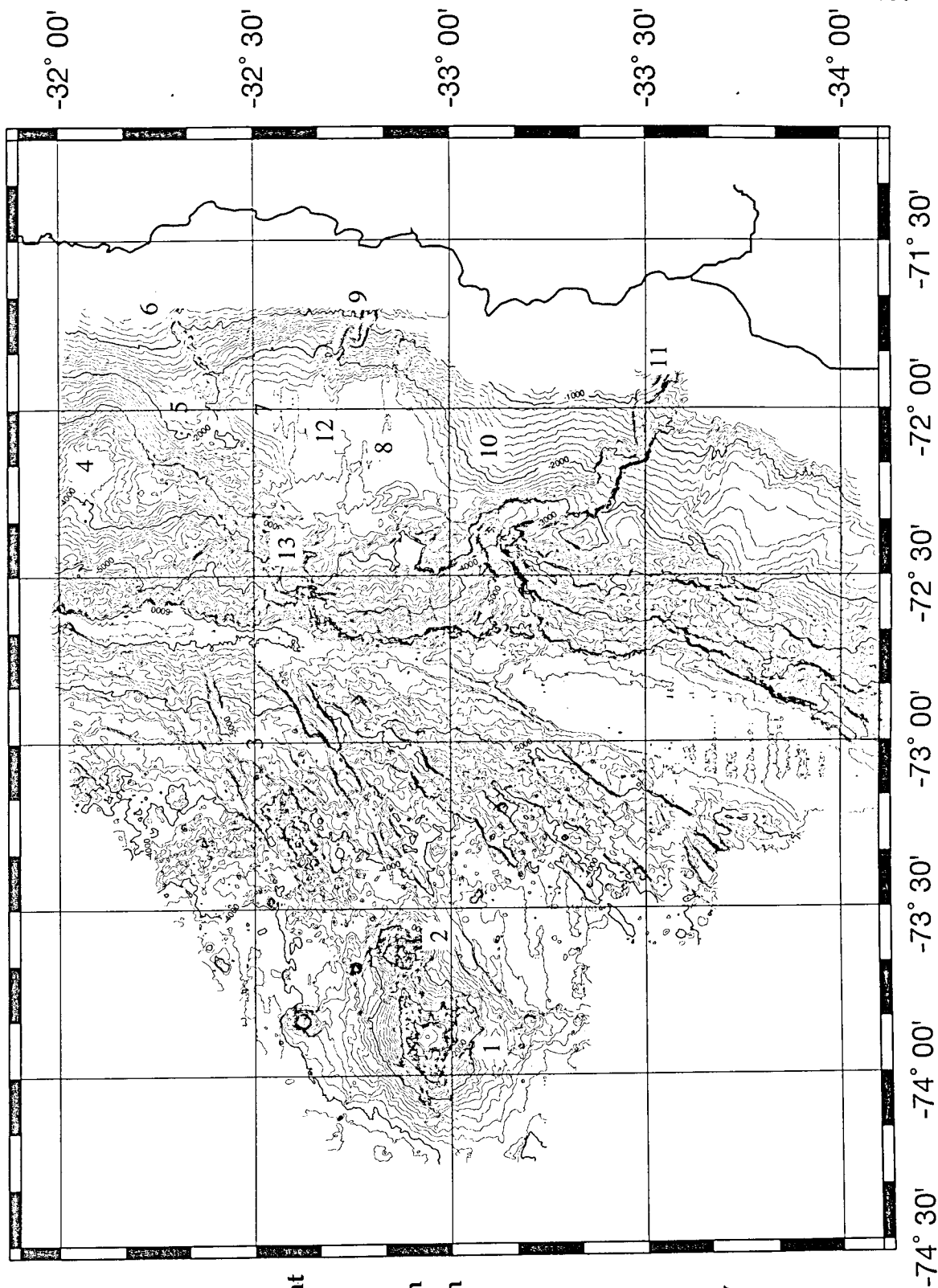
APPENDIX 1
Geographic names in this report



- 1 O'Higgins Guyot
- 2 O'Higgins Seamount
- 3 O'Higgins zone of fractures (OFZ)
- 4 Pta. Salinas Embayment
- 5 Pta. Salinas Ridge
- 6 La Liguria Canyon
- 7 Valparaiso Basin North
- 8 Valparaiso Basin South
- 7 & 8 collectively are Valparaiso Basin
- 9 Aconcagua Canyon
- 10 Topocalma Knoll
- 11 San Antonio Canyon
- 12 Montemar Ridge
- 13 Papudo mag. anomaly

APPENDIX 1
Geographic names in this report

- 1 O'Higgins Guyot
- 2 O'Higgins Seamount
- 3 O'Higgins zone of fractures (OFZ)
- 4 Pta. Salinas Embayment
- 5 Pta. Salinas Ridge
- 6 La Ligua Canyon
- 7 Valparaiso Basin North
- 8 Valparaiso Basin South
- 7 & 8 collectively are Valparaiso Basin
- 9 Aconcagua Canyon
- 10 Topocalma Knoll
- 11 San Antonio Canyon
- 12 Montemar Ridge
- 13 Papudo mag. anomaly



Anhang zum Kapitnsbericht 04/95 Reise SO 101/2

Der Fahrtabschnitt SO 101/2 war der seismischen Vermessung des Condor-Gebietes vorbehalten.

Noch im Hafen wurde die Seismik aufgebaut. Als das Schiff am 12.04.95 um 13.05 Uhr die Position fr das erste Seismikprofil erreichte konnte der Streamer und das Airgun-Array zu Wasser gebracht werden. Das Geschirr war um 13.40 Uhr ausgesetzt und erste Probeschsse konnten getriggert werden. Um 14.12 Uhr begannen wir mit der Profifahrt.

Die seismische Profile beendeten wir am 22.04.95 um 17.05 Uhr. Wir hatten auf insgesamt 38 Profilen 994 Seemeilen seismische Vermessungen absolviert.

Auf weiteren 19 Profilen mit 349 Seemeilen wurde neben dem Hydrosp sweep und Paradigma nur das Magnetometer eingesetzt.

Die wissenschaftlichen Vermessungsarbeiten beendeten wir am 23.04.95 um 13.12 Uhr.

Im Verlauf der Reise trafen wir neben einer stndigen SW'lichen Dnung vor allem SW'liche Winde an. Die maximale Windstrke lag bei Bft. 7. An Tagen mit N'lichen oder umlaufenden Winden betrug die Windstrke nur 1-2 Bft.



12.04.1995

Zeit: UTC - 4h

13:05 Beginn der Arbeiten zu wissenschaftlichen Messungen.
 13:40 Streamer und Airguns z.W.

Profil # 1-2

14:12 Beginn Profil # 1-2 33°30,0'S 071°56,0'W
 14:38 Magnetometer z.W.
 16:12 Ende Profil # 1-2 33°30,0'S 072°05,6'W
 Wind: NNE 4 See: 3
 16:15 - 16:35 Arbeiten am Streamer.

Profil # 2-3

16:55 Beginn Profil # 2-3 33°30,0'S 072°05,6'W
13.04.95 Zeit: UTC - 4h
 09:49 Ende Profil # 2-3 32°15,1'N 071°55,0'W
 Wind: N'l 4-2 See: 3-1
 09:50 - 10:15 Arbeiten am Streamer.

Profil # 3-4

10:45 Beginn Profil # 3-4 32°15,1'S 071°55,0'W
 21:22 Ende Profil # 3-4 32°13,0'S 072°54,8'W
 Wind: Var. - SW 2 See: 1
 21:23 - 21:58 Arbeiten am Streamer

Profil # 4-5

22:33 Beginn Profil # 4-5 32°13,0'S 072°54,8'W
14.04.95 Zeit: UTC - 4h
 00:18 Ende Profil # 4-5 32°04,6'S 072°54,8'W
 Wind: S 3 See: 2

Profil # 5-6

00:18 Beginn Profil # 5-6 32°04,6'S 072°54,8'W
 12:12 Ende Profil # 5-6 32°04,6'S 071°47,5'W
 Wind: S'l 3-2 See: 1

Profil # 6-7

12:12 Beginn Profil # 6-7 32°04,6'S 071°47,5'W
 12:15 - 13:45 arbeiten am Streamer
 16:45 Ende Profil # 6-7 32°26,1'S 071°44,5'W
 Wind: SSW 3-4 See: 2

Profil # 7-8

16:45 Beginn Profil # 7-8 32°26,1'S 071°44,5'W
 21:25 Ende Profil # 7-8 32°26,1'S 072°10,9'W
 Wind: SW 3-4 See: 2

Profil # 8-9

21:25 Beginn Profil # 8-9 32°26,1'S 072°10,9'W
 22:26 Ende Profil # 8-9 32°30,4'S 072°14,0'W
 Wind: SSW 3 See: 2

Profil # 9-10

22:26 Beginn Profil # 9-10 32°30,4'S 072°14,0'W
15.04.1995 Zeit: UTC - 4h
 03:38 Ende Profil # 9-10 32°30,4'S 071°45,4'W
 Wind: S 3-4 See: 2-3

Profil # 10-11

03:38 Beginn Profil # 10-11 32° 30,4'S 071° 45,4'W
 04:30 Ende Profil # 10-11 32° 35,2'S 071° 45,2'W
 Wind: S 3-4 See: 3

Profil # 11-12

04:30 Beginn Profil # 11-12 32° 35,2'S 071° 45,2'W
 12:30 Ende Profil # 11-12 32° 35,4'S 072° 31,0'W
 Wind: S - SE 3-0 See: 2-0
 12:40 - 13.25 arbeiten am Airgun-Array

Profil # 13-14

13:35 Beginn Profil # 13-14 32° 37,8'S 072° 31,0'W
 21:37 Ende Profil # 13-14 32° 38,7'S 071° 45,4'W
 Wind: Stille bis SW 3 See: 0-2
 21:27 - 22:24 arbeiten am Streamer und am Airgun-Array

Profil # 15-16

23:00 Beginn Profil # 15-16 32° 42,9'S 071° 45,5'W
16.04.1995 Zeit: UTC - 4h
 10:35 Ende Profil # 15-16 32° 42,9'S 072° 51,5'W
 Wind: S 3 - 6 See: 2-5

Profil # 16-17

10:35 Beginn Profil # 16-17 32° 42,9'S 072° 51,5'W
 12:20 Ende Profil # 16-17 32° 51,1'S 072° 51,5'W
 Wind: SSW 5-6 See: 4

Profil # 17-18

12:20 Beginn Profil # 17-18 32° 51,1'S 072° 51,5'W
 17:35 Profilunterbrechung 32° 51,8'S 072° 21,5'W
 arbeiten an Airgun-Array
 18:40 Fortsetzung Profil 32° 51,7'S 072° 25,7'W
 19:12 Profilunterbrechung 32° 51,7'S 072° 22,7'W
 arbeiten an Airgun-Array
 21:18 Fortsetzung Profil 32° 51,6'S 072° 26,4'W
17.04.1995 Zeit: UTC - 4h
 04:12 Ende Profil # 17-18 32° 52,5'S 071° 47,6'W
 Wind: S 6 See: 4

Profil # 18-19

04:12 Beginn Profil # 18-19 32° 52,5'S 071° 47,6'W
 05:04 Ende Profil # 18-19 32° 48,4'S 071° 47,0'W
 Wind: S 7 See: 5

Profil # 19-01

05:04 Beginn Profil # 19-01 32° 48,4'S 071° 47,0'W
 12:00 Ende Profil # 19-01 32° 48,4'S 072° 25,7'W
 Wind: S-SSW 7 See: 5

Profil # 01-02

12:00 Beginn Profil # 01-02 32° 48,4'S 072° 25,7'W
 17:00 Ende Profil # 01-02 32° 30,4'S 072° 06,3'W
 Wind: SSW 7-6 See: 5

17:10 Airguns a.D.

19:55 Airguns z.W.

Station # 010

01.15 Beginn Station # 010 33°08,7'S 072°33,3'W
 01.20 DR z.W. (W 6)
 02.55 DR Boko, Sl 5200 m, Wt 5020 m 33°08,7'S 072°33,3'W
 03.20 Beginn hieven, Sl 5200 m
 04.47 Ende Boko, Sl 3900 m, Wt 3849 m 33°09,9'S 072°32,5'W
 06.18 DR a.D.
 06.35 Ende Station # 010
 Wind: NNE 4-6 See: 3-4

Station # 011

07.12 Beginn Station # 011 33°09,0'S 072°33,7'W
 07.15 DR z.W. (W 6)
 09.00 DR Boko, Sl 5000 m, Wt 4955 m 33°08,9'S 072°33,6'W
 09.09 DR Sl max. 5200 m
 09.41 Beginn hieven, Sl 5200 m
 10.35 Brechen Station ab, Reparatur Seilführungsschlitten.
 10.50 Ende Boko, Sl 5039 m, Wt 4902 m 33°08,9'S 072°33,5'W
 13.00 DR a.D.
 13.18 DR z.W. (W 6)
 14.55 DR Boko, Sl 5200 m, Wt 5021 m 33°08,9'S 072°33,6'W
 15.12 Beginn hieven, Sl 5200 m, Wt 4685 m
 16.25 Ende Boko, Sl 3740 m, Wt 3842 m 33°03,8'S 072°32,2'W
 18.05 DR a.D.
 18.05 Ende Station # 011
 Wind: N'l 3 See: 2

Station # 012

19.14 Beginn Station # 012 33°00,9'S 072°29,5'W
 19.16 CTD/RO z.W. (W 5)
 21.04 CTD/RO Sl max. 4041 m, Wt 4078 m 33°00,9'S 072°29,5'W
 29.04.1995 Zeit: UTC - 4h
 01.20 CTD/RO a.D., Ausfall Seilmessungen. Winde spult schlecht.
 01.40 MUC z.W. (W 6)
 03.10 MUC Boko, Sl 4090 m, Wt 4076 m 33°00,9'S 072°29,5'W
 05.03 MUC a.D.
 05.18 MUC z.W. (W 6)
 06.50 MUC Boko, Sl 4060 m, Wt 4075 m 33°00,9'S 072°29,5'W
 08.30 MUC a.D.
 08.40 SL(12) z.W. (W 6)
 10.19 SL Boko, Sl 4063 m, Wt 4077 m 33°00,9'S 072°29,5'W
 12.25 SL a.D.
 12.30 Ende Station # 012
 Wind: N'l 3-6 See: 2-5

Station # 013

19.44 Beginn Station # 013 32°50,3'S 073°56,6'W
 19.44 DR z.W. (W 6)
 20.30 DR Boko, Sl 2350 m, Wt 2134 m 32°50,2'S 073°56,6'W
 20.50 Haker, Sl 2339 m, Wt 1889 m
 22.20 Ende Boko, Sl 2200 m, Wt 2234 m 32°50,1'S 073°56,8'W
 23.15 DR a.D.
 30.04.1995 Zeit: UTC - 4h
 00.25 DR z.W. (W 6)
 01.10 DR Boko, Sl 2300 m, Wt 2124 m 32°59,5'S 073°54,1'W
 02.05 Beginn hieven Sl 2350 m, Wt 1850 m
 02.25 Haker, Sl 2120 m, Wt 1631 m
 03.10 Ende Boko, Sl 1975 m, Wt 2025 m 32°59,6'S 073°54,3'W

Profil # 02-03

20:34 Beginn Profil # 02-03 32°30,4'S 072°06,3'W
 18.04.1995 Zeit: UTC - 4h
 00:40 Ende Profil # 02-03 32°49,9'S 072°09,6'W
 Wind: SSW 6-5 See: 5-4

Profil # 03-04

00:40 Beginn Profil # 03-04 32°49,9'S 072°09,6'W
 06:00 Ende Profil # 03-04 33°11,2'S 072°25,7'W
 Wind: SSW 6-5 See: 4

Profil # 04-05

06:00 Beginn Profil # 04-05 33°11,2'S 072°25,7'W
 08:00 Ende Profil # 04-05 33°02,2'S 072°29,2'W
 Wind: SSW 5 See: 4

Profil # 05-06

08:00 Beginn Profil # 05-06 33°02,2'S 072°29,2'W
 13:00 Ende Profil # 05-06 33°01,8'S 072°57,8'W
 Wind: SSW 5-3 See: 4-2

Profil # 06-07

13:00 Beginn Profil # 06-07 33°01,8'S 072°57,8'W
 14:00 Ende Profil # 06-07 33°06,8'S 072°58,0'W
 Wind: SW 3-4 See: 3

Profil # 07-08

14:00 Beginn Profil # 07-08 33°06,8'S 072°58,0'W
 19.04.1995 Zeit: UTC - 4h
 00:45 Ende Profil # 07-08 33°13,7'S 071°57,2'W
 Wind: SW - SSW 3-4 See: 3

Profil # 08-09

00:45 Beginn Profil # 08-09 33°13,7'S 071°57,2'W
 06.43 Ende Profil # 08-09 32°46,3'S 072°08,0'W
 Wind: SSW 5 See: 4

Profil # 09-10

06:43 Beginn Profil # 09-10 32°46,3'S 072°08,0'W
 16:00 Ende Profil # 09-10 33°30,4'S 072°12,5'W
 Wind: SSW 5-6 See: 4-5

16:05 Airgun-Array a.D.
 17:07 Airgun-Array z.W.

Profil # 10-11

17:18 Beginn Profil # 10-11 33°30,4'S 072°12,5'W
 17:30 Magnetometer a.D.
 20.04.1995 Zeit: UTC - 4h
 03:50 Ende Profil # 10-11 33°35,2'S 073°12,5'W
 Wind: S 6-7 See: 5

04:02 Airgun-Array a.D.
 05:30 Airgun-Array z.W.

Profil # 12-13

05:54 Beginn Profil # 12-13 33°36,7'S 073°12,6'W
 14:32 Unterbrechen Profil, Gegenkurs 33°48,7'S 072°26,1'W

14:45 Airgun-Array a.D.
 14:55 Streamer a.D.
 17.05 Streamer z.W.
 17:10 Airgun-Array z.W.
 17:40 Fortsetzung Profil auf 33°43,4'S 072°46,9'W
 23:32 Ende Profil # 12-13 33°51,8'S 072°14,6'W
 Wind: SzW 6-5, S 5, SSW 3, NE 2 See: 4-1

Profil # 02-03

23:32 Beginn Profil # 02-03 33°51,8'S 072°14,6'W
 21.04.1995 Zeit: UTC -4
 01:15 Ende Profil # 02-03 34°00,0'S 072°16,1'W
 Wind: NE 2-3 See: 2

Profil # 03-04

01:15 Beginn Profil # 03-04 34°00,0'S 072°16,1'W
 06:23 Ende Profil # 03-04 34°00,0'S 072°45,6'W
 Wind: N 2-3 See: 2

Profil # 04-05

06:23 Beginn Profil # 04-05 34°00,0'S 072°45,6'W
 12:17 Ende Profil # 04-05 33°48,5'S 073°16,9'W
 Wind: N 3 See: 2

Profil # 05-06

12:17 Beginn Profil # 05-06 33°48,5'S 073°16,9'W
 12:25 Airgun-Array a.D.
 12:40 Streamer a.D.
 12:45 Magnetometer z.W.
 13:40 Ende Profil # 05-06 33°36,1'S 073°16,6'W
 Wind: N 4 See: 3

Profil # 06-07

13:40 Beginn Profil # 06-07 33°36,1'S 073°16,6'W
 14:54 Ende Profil # 06-07 33°36,1'S 073°34,1'W
 Wind: N 4 See: 3

Profil # 07-08

14:54 Beginn Profil # 07-08 33°36,1'S 073°34,1'W
 15:41 Ende Profil # 07-08 33°26,6'S 073°34,1'W
 Wind: NNE 4-3 See: 3-2

Profil # 08-09

15:41 Beginn Profil # 08-09 33°26,6'S 073°34,1'W
 16:50 Streamer z.W.
 17:00 Airgun-Array z.W.
 17:30 Ende Profil # 08-09 33°12,5'S 073°42,4'W
 Wind: N 3 See: 2

Profil # 09-10

17:30 Beginn Profil # 09-10 33°12,5'S 073°42,4'W
 22:16 Ende Profil # 09-10 32°51,2'S 073°54,7'W
 Wind: N'l 2 See: 1

Profil # 10-11

22:16 Beginn Profil # 10-11 32°51,2'S 073°54,7'W
 22:57 Ende Profil # 10-11 32°53,7'S 073°57,2'W
 Wind: var. 1 See: 1

Profil # 11-12

22:57 Beginn Profil # 11-12 32°53,7'S 073°57,2'W
 22.04.1995 Zeit: UTC - 4h
 00:20 Ende Profil # 11-12 32°55,1'S 073°49,6'W
 Wind: var. 1 See: 1

Profil # 12-13

00:20 Beginn Profil # 12-13 32°55,1'S 073°49,6'W
 00:25 Airgun-Array a.D.
 00:40 Streamer a.D.
 05:08 Streamer z.W.
 05:16 Airgun-Array z.W.
 05:43 Ende Profil # 12-13 33°07,2'S 072°48,3'W
 Wind: NNW 1-2 See: 1

Profil # 13-14

05:43 Beginn Profil # 13-14 33°07,2'S 072°48,3'W
 08:00 Ende Profil # 13-14 33°17,8'S 072°52,4'W
 Wind: NNW 2 See: 1

Profil # 14-15

08:00 Beginn Profil # 14-15 33°17,8'S 072°52,4'W
 12:25 Ende Profil # 14-15 33°10,5'S 072°27,4'W
 Wind: NE 2 See: 1

Profil # 15-16

12:25 Beginn Profil # 15-16 33°10,5'S 072°27,4'W
 14:32 Ende Profil # 15-16 33°11,1'S 072°22,2'W
 Wind: NE 1 See: 1

Profil # 16-17

14:32 Beginn Profil # 16-17 33°11,1'S 072°22,2'W
 17:05 Ende Profil # 16-17 33°07,7'S 072°08,4'W
 Wind: var. 1-2 See: 1

Profil # 01-02

17:05 Beginn Profil # 01-02 33°07,7'S 072°08,4'W
 17:10 Airgun-Array a.D.
 17:25 Streamer a.D.
 19:35 Ende Profil # 01-02 33°36,2'S 072°11,8'W
 Wind: var. 1 See: 0

Profil # 02-03

19:35 Beginn Profil # 02-03 33°36,2'S 072°11,8'W
 21:28 Ende Profil # 02-03 33°59,5'S 072°18,1'W
 Wind: var. 1 See: 0

Profil # 04-05

21:34 Beginn Profil # 04-05 33°59,5'S 072°16,4'W
 23:33 Ende Profil # 04-05 33°36,2'S 072°10,2'W
 Wind: var. 1 See: 0

Profil # 06-07

23:40 Beginn Profil # 06-07 33°36,2'S 072°08,4'W
 23.04.1995 Zeit: UTC - 4h
 01.35 Ende Profil # 06-07 33°59,2'S 072°15,1'W
 Wind: var. 1 See: 0

Profil # 08-09

01:40 Beginn Profil # 08-09 33°59,5'S 072°13,7'W
 04:06 Ende Profil # 08-09 33°31,5'S 072°05,7'W
 Wind: SSE 2 See: 1

Profil # 10-11

04:13 Beginn Profil # 10-11 33°31,5'S 072°04,4'W
 07:31 Ende Profil # 10-11 33°59,5'S 072°12,3'W
 Wind: SSE 1-2 See: 1

Profil # 12-13

07:37 Beginn Profil # 12-13 33°59,5'S 072°11,2'W
 08:50 Ende Profil # 12-13 33°31,5'S 072°03,2'W
 Wind:

Profil # 14-15

08:57 Beginn Profil # 14-15 33°31,5'S 072°01,8'W
 10:13 Ende Profil # 14-15 33°47,5'S 072°06,5'W
 Wind:

Profil # 16-17

10:19 Beginn Profil # 16-17 33°47,5'S 072°05,2'W
 11:34 Ende Profil # 16-17 33°31,3'S 072°00,7'W
 Wind: SSW 2 See: 1

Profil # 17-18

11:34 Beginn Profil # 17-18 33°31,3'S 072°00,7'W
 12:00 Ende Profil # 17-18 33°31,3'S 071°54,4'W
 Wind: SSW 2 See: 1

Profil # 18-19

12:00 Beginn Profil # 18-19 33°31,3'S 071°54,4'W
 12:07 Ende Profil # 18-19 33°32,9'S 071°54,4'W
 Wind: SSW 2-3 See: 1-2

Profil # 19-20

12:07 Beginn Profil # 19-20 33°32,8'S 071°54,4'W
 12:30 Ende Profil # 19-20 33°32,8'S 071°59,8'W
 Wind: SSW 2-3 See: 1-2

Profil # 20-21

12:30 Beginn Profil # 20-21 33°32,8'S 071°59,8'W
 12:33 Ende Profil # 20-21 33°33,7'S 071°59,8'W
 Wind: SSW 2-3 See: 1-2

Profil # 21-22

12:33 Beginn Profil # 21-22 33°33,7'S 071°59,8'W
 12:52 Ende Profil # 21-22 33°33,7'S 071°54,8'W
 Wind: SSW 2-3 See: 1-2

13:12 Magnetometer a.D. Ende der wissenschaftlichen Profilmfahrten.

Numbering of dredge and core stations was consecutive in the bridge whereas dredge and core stations were separated in the scientific descriptions. The equivalent stations are as follows:

ships log number	core & dredge number
001	C1
002	C2
003	C3
004	D1
005	D2
006	C4 (C+D)
007	C5
008	D3
009	D4
010	D5
011	D6
012	C6
013	D8
014	D9
015	C7
016	C8
017	D10

ships log number	core & dredge number
018	C8
019	D11
020	D12
021	C9
022	D13 D14
023	C10
024	D15
025	D16
026	D17
027	D18
028	D19
029	D20
030	D21
031	D22
032	D23
033	C11

Anhang zum Kapitansbericht 05/95 Reise SO 101/3

Der dritte Abschnitt der Reise SO 101 war der geologischen Beprobung vorbehalten.

Am 25. April 1995 um 16.00 Uhr begannen wir die Stationsarbeiten. Als erstes Gerät wurde der Multicorer eingesetzt. Nach einem Fehlversuch, die Einstellung der Vorspannung der Verschlüsse mußte erst optimal eingestellt werden, kam beim zweiten Einsatz eine gute Probe an Deck. Anschließend sollte der Kleinkastengreifer zum Einsatz kommen. Aber da die Auslösesicherung erst geändert werden mußte nahmen wir das Gerät wieder an Deck. Der Einsatz eines 12 m Schwerelots lief problemlos.

Die Auslösesicherung des Kleinkastengreifers wurde am 26. April geändert. Auf der Station # 6 kam er auch am 27. April zum Einsatz. Leider legte sich eine Bucht des Tiefseeseils um das Gerät, sodaß es nicht schloß. Anschließend wurde der Kleinkastengreifer nicht mehr eingesetzt.

Auf der Station # 4 wurde am 26. April der erste Dredgeinsatz gefahren. Damit waren alle Geräte zur Erlangung von geologischen Proben einmal zum Einsatz gekommen.

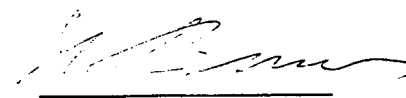
Die Stationsfolge lief ohne Probleme ab. Die Dredgeinsätze am San Antonio Canyon blieben allerdings erfolglos. Erst beim 11 Einsatz brachte die Dredge das gewünschte Material an Deck. Allerdings ließ die Dredge bei diesem Einsatz auch alle Zähne einer Seite. Selbst die Aufhängung erlitt Verbiegungen. Die maximal Lasten auf der Lastanzeige der geologischen Winde lag bei 14 to wie auch schon auf anderen Stationen.

Die tiefste Station für ein Schwerelot wurde am 3. Mai 1995 auf 5419 m gefahren. Am 04. Mai wurde in dieser Tiefe noch einmal der Kleinkastengreifer erfolgreich eingesetzt. Die maximal ausgesteckte Seillänge an der Geologiewinde betrug 5450 m auf einer Dredgestation bei einer Wassertiefe von 4951 m. Am 06.05.1995 um 09.05 Uhr beendeten wir die wissenschaftlichen Stationsarbeiten und traten die Reise nach Valparaiso an.

Auf insgesamt 33 Stationen wurden 6 mal das Schwerelot mit 12 m Rohrlänge, 6 mal das Schwerelot mit 6 m Rohrlänge, 11 mal der Multicorer, 3 mal der Kleinkastengreifer und 24 mal die Dredge mit der Geologiewinde eingesetzt. Die CTD-Wasserschöpferrosette wurde 3 mal mit der Hydrographiewinde II am Rochesterkabel gefahren.

Mit dem Wetter hatten wir Glück. Nur vom 01. Mai um 20.00 Uhr bis zum 2. Mai um 12.00 Uhr mußten wir bei Windstärken um 8 und einer hohen Dünung die Arbeiten einstellen. Die vorherrschende Windrichtung war Süd bis Südwest mit Windstärken um Bft. 5. Nur an den ersten 4 Tagen der Reise wehte ein Nordwestwind mit Bft. zwischen 3 und 6. Aber an allen Tagen läuft in diesem Seegebiet eine ausgeprägte südwestliche Dünung.

Auf See, den 06. Mai 1995


H. Bruns
Kapitän

STATIONSPROTOKOLL F.S. "SONNE" SO-101/3

25.04.1995

Zeit: UTC - 4h

16.00 Beginn der wissenschaftlichen Stationsarbeiten.

Station # 001

16.00 Beginn Station # 001 33°08,7'S 071°58,9'W
 16.00 MUC z.W. (W 6)
 16.25 MUC Boko, Sl 965 m, Wt 969 m 33°08,8'S 071°58,9'W
 16.50 MUC a.D.
 17.15 MUC z.W. (W 6)
 17.37 MUC Boko, Sl 971 m, Wt 970 m 33°08,8'S 071°58,9'W
 18.05 MUC a.D.
 18.33 KKG z.W. (W 6)
 18.39 KKG a.D. Auslösesicherung muß geändert werden.
 20.15 SL(12) z.W. (W 6)
 20.33 SL Boko, Sl 964 m, Wt 974 m 33°08,8'S 071°58,9'W
 21.15 SL a.D.
 21.15 Ende Station # 001
 Wind: SSW 3 See: 2

Station # 002

22.20 Beginn Station # 002 33°13,2'S 072°05,2'W
 22.55 SL(6) z.W. (W 6)
 23.35 SL Boko, Sl 1492 m, Wt 1498 m 33°13,1'S 072°05,4'W

16.04.1995

Zeit: UTC - 4h

00.32 SL a.D.
 01.13 MUC z.W. (W 6)
 01.45 MUC Boko, Sl 1497 m, Wt 1502 m 33°13,1'S 072°05,4'W
 02.23 MUC a.D.
 02.30 Ende Station # 002
 Wind: SSW 2 - S'l 1 See: 1

Station # 003

03.15 Beginn Station # 003 33°12,4'S 072°10,5'W
 03.35 MUC z.W. (W 6)
 04.15 MUC Boko, Sl 1940 m, Wt 1983 m 33°12,4'S 072°10,5'W
 05.04 MUC a.D.
 05.28 SL(6) z.W. (W 6)
 06.14 SL Boko, Sl 1941 m, Wt 1984 m 33°12,4'S 072°10,5'W
 07.10 SL a.D.
 07.17 Ende Station # 003
 Wind: E'l 1 - Stille See: 0

Station # 004

08.15 Beginn Station # 004 33°10,4'S 072°18,0'W
 08.17 DR z.W. (W 6)
 09.55 DR Boko, Sl 3400 m, Wt 3357 m 33°10,3'S 072°19,7'W
 10.19 DR Sl max. 3500 m, Wt 3360 m
 10.57 DR Beginn hieven
 12.12 DR Ende Boko, Sl 2400m, WT 2402m 33°10,6'S 072°22,1'W
 13.05 DR a.D.
 13.20 Ende Station # 004
 Wind: N'l 2 See: 1

Station # 005

13.45 Beginn Station # 005 33°09,5'S 072°20,0'W
 13.55 DR z.W. (W 6)
 15.00 DR Boko, Sl max.3500 m, Wt 3480 m 33°09,5'S 072°20,1'W
 15.23 DR Beginn hieven
 16.23 DR Ende Boko, Sl 2463m, Wt 2480m 33°09,8'S 072°21,7'W
 17.20 DR a.D.
 17.30 Ende Station # 005
 Wind: N'l 2 See: 1

Station # 006

19.28 Beginn Station # 006 32°53,4'S 072°11,5'W
 19.28 CTD/RO z.W. (W 5)
 20.24 CTD/RO Sl max. 2372m, Wt 2412m 32°53,3'S 072°11,6'W
 21.55 CTD/RO a.D.
 22.19 CTD/RO z.W. (W 5)
 22.35 CTD/RO Sl max. 500m, Wt 2411m 32°53,4'S 072°11,6'W
 23.08 CTD/RO a.D.
 23.22 MUC z.W. (W 6)

27.04.1995Zeit: UTC - 4h

00.13 MUC Boko, Sl 2395 m, Wt 2413 m 32°53,4'S 072°11,5'W
 01.13 MUC a.D.
 02.05 KKG z.W. (W 6)
 02.55 KKG Boko, Sl 2416 m, Wt 2412 m 32°53,4'S 072°11,5'W
 04.00 KKG a.D. nicht ausgelöst durch Schlinge des Tiefseeseils.
 04.38 SL(12) z.W. (W 6)
 05.32 SL Boko, Sl 2393 m, Wt 2411 m 32°53,4'S 072°11,5'W
 06.40 SL a.D.
 06.48 Ende Station # 006
 Wind: NNE 4-5 See: 3

Station # 007

08.00 Beginn Station # 007 32°51,1'S 072°25,4'W
 08.12 SL(12) z.W. (W 6)
 09.09 SL Boko, Sl 3006 m, Wt 3028 m 32°51,1'S 072°25,4'W
 10.30 SL a.D.
 10.40 MUC z.W. (W 6)
 11.45 MUC Boko, Sl 3006 m, Wt 3029 m 32°51,1'S 072°25,4'W
 13.05 MUC a.D.
 13.10 Ende Station # 007
 Wind: N'l & See: 4-5

Station # 008

14.33 Beginn Station # 008 33°06,5'S 072°26,6'W
 14.37 DR z.W. (W 6)
 15.55 DR Boko, Sl 4300 m, Wt 4110 m 33°06,6'S 072°26,6'W
 16.45 Beginn hieven, Sl 4300 m
 17.18 Ende Boko, Sl 3100 m, Wt 3197 m 33°07,1'S 072°25,5'W
 18.43 DR a.D.
 18.48 Ende Station # 008
 Wind: N'l 6 See: 5

Station # 009

19.20 Beginn Station # 009 33°04,5'S 072°28,3'W
 19.23 DR z.W. (W 6)
 20.56 DR Boko, Sl 4850 m, Wt 4689 m 33°04,1'S 072°28,3'W
 21.10 Beginn hieven, Sl 4850 m
 22.25 Ende Boko, Sl 3700 m, Wt 3776 m 33°03,1'S 072°28,6'W

28.04.1995Zeit: UTC -4

00.25 DR a.D.
 00.35 Ende Station # 009
 Wind: N'l 6-4 See: 5-3

Station # 010

01.15 Beginn Station # 010 33°08,7'S 072°33,3'W
 01.20 DR z.W. (W 6)
 02.55 DR Boko, Sl 5200 m, Wt 5020 m 33°08,7'S 072°33,3'W
 03.20 Beginn hieven, Sl 5200 m
 04.47 Ende Boko, Sl 3900 m, Wt 3849 m 33°09,9'S 072°32,5'W
 06.18 DR a.D.
 06.35 Ende Station # 010
 Wind: NNE 4-6 See: 3-4

Station # 011

07.12 Beginn Station # 011 33°09,0'S 072°33,7'W
 07.15 DR z.W. (W 6)
 09.00 DR Boko, Sl 5000 m, Wt 4955 m 33°08,9'S 072°33,6'W
 09.09 DR Sl max. 5200 m
 09.41 Beginn hieven, Sl 5200 m
 10.35 Brechen Station ab, Reparatur Seilführungsschlitten.
 10.50 Ende Boko, Sl 5039 m, Wt 4902 m 33°08,9'S 072°33,5'W
 13.00 DR a.D.
 13.18 DR z.W. (W 6)
 14.55 DR Boko, Sl 5200 m, Wt 5021 m 33°08,9'S 072°33,6'W
 15.12 Beginn hieven, Sl 5200 m, Wt 4685 m
 16.25 Ende Boko, Sl 3740 m, Wt 3842 m 33°03,8'S 072°32,2'W
 18.05 DR a.D.
 18.05 Ende Station # 011
 Wind: N'l 3 See: 2

Station # 012

19.14 Beginn Station # 012 33°00,9'S 072°29,5'W
 19.16 CTD/RO z.W. (W 5)
 21.04 CTD/RO Sl max. 4041 m, Wt 4078 m 33°00,9'S 072°29,5'W
29.04.1995 **Zeit: UTC - 4h**
 01.20 CTD/RO a.D., Ausfall Seilmessungen. Winde spult schlecht.
 01.40 MUC z.W. (W 6)
 03.10 MUC Boko, Sl 4090 m, Wt 4076 m 33°00,9'S 072°29,5'W
 05.03 MUC a.D.
 05.18 MUC z.W. (W 6)
 06.50 MUC Boko, Sl 4060 m, Wt 4075 m 33°00,9'S 072°29,5'W
 08.30 MUC a.D.
 08.40 SL(12) z.W. (W 6)
 10.19 SL Boko, Sl 4063 m, Wt 4077 m 33°00,9'S 072°29,5'W
 12.25 SL a.D.
 12.30 Ende Station # 012
 Wind: N'l 3-6 See: 2-5

Station # 013

19.44 Beginn Station # 013 32°50,3'S 073°56,6'W
 19.44 DR z.W. (W 6)
 20.30 DR Boko, Sl 2350 m, Wt 2134 m 32°50,2'S 073°56,6'W
 20.50 Haker, Sl 2339 m, Wt 1889 m
 22.20 Ende Boko, Sl 2200 m, Wt 2234 m 32°50,1'S 073°56,8'W
 23.15 DR a.D.
30.04.1995 **Zeit: UTC - 4h**
 00.25 DR z.W. (W 6)
 01.10 DR Boko, Sl 2300 m, Wt 2124 m 32°59,5'S 073°54,1'W
 02.05 Beginn hieven Sl 2350 m, Wt 1850 m
 02.25 Haker, Sl 2120 m, Wt 1631 m
 03.10 Ende Boko, Sl 1975 m, Wt 2025 m 32°59,6'S 073°54,3'W
 04.00 DR a.D.
 04.10 Ende Station # 013
 Wind: NW 4 - SW 3 See: 3-2

Station # 014

04.55 Beginn Station # 014 32°58,5'S 073°56,5'W
 05.00 DR z.W. (W 6)
 05.41 DR Boko, Sl 2035 m, Wt 1975 32°58,5'S 073°56,4'W
 06.15 Beginn hieven Sl 2200 m, Wt 1830 m
 06.17 Haker, Sl 2192 m, Wt 1830 m
 07.17 Ende Boko, Sl 2018 m, Wt 2100 m 32°58,7'S 073°56,4'W
 08.11 DR a.D.
 08.11 Ende Station # 014
 Wind: SW 3 See: 2

Station # 015

09.10 Beginn Station # 015 32°53,9'S 073°54,6'W
 09.23 SL(6) z.W. (W 6)
 09.35 SL Boko, Sl 426 m, Wt 435 m 32°54,2'S 073°54,6'W
 09.56 SL a.D.
 10.15 SL(6) z.W. (W 6)
 10.28 SL Boko, Sl 420 m, Wt 432 m 32°53,9'S 073°54,6'W
 10.50 SL a.D.
 10.54 Ende Station # 015
 Wind: SW 3 See: 2

Station # 016

12.25 Beginn Station # 016 33°07,9'S 073°44,9'W
 12.30 SL(12) z.W. (W 6)
 13.45 SL Boko, Sl 3597 m, Wt 3625 m 33°07,9'S 073°44,9'W
 15.30 SL a.D.
 16.20 SL(12) z.W. (W 6)
 17.32 SL Boko, Sl 3604 m, Wt 3621 m 33°07,9'S 073°44,9'W
 19.02 SL a.D.
 19.16 MUC z.W. (W 6)
 20.30 MUC Boko, Sl 3604 m, Wt 3620 m 33°07,9'S 073°44,9'W
 21.57 MUC a.D.
 22.00 Ende Station # 016
 Wind: SSW 3 See: 2

Station # 017

23.04 Beginn Station # 017 32°58,7'S 073°53,5'W
 23.04 DR z.W. (W 6)
01.05.1995 Zeit: UTC - 4h
 00.10 DR Boko, Sl 2100 m, Wt 1935 m 32°58,5'S 073°53,5'W
 00.45 Beginn hieven, Sl 2100 m, Wt 1680 m
 00.55 DR Haker,
 01.40 Ende Boko, Sl 1890 m, Wt 1989 m
 01.55 Erneut Boko, Sl 2000 m, Wt 1593 m 32°58,6'S 073°53,6'W
 02.45 Beginn hieven, Sl 2030 m, Wt 1593 m
 03.05 Haker, Sl 1898 m, Wt 1551 m
 04.26 Ende Boko, Sl 1546 m, Wt 1587 m 32°58,0'S 073°53,7'W
 05.04 DR a.D.
 05.15 Ende Station # 017
 Wind: S 6 See: 4-5

Station # 018

11.28 Beginn Station # 018 33°07,9'S 073°44,9'W
 11.31 MUC z.W. (W 6)
 12.47 MUC Boko, Sl 3632 m, Wt 3631 m 33°07,9'S 073°44,9'W
 14.13 MUC a.D.
 14.25 Ende Station # 018
 Wind: S'l 6-7 See: 5-6

20.00 - 24.00 wettern ab.

02.05.1995

Zeit: UTC - 4h

00.00 - 12.00 wettern ab.

Station # 019

12.45 Beginn Station # 019 33°08,5'S 072°31,4'W
 12.50 DR z.W. (W 6)
 14.25 DR Boko, Sl 5000 m, Wt 4887 m 33°08,6'S 072°31,4'W
 14.55 DR Beginn hieven Sl 5000 m, Wt 4498 m
 16.45 Ende Boko, Sl 3860 m, Wt 3860 m 33°09,9'S 072°32,5'W
 18.00 DR a.D.
 18.00 Ende Station # 19
 Wind: S'l 6 See: 4-5

Station # 020

18.37 Beginn Station # 020 33°08,4'S 072°30,9'W
 18.40 DR z.W. (W 6)
 20.22 DR Boko, Sl 5081 m, Wt 4903 m 33°08,4'S 072°31,0'W
 21.05 Beginn hieven, Sl 5130 m, Wt 4610 m
 22.42 Ende Boko, Sl 3800 m, Wt 3800 m 33°09,8'S 072°31,6'W

03.05.1995Zeit: UTC - 4h

00.15 DR a.D.
 00.28 Ende Station # 020
 Wind: S'l 6-5 See: 4

Station # 021

02.20 Beginn Station # 021 33°09,4'S 072°49,4'W
 02.48 SL(6) z.W. (W 6)
 04.30 SL Boko, Sl 5326 m, Wt 5419 m 33°09,4'S 072°49,4'W
 07.07 SL a.D.
 07.10 Ende Station # 021
 Wind: S'l 5 See: 4

Station # 022

08.45 Beginn Station # 022 33°08,5'S 072°33,4'W
 09.15 DR z.W. (W 6)
 10.50 DR Boko, Sl 5250 m, Wt 5073 m 33°08,6'S 072°33,3'W
 11.12 Beginn hieven, Sl 5250 m, Wt 4761 m
 12.40 Ende Boko, Sl 3880 m, Wt 3901 m 33°09,7'S 072°32,3'W
 14.25 DR a.D.
 15.00 DR z.W. (W 6)
 16.35 DR Boko, Sl 5250 m, Wt 5026 m 33°08,6'S 072°33,3'W
 16.50 Beginn hieven, Sl 5250 m, Wt 4850 m
 18.00 Ende Boko, Sl 3900 m, Wt 3967 m 33°09,6'S 072°32,5'W
 19.40 DR a.D.
 19.40 Ende Station # 022
 Wind: S'l 4 See: 3

Station # 023

22.20 Beginn Station # 023 33°14,6'S 072°50,3'W
 22.20 KKG z.W. (W 6)

04.05.1995Zeit: UTC - 4h

00.05 KKG Boko, Sl 5387 m, Wt 5412 m 33°14,6'S 072°50,3'W
 02.30 KKG a.D.
 02.45 Ende Station # 023
 Wind: SW 4-5 See: 3

Station # 024

07.00 Beginn Station # 024 32°35,7'S 072°35,0'W
 07.03 DR z.W. (W 6)
 08.36 DR Boko, Sl 5150 m, Wt 4961 m 32°35,9'S 072°35,0'W
 09.24 Beginn hieven, Sl 5150 m, Wt 4661 m
 11.00 Ende Boko, Sl 3350 m, Wt 3372 m 32°37,8'S 072°32,5'W
 12.15 DR a.D.
 12.20 Ende Station # 024
 Wind: S'l 5-4 See: 3

Station # 025

13.00 Beginn Station # 025 32°35,6'S 072°34,8'W
 13.05 DR z.W. (W 6)
 14.45 DR Boko, Sl 5200 m, Wt 4974 m 32°35,6'S 072°34,7'W
 15.45 Beginn hieven, Sl 5200 m, Wt 4712 m
 17.45 Ende Boko, Sl 3666 m, Wt 3680 m 32°37,2'S 072°33,2'W
 18.46 DR a.D.
 18.46 Ende Station # 025
 Wind: S'l 4-5 See: 3

Station # 026

20.08 Beginn Station # 026 32°36,6'S 072°37,8'W
 20.08 DR z.W. (W 6)
 22.00 DR Boko, Sl 5450 m, Wt 5210 m 32°36,8'S 072°37,7'W
 22.52 Beginn hieven, Sl 5450 m, Wt 4951 m

05.05.1995Zeit: UTC - 4h

00.30 Ende Boko, Sl 4450 m, Wt 4463 m 32°37,6'S 072°36,8'W
 01.55 DR a.D.
 02.00 Ende Station # 026
 Wind: SSW 5 See: 3-4

Station # 027

03.30 Beginn Station # 027 32°53,5'S 072°29,8'W
 03.35 DR z.W. (W 6)
 04.45 DR Boko, Sl 3521 m, Wt 3424 m 32°53,4'S 072°29,8'W
 04.48 Sl max. 3600 m
 05.23 Beginn hieven, Sl 3600 m, Wt 3054 m
 06.08 Ende Boko, Sl 2611 m, Wt 2579 m 32°53,6'S 072°28,2'W
 06.57 DR a.D.
 07.00 Ende Station # 027
 Wind: SSW 5 See: 3-4

Station # 028

07.43 Beginn Station # 028 33°01,2'S 072°28,2'W
 07.48 DR z.W. (W 6)
 09.01 DR Boko, Sl 4200 m, Wt 3999 m 33°01,2'S 072°28,2'W
 09.55 Beginn hieven, Sl 4200 m, Wt 3628 m
 11.55 Ende Boko, Sl 2850 m, Wt 2865 m 33°01,0'S 072°25,3'W
 12.42 DR a.D.
 12.48 Ende Station # 028
 Wind: SSW 5 See: 3-4

Station # 029

13.45 Beginn Station # 029 33°07,5'S 072°17,0'W
 13.50 DR z.W. (W 6)
 14.47 DR Boko, Sl 3300 m, Wt 3282 m 33°07,6'S 072°17,1'W
 15.22 Beginn hieven, Sl 3300 m, Wt 2789 m
 16.05 Ende Boko, Sl 2463 m, Wt 2519 m 33°06,9'S 072°16,1'W
 16.55 DR a.D.
 17.00 Ende Station # 029
 Wind: SSW 6-7 See: 4-5

Station # 030

18.30 Beginn Station # 030 33°19,9'S 072°17,7'W
 18.31 DR z.W. (W 6)
 19.31 DR Boko, Sl 3000 m, Wt 2718 m 33°20,2'S 072°18,0'W
 20.00 Beginn hieven, Sl 3000 m, Wt 2411 m
 21.00 Ende Boko, Sl 1950 m, Wt 1988 m 33°21,2'S 072°19,0'W
 21.35 DR a.D.
 21.35 Ende Station # 030
 Wind: SSW 6-7 See: 5

Station # 031

22.45 Beginn Station # 031 33°15,3'S 072°18,9'W
 22.45 DR z.W. (W 6)
 23.45 DR Boko, Sl 3100 m, Wt 2811 m 33°15,5'S 072°19,0'W
06.05.1995 Zeit: UTC - 4h
 00.12 Beginn hieven, Sl 3100 m, Wt 2573 m
 01.05 Ende Boko, Sl 2350 m, Wt 2417 m 33°16,5'S 072°19,6'W
 01.50 DR a.D.
 02.00 Ende Station # 031
 Wind: SSW 5 See: 4

Station # 032

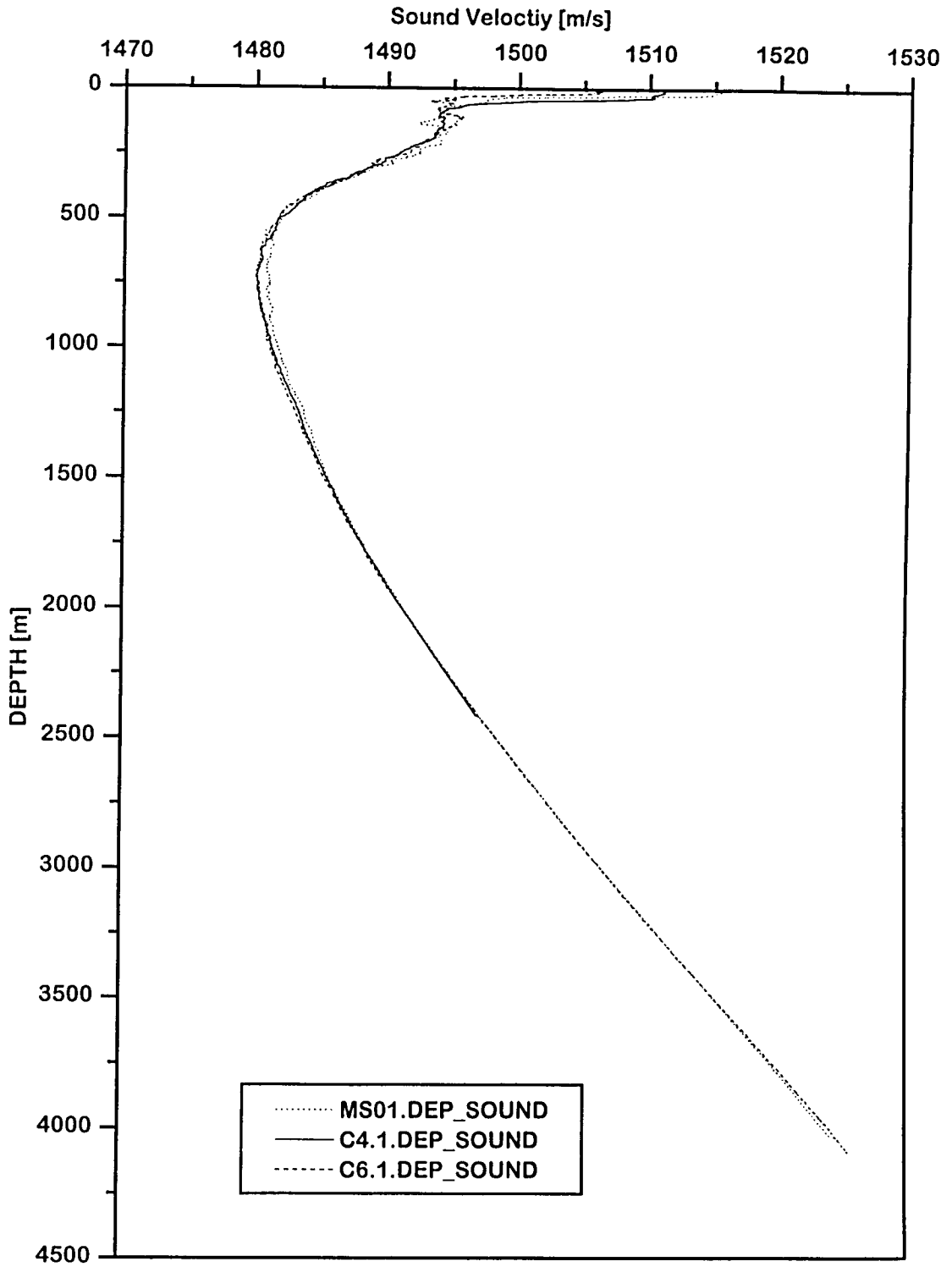
03.10	Beginn Station # 032	33°26,1'S 072°09,7'W
03.15	DR z.W. (W 6)	
04.00	DR Boko, Sl 2250 m, Wt 2049 m	33°26,2'S 072°09,7'W
04.10	Beginn hieven, Sl 2250 m, Wt 1720 m	
04.48	Ende Boko, Sl 1410 m, Wt 1365 m	33°26,1'S 072°10,7'W
05.20	DR a.D.	
05.20	Ende Station # 032	
Wind:	SSW - S 5	See: 4

Station # 033

06.34	Beginn Station # 033	33°36,5'S 072°02,8'W
06.45	SL(6) z.W. (W 6)	
07.02	SL Boko, Sl 468 m, Wt 472 m	33°36,5'S 072°02,8'W
07.19	SL a.D.	
07.38	MUC z.W. (W 6)	
07.50	MUC Boko, Sl 468 m, Wt 472 m	33°36,5'S 072°02,8'W
08.03	MUC a.D.	
08.05	Ende Station # 033	
Wind:	SSW-S 5	See: 4

08.05 Ende der wissenschaftlichen Stationsarbeiten.

CRUISE: SO101 STATIONS: MS01, C4, C6



Converted from file: J:\SO101\c4_lup.mer

>>> R / V S O N N E --- MULTISONDEN - DATEN <<<

```

-----
Fahrt:      SONNE 101-3                GEOMAR - KIEL
Areal:      CONDOR                    Latitude:   32° 53.40' S
Station:    MS 06, C4                 Longitude: 072° 11.50' W
Date (UTC): 27-APR-1995              SONDE:    KMS086
File:       C4_1, C4_lup, C4_2, C4_2up

```

```

Input-File:  sol101\c4_lup.asc          calculated with program DEPTH
Output-File:  sol101\c4_lup.DEP        used formulas from UNESCO 1981
Protocol-File: sol101\c4_lup.P32'53.40' latitude used for calculation
Errorlog-File: no errors                0 records per arith. mean (dep-File)
-----

```

First cast:

PROBE No.	DEPTH [m]	PRESS [dbar]	Temp [°C]	THETA [°C]	SAL [ppt]	O2 [mg/l]	TRANS [%]	COND [mS]
12	626.1	631.5	5.221	5.169	34.372	3.29	95.59	33.393
11	726.9	733.4	4.663	4.605	34.398	2.81	95.79	32.963
10	827.6	835.1	4.296	4.232	34.445	2.59	95.96	32.722
9	927.0	935.7	4.014	3.944	34.499	2.50	96.08	32.561
8	1030.0	1039.9	3.719	3.642	34.541	2.49	96.30	32.380
7	1130.6	1141.7	3.495	3.412	34.576	2.51	96.49	32.255
6	1231.8	1244.2	3.323	3.233	34.598	2.58	96.66	32.166
5	1332.6	1346.4	3.107	3.011	34.621	2.73	96.78	32.037
4	1534.7	1551.3	2.768	2.658	34.655	2.90	97.15	31.853
3	1833.6	1854.8	2.378	2.248	34.690	3.10	97.91	31.666
2	2141.1	2167.4	2.094	1.941	34.716	3.31	98.67	31.564
1	2414.3	2445.6	1.903	1.729	34.731	3.49	99.08	31.519

Second cast:

PROBE No.	DEPTH [m]	PRESS [dbar]	Temp [°C]	THETA [°C]	SAL [ppt]	O2 [mg/l]	TRANS [%]	COND [mS]
11	21.8	22.0	16.315	16.312	34.409	1.94	92.99	43.558
10	54.8	55.2	12.579	12.572	34.250	1.67	93.99	39.803
9	74.4	74.9	11.584	11.575	34.290	1.43	94.14	38.911
8	135.6	136.6	10.802	10.785	34.548	.65	94.48	38.462
7	187.4	188.8	10.450	10.428	34.677	.85	94.62	38.282
6	238.3	240.1	9.748	9.721	34.645	1.18	94.72	37.614
5	288.6	290.9	8.800	8.769	34.600	1.50	94.77	36.710
4	339.5	342.2	8.066	8.031	34.558	1.85	94.86	36.015
3	389.0	392.1	7.217	7.179	34.494	2.19	94.96	35.200
2	442.4	446.0	6.565	6.524	34.460	2.25	95.07	34.599
1	498.3	502.4	6.104	6.060	34.425	1.87	95.16	34.176

Converted from file: J:\S0101\c6_lup.mer

>>> R / V S O N N E --- MULTISONDEN - DATEN <<<

```

-----
Fahrt:      SONNE 101-3          GEOMAR - KIEL
Areal:      CONDOR              Latitude:  33' 00.90' S
Station:    C 6 - MS12          Longitude: 072' 29.50' W
Date (UTC): 27-APR-1995        SONDE:    KMS086
File:       C6_1, C6_lup
    
```

```

-----
Input-File:  sol101\c6_lup.asc      calculated with program DEPTH
Output-File: sol101\c6_lup.DEP      used formulas from UNESCO 1981
Protocol-File: sol101\c6_lup.P33* 0.90' latitude used for calculation
Errorlog-File: sol101\c6_lup.LOG 10 records per arith. mean (dep-File)
    
```

PROBE No.	DEPTH [m]	PRESS [dbar]	Temp [°C]	THETA [°C]	SAL [ppt]	O2 [mg/l]	TRANS [%]	COND [mS]
12	594.9	600.0	5.244	5.195	34.383	3.88	89.31	33.409
10	694.0	700.1	4.800	4.744	34.396	3.51	89.50	33.068
9	790.6	797.7	4.382	4.321	34.450	2.96	89.67	32.786
8	893.5	901.8	4.023	3.955	34.510	2.79	89.83	32.564
7	1018.7	1028.5	3.703	3.627	34.546	2.74	90.04	32.366
6	1421.8	1436.8	2.886	2.784	34.650	3.13	90.81	31.905
5	1928.0	1950.8	2.250	2.114	34.699	3.74	91.80	31.599
4	2463.9	2496.2	1.926	1.747	34.734	4.33	93.16	31.562
3	3036.2	3080.1	1.796	1.564	34.751	4.64	94.80	31.683
11	3056.6	3100.9	1.796	1.562	34.757	4.61	94.80	31.696
2	3541.3	3596.8	1.796	1.512	34.742	4.97	96.19	31.864
1	4093.9	4163.4	1.759	1.414	34.747	5.70	97.69	32.034

Position MS01, S0101-1

-72°19.49' -32°02.0'

water depth: 4,050 m

Time of acquisition: 20:30 23:40 / 24/03/95